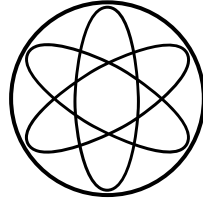


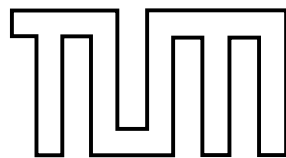
PHYSIK-DEPARTMENT



Radionuclides at MAFF

Dissertation
von

Florian M. Nebel



TECHNISCHE
UNIVERSITÄT
MÜNCHEN

Fakultät für Physik der Technischen Universität München
Physik Department E12

Radionuclides at MAFF

Florian M. Nebel

Vollständiger Abdruck der von der
Fakultät für Physik der Technischen Universität München
zur Erlangung des akademischen Grades eines

Doktors der Naturwissenschaften (Dr. rer. nat.)

genehmigten Dissertation.

Vorsitzender: Univ.-Prof. Dr. M. Kleber
Prüfer der Dissertation:
1. Univ.-Prof. Dr. R. Krücken
2. Univ.-Prof. Dr. O. Zimmer

Die Dissertation wurde am 30.10.2006 bei der Technischen Universität München eingereicht und durch die Fakultät für Physik am 13.12.2006 angenommen.

Für
meinen Vater, meine Mutter
und die ganze Familie

Abstract

The purpose of this work was to re-evaluate and improve important parts of the concept of the Munich Accelerator for Fission Fragments (MAFF) to the point, where the realization and authorization procedure can be started. MAFF is a reactor based next generation radioactive ion beam facility dedicated to the production of neutron-rich rare isotopes for science, medicine, and industry, with ion beam intensities about thousand times higher compared to present installations. In order to produce fission fragments in an ion source close to the reactor core and extract them out of the reactor environment it is necessary to move ion source and extraction optics on rail-bound trollies into the through going vacuum tube. After the extraction, the ions are mass-separated and transported to low and high energy experiments.

Within the scope of this work all safety and user relevant aspects of MAFF have been studied with a clear emphasis on radiation safety and ion beam handling. The outcome of this studies influenced the re-design of the MAFF system.

The ion optic design for the complete low energy beam transport system, from the ion source to the ion beam coolers, has been studied in detail. Special attention had to be paid to the challenges arising from the installation of the facility at a reactor environment, particularly for the design of the in-pile beam transport system. For the design of the mass separator, an in-depth study of a modified Mattauch-Herzog type layout and its unique features has been performed. For the slit system in the focal plane of the mass separator a new concept has been developed, where the slits are designed as electrostatic deflectors, in order to change the mass ratio of the transmitted beams. This would lead to a higher flexibility in the combination of future high and low energy experiments. For the transport of low and high mass beams to the dedicated low and high energy beam coolers, located in the Reactor-Building East, a feasible layout has been developed, giving the possibility to switch the low and high mass beam between the two beam coolers, using electrostatic deflectors.

With respect to radiation safety the spacial distribution and temporal evolution of radionuclides within the MAFF system has been studied. Thereby, special attention has been paid to evaluate the chances of uncontrolled radiation release from the system via multiple routes. A concept of operation accounting for these possibilities has been developed, in addition analyses and risk assessments of conceivable emergency scenarios have been performed. Emergencies are detected by a specially adapted early warning concept. For the time after an emergency has occurred suggestions for reasonable follow-up procedures are made.

Finally, technical investigations of several key components crucial for a safe operation of MAFF have been undertaken. For the surface of the slit system a material was searched for and found, which reduces the sputter factor, and hence the release of previously implanted radionuclides, from the slit system into the vacuum chamber by a factor of thousand. Furthermore, the mechanical behavior and reliability of the two trollies and related systems were investigated at the example of the lens trolley. Also the mechanical properties of gadolinium have been investigated with the aim to verify the possibility of using gadolinium as a neutron absorber at MAFF.

It is the outcome of this work, that it is possible to handle the additional safety challenges of a next generation radioactive ion beam facility, such as MAFF, if new safety features and special operational modes are applied.

Abstrakt

Der Zweck dieser Arbeit war es, wichtige Teile des Konzeptes des Münchner Spaltfragmentbeschleunigers, MAFF (Munich Accelerator for Fission Fragments), im Hinblick auf die technische Realisierung und das anvisierte Genehmigungsverfahren zu verbessern und zu überarbeiten. Bei MAFF handelt es sich um eine an einem Kernreaktor stationierte Anlage zur Produktion neutronenreicher, radioaktiver Ionen für die Verwendung in Forschung, Medizin und Industrie. Als Einrichtung der nächsten Generation bietet MAFF ca. 1000-fach intensivere Ionenstrahlen als gegenwärtige Anlagen. Um die Spaltprodukte aus dem Reaktorbereich extrahieren zu können, werden bei MAFF Ionenquelle und Extraktionsoptik mit auf Schienen fahrenden Wagen in den durchgehenden Neutronenleiter eingebracht. Die extrahierten Ionen werden massensepariert und zu den Nieder- und Hochenergie-Experimenten transportiert.

Im Rahmen dieser Arbeit wurden alle sicherheits- und anwenderrelevanten Aspekte unter dem Gesichtspunkt Strahlenschutz und Strahlhandhabung untersucht. Die Ergebnisse dieser Untersuchungen sind in die Überarbeitung des MAFF Konzeptes eingeflossen, dessen Aufbau in dieser Arbeit in einem Überblick dargestellt wird.

Das komplette ionenoptische System für die Niederenergie-Strahlführung, von der Ionenquelle bis zu den Strahlkühlern, wurde im Detail untersucht. Dabei mußten die Randbedingungen, die sich aus der Installation an einem Reaktor ergeben, besonders bei dem Design des Strahltransportes innerhalb des Reaktors berücksichtigt werden. Als Massenseparator wurde eine Modifikation des Mattauch-Herzog Massenseparators mit ihren besonderen Eigenschaften untersucht. Für das Schlitzsystem hinter dem Massenseparator wurde ein neues Konzept entwickelt, das die Konstruktion der Schlitze selbst als elektrostatische Deflektoren vorsieht und so die Möglichkeit bietet, das Massenverhältnis der transmittierten Strahlen zu verändern, was eine größere Flexibilität bei der Kombination zukünftiger Experimente ermöglicht. Für den anschließenden Transport der Ionenstrahlen leichter und schwerer Masse zu den dedizierten Nieder- und Hochenergie-Strahlkühlern im Reaktorgebäude Ost wurde eine mögliche Anordnung entwickelt, die auch eine Möglichkeit vorsieht die Ionenstrahlen leichter und schwerer Masse zwischen den Strahlkühlern umzuschalten.

Zur besseren Beurteilung der Belastung durch γ -Strahlung wurde die räumliche Ausbreitung sowie die zeitliche Entwicklung der Radionuklide innerhalb des MAFF Systems untersucht. Dabei wurde besonderer Wert auf die Beurteilung der Wahrscheinlichkeiten für unkontrollierte Freisetzung von Strahlung über verschiedenste Wege gelegt, woraus ein Betriebskonzept, welches diese Möglichkeiten in Betracht zieht, entwickelt wurde. Zusätzlich wurden vorstellbare Notfallszenarien analysiert, die mittels eines speziell angepaßten Frühwarnsystems detektiert werden. Darüber hinaus werden Vorschläge für zweckdienliche Folgemaßnahmen gemacht, die in der Zeit nach einem eventuellen Störfall einzuleiten sind.

Des weiteren wurden technische Untersuchungen zahlreicher Schlüsselkomponenten durchgeführt, die für den sicheren Betrieb von MAFF unerlässlich sind. Um die Menge an Radionukliden, die vom Schlitzsystem durch Oberflächenabtrag freigesetzt werden, zu reduzieren, wurde eine experimentelle Suche nach einem Material erfolgreich abgeschlossen, das nur ein tausendstel der einfallenden Radionuklide wieder freisetzt. Darüber hinaus wurde das mechanische Verhalten und die Zuverlässigkeit der Wagen und zugehöriger Teilkomponenten am Beispiel des Linsenwagens untersucht. Eine Materialstudie der mechanischen Eigenschaften von Gadolinium wurde mit dem Ziel begonnen, die Möglichkeiten auszuloten, Gadolinium zur Neutronenabschirmung zu benutzen.

Als Ergebnis dieser Arbeit kann festgestellt werden, dass die zusätzlichen sicherheitstechnischen Anforderungen, die sich für den Betrieb von MAFF ergeben, gemeistert werden können, wenn neue Methoden der Radioaktivitätshandhabung und Betriebsweise angewendet werden.

Contents

1	Introduction	1
1.1	Motivation	1
1.2	Project Overview	2
2	The MAFF Project	7
2.1	MAFF I	7
2.1.1	Source Side	7
2.1.2	Extraction side	14
2.1.3	Common components	17
2.2	MAFF II	18
2.3	Physics program	20
2.3.1	MAFF I	20
2.3.2	MAFF II	21
3	Ion transport	23
3.1	Ion optic design	23
3.1.1	Beam extraction	26
3.1.2	Mass pre-separator	37
3.1.3	Transport to beam coolers	48
3.2	Beam Diagnostics	52
4	Atom distribution	55
4.1	Investigative Tools	55
4.1.1	Time independent simulations	56
4.1.2	Time dependent simulations	58
4.1.3	Analytical calculations	61
4.2	Discussion	63
4.2.1	Contamination by the ion beam	65
4.2.2	Ion gas collisions	66
4.2.3	Neutral isotopes	67
4.2.4	Volatile compounds	71
4.2.5	Aerosols	72
4.2.6	α Activity	75
4.2.7	Activity from delayed neutrons	76
4.2.8	Volume activity	76
4.2.9	Graphite	77
4.2.10	Core radiation	78
4.2.11	Summary	78
4.3	Measurements	78
4.3.1	γ -Radiation in the neutron guide tunnel	79
4.3.2	Neutron radiation in the neutron guide tunnel	82

5	Operational modes	89
5.1	Start-up Phase	89
5.2	Normal operation	91
5.2.1	Maintaining vacuum at all times	91
5.2.2	Regeneration of cryo surfaces	92
5.2.3	Storage in decay tanks	93
5.2.4	Shielding of hot spots	94
5.2.5	Stopping undesirable mass branches	94
5.3	Maintenance procedures	95
5.4	Emergency operation	97
5.4.1	Helium leak	98
5.4.2	Water leak	101
5.4.3	Air leak	101
5.4.4	Summary	102
6	Slit system	105
6.1	Simulations	105
6.2	Experiments	111
6.3	Conclusion	124
7	Technical investigations	127
7.1	Quadrupole triplet	127
7.1.1	Design specifications	127
7.1.2	Tests	130
7.2	Lens Trolley	134
7.2.1	Design specifications	134
7.2.2	Tests	141
7.3	Material analysis	150
7.3.1	Vacuum greases	150
7.3.2	Gadolinium	152
7.4	Conclusion	158
8	Summary and conclusion	161
A	MLL-Emi Manual	163
A.1	Introduction	163
A.2	List of hardware components	163
A.3	Required software	165
A.4	Assembly Instructions	166
A.5	Measurement	167
A.6	Output	168
A.7	General remarks	169
B	Mattauch Herzog separator	171
C	Beam emittance definitions	175
D	Matrix elements	179
E	Radionuclide distribution	185

List of Figures

1.1	Comparison of various mass models to experimental data for Cs isotopes	2
1.2	The MAFF facility. Brief overview	3
1.3	^{235}U fission fragment distribution	4
2.1	Schematic drawing of the MAFF ion source	8
2.2	Surface ionization yields	9
2.3	Photograph of MAFF ion source prototype without heat shields	10
2.4	Source trolley	10
2.5	Source exchange side	11
2.6	Source Exchange Unit	12
2.7	Lead shield locking station	13
2.8	Removing the transport bottle	13
2.9	Extraction side	14
2.10	Vacuum system	16
2.11	Cryo-panel	17
2.12	MAFF II schematics	18
2.13	Beam cooler RF-funnel	19
2.14	ECRIS	20
3.1	Neumann type boundary condition	24
3.2	Energy development in multiplet with Neumann type boundary condition	24
3.3	Dirichlet and Neuman type boundary conditions	25
3.4	Energy development in multiplet with Dirichlet and Neumann type boundary condition	25
3.5	Section 1 COSY calculations	27
3.6	Starting emittance	28
3.7	Emittance after acceleration	28
3.8	Acceleration electrode	29
3.9	Emittance after acceleration with offset	30
3.10	Explanation of tilts in emittance ellipses	31
3.11	Emittance at mass the separator object position for 5 mm offset	31
3.12	Emittance at mass separator object position. No offset compared to 8 mm offset	32
3.13	Summary of section 1 beam transport	33
3.14	Beam tube bending	34
3.15	Consequences of tilt effect	34
3.16	SIMION space charge simulation	35
3.17	Extraction electrode design study	36
3.18	Mattauch-Herzog mass separator	37
3.19	L_3 dependence on L_2 and A	41
3.20	Dependence of mass resolving power on L_2 and A	41
3.21	L_1 dependence on L_2 and A	42
3.22	COSY simulation for separator section	42
3.23	Second-order aberrations in x-a phase space	43

3.24	Emittance and layout of electrostatic deflector.	44
3.25	Emittance after magnetic deflector	45
3.26	Mass resolving power	45
3.27	Influence of hole in ED1	46
3.28	COSY simulation for 2nd and 3rd section	49
3.29	Beam transport to ion cooler.	50
3.30	Beam switch before coolers.	51
3.31	Phase space diagram for heavy mass at dedicated low energy cooler	51
3.32	Phase space diagram for heavy mass at dedicated high energy cooler	52
4.1	Extraction side (A-side) cryo surfaces	56
4.2	Source side cryo surfaces	57
4.3	Sample output of time dependent simulation for ^{133}Te	59
4.4	Sample output of time dependent simulation for ^{91}Kr	60
4.5	Dose rate calculation at slit system	61
4.6	Shielding performance for various elements	62
4.7	Dose rate constant	63
4.8	Ion yield at slit system	64
4.9	Relative percentages of volatile, refractory and ionized particles	65
4.10	Distribution of ^{133}Xe	67
4.11	Aerosol activity relative to legal limit	75
4.12	γ activity measurements in neutron guide tunnel	80
4.13	Dose rate distribution in neutron guide tunnel	80
4.14	Dose rate fit functions	81
4.15	γ -Activity at measured positions in the neutron guide tunnel	81
4.16	Time dependent γ activity in the neutron guide tunnel	81
4.17	Total cross-sections for $^{58}\text{Ni}(n,p)^{58}\text{Co}$ reactions	82
4.18	Positions of neutron detectors in the neutron guide tunnel	84
4.19	Development of neutron flux measured with Co samples	85
4.20	Development of neutron flux measured with Au samples	85
6.1	Schematic drawing of the slit system	105
6.2	Sputter atom yield	107
6.3	Sputter atom energies	108
6.4	Sputter yield reducing slit system layout	109
6.5	Sputtering on a single wedge	110
6.6	Sputtering on multiple wedges	111
6.7	Results of wedge sputtering calculations	112
6.8	Released percentage following cosine distribution	112
6.9	Dependence of the sputter factor on the impact angle	113
6.10	Photograph of the experimental setup for sputter yield measurement	114
6.11	Systematic drawing of the MLL ion source test stand	115
6.12	Typical ion current development in time.	115
6.13	Photograph of the wedge structure	116
6.14	x-Sputter atom distribution on wedge target	118
6.15	y-Sputter atom distribution on wedge target	118
6.16	x-Sputter atom distribution on flat target	118
6.17	y-Sputter atom distribution on flat target	119
6.18	Sputter distribution for Mach12 experiment.	120
6.19	Sputter distribution for Mach50 experiment.	120
6.20	Mach12 iodine sputter matrix	121

6.21	Mach12 copper and steel sputter matrix	122
6.22	POCO graphite iodine sputter distribution	124
6.23	Density dependent carbon sputter yield	125
7.1	Technical drawing of the triplet prototype pole shoe	128
7.2	Picture of the triplet prototype	129
7.3	Schematic setup for the triplet test	130
7.4	Allocation of connectors for the triplet prototype test	131
7.5	Measurement of emittance growth by triplet	133
7.6	Trolley prototype test setup	135
7.7	Breaker-plate-section	135
7.8	Retractable motor unit	136
7.9	Technical drawing of adjustment system	137
7.10	Technical drawing of adjustment system with trolley	137
7.11	Technical drawing of electrical connectors	138
7.12	Technical drawing of one electrical connector	139
7.13	Supply section	140
7.14	Picture of lens trolley prototype	141
7.15	Picture of aluminum support with guiding rolls	142
7.16	Picture of cog wheel engaging the transmission chain	143
7.17	Stepper motor current evolution	144
7.18	Time-position relation for stepper motors	144
7.19	Picture of the fixed motor unit	145
7.20	Picture of the retractable motor unit	146
7.21	Picture of the adjustment system	147
7.22	Hysteresis curve of the adjustment system	148
7.23	Picture of assembled structure of fixed pins	148
7.24	Vacuum compatibility tests	150
7.25	Range of thermal neutrons in Gd	153
7.26	Time dependent isotope composition of Gd in neutron flux	154
7.27	Time dependent cross-section development of Gd	155
7.28	Lump Gd cylinder	156
7.29	Milled Gd pieces	157
7.30	Gd sample tempered to melting point	157
7.31	Gd sample tempered to red heat	158
7.32	Gd samples welded together	158
A.1	MLL-Emi double-cross	164
A.2	MLL-Emi front side	164
A.3	MLL-Emi feedthrough side	165
A.4	Cable Junction	165
A.5	Control Unit front side	166
A.6	MLL-Emi driver config	166
A.7	MLL-Emi configuration of channels	167
A.8	MLL-Emi measurement program	168
C.1	Statistical distribution of points.	176
C.2	Ellipse and Twiss parameters.	177

List of Tables

2.1	Volumes of MAFF vacuum system sections	17
2.2	Beam cooler properties	18
3.1	Meaning of transfer matrix terms	38
3.2	Mass separator values	39
3.3	Comparison of 1st order calculations	43
3.4	Second order Cosy terms	43
3.5	Mass ratio variations	47
4.1	Results of time independent simulations	57
4.2	Comparison of the codes	59
4.3	Isotope dose rates from ion beam	66
4.4	Mass branch dose rates from ion beam	66
4.5	Activity from Kr isotopes	68
4.6	Activity from Br isotopes	68
4.7	Activity from I isotopes	69
4.8	Activity from Xe isotopes	69
4.9	Legal emission limits for various radionuclides	69
4.10	List of volatile compounds	72
4.11	List of volatile compounds (continued)	73
4.12	Tellurium isotopes	73
4.13	Refractory aerosol candidates	74
4.14	Volatile aerosol candidates	74
4.15	Isotope ratio at the slit system	76
4.16	α activity at the slit system	76
4.17	Delayed neutron radiators	77
4.18	Summary of dose rates at centers of contamination	79
4.19	Possible sources for identified isotopes	83
4.20	Specific activity of neutron detectors after irradiation	83
4.21	Neutron flux at irradiation positions	84
4.22	Expected stainless steel activation	86
4.23	Expected aluminum activation	87
5.1	Protective pressure levels	91
5.2	Hot spot overview	94
5.3	Omitted mass branches	94
5.4	Maintenance scenarios	95
5.5	Simple failure matrix	97
5.6	Detailed failure matrix	103
5.7	Severity classes	103
5.8	Occurrence classes	103

6.1	Sputter yields and other data for various elements	106
6.2	Sputter yields and other data for copper iodine alloy	106
6.3	Sputter yields and other data for aluminum alloys	106
6.4	Penetration depth of sputtered atoms	108
6.5	Irradiation conditions for flat and wedge targets	117
6.6	Effective sputter yield for flat and wedge targets	119
6.7	Irradiation conditions for Mach12, Mach50 and POCO targets	120
6.8	Effective sputter yield for Mach12	122
6.9	Effective sputter yield for Mach50	123
6.10	Summary of effective iodine sputter yields	124
7.1	Dependence of test ion source emittance on target distance	132
7.2	Settings of stepper motor parameters	143
7.3	Gadolinium composition	154
7.4	Properties of possible Gd-alloy partners	159
D.1	First and second order COSY terms after magnet	179
D.2	First and second order COSY terms after ED2	180
D.3	First and second order COSY terms after ED3	181
D.4	First and second order COSY terms after T4	182
D.5	First and second order COSY terms after T6	183
D.6	First and second order COSY terms after ED5	184
E.1	⁸⁵ Kr distribution	185
E.2	⁸⁹ Sr distribution	185
E.3	⁹⁰ Y	186
E.4	⁹⁰ Sr	186
E.5	⁹¹ Y distribution	187
E.6	⁹³ Zr distribution	187
E.7	⁹⁵ Nb distribution	187
E.8	⁹⁵ Zr distribution	188
E.9	¹²⁵ Sb distribution	188
E.10	¹²⁹ I distribution	188
E.11	¹³⁵ Cs distribution	188
E.12	¹³⁷ Cs distribution	189
E.13	¹⁴¹ Ce distribution	189
E.14	¹⁴⁴ Ce distribution	189

1 Introduction

1.1 Motivation

Since ancient times, men have been fascinated by exploring the world and by map-making. The unknown areas beyond the established frontiers have always been an important motivation to go where no man has gone before and see what nobody has ever seen. Areas of interest, yet not conquered by men, have been left blank on maps since the days of old and people have always been speculating what might be in those unknown places. Hence tales arose speaking of dragons and sea-monsters that inhabit these realms.

Today, we know better, the whole world has been mapped with great accuracy, so that new discoveries can best be made by investigating phenomena at smaller or larger scales. At the latter, the universe can be studied, but it is far too vast to be conquered, therefore it is unlikely that men will ever succeed in uncovering all its mysteries and there will be always a secret left to reveal. At smaller scales, on the other hand, we find the subatomic world. Everything we see, on earth and in the sky is made from atoms, which were long believed to be the smallest part of matter, but are in fact made of the atomic nucleus and an electron shell. While the electron shell is well understood and theoretically described, the understanding of the nucleus, made from protons and neutrons bound together by the nuclear forces, is still being increased. Hence, the map of the nuclear landscape, the table of isotopes still holds many secrets. One of them is the nature of the *r*-process path, important for describing the synthesis of elements beyond nickel. However, the map still contains many blank areas and its exact borders are only known in one direction, the proton rich side.

Therefore, it is no surprise that scientists all over the world are trying to extend the map and fill in the blanks in the table of isotopes. Hereby, neutron capture was very successful in exploring the north of the map expanding the table of isotopes towards heavy nuclei up to fermium. Even heavier elements, so called super heavy elements, became available with newer methods like hot and cold fusion reactions, with the leading facilities being GSI, Dubna, Berkeley and RIKEN. In the west of the map proton rich nuclei at the proton dripline and nearby are studied for example by facilities like GSI, NSCL/MSU [1], ISOLDE [2, 3, 4] at CERN, RIKEN, and GANIL using radioactive ion beams.

However, reaching the neutron dripline in the east of the map has, so far, only been possible for the lightest elements, but is important for astrophysical models and to test theories concerning the nuclear force. As shown in Fig. 1.1 [5] at the example of Cs isotopes, there are various models calculating the masses for a large number of nuclei. While all models agree fairly well with each other and the experimental data for known isotopes, they tend to disagree if unknown isotopes are described. Therefore, the investigation of neutron-rich nuclei, also studied at the aforementioned facilities, will help to distinguish between different theories and subsequently improve our theoretical understanding of the nuclear forces.

However, theoretical models can not only be tested by comparing their predictions for neutron-rich nuclei with experimental results but also by comparing theoretical predictions for proton rich super

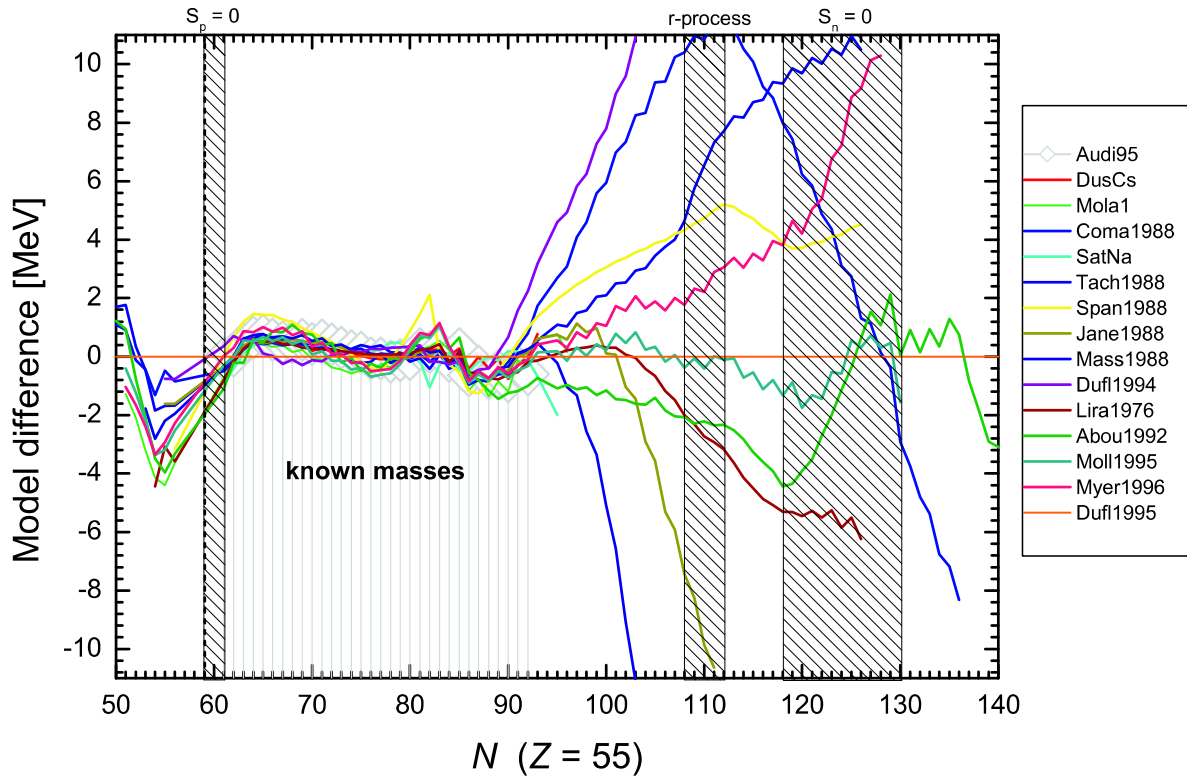


Figure 1.1: Comparison of various mass models to experimental data for Cs isotopes [5], which agree very well for known nuclei but show a vast difference in their predictions for unknown nuclei. Experimental studies of more exotic nuclei will allow to distinguish between different models and improve theoretical understanding.

heavy elements (SHE). The SHE produced in fusion reactions with stable elements are neutron deficient, which leads to a very low survival probability for the compound nucleus resulting in very low production cross-sections for SHE. Therefore, the study of SHE is particularly time consuming and difficult. This situation can potentially be improved by a facility offering high intensity neutron-rich beams, which might allow larger production cross-sections for SHE [6, 7].

1.2 Project Overview

Up to now high intensity neutron-rich beams have been difficult to attain, but since quite some time the fission of neutron-rich uranium is considered the most promising approach. It can be induced in ^{235}U with thermal neutrons (MAFF) or in ^{238}U with fast neutrons (SPIRAL2, ISAC-II [8], EURISOL [9]) and protons (ISOLDE, HIE-ISOLDE [10], EURISOL).

A small scale program exploiting neutron induced fission of uranium was the OSIRIS facility at Studsvik [11, 12, 13]. Inspired by OSIRIS, the first approach to build a large scale facility using neutron induced fission of uranium was the PIAFE project [14, 15, 16] at Grenoble, which was cancelled due to lack of funding, so that today only two other projects remain. SPIRAL2 [17, 18, 19] in France and the Munich Accelerator for Fission Fragments (MAFF) [20, 21, 22]. SPIRAL2 uses deuterons to produce fast neutrons for ^{238}U fission, while in Munich ^{235}U is used as a fission target for thermal neutrons provided by the FRM-II [23] a recently commissioned high yield nuclear reactor. The fission cross section for thermal fission of ^{235}U is approximately 500 times higher compared to fission of ^{238}U with fast neutrons, resulting in 500 times lighter targets. Additionally, the 99% enriched ^{235}U target has only a very small ^{238}U content, hence

limiting the production of plutonium to a negligible level, as will be shown later in this work. Plutonium isotopes have much shorter half-lives compared to uranium isotopes, therefore leading to an increased activity of α -radiation, resulting in problems with legal limits for α -radiation.

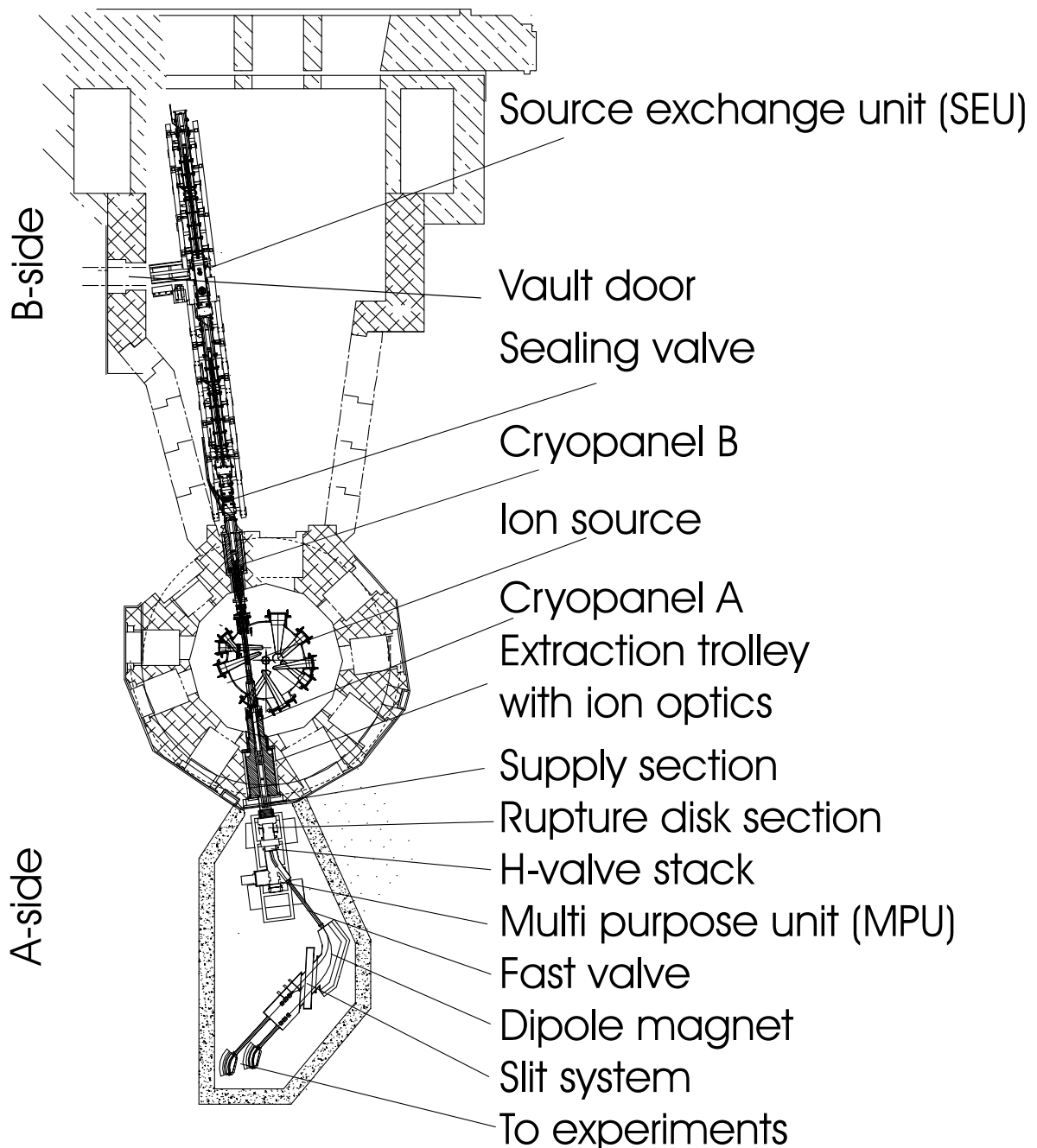


Figure 1.2: Brief overview of the ion production and extraction part of the MAFF facility. The ion source is inserted in the reactor from the B-side, the ions are extracted from the A-side and electrostatically guided to the experiments after mass pre-separation.

At MAFF, as shown in the overview in Fig. 1.2, the ion source is loaded with about 1 g of ^{235}U as a fission target and is located in the center of the through-going vacuum tube. The source is inserted into the tube by the source trolley and exchanged with the source exchange unit (SEU) after every reactor cycle (52 days), when a new source will be inserted with the reversed procedure. The fission fragments, produced and ionized in the source, will be accelerated and extracted from

the source by electrostatic means. The necessary ion optical elements are inserted on a trolley similar to the source trolley from the A-side, where the beam is guided out of the reactor towards a low resolution mass separator, where two masses of the fission fragment distribution (Fig. 1.3), one from each mass peak, are selected for the use in experiments further downstream.

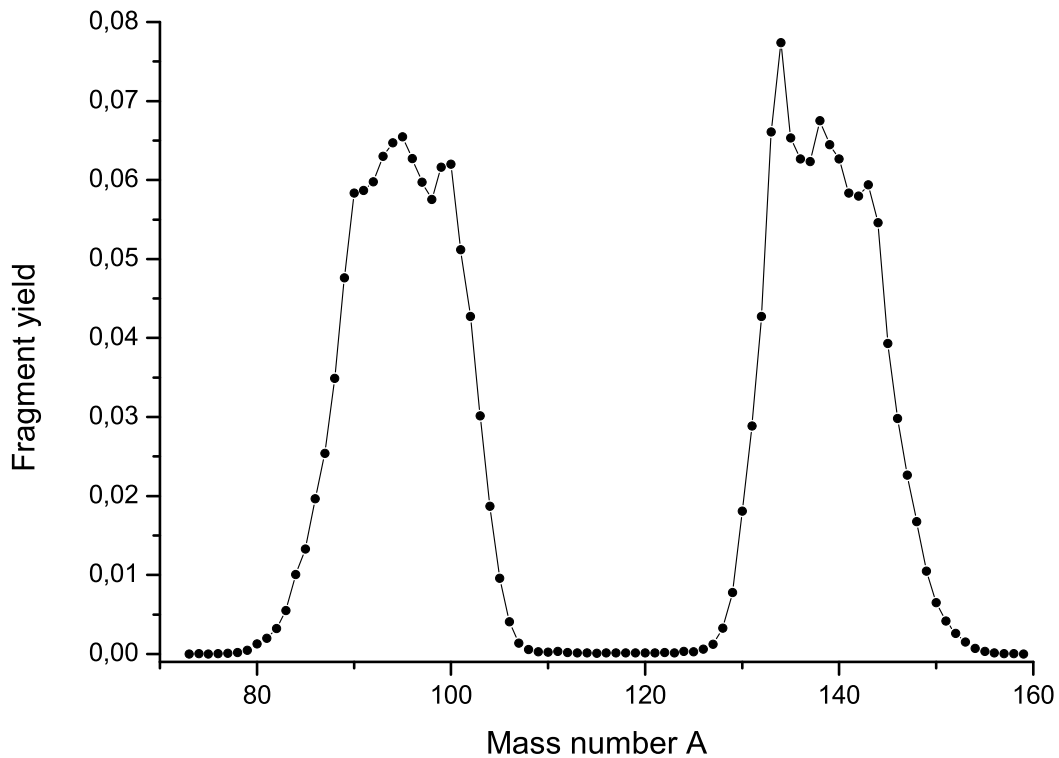


Figure 1.3: In the distribution of fragments from ^{235}U fission a heavy and a low mass peak are noticeable [24]. At MAFF one mass from each peak is selected and transported to two different experiments.

It is planned to use one of the masses for fundamental research in physics and the other one for fundamental research in physics and medicine, or medical applications.

As a German **R**adioactive **I**on **B**eam (RIB) facility in a reactor environment the reactor safety laws apply to MAFF as well and a technical inspection procedure supervised by the TÜV is required, that makes sure that everything possible is done to achieve a maximum in security and radiation safety, which is the foremost interest of the experimenting physicists.

Within this work the distribution of radionuclides at MAFF is studied for the first time. The first major section focuses on the transport of ionized nuclei from the source towards the experimental areas. A loss free (within the simulation environment) beam transport system will be introduced and sections of special interest will be pointed out.

The second major part is concerned with the distribution of neutral radionuclides spreading from the ion source throughout vast areas of the beam line. The sheer amount of activity inserted in this manner into the beam line poses a major threat in terms of radiation safety. Results of different simulations dealing with the distribution of neutral radionuclides will be shown and discussed in

detail. Based on these results a concept of operation under normal and emergency conditions is given.

Special attention is paid to the slit system where the majority of the beam is deposited. Subsequently, the activity placed there is a major part of the radioactive inventory and release of the deposited ions through sputtering is especially undesirable. Therefore, the behavior of implanted ions is investigated both theoretically and experimentally. Obtained results are shown and a solution to reduce the sputtering is given.

The final part summarizes technical investigations undertaken so far to test the feasibility of the construction and function of light weight quadrupole triplets and the extraction trolley itself. The design under investigation will be introduced, the performed tests explained and the obtained results discussed. In addition, material investigations have been performed, investigating a suitable lubricant under ultra high vacuum conditions and radiation field as well as gadolinium as a neutron absorber.

2 The MAFF Project

2.1 MAFF I

The MAFF project is split into two stages, with the first stage, MAFF I, including the development and construction of the source and extraction side up to the mass pre-separator and experiments requiring only low energy beams. The second stage, MAFF II, includes the more elaborated physics program following the pre-separator, comprising high resolution mass separation, charge breeding, accelerated high energy beams and related experiments.

Parallel to the work for this thesis, the design status of all MAFF-I components has been re-evaluated and adjusted when necessary. For many subsystems, the design depth has been increased and raised to a level appropriate to start the authorization procedure.

The following paragraphs give an overview of the outcome of this work. More detailed information is summarized in the user and management specifications, only available as internal papers, written in German.

2.1.1 Source Side

The source side is located in the neutron guide tunnel of the FRM-II. The major component of the source side is the MAFF ion source, which is, in its inserted position, located 80 cm away from the reactor core in the middle of the through-going vacuum tube SR6 (Strahlrohr 6) allocated for MAFF. The initial source design is inspired by the layout of the OSIRIS source in Studsvik and can be seen in the schematic drawing in Fig. 2.1 [25].

The fissile ^{235}U is embedded in a 25 g graphite matrix. Various forms of graphite have been under investigation [26, 27] with the graphite of choice showing a high porosity, decent mechanical stability and good uranium distribution. The uranium-carbide target is enclosed in a rhenium cylinder, with only a small opening for ion extraction. Rhenium was chosen as a container material, because it has high temperature stability (melting point: 3459 K) and shows almost no chemical reaction with carbon, which is necessary to achieve a long operation time of 52 days. The ANUBIS source at OSIRIS, for comparison, was operating for approximately 20 days. The chemical inertness is in fact so important that it outweighs various disadvantages of rhenium such as availability, cost, difficult machining, and a rather high neutron capture cross section of 90 b, which is higher than alternative high temperature stable materials like tantalum (20 b), tungsten (18 b), niobium (1.1 b) or molybdenum (2.5 b).

The uranium load required in the final stage has been calculated to 1.18 g [28] with the option to use up to 2.0 g if higher amounts are necessary to achieve the desired fission rate of $1 \cdot 10^{14}$ 1/s. However, in the start-up phase smaller amounts of fissile material will be used to gather experience with lower radionuclide production. In this phase nuclear heating is insufficient to maintain the operating temperature of 2700 K, and must be supported by external electric heating and heat shields. Hereby, especially the central heat shields are exposed to the highest temperatures and will be made from rhenium, while the outer ones, exposed to lower temperatures, will be constructed

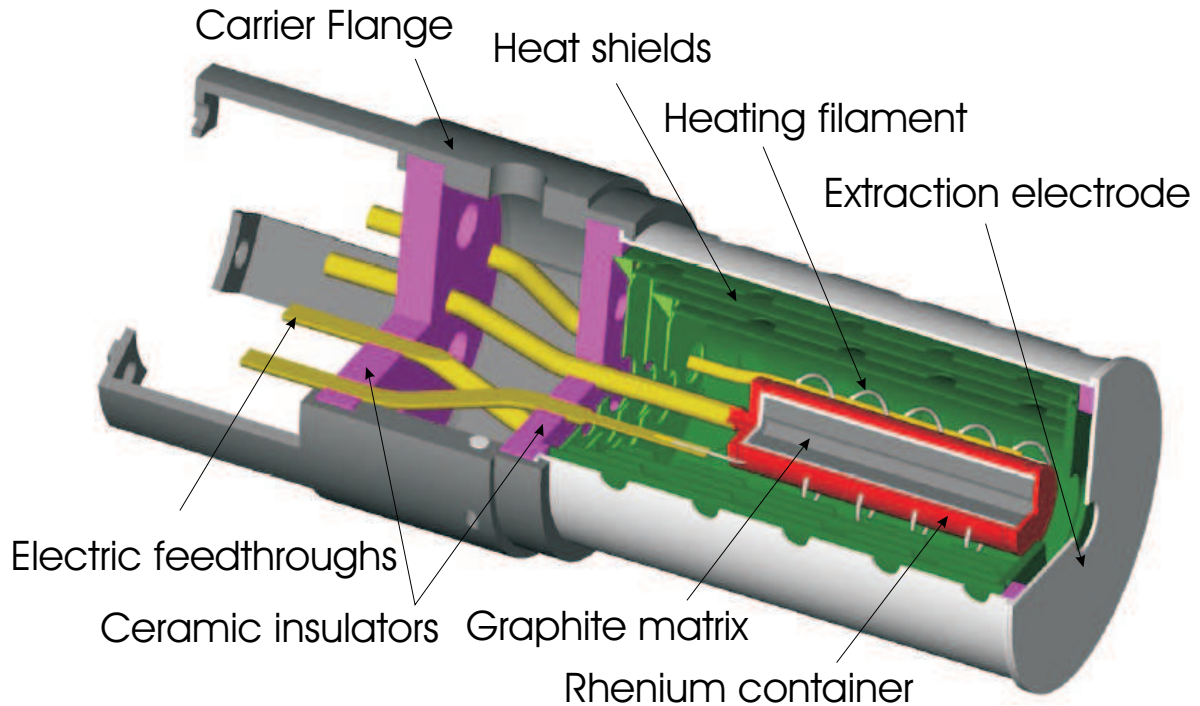


Figure 2.1: Schematic drawing of the MAFF ion source, which will be operated at 2700 K. The 25 g graphite matrix is loaded with 1.2 g of uranium resulting in a fission rate of 10^{14} fissions per second.

from molybdenum. In addition to the heat shields the target will be actively heated by electron bombardment, which will also be required in the final phase in order to compensate the loss in nuclear heating due to consumption of uranium in the target. In order to extract ions from the source, the target is kept on an electric potential of +30 kV, while the extraction electrode and heat shields are at a potential of +29 kV, which drops to zero at the lens trolley, so that the positively charged ions will reach a final energy of 30 keV. The ionization scheme used for the first sources will be surface ionization, which offers different ionization probabilities for various elements as can be seen in Fig. 2.2, where the surface ionization probabilities on rhenium at 2700 K are given for both, positively and negatively charged ions. For positive ionization the group 1 elements cesium and rubidium can be ionized best, while the yield for the noble gases krypton and xenon is negligible. Negative ionization promises much better yields for bromide and iodine, but can probably not be realized, since this would require to reverse the polarity of the complete ion optic system. However, this option will not be installed for financial reasons.

For electric insulation of the electrodes, temperature stable insulators are required. Insulators, heat shields and extraction electrode are mounted on a titanium carrier flange, which in turn is mounted on the source trolley. A prototype of the ion source, as shown in Fig. 2.3, using alternative materials has been constructed to measure the temperature profile and to compare the ion optic properties with simulations [30].

The results obtained from measurements with this prototype were inconclusive regarding the comparison with simulations, since the simulation environment vastly differed from the experimental setup. Nevertheless, a rough temperature profile could be measured, but not up to 2700 K, since the materials used had lower melting points. Currently, similar tests with a second prototype using appropriate materials are under preparation.

The purpose of the source trolley, as shown in Fig. 2.4 with mounted ion source, is the transport of the ion source to and from the Source Exchange Unit (SEU). The trolley has a massive body to

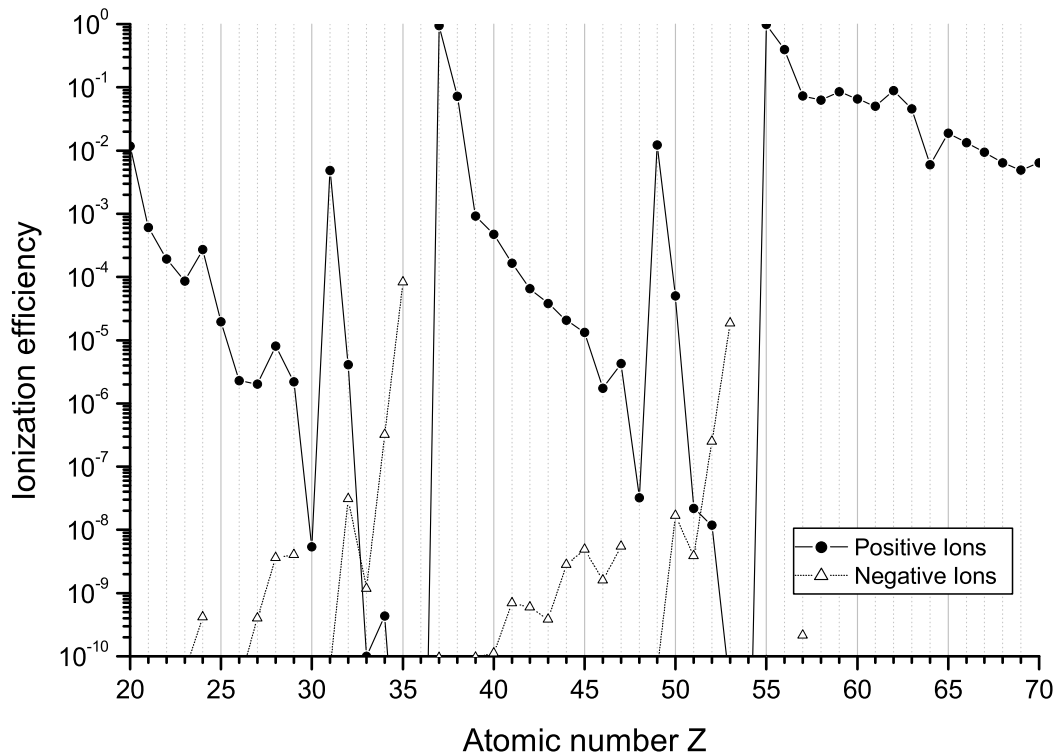


Figure 2.2: Surface ionization yields, based on the Langmuir-equation [29], for negative and positive ions on 2700 K rhenium surface.

reduce the open area in the beam tube and functions as an absorber for neutron and γ -radiation. From this body, a long rod holding the ion source extends to the core of the reactor. The trolley also houses electric connections for the filament heating and extraction voltages.

The source trolley is moved from its initial position in the shielded *transport bottle*, through the Source Exchange Unit and Transfer Section into the reactor plug, as can be seen in the schematic overview of the complete B-side given in Fig. 2.5. Once in the reactor plug, the trolley is secured in its final position and the required electrical connections are provided by the Supply Section.

The RSK-Section (Reaktor Sicherheitskommission) behind the Supply Section consists of a vacuum chamber with a rupture disk (rupture disk section), and up to two cryo-pumps. The rupture disk is necessary to release severe overpressure, in the event of a hypothetical steam bubble explosion of the reactor, to avoid destruction of components prior to the RSK-Section. The shock wave following this explosion would be released by the rupture disk and, as a result of the shock wave, the SR6 would be destroyed and water from the reactor pool would pour out. This water flow is stopped by the RSK-valve, which closes after the shock wave has passed. The rupture disk section is followed by a heavy radiation shield, which functions as an additional absorber for neutron and γ -radiation, and a vacuum valve, which is a commercial valve to separate different vacuum sections. Both valves are closed during normal operation.

The most complex device on the B-side is the Source Exchange Unit, as seen in Fig. 2.6. This automated machine, placed a few meters from the reactor wall next to the vault door, is designed to remove the used ion source from the trolley and position it into a storage container. Once the source trolley has moved in the exchange position (Fig. 2.6a)) it is secured in a well defined

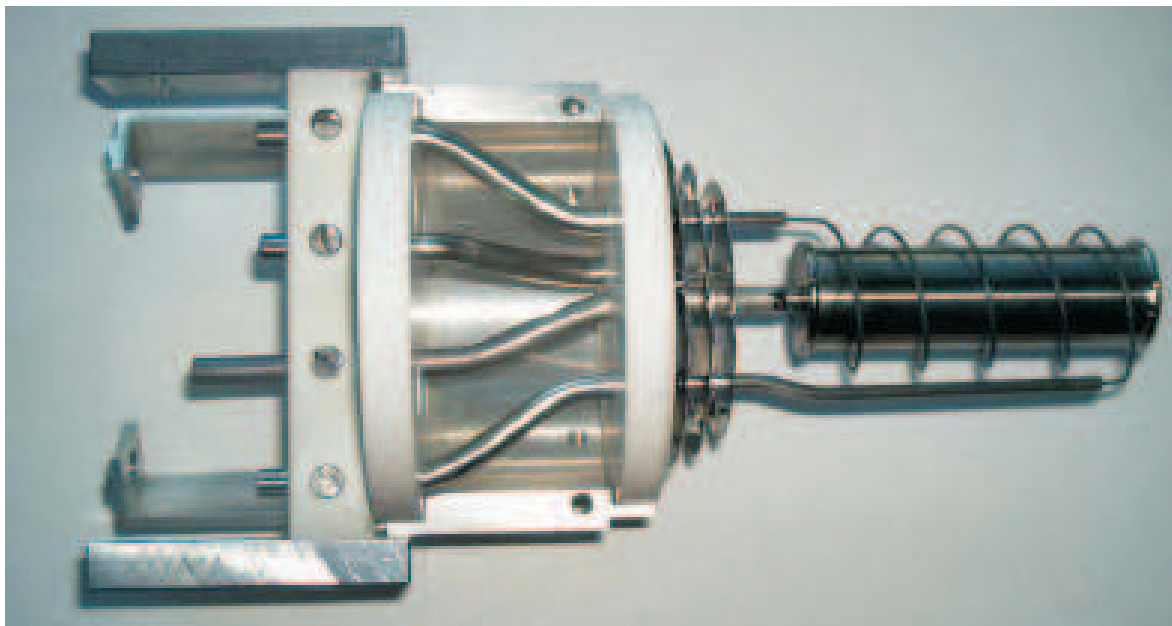


Figure 2.3: Photograph of MAFF ion source prototype without heat shields as used for first tests [30]. This prototype is constructed from alternative materials unable to withstand the high temperature, but a new source with the required refractory materials is under construction.



Figure 2.4: Schematic drawing of the source trolley with mounted ion source.

position by holding clamps (Fig. 2.6b)), which also open the lock, that secures the ion source to the trolley. A remotely operated mechanical picker grabs the source from above, so that the trolley can move backwards to release the source. After the picker arm moved down and positioned the

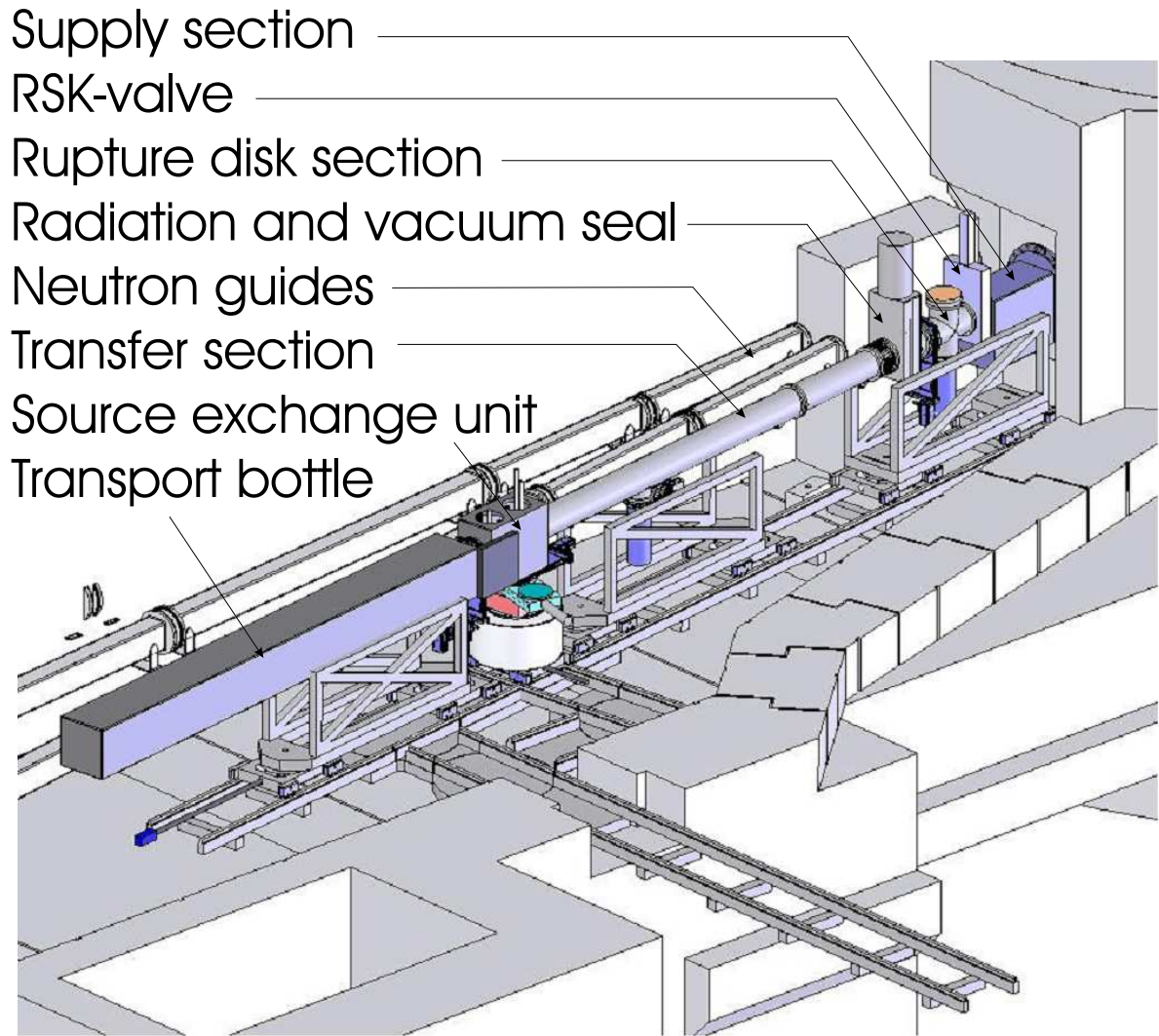


Figure 2.5: Schematic drawing of the source exchange side.

used source into the storage container surrounded by a 2 t lead shield, it moves up again and grabs the lid for the container, which is supplied by a dedicated device. The lid is placed on the container before the picker arm moves back in its initial position and the vacuum valve closes above the container. Now, the volume between the valve and the lid is vented and air pressure holds the lid to the container. The remote controlled fast release flange is opened and the container separated from the SEU. Still remotely operated the container and its lead shield are moved on rails into the locking station, as shown in Fig. 2.7. Here the lead lid is lowered onto the lead shield in order to complete the radiation protection, so that personnel can enter the area, and move the used source with the lead shield. The lid of the lead shield has an integrated second lid, a metal sealed vacuum flange for the source container, which can be screwed to the container with screwdrivers integrated in the lead lid (not shown in Fig. 2.7). Now, the lead shield with the ion source can be transported to the hot cell of the FRM-II, where the lead shield can be opened, the source container removed and finally be placed in the storage pool for spent fuel elements.

A new source is inserted in the same way reversing the steps described above.

In case of a defect or broken source trolley, the source trolley can be moved into the shielded transport bottle, which can be separated and decoupled from the SEU by means of another remote operated fast release flange. Still remotely controlled the bottle moves back and a lead

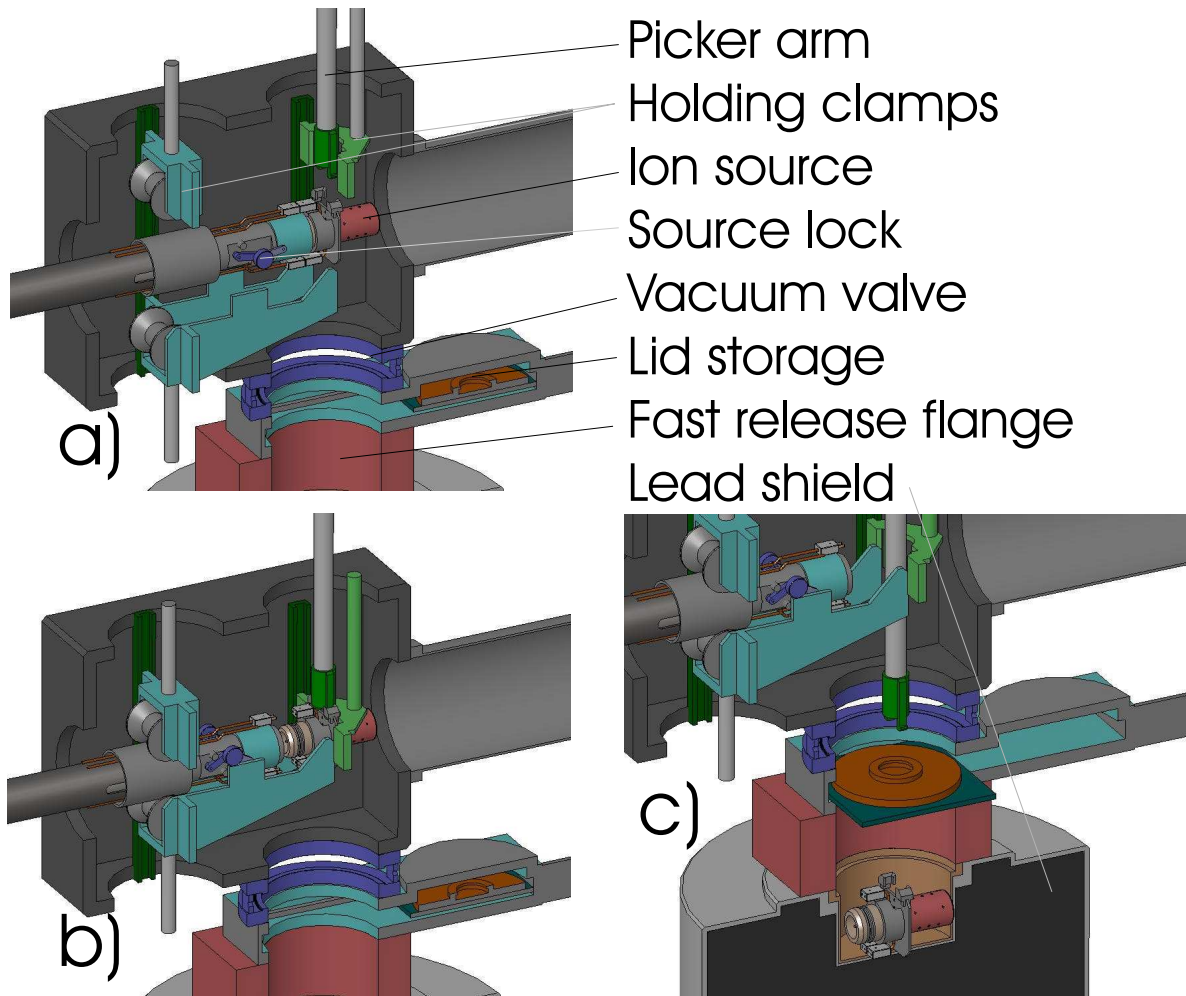


Figure 2.6: Illustration of the source exchange process. Fig. a) shows the trolley, picker arm and holding clamps in initial position. Fig. b) shows holding clamps fixing the trolley in a well defined position and the picker arm grabbing the source. In Fig. c), the source has been lowered into the storage container. Once the container lid is moved out of the lid storage, the picker arm can grab the lid and place it on top of the container.

door closes the bottle, completely shielding the source trolley. Now, personnel can enter the room and move the bottle out, using the rail system as shown in Fig. 2.8.

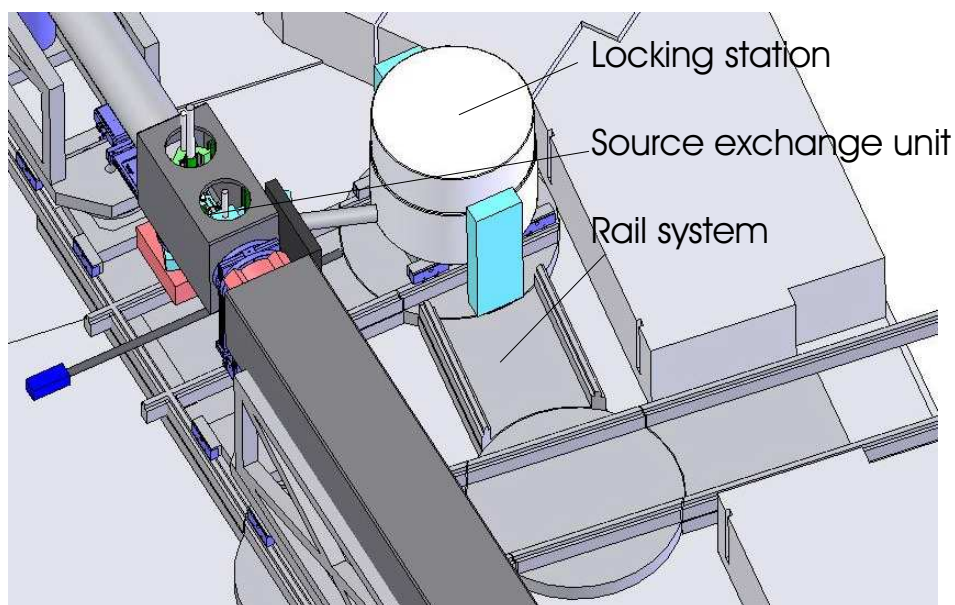


Figure 2.7: Lead shield locking station. The lead shield is remotely moved on a rail system from the SEU to the locking station, where a lead lid is released onto the lead shield to complete the radiation protection, so that manual manipulation of the lead shield is possible.

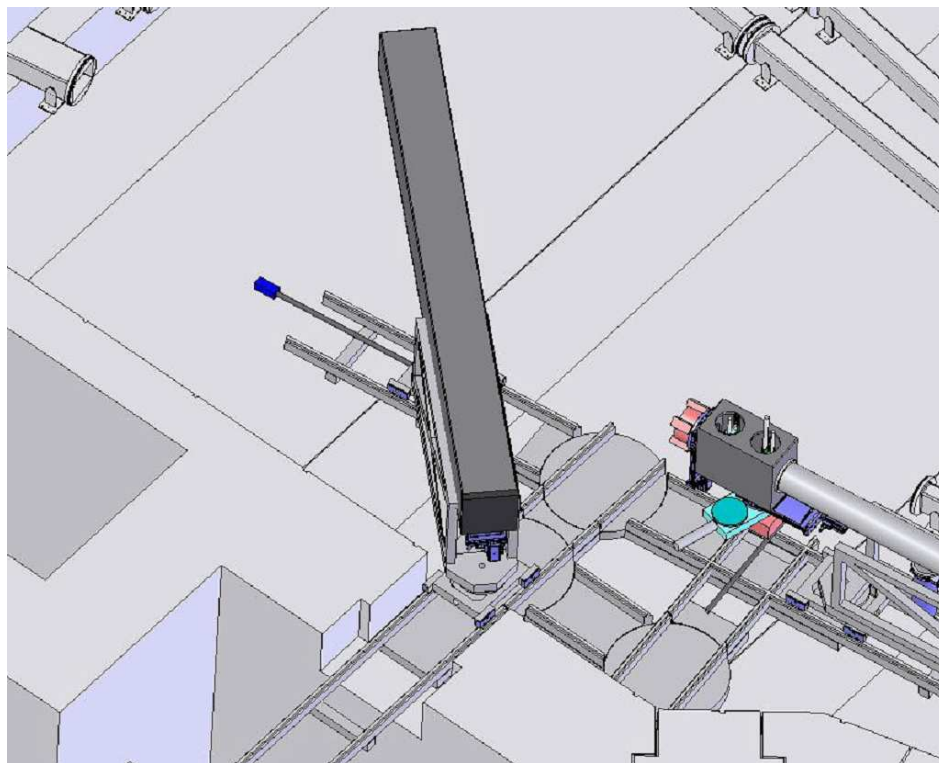


Figure 2.8: The source trolley can be moved in and out of the neutron guide tunnel in the shielded transport bottle taking advantage of the installed rail system.

2.1.2 Extraction side

The extraction side, as shown in the schematic 3D drawing in Fig. 2.9, consists of the beam extraction and related components, with the parts to the left being inside the reactor plug. It can be seen, that the ion optical installations are mounted on the extraction trolley, which is remotely similar to the source trolley since it also has a heavy body, but the long rod is replaced by a titanium tube that contains the electrostatic lenses. Because the body needs to have an opening for the ion beam, the neutron- and γ -radiation absorbing properties of the trolley are reduced, which is partially countered by carefully placing absorbers at beam waists. For alignment both extraction and source trolley will contain some mechanics that aim to reduce possible offsets between the ion sources extraction electrode exit hole and the source trolleys acceleration electrode entrance hole.

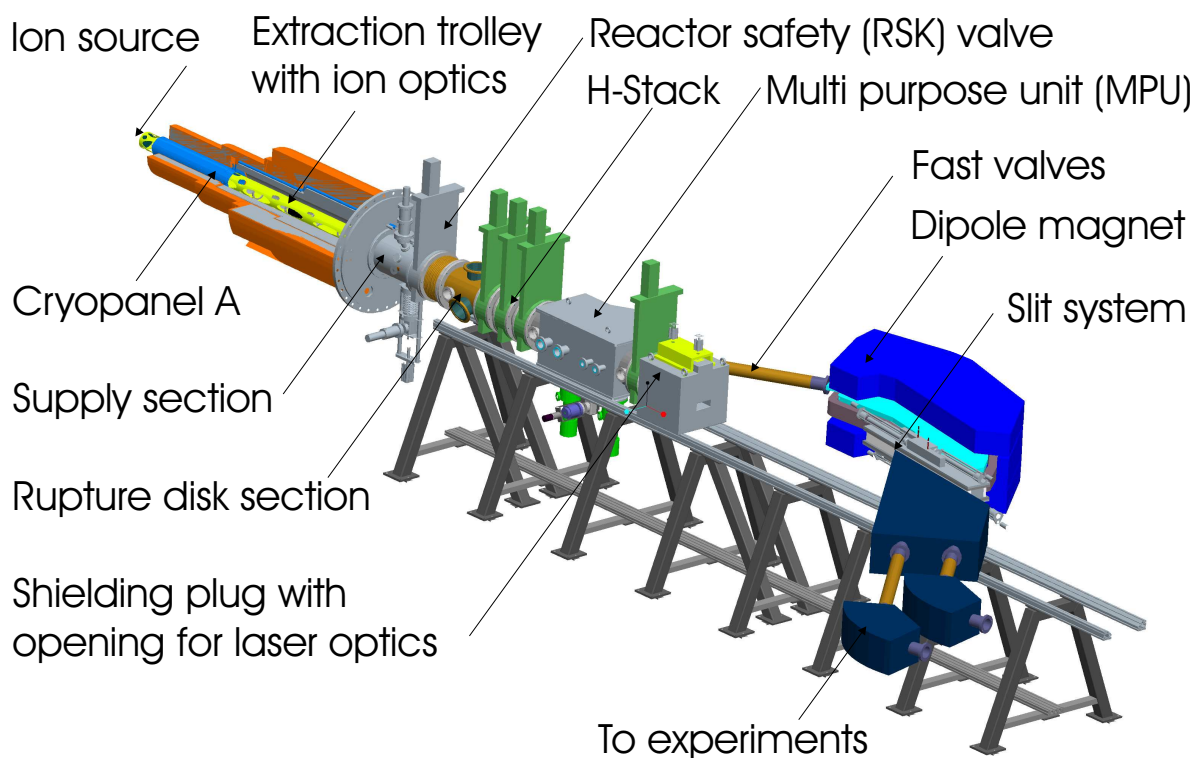


Figure 2.9: Schematic drawing of the extraction side. Everything from the source to the supply section is within the reactor wall. The rupture disk section and H-valve stack are needed for safety reasons, while cryo-panels provide good vacuum conditions close to the source and absorb the majority of volatile nuclides.

The first component outside the reactor is the supply section, where all electrical and mechanical connections to the trolley are made. It is followed by a large slowly closing valve (RSK-valve) and another rupture disk section, both serving the same purpose as their B-side counterparts, which makes the rupture disk section also the first pumping station. The following H-valve stack, a combination of three valves for both daily operation and radiation safety, plays an important role for beam diagnostics and radiation containment. Details on their specific purpose and layout will be discussed at several points in the following chapters. The second major component, next to the extraction trolley, is the Multi Purpose Unit (MPU), with the first and foremost purpose of housing the electrostatic deflector necessary for the ion beam transport. The retractable deflector

can give way to the trolley in case it needs to be moved through the lock of two valves at the end of the MPU, into the transport container. However, during normal operation the transport container is removed and a heavy concrete block is placed as a shield from direct neutron and γ -radiation of the reactor core behind the first valve of the lock, which is normally closed by a blank flange with a glass viewport. In the early stages of MAFF the viewport will be used for pyrometrical temperature measurements of the ion source and for adjusting the source and lens trolley onto each other. Later on the viewport can be used for operating a laser ion source.

The previously mentioned dipole magnet is completing the mass separation, where the slit system placed in the magnets focal plane stops all but two masses for use in low and high energy experiments further downstream. The design of the mass separator and slit system is discussed in detail in the Chapters 3 and 6.

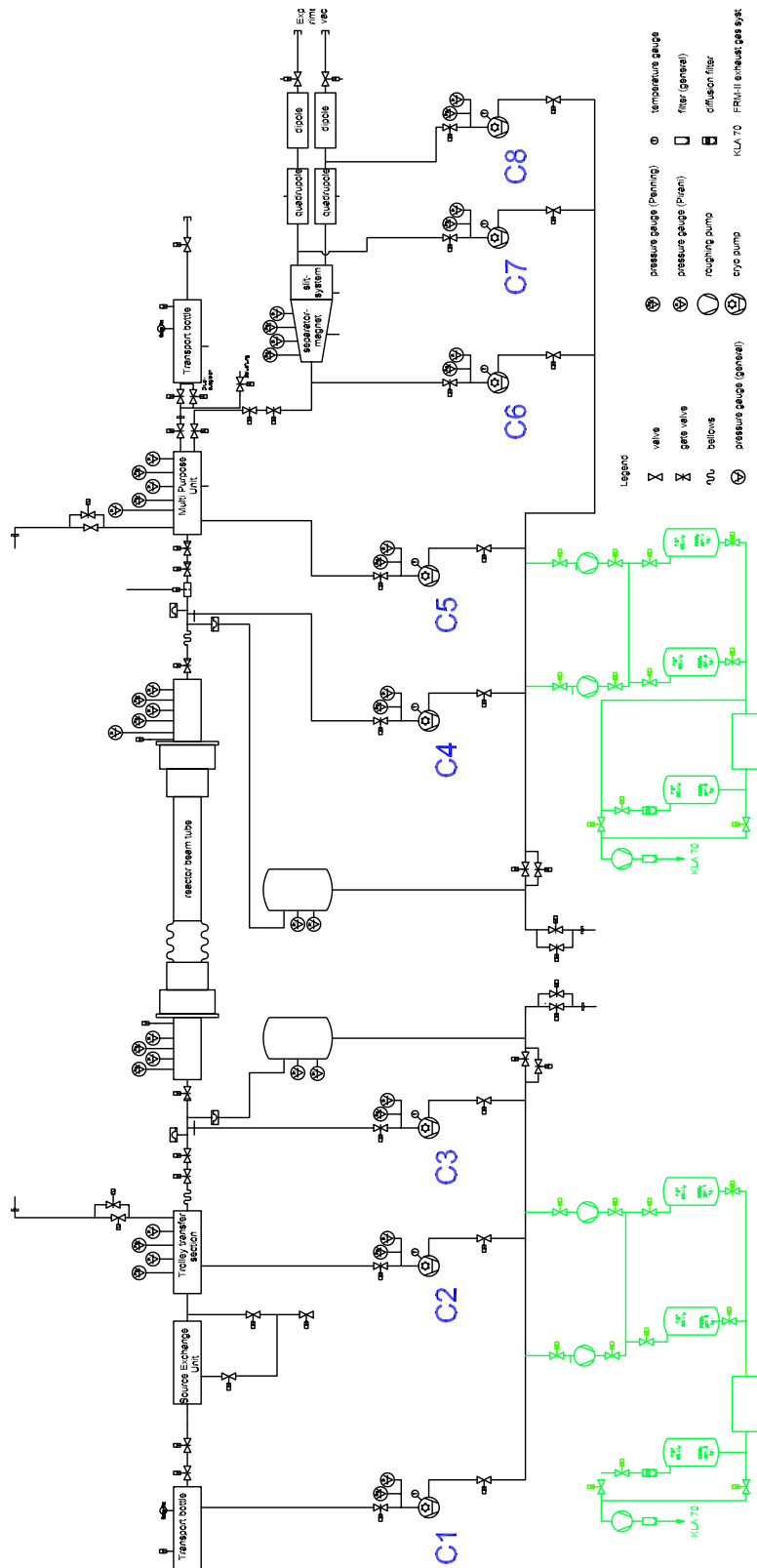


Figure 2.10: Overview of the MAFF vacuum system. Cryo-pumps are used, to maintain vacuum during operation and collect radioactive atoms in the residual gas, until the cryo-pumps are regenerated into the decay tanks.

2.1.3 Common components

Common to both sides of MAFF are the vacuum system, see Fig. 2.10 and related components [31]. For reasons of radiation safety cryo-genic vacuum pumps have been chosen, because they have many advantages over turbomolecular pumps, beginning with the freezing out of radionuclides and decay thereof in a localized volume, which gives a big advantage for radiation control as will be seen later on.

Table 2.1: List of different vacuum sections with corresponding volumes.

Section	Volume [dm ³]
B-side transport bottle	300
Source exchange unit	130
Transport section	230
B-side RSK-section	160
SR6 up to H-Stack	450
Multi-Purpose-Unit	230
Magnet, slit system, and further components	≈400

The vacuum system and hence the beam line is split into different sections as listed in Table 2.1. The first cryo-pumps are placed at the rupture disk sections on both sides, which would only allow a vacuum of 10^{-4} - 10^{-5} hPa in the vicinity of the ion source. Therefore additional in-pile cryo-panels are installed on both sides of the source.

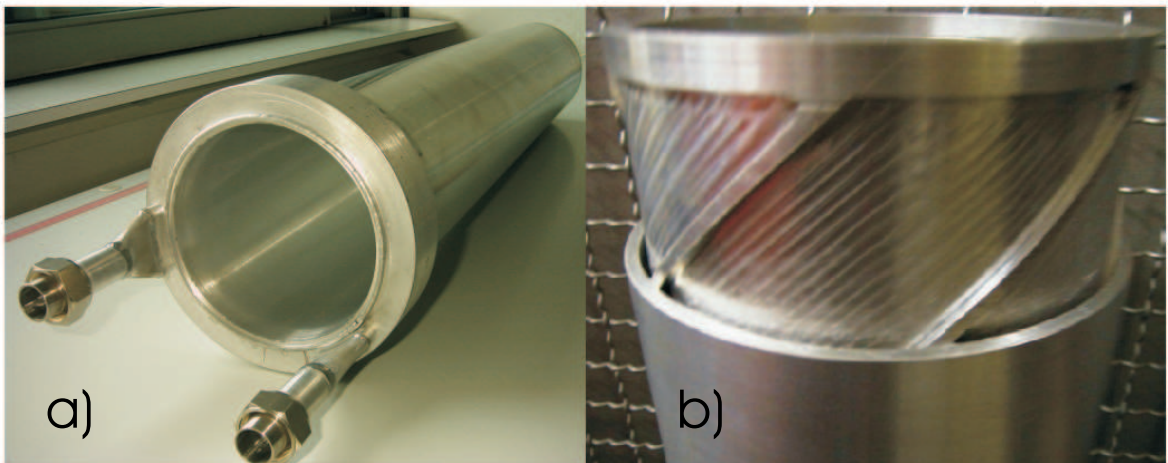


Figure 2.11: Photographs of the cryo-panel prototype made from aluminum. a) Completed panel with connectors for helium supply and b) during production, where the outer shell was shrunk onto the inner fin construction [32].

The cryo-panels operate at 15 K and are cooled with helium gas at an elevated pressure (≈ 3 bar). There has been some concern in the past that the production of radioactive tritium from ^3He could pose a safety hazard. However, after careful investigation of the issue, it was found that the maximum amount of produced tritium per reactor cycle ($3.9 \cdot 10^8$ Bq) [33] is very far below the allowed yearly threshold ($3 \cdot 10^{10}$) for release by the FRM-II.

2.2 MAFF II

Following the completion of MAFF I, which will offer low energy beams to experiments, it is planned to continue with the construction of the second stage of MAFF. MAFF II will be located in the Reactor Building East, currently under construction, as shown in Fig. 2.12, which is expected to be completed in November 2006.

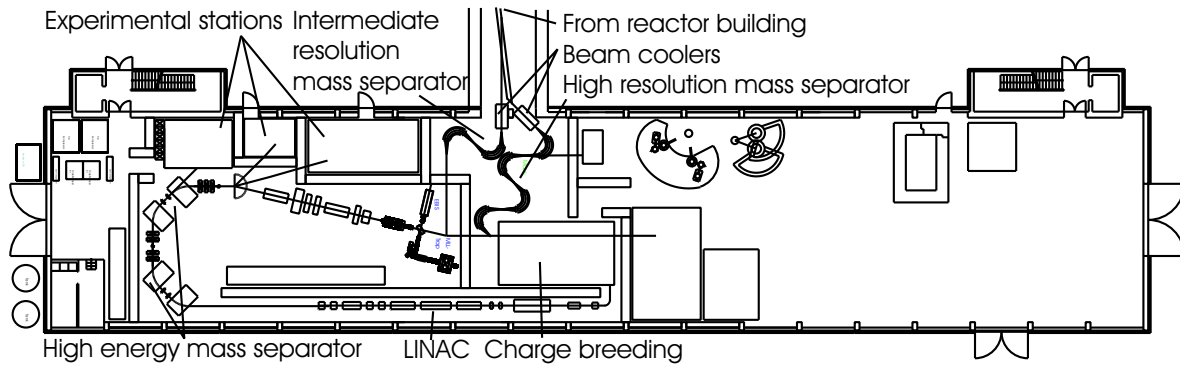


Figure 2.12: Schematic drawing of the preliminary MAFF II layout in the new Reactor Building East.

The two ion beams, selected at the slit system, enter the building through the wall of the main reactor building and arrive at the beam coolers. The ideal position of the beam coolers is still a major question and will be discussed in detail in Chapter 3.

The two identical beam coolers [34], with properties as summarized in Table 2.2, operate on a two step process. In the first step the incoming 30 keV beam is decelerated to approximately 100 eV, causing the beam emittance, the product of waist diameter and opening angle, to grow 17-fold, proportional to the inverse energy square root.

Table 2.2: Summary of beam cooler properties.

Helium pressure	0.1 hPa
RF-frequency	5 MHz
RF-amplitude	100-150 V _{PP}
DC field	0.5 V/cm
Angular acceptance	65° (simulated)
Transmission	90% (simulated)
Transmission	50% (experiment)
Input energy spread	100 eV
Output energy spread	5 eV
Input emittance	36π mmm·rad at 30 keV
Output emittance	6π mmm·rad at 30 keV

In the second step, the decelerated beam enters into an electrode array as shown in Fig. 2.13a) [34], where a radio-frequency is applied to the electrodes resulting in an RF field, which is repelling on average, so that the ions are trapped inside the funnel as shown in Fig. 2.13b). A small field gradient is applied over the structure to guide the ions to the rear end of the cooler, where the inner electrode diameter gradually decreases to form the actual funnel. The whole structure is filled with helium, which does not react with beam ions in the 1⁺ charge state due to its high

ionization potential, so that the ions charge state will be 1^+ . Nevertheless ions collide with helium and are therefore cooled to the temperature of the helium atoms. Hence reducing the energy spread of the ions and the beam dimensions in this way. Subsequently the ions are re-accelerated to ground potential and the beam leaving the cooler is of much higher quality.

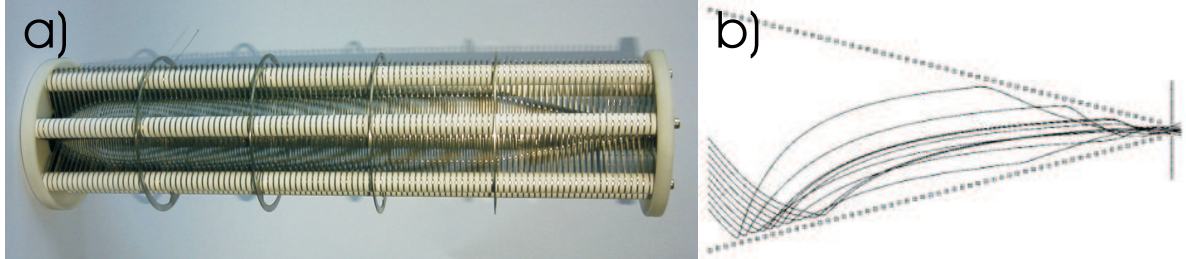


Figure 2.13: a) shows a photograph of the RF-funnel prototype, while b) gives some insight into the ion trapping with repelling RF-fields in the funnel. The beam enters from the left, ions are repelled by the RF-fields and guided to the right by the field gradient. The beam is cooled and emittance reduced by collisions with helium atoms [34].

So far a prototype of the cooler has been constructed and tested [34]. Due to limitations in the testing environment the tests could not exploit the whole range of operation, especially the angular acceptance is a major uncertainty, so that more tests will be required in the future.

At Jyväskylä (Finland) [35] a different type of beam cooler using RF-quadrupoles for radial confinement is working with similar results: Output energy spread is in the 1 eV region, experimental determined transmission is between 60% and 70%.

For the dedicated low energy beam it has been decided to use only an intermediate resolution mass separator with a mass resolving power of 2000. This is sufficient to prepare high yield nuclei with small impurities for pharmaceutical use or solid state physics. Probably a variation of the high resolution separator (HRS), as it is under design for the Eurisol project [9], with only two magnets will be used, which promises a mass resolution of 16.000 for an initial beam emittance of 3π mm·mrad.

The dedicated high energy beam, on the other hand, will undergo high resolution mass separation. The mass separator for this purpose will also be based on the design of the mass separator developed for Eurisol [9]. With four magnets instead of two it has a proposed resolving power of 64,000, if an incoming emittance of 3π mm·mrad can be provided. This would be sufficient to separate isobars with very little impurities and provide optimal conditions for rare nuclei studies.

Before the mass separated beam can be accelerated efficiently it is necessary to increase the charge state of the ions. This is achieved with an ECRIS (Electron Cyclotron Resonance Ion Source) [36] or an EBIS (Electron Beam Ion Source) [37]. A picture of the PHOENIX test ECRIS at REX-ISOLDE is shown in Fig. 2.14 next to a schematic drawing, which shows that an ECRIS uses magnetic fields to confine a plasma in radial and axial direction. In addition an electric HF field of 14 GHz is used to heat the plasma and increase the charge state of the trapped ions. The breeding time, required to reach the saturation charge state is approximately 50 ms, but can be reduced for isotopes with smaller half-life. While an ECRIS has the advantages of high intensities (10^{12} ions/s) and a small uncomplicated setup, requiring only the plasma chamber to be on high voltage, it has the disadvantage of longer breeding times compared to an EBIS and a broader charge state distribution caused by the use of a plasma.

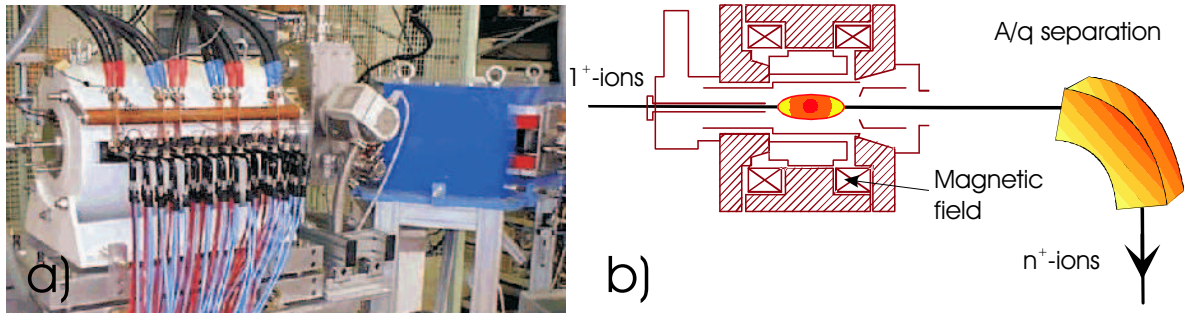


Figure 2.14: a) shows a photograph of the PHOENIX ECRIS. b) shows the schematics of ECRIS operation, which uses a heated plasma to increase the charge state of the trapped ions. Therefore, it can handle high intensities, but breeding takes some time and the charge state distribution is rather broad [38].

An EBIS on the other hand is using an electron beam of up to 1000 A/cm^2 to increase the charge state by electron collisions and a magnetic field to radially confine the ions. For a high electron current the EBIS has very short breeding time, provides a small beam emittance and the operation under UHV conditions allows a narrow charge state distribution. However, the setup is large, a high voltage platform is required and the space charge capacity is limited. Therefore, it is proposed to install both charge breeders at MAFF. An EBIS for low yield short lived particles and an ECRIS for those fission fragments with high intensities.

The charge breeder is followed by a magnet for q/A separation, so that ions with a well defined $q/A > 0.16$ are delivered to the accelerator.

The heart of MAFF II is the linear accelerator (LINAC) for the production of high energy beams. Its design energy range is 3.7 to 5.9 MeV/u with an increase to 7 MeV/u being currently under discussion. The major components of the LINAC are a Radio Frequency Quadrupole (RFQ) accelerator, three interdigital H-type (IH) structures as well as two additional seven-gap IH-resonators to tune the final energy. Prototypes of the IH-structures have already been constructed and are currently used at REX-ISOLDE.

2.3 Physics program

The MAFF project is included in the NuPECC long-range plan [39] as an intermediate-generation facility helpful for the realization of the long-term EURISOL project. Detailed information on the MAFF physics program is included in Ref. [33], while more general information on radioactive ion beam reactions with neutron-rich nuclei can be found in Ref. [40].

2.3.1 MAFF I

The MAFF I physics program will consist of two experiments placed in the experimental hall of the FRM-II. The experiments most likely installed will be a fast tape transport system and a penning trap.

MLL-trap

This penning trap system is currently being set up at the Maier-Leibnitz-Laboratory [41]. Even without the support of the high resolution mass separators, the combination of a cleaning and

a measurement trap will allow to study a variety of physics aspects on neutron rich isotopes by measuring masses and half-lives.

By determining nuclear binding energies and Q-values with mass measurements, MLL-trap can contribute to nuclear physics and studies of nuclear structure. Shell closures, pairing energies, core deformation, and isomeres can be investigated with precise mass measurements. In addition, the fundamental properties of matter can be studied by comparing experimentally determined masses of neutron rich isotopes to theoretical predictions of different nuclear models. Finally, MLL-trap can contribute towards nuclear astrophysics by studying nuclei on the r-process path, which is determined by the masses and half-lives. The determination of the r-process path will increase the understanding of nuclear synthesis in the early universe and in supernovae.

In a later stage MLL-trap might be upgraded to allow trap assisted decay and laser spectroscopy.

Tape station

It is planned to have a fast tape station with subsequent γ -ray detection system available, where one or more MINIBALL [42] or AGATA [43] detectors could be used. This rather simple setup will allow half-life determination of very short lived nuclei. Also the measurement of branching ratios and β -decay level schemes of exotic nuclei is possible.

It can be seen, that already with MAFF I a broad range of physics aspects can be investigated by studying previously inaccessible neutron rich nuclei.

2.3.2 MAFF II

With the additional space available in the Reactor Building East, it will be possible to install a larger variety of physics experiments. In addition to experiments with the low energy beams available at MAFF I, it will be possible to use the accelerated isotopes for nuclear reactions.

MINIBALL/AGATA

Either one of the detector arrays MINIBALL [42] or AGATA [43] could be used at MAFF for γ -spectroscopy and investigation of reactions with neutron-rich isotopes. In transfer reactions shell closures can be tested by studying the single-particle structure of exotic nuclei. Coulomb excitation can be used to study the neutron-pairing energies of neutron rich isotopes by measuring B(E2) values and 2^+ energies. Spectroscopy on neutron-rich transactinides around $Z \approx 100$, created in fusion reactions, can be used to verify decay chains found at Dubna for super-heavy elements.

Radiochemistry experiments

Chemical properties of exotic super-heavy isotopes, produced in fusion reactions, can be studied with the *rapid chemical separation and on-line detection method* [44]. Currently experiments [45] using this method are performed at GSI by the TUM radiochemistry department but will also benefit from neutron-rich beams at MAFF.

MLL-trap

The trap experiments started in MAFF I can be extended to reaction products, and therefore to even more-exotic nuclei as well as to isotopes not available from a fission source. In addition

charge breeding can be used to increase the charge state of ions prior to injection into the penning trap, which will increase the accuracy of the mass measurements.

Solid state physics

At an experimental station dedicated to solid state physics, radionuclides can be implanted into a sample and used as probes to study the crystal structure. Also the homogeneity of the implantation process can be analyzed with radioactive nuclei.

Live science

The high production yield of radionuclides used in cancer treatment available as a mass separated ion beam will allow the creation of very small *seeds* for brachytherapy. The aim of this method is to implant very small radioactive samples in the middle of a tumor and thus protect as much healthy tissue as possible. Using the MAFF ion beam, small seeds offering high dose rates can be created easily and quickly.

3 Ion transport

3.1 Ion optic design

Within this chapter, the low energy beam transport from the ion source to the ion beam cooler is studied in detail by simulations, with the aim to establish a feasible ion optical system for loss free beam transport and mass separation. The emittance of the beam shall be kept as smaller than the input emittance of the beam cooler, which gives an upper limit of 36π mm·mrad.

The MAFF low energy beam line can be split into three distinctive sections, with the first being the section from the ion source out of the reactor up to the point where the object for the mass pre-separator is formed. This is the start of the separator section, which ends at the slit system. Everything beyond this point up to the beam cooler is the third and last section.

For the calculations of the ion optical system three methods have been applied. First of all there are pen and paper calculations using the matrix formalism following the notation by Wollnik [46]. More information about this method and the calculations made can be found in Appendix B and C. First order matrix calculations have been performed by hand to get a better understanding of the parameters at work, and their influence on the ion optic system. For higher order calculations the amount of parameters is too large to keep track and an ion optic code must be used.

COSY infinity [47] is such a code based on the matrix formalism by Wollnik and uses differential algebra to calculate solutions in theoretically arbitrary order. COSY calculations have the advantage of being easily traceable up to first order where comparison with pen and paper calculations is possible. The code offers a variety of standard optical components to choose from and the possibility to vary typical dimensions of lenses or dipoles to fit the individual needs. Based on the transfer matrices of the ion optical components chosen, COSY calculates the transfer matrix for the whole optical system, therefore only components with known transfer matrices can be used. Rays can be traced throughout ion optical instances, which works very fast and offers the function to fit for different variables, so that foci or beam waists can easily be generated at any point. However, the code has certain limitations. For a system with a moderate number of elements (four or more) third order is the maximum COSY can calculate without reaching memory limitations. Therefore, it can only calculate third or higher orders for systems with four elements or less.

The program SIMION7 [48] is a good choice for ion optical simulations once a general layout of the system is established. Different than COSY it is not using a matrix formalism, but is numerically solving the Laplace equation. Therefore, arbitrary electrode potentials and structures can be defined using the implemented programming language or the integrated graphic interface. Most of the geometries, which define the base potential, have been created using the programming language. Based on the defined potentials SIMION is calculating the field of the electrode with an accuracy of up to 10^{-7} by numerically solving the Laplace equation. Field maps of multi electrode structures are calculated by superposition within a pre-defined cuboidal volume, the size of which defines the memory requirements of the program. At the edges of the field map a Neumann type

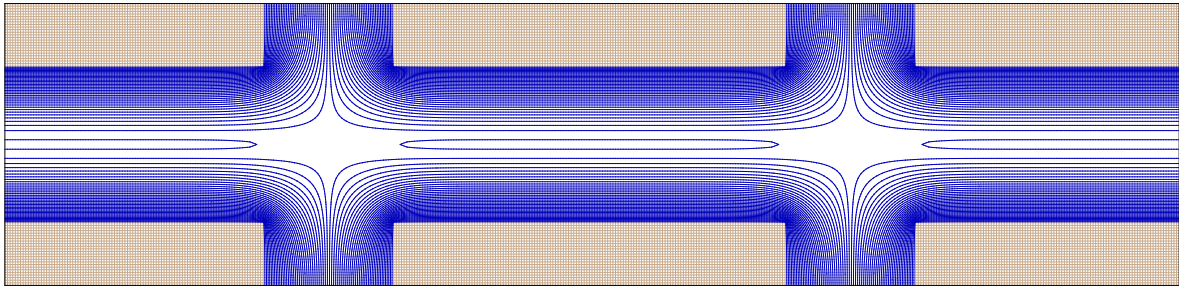


Figure 3.1: SIMION7 output for potential lines for quadrupole triplet with Neumann type boundary conditions.

boundary condition is used, forcing the potentials to be perpendicular to the edge. An exemplary potential map is shown in Fig. 3.1 for a mid-plane cut of a quadrupole triplet.

It can be seen from Fig. 3.1, that the equipotential lines are perpendicular to the boundaries of the simulated volume. While this boundary condition is helpful at the flanks of the triplets (top and bottom edge in the figure) it is leading to undesirable results at the front and rear. Particles entering and leaving the multiplet at different radial positions experience an acceleration or deceleration, as shown in Fig. 3.2, depending on their trajectory.

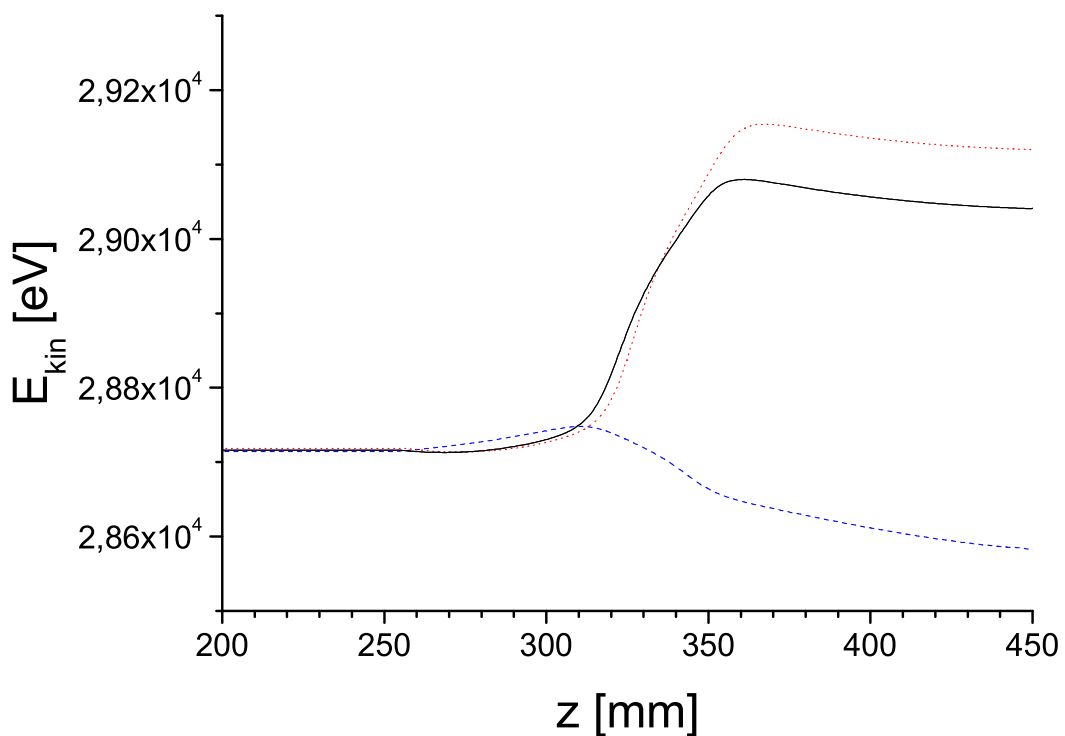


Figure 3.2: The energy development in a multiplet with Neumann type boundary condition, here a doublet, shows that three particles (different lines) entering the multiplet with equal initial energy but different radial position (what cannot be seen from this figure), leave the multiplet with different energies.

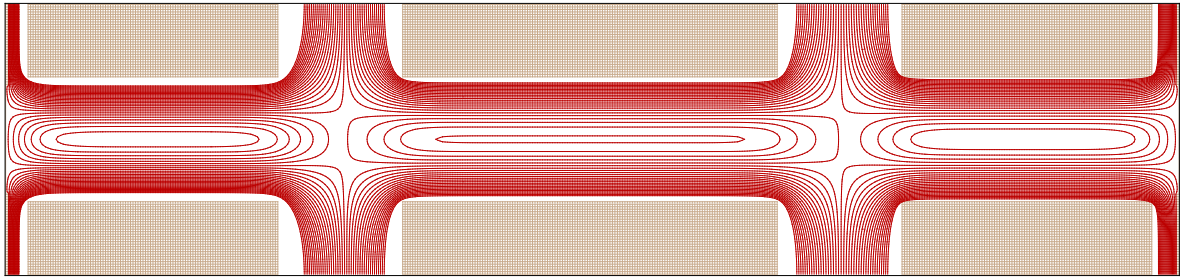


Figure 3.3: SIMION7 output for same triplet as in Fig. 3.1, but with Dirichlet type boundary conditions at front and rear side.

From Fig. 3.2 one can see, that in case of a multiplet the Neumann type boundary condition at front and rear is causing an artificial energy spread, which can be overcome if two potential electrodes (transparent to the ion beam) are placed at the front and rear of the multiplet, as shown in Fig. 3.3 for the same triplet as in Fig. 3.1.

If a Dirichlet type boundary condition is created at the front and rear by choosing ground potential for the electrodes in question, the energy change is no longer possible, because all particles enter and leave the multiplet on the same potential lines, so that the energy development of Fig. 3.2 changes to Fig. 3.4.

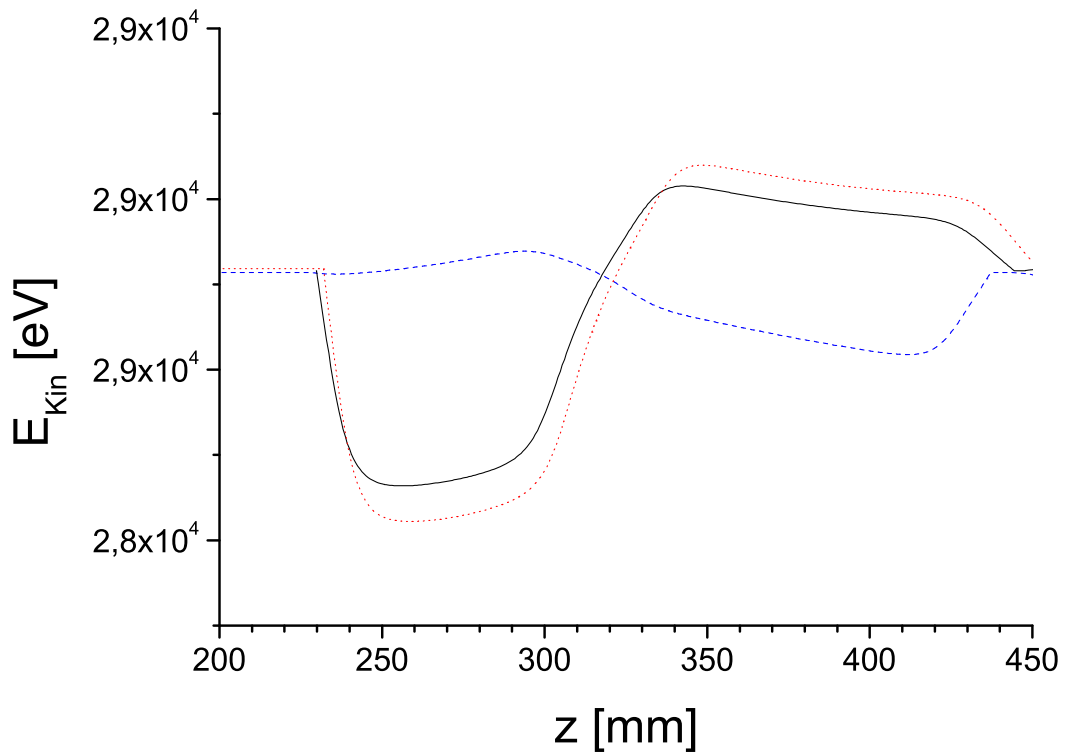


Figure 3.4: Same as Fig. 3.2, but with Dirichlet boundary conditions at the front and rear end of the doublet. No artificial energy spread can be observed.

Figures 3.2 and 3.4 have been created using SIMION's ray tracing options, which can trace up to 500 rays throughout the ion optical system. A data taking system allows to write down various beam parameters, like position, velocity, energy, energy spread at the location of an imaginary detector, that can only be placed in the x-y, x-z or y-z plane. However, this restriction to the mentioned planes leads to problems if the emittance of a beam at an finite angle with respect to the major axes shall be determined. In this case, phase space diagrams obtained in this way need to be scaled by the cosine of the average angle of deflection. This scaling method is not perfectly exact but also does not add a major uncertainty to the determination of the emittance, which is generally measured by finding a geometrical shape, e.g. ellipse, square circle or combination of shapes and fitting them into the phase space diagram by hand. Calculating the sum of the shape areas gives the emittance. This method is not very accurate but yields a reasonably good approximation for the emittance and allows to determine whether the emittance grew, stayed constant or shrunk.

However, SIMION also has some limitations. Creating new or changing old geometries is rather time consuming since calculations of the fields can take hours. There is no quick way to see how a small change affects the system. Also every component in the ion optical system takes up a huge amount of system memory, with too many components making ray tracing incredibly slow and system performance comes close to a hold even on fast machines. This problem was reduced by running the simulations in three parts similar to the arrangement of sections within this chapter.

3.1.1 Beam extraction

This subsection is concerned with the beam transport from the ion source up to the object point of the mass separator. All ion optical components must be placed in a beam tube with an outer diameter of 140 mm. The distance from the source to the end of the last lens is also given to be approximately 5 m and the design requirements are as follows:

Primary objective

- Beam transport from the source to separator

Secondary objectives

1. Loss free transport
2. No emittance growth
3. x-Focus in front of the separator
4. Slightly converging beam in y at separator
5. Intermediate focusing between lenses
6. Offset correction between lenses and source
7. Compensation of downward bends of beam tube due to gravity

Secondary objectives 1 and 2 are clear and the requirements 3 and 4 will become clearer in the next subchapter when the operating principle of the mass separator is explained. Objective 5 is a tribute to radiation safety. It is planned, that at beam waits between lenses absorbers for

neutron and gamma radiation from the core will be installed, which will have sufficient holes for the ion beam to pass through. Objectives 6 and 7 come from the requirement, that the beam tube must not touch the through going vacuum tube, SR6, hence source and lens trolley must support themselves for about 3 m each. Therefore both will bent downwards due to gravitation and it might not be feasible to perfectly align both trolleys to another. Therefore, an offset of up to 5 mm is considered possible, which the beam transport optics should be capable of handling as well as the downward bent of the beam tube, while still meeting all other objectives.

Given all the boundary conditions and the seven secondary objectives it was decided early on to use two quadrupole triplets as the first two lenses and a doublet as the third one. The advantage of quadrupoles over Einzel-lenses lie in the higher quality of the image which results in a "rounder" beam spot. This is advantageous for objective 5 since a round spot allows a smaller hole in the radiation shield. Additionally, quadrupoles have enhanced steering capabilities, which are especially helpful to fulfill requirements 6 and 7. Finally, the voltage required to operate a quadrupole is small compared to Einzel-lenses, hence reducing the probability of high voltage sparks. The reason for choosing a doublet over a triplet for the last lens is easily found in objectives 3 and 4, that require no y -focus and therefore are best met by a doublet.

First simulations have been performed with COSY infinity as shown in Fig. 3.5. With COSYs fitting capability it is easily possible to fit any parameter of the transfer matrix to the desired value, thus creating foci at whatever position is desired. If the transfer matrix elements $(x|a)$ and $(a|x)$ are fitted to vanish simultaneously in x and y , (with a being the angle of a ray in the x - z plain, with respect to the z -axis), a *double telescopic system* can be achieved with the first two triplets, which has the advantage that all second order effects add to zero. However, in practice it was found impossible to achieve the desired fit with COSY for all four matrix elements simultaneously. Nevertheless, the influence of second order effects is at an acceptable level at this point.

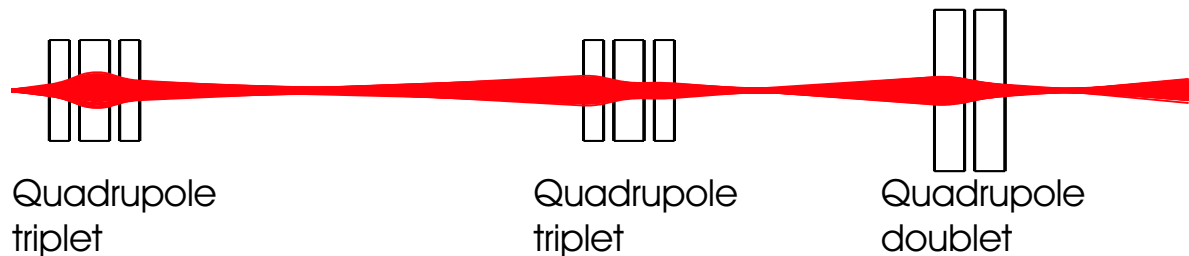


Figure 3.5: Typical COSY output for section 1 simulations in x . Intermediate focusing can easily be achieved at any position using the fitting routines.

Knowing from COSY simulations that objectives 3 and 4 can be met, SIMION was used to verify 1 and 2 and develop solutions for problems 6 and 7. In a first step the three lenses have been created from the layout of an already constructed triplet prototype and subsequently arranged, in the SIMION environment, in the same way as in the COSY simulation.

Ion acceleration

Special attention was paid to the starting conditions of the ions exiting the source. Values obtained from IGUN calculations by O. Kester [38] have been turned over to SIMION at the beam waist located at the ion source exit electrode, where the beam has an emittance of 60π mm·mrad @ 1keV as shown in Fig. 3.6.

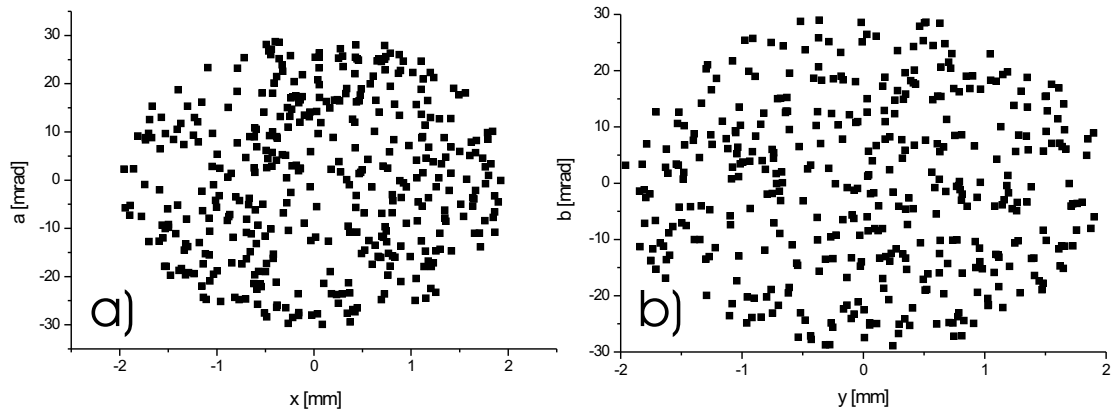


Figure 3.6: Emittance turned over from IGUN to SIMION at 1 keV.

Within the next 35 mm after the extraction electrode the beam passes through a potential of 29 kV and is accelerated to the final energy. In agreement with the square root law the emittance drops to 11π mm·mrad (Fig. 3.7). Up to this point the emittance can easily be calculated from the figures by simply calculating the area using the formula for an ellipse.

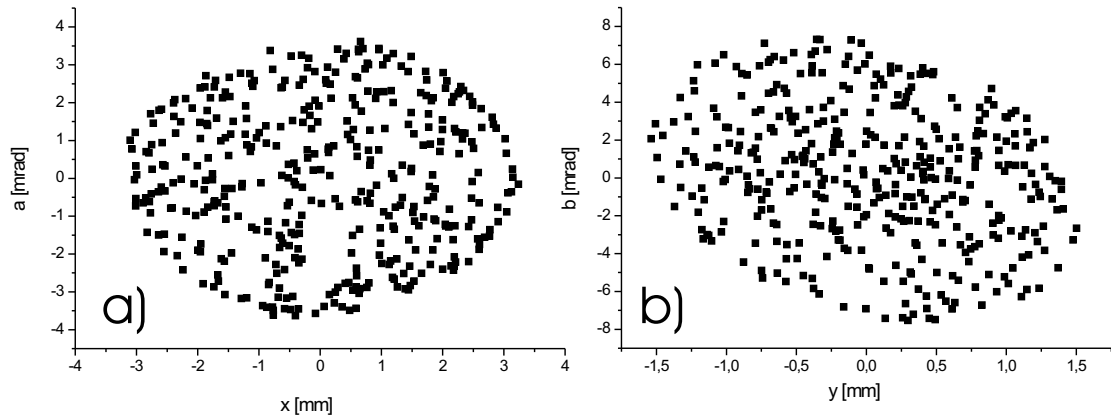


Figure 3.7: A very slight deviation from the circular shape can be seen in the emittance figure after acceleration by 30 kV.

Offset compensation

While the beam can be transported smoothly without any offset in the system, compensating an offset of 5 mm between the source extraction electrode and the acceleration electrode is more challenging. Since the system is symmetric it does not matter in which direction the offset is introduced. The y-direction has been chosen, because the beam tube bends this way and it seems to be the most likely direction an offset may occur.

The goal is to steer the beam back to the original z-axis, which requires two steering voltages. One is applied to the middle section of the first triplet and the other one needs to be applied to the acceleration electrode itself, thus requiring the electrode to be segmented. For the simulations

a four segment electrode as shown in Fig. 3.8 has been used with an applied voltage in the order of 1 kV, which is sufficient to achieve the desired steering effect.

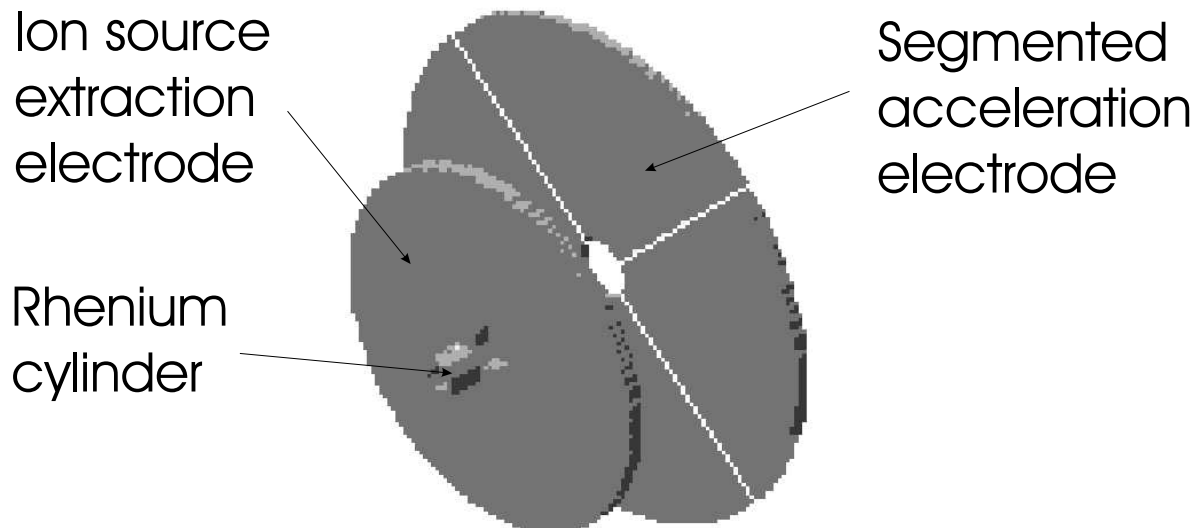


Figure 3.8: Four segment acceleration electrode for offset correction and ion source extraction electrode. Electrode segments should be in one plain and have a centric hole of 16 mm diameter.

During the acceleration process the beam picks up an energy spread, which is, however, not specific to the offset case. Analyzing the energy distribution of the beam, an average post acceleration energy of 28,457 eV can be determined with a standard deviation of 27 eV. The average energy is lower than expected, due to inhomogeneities in the electric field, as ions did start at the end of the 2 mm thick extraction electrode of the ion source. However, the energy discrepancy is not of serious concern. In fact it can be decreased by moving the starting point of the ions 2 mm back to the beginning of the electrode. Now the average energy is 29,462 eV and the standard deviation decreases to 11 eV. The change in energy spread is also understood and originates in the fact, that all starting ions have the same z position and energy, while the potential lines are not constant in the x-y plane. This effect worsens the more space the electric field has to develop and could be avoided in principle by using SIMION to describe the complete acceleration process from thermal energies to 30 keV. However, SIMION has a poor reputation [38] in describing ions in the meV range. Furthermore, there is no guarantee that the final setup will have a zero energy spread and therefore it has been decided to accept the lower energy and higher energy spread for the following simulations. The fact that the beam energy is off by 5% from the desired value is not a big issue. From the variables that depend on the energy, like the voltages applied to the electrostatic elements, the bending radius of the magnet, and the emittance only the last one is of any importance. However, performing calculations with a 3% larger emittance leads to a more

conservative estimate.

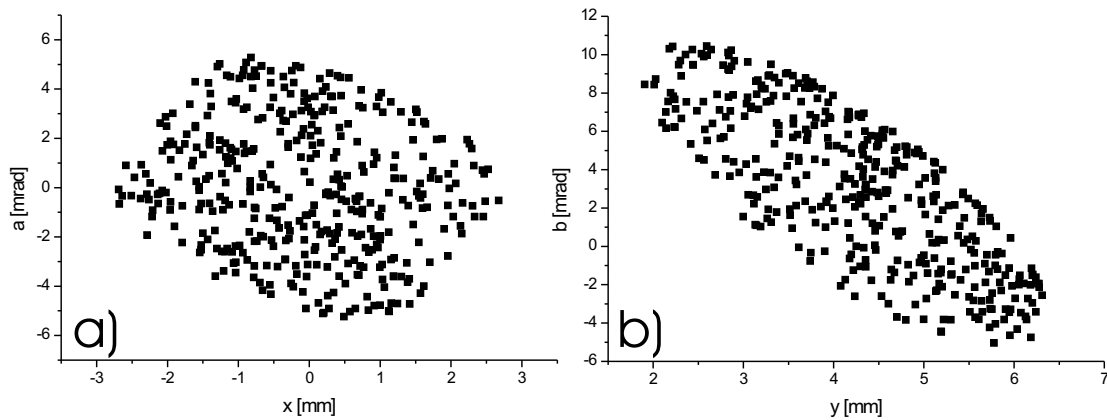


Figure 3.9: Emittance after acceleration with offset. The deviation from a circular shape has increased and the position of the y -focus has shifted down-streams resulting in a tilted ellipse, see text for details.

The offset and no-offset cases can first be compared just after accelerating the beam to its final energy. From Fig. 3.9, showing x and y emittance in the offset case for equal z position as in Fig. 3.7, it can be seen that the phase space ellipse is slightly distorted and resembles more a square than a ellipse. This is because the beam is now passing through the acceleration electrode off center, which also causes the y -ellipse to change, however, without a visible distortion. Nevertheless, the position of the waist has shifted down-stream, which can be seen from the angle of the tilt, as explained in Fig. 3.10. If the beam converges, negative x -values (or y -values) correspond to positive values for the angle a (or b), as it is the case in Fig. 3.9.

Assuming ellipses for both phase space diagrams in Fig. 3.9 and multiplying the half axes' with π an emittance increase to 14π mm·mrad for x and 24π mm·mrad for y can be found. The situation relaxes during transport to the final focus, where the phase space diagram looks as shown in Fig. 3.11.

At the mass separator object position, the emittance growth is under control and the y -emittance is back to the starting value (11π mm·mrad). From the orientation of the ellipse one can judge that the beam is in fact converging, as required. The x -emittance looks good with respect to phase space volume, but the shape of the ellipse shows some distortion. This aberration is a well familiar phenomenon to quadrupole lenses [49] known as *standard quadrupole aberration*. The x -emittance increase is about 1π mm·mrad or 10%, but can be reduced by increasing the inner diameter of the quadrupole. This has already been done for the doublet to improve Fig. 3.11. Ideally, the illuminated area of a lens is smaller than 66% of the lens cross-section to avoid fringe field effects. In case of the third lens, the quadrupole doublet, illumination was well beyond the ideal value. The other two lenses, however, are decently illuminated and a replacement with larger ones is not necessary.

From Fig. 3.12, comparing the energy spread in the no-offset case a) at the x -focus before the first electrostatic deflector to the situation with an 8 mm offset b), it can be seen that the transverse emittance is only slightly increased as is the energy spread. Comparing Fig. 3.12 a) with Fig. 3.11 shows, that the only difference between a 5 mm offset and no offset is the increased standard

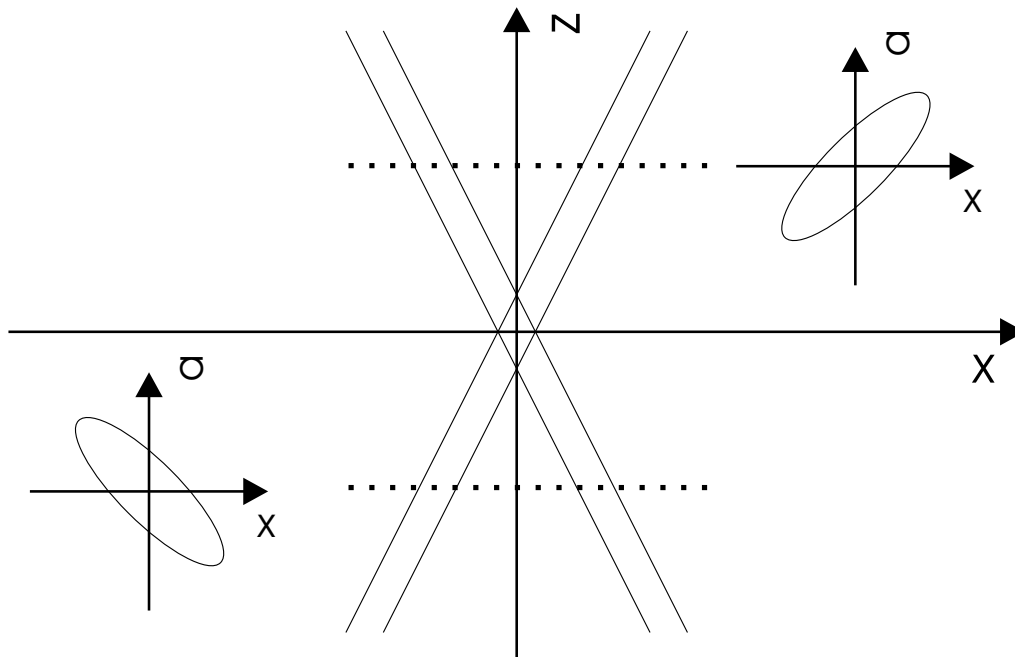


Figure 3.10: Tilts in emittance ellipses result from measuring the emittance before or after a focus. For a diverging beam after the focus, negative angles a coincide with negative values for x , resulting in a tilted ellipse.

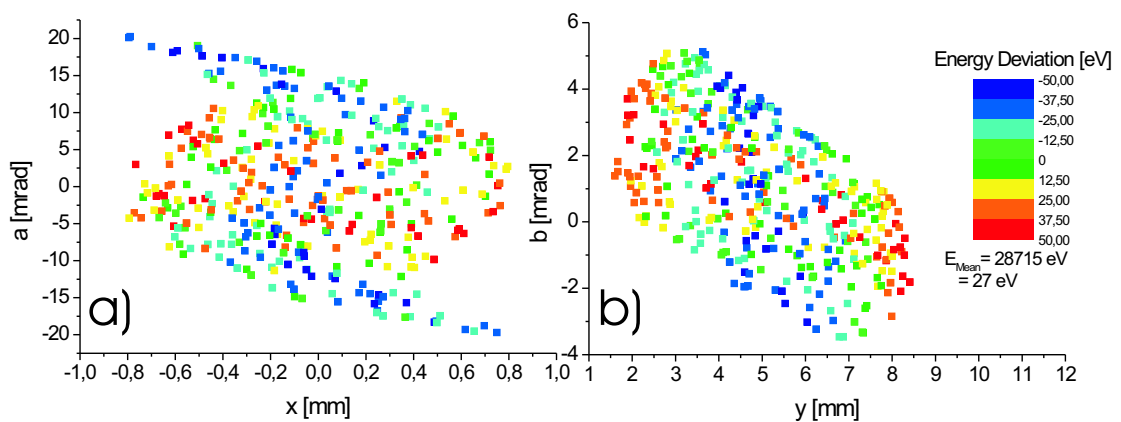


Figure 3.11: Emittance at mass separator object position. Here only an x -focus is required and the x - a phase space shows the standard quadrupole aberration, which has already been reduced by increasing the active diameter of the doublet. The color coding shows the distribution of the energy deviation.

quadrupole error with increasing offset, because increasing offsets require more asymmetric voltages in the first triplet, which in turn increases the standard quadrupole aberration.

A complete overview of the simulation results for the 5 mm offset case is given in Fig. 3.13, where a complete summary of the above ion optical calculations is given. The content of Fig. 3.13 is explained in the following:

- Figure 3.13 a) shows the beam evolving in y - z plane throughout the lenses.

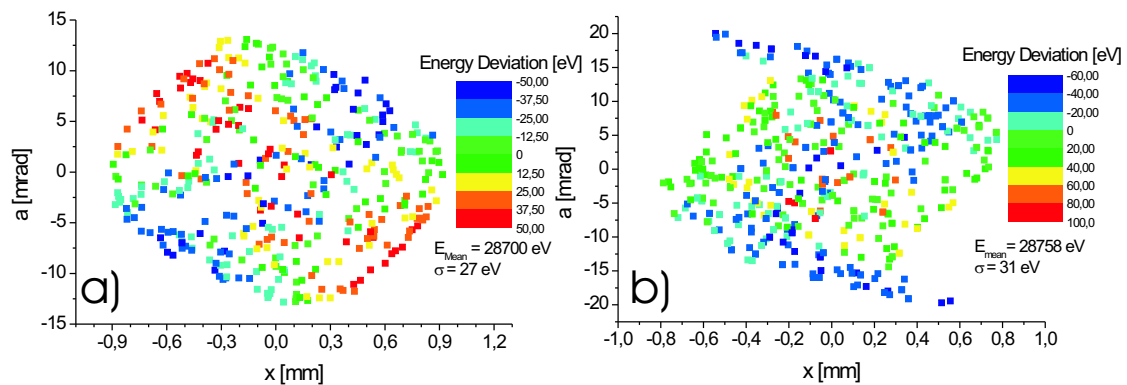


Figure 3.12: As Fig. 3.11 but for a) no offset compared to b) 8 mm offset. Energy spread and standard quadrupole error increase.

- All numbers lacking units are distances in mm, with some distances looking like an unexpected choice. This is because SIMION abstracts 1 mm during the compilation of the geometry files.
- Voltages given in 3.13 a) and b) are applied to the electrodes, with offset voltages not mentioned.
- Figure 3.13 b) is a magnification of the source area in a).
- Figure 3.13 c) shows the x-z plane to complete the information. It is here where the higher illumination of the doublet in comparison with the triplets becomes obvious.
- Numbers with units in between the optic elements refer to the dimension of the beam. At the first focus, for example, the beam radius is smaller than 5 mm for 490 mm on each side of the focus. This information is required for placement of radiation shields.
- The heat shield has no influence on the beam and is just drawn for completeness. It shall protect the first triplet from the source temperature.
- The iris marks the approximate position of the H-valve stack. It also has no influence on the beam as long as it fits through.
- The darker line crossing the beam in picture 3.13 a) and c) mark the position of the x-focus.

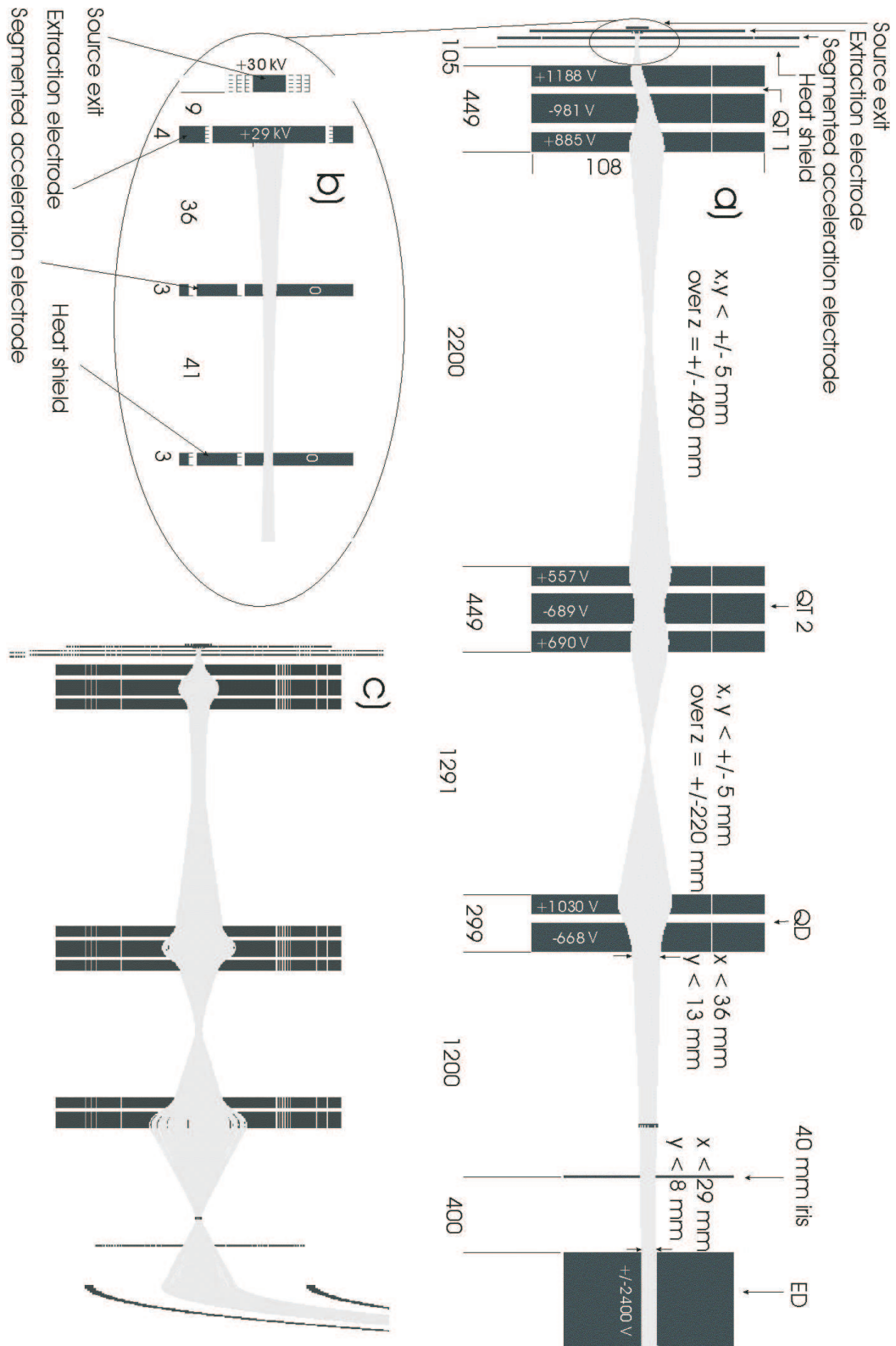


Figure 3.13: Summary of section 1 beam transport. a) Correction of the 5 mm offset can be seen clearly in the y-z plane. b) shows a close up view of the acceleration and steering electrodes. c) Shows the x-z plane with x focus at mass separator object position. All numbers given without units are distances in mm.

Beam tube bending

The need for the capability to compensate a downward bent of the beam tube is illustrated in Fig. 3.14, which shows a multi-color drawing of the actual design for the extraction trolley's beam tube extension. The design has been optimized by the engineering department of the FRM-II and achieves a bending of 1.3 mm over 2.8 m, which is of far less impact than the correction of a 5 mm offset within the first half meter after the source. For a quantitative analysis of this bending, the

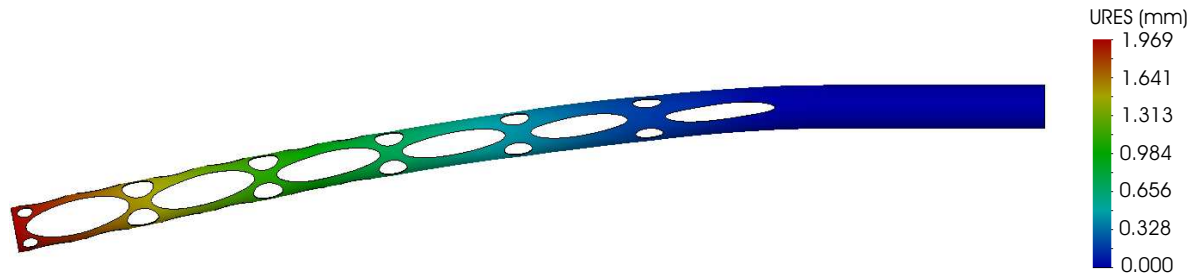


Figure 3.14: Bending of the beam tube due to gravitational influence. The tube has some clearances for weight reduction and bends a total of 1.3 mm over 2.8 m.

acceleration electrode has been tilted with respect to the 1st triplet, simulating a very severe bend of the beam tube. Results for 0.3° and 0.4° are shown in Fig. 3.15. The angles correspond to a downward bend of 14.7 mm and 19.5 mm respectively, representing an exaggeration of the worst possible situation. It can be seen that there is no mentionable emittance growth up to a bent of 0.3° .

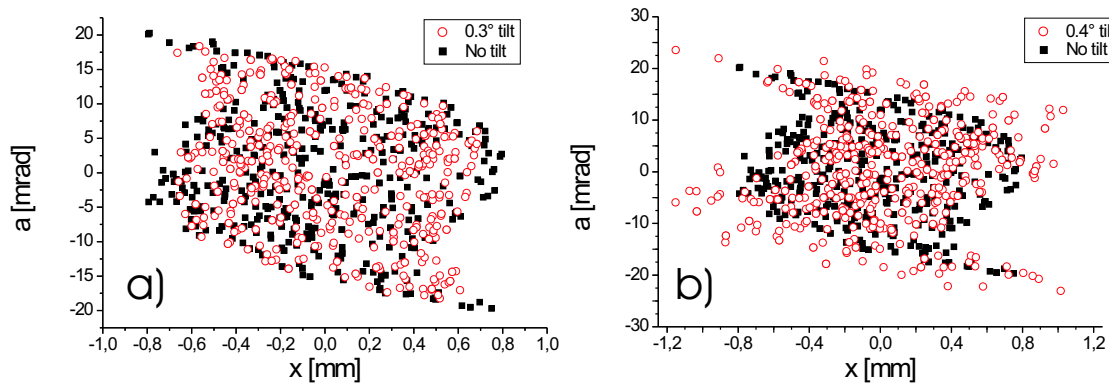


Figure 3.15: Bending of the beam tube or misalignment of ion optic components can cause a tilt effect. Expected influence of the tilt on the phase space area is shown in a) and b) for tilts corresponding to downward bends of 14.7 mm and 19.5 mm, respectively.

Space charge effects

Finally, SIMION7 can be used to determine the effect of space charge on the emittance in order to verify calculations performed in an earlier work [30] for the ion source design with the IGUN code [50]. It has been found, in that work, that space charge effects on the emittance in the MAFF geometry are smaller than 1% for ion currents of $10 \mu\text{A}$ with expected maximum ion currents at

MAFF of $0.6 \mu\text{A}$. Fig. 3.16 gives a comparison between no beam charge and $1 \mu\text{A}$ ion current at the focus in front of the mass separator in analogy to the situation in Fig. 3.11. It can be seen from this picture that space charge is of little impact over all but causes some runaway ions, which can be neglected considering the accuracy of SIMIONs space charge calculation capabilities. Also, simulations with space charge require an exorbitant amount of time, therefore all other simulations are done without space charge.

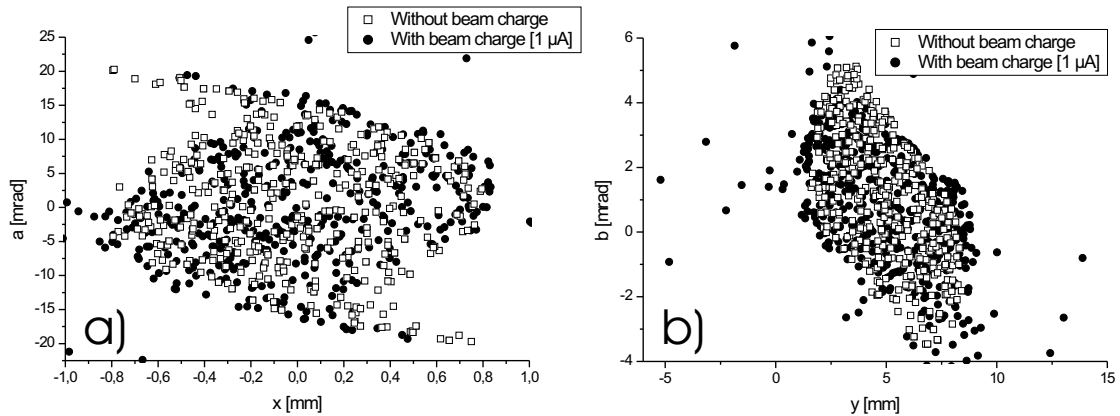


Figure 3.16: SIMION space charge simulation at x-focus before first electrostatic deflector. Runaway ions can be neglected within the accuracy of the space charge calculations.

Conclusion

To conclude this section, it can be said that the primary objective and all seven secondary requirements can be met.

1. Loss free beam transport is possible with and without a 5 mm offset if a segmented acceleration electrode is used with a minimum hole diameter of 16 mm. The same setup can also compensate an 8 mm offset at the cost of slightly increased emittance.
2. In all cases no serious emittance growth can be found. Standard quadrupole aberration causes image distortion at focal points. The effect has been successfully reduced by increasing the active diameter of the doublet from 50 mm to 60 mm.
3. An x-focus can be achieved at any point in front of the separator.
4. A slightly converging beam in y after the doublet is possible.
5. There is large freedom in positioning the intermediate foci. They can be moved around if necessary, but it must be kept in mind, that by moving the focus closer to one multiplet the illumination in the other one will increase, possibly causing larger image distortions. The suggested focus positions give more than enough room to place shielding plugs, with a suggested opening diameter of 15 mm or more depending on the length of the plug.
6. Offset correction is possible, if the acceleration electrode is segmented to apply a steering voltage additional to the steering capabilities of the first triplet. The distance from the acceleration electrode to the first triplet has been found to be crucial, with an increase leading to too much steering in one direction. As a result the beam enters the triplet too

close to the electrode and fringe field effects start to dominate, which leads to undesirably large emittance growth.

In addition, the segmented acceleration electrode is a special engineering challenge, since it has to withstand temperatures of up to possibly 1300 K caused by the ion source, and operate under continuous bombardment from radionuclides and graphite originating from the source. The latter is considered a special problem since it will inevitably create a conducting layer on whatever surface visible from the source. However, the segmented electrode will require insulation between the segments, which must be hidden from the ion source to avoid the graphite layer.

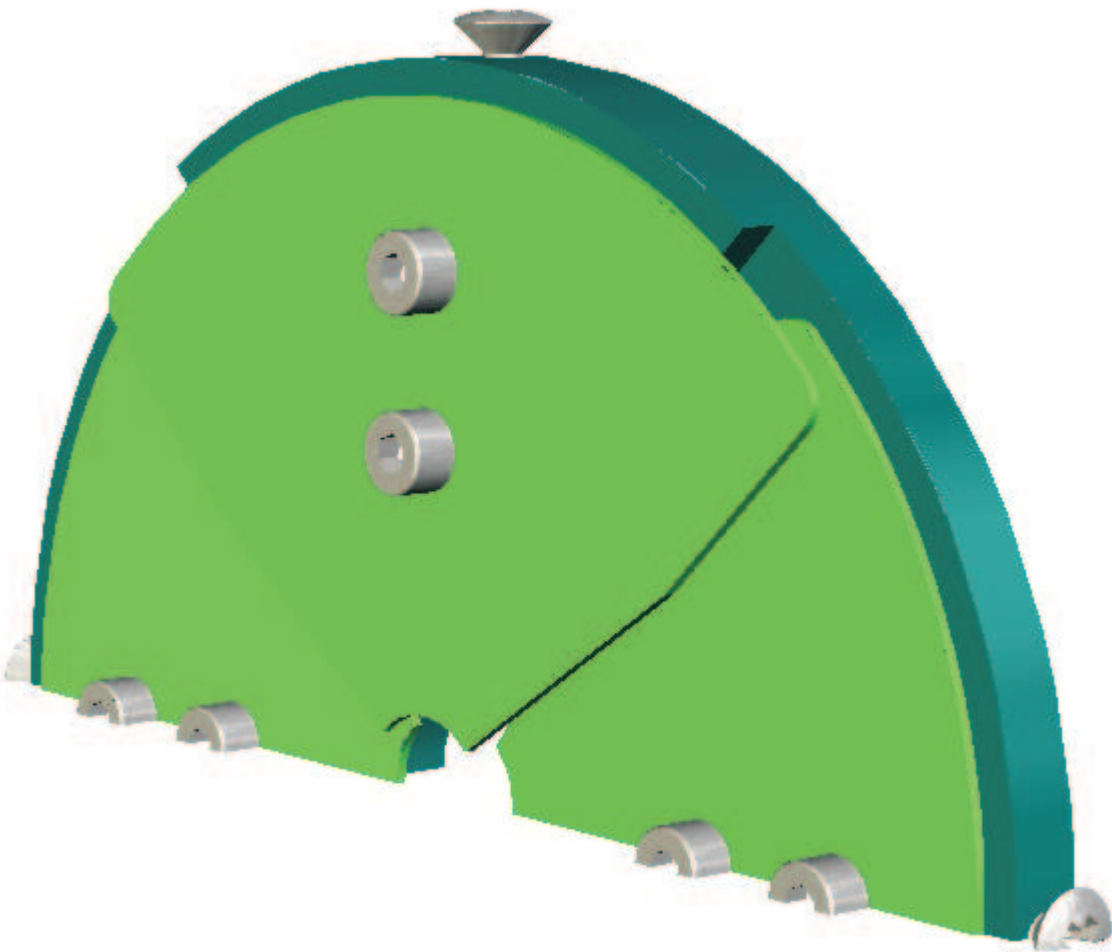


Figure 3.17: Extraction electrode design study: The steering electrodes are arranged in 2 planes. This layout increases the emittance by roughly 3π mm·mrad.

Fig. 3.17 shows a proposed solution for the problem of hiding the insulators. It is considered to place the electrodes of the four segments in different planes as shown in Fig. 3.17. Simulation shows that a 3 mm difference between the electrode planes (having only 2 planes, with the two opposing electrodes in equal planes) causes an emittance growth of roughly 3π mm·mrad. Something that should be avoided if possible.

7. A downward bent of up to 14.7 mm or another misalignment of up to 0.3° can be compensated with the available steering capabilities.

3.1.2 Mass pre-separator

To select the mass numbers delivered to the intermediate and high resolution mass separators and to contain all other masses in a well restricted space, a low resolution mass separator is needed. With the heaviest fission fragments weighing 159 u, a separator with a resolving power $m/\Delta m > 160$ is sufficient. Further requirements to the separator layout come from the space restrictions in the FRM-II experimental hall. MAFF I has to fit in a small segment at the reactor as seen in Fig. 1.2. Therefore a compact design was sought and found in the Mattauch-Herzog mass separator [51], which can be placed in a space saving S-shape. The separator consists of a drift (D_1) from object to the electrostatic deflector (E), followed by a second drift (D_2) and a magnetic dipole (M). A third drift (D_3) from the magnet to the slits is zero. An additional advantage is that only one magnet is needed, which also saves a lot of space needed for other equipment.

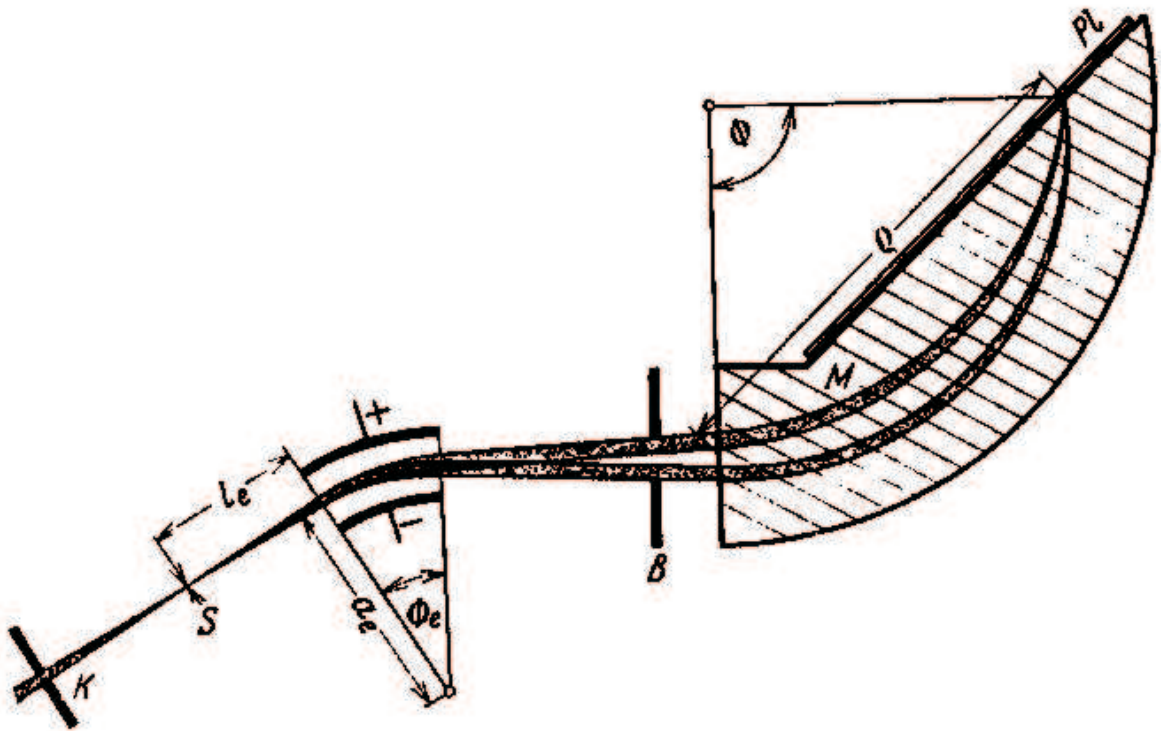


Figure 3.18: Original drawing of the separator by Mattauch and Herzog [51] consisting of an electrostatic and a magnetic deflector.

Matrix calculations

The ion optic properties of the mass separator have been theoretically investigated at first by J. Mattauch and R. Herzog in 1934 [51]. The original drawing of the spectrograph from their initial paper is shown in Fig. 3.18. Within Appendix B the ion optic calculations for the separator are elaborated in detail using the transfer matrix formalism. At this point only the final transfer matrix shall be shown. At first, however, a small introduction to the transfer matrix formalism and the meaning of the matrix components shall be given for better understanding.

The relation between a position vector \vec{x}_0 before an optical system and \vec{x}_1 at a position after the optical system can be written as:

$$\begin{pmatrix} x_1 \\ a_1 \\ \delta_k \\ \delta_m \end{pmatrix} = \begin{pmatrix} (x|x) & (x|a) & (x|\delta_k) & (x|\delta_m) \\ (a|x) & (a|a) & (a|\delta_k) & (a|\delta_m) \\ 0 & 0 & 1 & 0 \\ 0 & 0 & 0 & 1 \end{pmatrix} \begin{pmatrix} x_0 \\ a_0 \\ \delta_k \\ \delta_m \end{pmatrix} \quad (3.1)$$

Where x is the distance from the optical axis, a is the angle of inclination towards the optic axis, δ_m and δ_k are the mass dispersion and the energy dispersion, respectively. The matrix is called the transfer matrix for the optical system. Each of the matrix elements has a specific meaning, explained in Table 3.1.

Table 3.1: Description of first order transfer matrix terms and effect on x-a phase space ellipse.

Element	Description	Effect
$(x x)$	Lateral magnification	Change in width
$(x a)$	Vanishes in point-to-point focusing	Tilt
$(x \delta_k)$	Lateral energy over charge dispersion	x-displacement
$(x \delta_m)$	Lateral mass over charge dispersion	x-displacement
$(a x)$	Vanishes in parallel-to-parallel focusing	Tilt
$(a a)$	Angular magnification	Change in height
$(a \delta_k)$	Angular energy over charge aberration	a-displacement
$(a \delta_m)$	Angular mass over charge aberration	a-displacement

The transfer matrix of the Mattauch and Herzog mass separator can be obtained by multiplying the transfer matrices for the sub elements D_1 , D_2 , D_3 , E and M.

$$T = D_3 \cdot M \cdot D_2 \cdot E \cdot D_1 \quad (3.2)$$

Using the known transfer matrices for drift lengths and sector fields the transfer matrix for the whole system can be determined as shown in equation 3.3.

$$T_{MH} = \begin{pmatrix} \rho_m/\rho_e & 0 & 0 & \frac{1}{2}\rho_m \\ \frac{1}{2}\frac{\sqrt{2\rho_e-2L_2}}{\rho_m\rho_e} & \frac{\rho_e}{\rho_m} & -\frac{1}{4}\frac{-2\rho_e+\sqrt{2\rho_e-2L_2}+2\rho_m}{\rho_m} & -\frac{1}{2} \\ 0 & 0 & 1 & 0 \\ 0 & 0 & 0 & 1 \end{pmatrix} \quad (3.3)$$

The Mattauch and Herzog mass spectrograph is designed to be double-focusing in space and energy, that means the matrix elements $(x|a)$ and $(x|\delta_k)$ vanish simultaneously, which has the major advantage that the resolution does not depend on the energy spread, but leads to special requirements for some values as summarized in Table 3.2 together with explanation of terms.

With the transfer matrix at hand the mass resolving power $\frac{m}{\Delta m}$ can easily be calculated. It increases with $(x|\delta_m)$, but is indirectly proportional to the x diameter R in the focal plane, which is given by

$$R = (x|x)2x_0 \quad (3.4)$$

with x_0 as the initial x deviation from the optic axis. From this value the mass resolving power can be derived:

Table 3.2: Summary of mass separator values.

ρ_e	Radius of electrostatic deflector
ρ_m	Radius of magnetic deflector
L_2	Drift distance between electric and magnetic dipole
$L_1 = \rho_e / \sqrt{2}$	Distance of object to electric dipole
$\Phi_e = \frac{\pi}{4\sqrt{2}}$	Angle of electric deflection
$\Phi_e = \pi/2$	Angle of magnetic deflection

$$\frac{m}{\Delta m} = \frac{(x|\delta_m)}{R} \quad (3.5)$$

$$= \frac{(x|\delta_m)}{(x|x)2x_0} \quad (3.6)$$

$$= \frac{\frac{1}{2}\rho_m}{2\frac{\rho_m}{\rho_e}x_0} \quad (3.7)$$

$$= \frac{\rho_e}{4x_0} \quad (3.8)$$

It is interesting to see, that the mass resolving power does not depend on the strength or size of the magnet, but on the radius of the electrostatic deflector, which can be advantageous since it is much cheaper to increase the size of the electric dipole compared to upgrading the magnet.

From Fig. 3.11 the object width can be determined to 1.6 mm and used in equation 3.5, together with a radius for the electrostatic dipole of 1 m, to determine the mass resolving power to:

$$\frac{m}{\Delta m} = \frac{1000}{2 \cdot 1.6} = 312.5 \quad (3.9)$$

This is about twice the required resolution. As a double focusing system lateral energy aberration is not a problem, because $(x|\delta_k) = 0$. Angular energy aberration $(a|\delta_k)$ however, is not, which will cause growing energy aberration with increasing distance from the focal plain of the separator.

Theoretically it would be possible to find a L_2 in order to make $(a|\delta_k)$ disappear. However, the radius of deflection in the magnet depends on mass and energy, therefore a different L_2 for every mass would be needed, which is simply not possible. Although it would be tempting to look for the best value of L_2 to achieve the lowest energy aberration possible, however this is not really an option, since the distance L_2 is basically given by the boundary conditions in the MAFF sector at the FRM-II and will be as large as possible to make the most of the available space.

However, this is not the only reason why this calculation would be in vain. As seen in Fig. 3.18 the focal plane coincides with the end of the magnet, which is a rather poor position to place a slit system. In order to have enough space to accommodate the slit system, the focal plane must be moved by reducing the angle of the magnet from 90° to 80° , so that the focal plane is shifted by a distance L_3 away from the magnet, so that the drift D_3 is no longer zero and the transfer matrix T_{MH} is no longer complete. The additional drift must be taken into account leading to a very complex result, of which only the matrix components of interest will be discussed in the following.

$$\begin{aligned}
(x|x) = & -[-\cos(\Phi_m)\rho_e\rho_m \cos(\sqrt{2}\Phi_e) + \rho_m \sin(\sqrt{2}\Phi_e)\sqrt{2} \cos(\Phi_m) \\
& + \sin(\sqrt{2}\Phi_e)\sqrt{2} \sin(\Phi_m)\rho_m^2 + L_3\rho_e \cos(\sqrt{2}\Phi_e) \sin(\Phi_m) \\
& - \sqrt{2}L_2L_3 \sin(\sqrt{2}\Phi_e) \sin(\Phi_m) \\
& + \sqrt{2}L_3\rho_m \sin(\sqrt{2}\Phi_e) \cos(\Phi_m)]/(\rho_e\rho_m)
\end{aligned} \tag{3.10}$$

$$\begin{aligned}
(x|a) = & \frac{1}{2}[2L_1 \cos(\Phi_m) \cos(\sqrt{2}\Phi_e)\rho_e\rho_m - 2\sqrt{2}L_1L_2\rho_m \cos(\Phi_m) \sin(\sqrt{2}\Phi_e) \\
& - 2L_1\rho_m^2 \sin(\Phi_m) \sin(\sqrt{2}\Phi_e) + \sqrt{2}\rho_e^2\rho_m \cos(\Phi_m) \sin(\sqrt{2}\Phi_e) \\
& + 2L_2\rho_e\rho_m \cos(\Phi_m) \cos(\sqrt{2}\Phi_e) + 2\rho_m^2\rho_e \sin(\Phi_m) \cos(\sqrt{2}\Phi_e) \\
& 2L_1L_3\rho_e \cos(\sqrt{2}\Phi_e) \sin(\Phi_m) + 2\sqrt{2}L_1L_2L_3 \sin(\sqrt{2}\Phi_e) \sin(\Phi_m) \\
& - 2\sqrt{2}L_1L_3\rho_m \sin(\sqrt{2}\Phi_e) \cos(\Phi_m) + \sqrt{2}\rho_e^2L_3 \sin(\sqrt{2}\Phi_e) \sin(\Phi_m) \\
& - 2\rho_eL_2L_3 \cos(\sqrt{2}\Phi_e) \sin(\Phi_m) \\
& + 2\rho_e\rho_mL_3 \cos(\sqrt{2}\Phi_e) \cos(\Phi_m)]/(\rho_e\rho_m)
\end{aligned} \tag{3.11}$$

$$\begin{aligned}
(x|\delta_k) = & \frac{1}{2}[\rho_e\rho_m \cos(\Phi_m) - \rho_e\rho_m \cos(\Phi_m) \cos(\sqrt{2}\Phi_e) \\
& + \rho_m\sqrt{2}L_2 \cos(\Phi_m) \sin(\sqrt{2}\Phi_e) + \rho_m^2 + \rho_m^2 \sin(\Phi_m) \sin(\sqrt{2}\Phi_e) \\
& - \rho_m^2 \cos(\Phi_m) - \rho_e \sin(\Phi_m) + \sqrt{2}L_2L_3 \sin(\Phi_m) \sin(\sqrt{2}\Phi_e) \\
& + \sqrt{2}L_3\rho_m \cos(\Phi_m) \sin(\sqrt{2}\Phi_e) + L_3\rho_m \sin(\Phi_m)]/\rho_m
\end{aligned} \tag{3.12}$$

$$(x|\delta_m) = \frac{1}{2}(\rho_m - \rho_m \cos(\Phi_m) + L_3 \sin(\Phi_m)) \tag{3.13}$$

The new transfer matrix is similar to the matrix obtained for the Mattauch-Herzog layout, but with more complex terms. Again it is desired to achieve a double focusing system, requiring to solve the equations $(x|a) = 0$ and $(x|\delta_k) = 0$, which can be achieved by two different approaches. Both require to solve the equations for $L_2(L_1, L_3)$ respectively $L_3(L_2)$. In a first attempt $L_2(L_1, L_3)$ can be eliminated in $L_3(L_2)$ resulting in a correlation between L_3 and L_1 , with $L_3(L_1)$ also depending on the radius of deflection ρ_m and hence the mass of the particle. The correlation between nuclear mass number A and drift length L_3 for all values as described above and magnetic field of $B=0.5$ T is approximately given by:

$$L_3 \approx 17.19\sqrt{A}[mm] \tag{3.14}$$

Equation 3.14 is true if the x_0 focus stays in place, which may not be the best choice if the highest resolving power shall be maintained. While $(x|\delta_m)$ is almost unaltered by adding non-zero L_3 , the matrix element $(x|x)$ shows a singularity for $L_1 = \frac{\rho_e}{\sqrt{2}}$ if L_2 is eliminated using $L_2(L_1, L_3)$. If L_2 is not eliminated from $(x|x)$ and L_3 is determined with $L_3(L_2)$ the fraction $(x|\delta_m)/(x|x)$ can be calculated. The obtained result is 492 mm with very little dependance on A and L_2 , which is 1.6% lower than the value of 500 mm ($500/1.6=312.5$) achieved with the classic layout.

The alternative way to achieve $(x|a) = 0$ and $(x|\delta_k) = 0$ is to use $L_3(L_2)$, since it does not depend on L_1 , as an input in $(x|a) = 0$ and solve this equation for $L_1(L_2)$. This allows to calculate the A dependance of L_1 , L_3 and $(x|\delta_m)/(x|x)$ for a given L_2 , or the L_2 dependance for a given A. It can be seen from the Figures 3.19 to 3.21 that the effects on L_1 position and mass resolving power over a wide range of masses or distances are small. However, it must be noted, that L_1 is smaller than $\rho_e/\sqrt{2}$. Finally the mass resolving power can be calculated if $(x|\delta_m)/(x|x)$ is divided by $2x_0$.

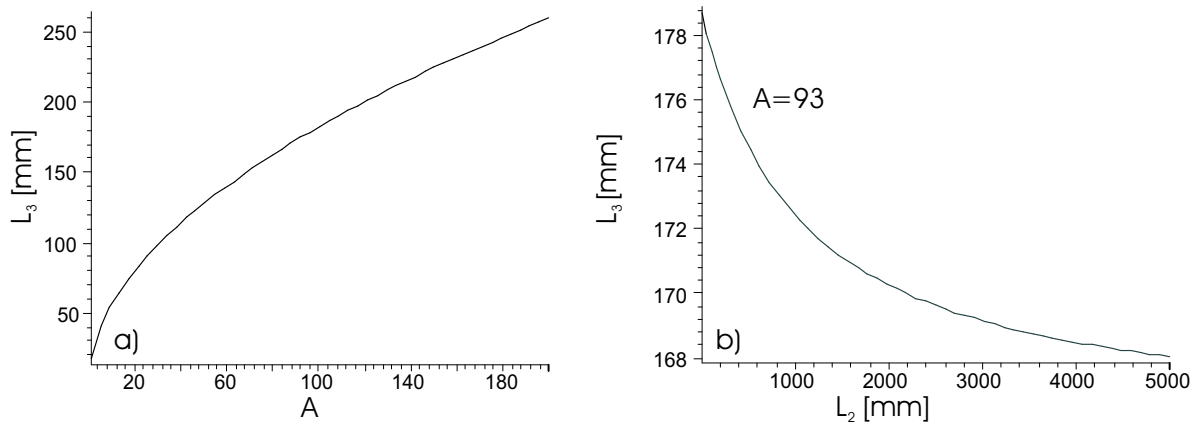


Figure 3.19: L_3 dependence on L_2 for constant A and L_3 dependence on A for constant L_2 . It can be seen, that L_3 does not depend on L_2 very much, hence the variation over a large scale of L_2 is small, while the A dependance grows with the square root of A

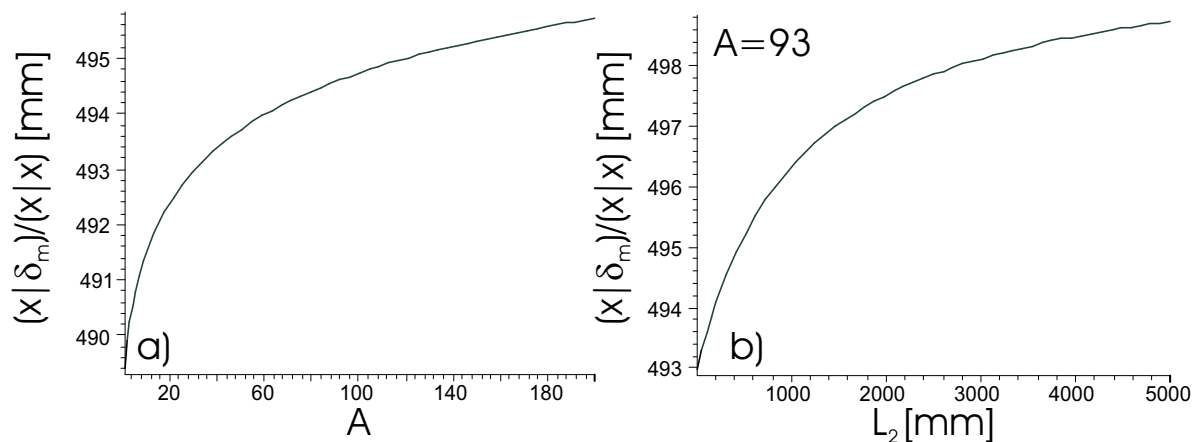


Figure 3.20: Dependence of the mass resolving power on L_2 for constant A and on A for constant L_2 . It can be seen, that the mass resolving power does not vary very much with A or L_2 .

To conclude the matrix calculations it can be said, that the dependence of the mass separator on L_2 is not crucial. The influence of various masses is also not of concern. However, it can be seen that the optimal value of L_1 is likely to be smaller than $\rho_e/\sqrt{2}$ (707 mm).

Simulations with COSY infinity

In a next step the configuration was put into COSY to deepen the understanding of the hole system. Initial simulations were done in first order with the separator system, including ion trajectories,

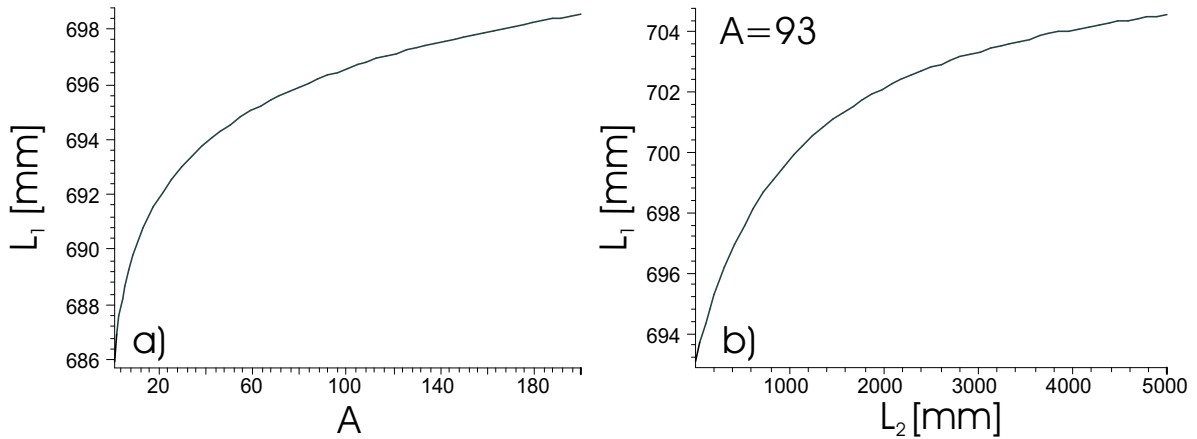


Figure 3.21: L_1 dependence on L_2 for constant A and on A for constant L_2 . L_1 does also not vary a lot but is smaller than the value expected for the unaltered Mattauch-Herzog design.

as shown in Fig. 3.22 in the x-z plane. The corresponding first order matrix values are given in

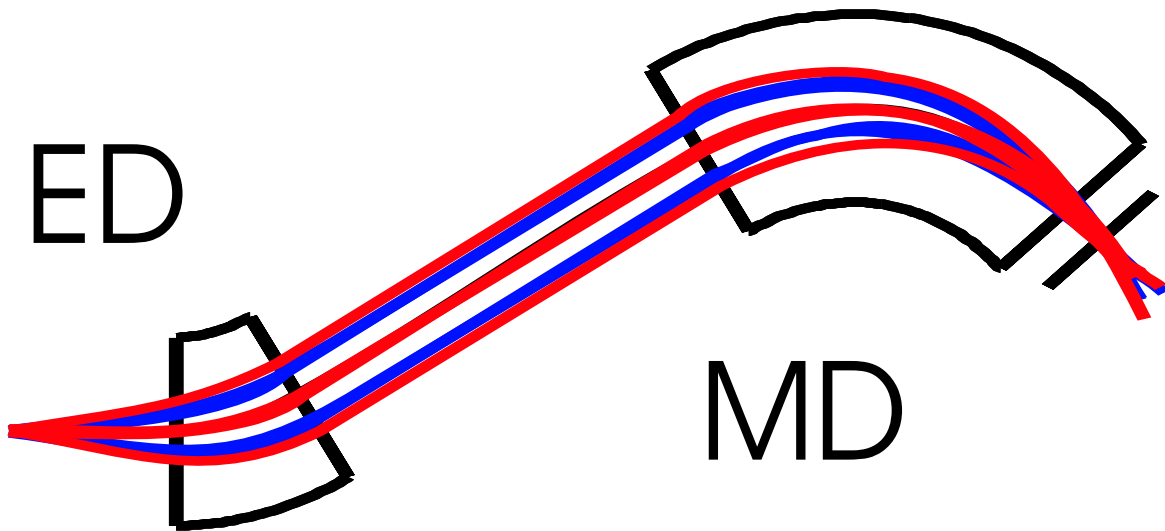


Figure 3.22: COSY simulation for the separator section. The foci at image and object position are achieved, between the ion optical elements the beam is nearly parallel, resulting in a very small influence of this drift.

Table 3.3.

From Table 3.3 it is rather obvious that the over all effect on the matrix values due to the alteration of the magnet angle is not large, the lateral magnification is almost completely unchanged. $(x|a)$ has been fitted to be as small as possible by the fit routine, since a x-focus is required. $(x|\delta_k)$ is in agreement with zero, while $(x|\delta_m)$ shows the largest deviation of 2.2%. The increase can be understood from equation 3.13 when a negative angle for the magnet is used to account for the antisymmetry in the system.

Second order terms have been calculated with COSY as well and are summarized in Table 3.4.

From the COSY simulations it can be seen, that they agree with the matrix calculations. The deviation from the standard Mattauch-Herzog design due to the change in magnetic deflection is smaller than the actual change of 12% in the angle and is better described by a *sine* dependence,

Table 3.3: Comparison of 1st order COSY calculations, for the classical Mattauch and Herzog (M+H) mass separator behind the magnetic dipole (MD) with COSY simulations of the MAFF pre-separator behind the magnetic dipole and behind the electrostatic deflector (ED)

Element	M+H b. MD	MAFF b. MD	MAFF b. ED
$(x x)$	-1.000	-1.004	-0.465
$(x a)$	0	$6.82 \cdot 10^{-6}$	-1.003
$(x \delta_k)$	0	$1.49 \cdot 10^{-2}$	0.268
$(x \delta_m)$	0.500	0.511	$3.10 \cdot 10^{-8}$

Table 3.4: Second order Cosy terms.

$(x xx)$	1.687	Aberration due to x_0 deviation
$(x xa)$	0.824	Mixed xa aberration
$(x aa)$	0.641	a-Aperture aberration
$(x x\delta_k)$	0.584	Mixed x energy aberration
$(x x\delta_m)$	-2.072	Mixed x mass aberration
$(x a\delta_k)$	2.090	Mixed a energy aberration
$(x a\delta_m)$	0.708	Mixed a mass aberration
$(x \delta_k\delta_k)$	-0.788	Quadratic energy aberration
$(x \delta_m\delta_m)$	-0.128	Quadratic mass aberration

which changes by only 1.5%.

Simulations with SIMION7

COSY has proven that the system generally works and first order deviations from the classical design are small. However, the influence of higher order effects is still not investigated as well as is the impact of fringe fields. Therefore additional SIMION simulations are needed for this part of the beam.

In a first step all geometries are taken from COSY and added to the existing SIMION workbench. The distance between the entrance of the electrostatic deflector and the x focus after the doublet has been set to 707 mm as required. The average radius for the deflector is 1 m. The field strength chosen for the magnet is 0.25 T.

To be able to identify second order distortions, it is imperative to know how they look like. Therefore, typical second order aberrations are shown in Fig. 3.23 and discussed in the following [52].

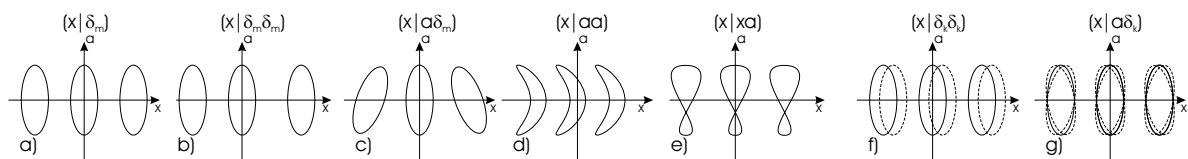


Figure 3.23: Second-order aberrations in x-a phase space for three different masses.

a) First order mass dispersion.

- b) Second order mass dispersion adds a non-linearity to the mass resolution.
- c) Tilt effect in focal plane. Occurs when focal and detector plane do not coincide.
- d) Ordinary sextupole aberration also known as a-aperture aberration.
- e) Second-order mixed $x\alpha$ aberration. Causes a *twist* in the phase space ellipse.
- f) Second-order energy dispersion, causing particles with different energies (dashed lines) to *walk* sideways from the mean energy.
- g) Energy-angle distortion. Particles with different energies (dashed) *wobble* around the mean.

The first second-order distortion can be seen in Fig. 3.24a) taken after the first electrostatic bent. At this point the beam should be parallel resulting in a horizontal line. However, an opening angle of 10 mrad can be found. The approximated total emittance at this point is 23π mm·mrad. To reduce this effect a curved shunt has already been added to the front of the deflector and a flat shunt to the back, as illustrated in Fig. 3.24b), to reduce fringe field effects.

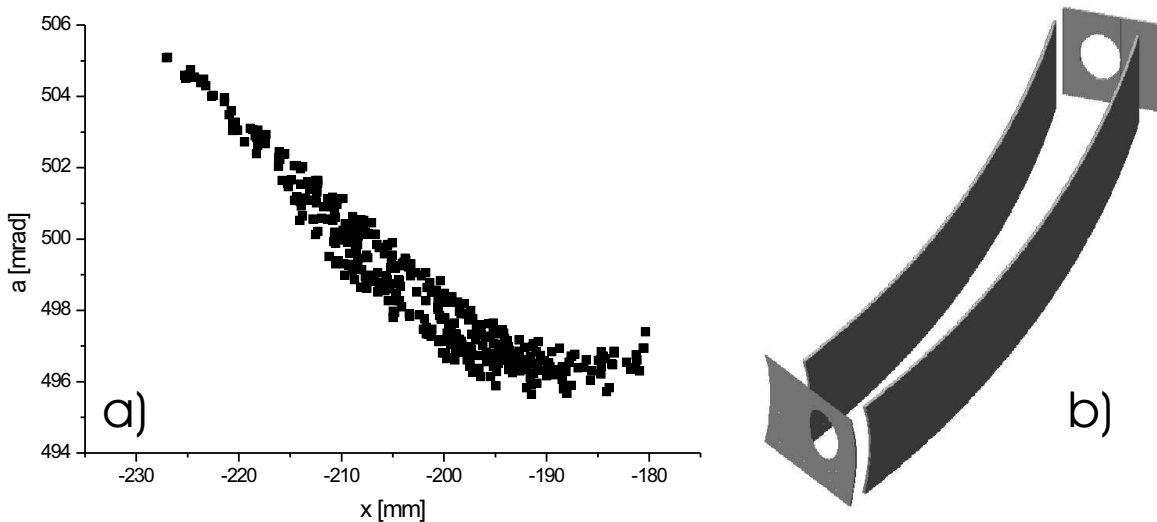


Figure 3.24: a) Emittance after electrostatic deflector shows, that the beam is not perfectly parallel and shows signs of distortion. b) Electrostatic deflector with curved shunts, which reduce higher order aberrations.

The nature of the distortion becomes more apparent at the x focus after the magnet, where the first order terms $(x|a)$ and $(x|\delta_k)$ become very small giving comparably more influence to the otherwise insignificant second order terms $(x|aa)$, $(x|a\delta_k)$ and $(x|\delta_k\delta_k)$, which should lead to a crescent shaped form with increased emittance due to *walk* and *wobble* errors. Fig. 3.25a) shows the situation without any of the modifications at the electrostatic deflector and the typical crescent shape from ordinary sextupole aberration can be seen clearly. It can be partially corrected by the modifications applied to the electrostatic deflector as can be seen in Fig. 3.25b). Note, that the crescent shape is opened in the opposing direction, which is because the position of the focus has shifted a bit. The approximated total emittance as measured from Fig. 3.25b) is 14π mm·mrad, which is a decrease almost to the original value, supporting the assumption that first order energy dispersion $(x|\delta_k)$ is responsible for the emittance growth after the electrostatic deflector.

The remaining emittance growth supports the idea of *walk* and *wobble* errors being present. Both errors can theoretically be corrected by sextupoles. However, attempts with sextupoles did not

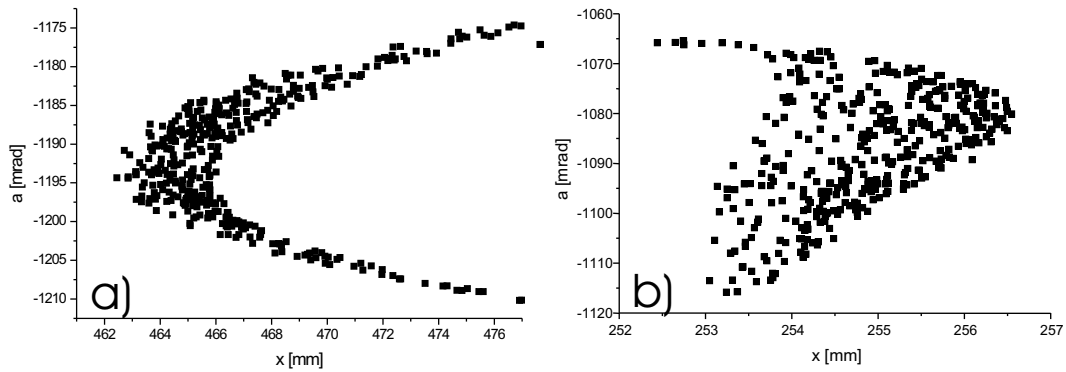


Figure 3.25: Emittance after magnetic deflector, a) without shunts at the ED and b) with shunts. The effects on the crescent shape caused by the sextupole error is clearly visible.

yield any immediate results and were put on hold, since sextupoles are unsuited for the MAFF beam-line for other reasons.

Now that second order effects on emittance after the mass separator have been studied and understood it is interesting to see how the mass resolving power is influenced. For this purpose a beam with mass 139 u and 140 u was sent through the separator as shown in Fig. 3.26, where the x-y plane and a-x phase space perpendicular to the beam in the focal plane of the magnet can be seen. To obtain this picture the mass resolving power was optimized by varying the drift length

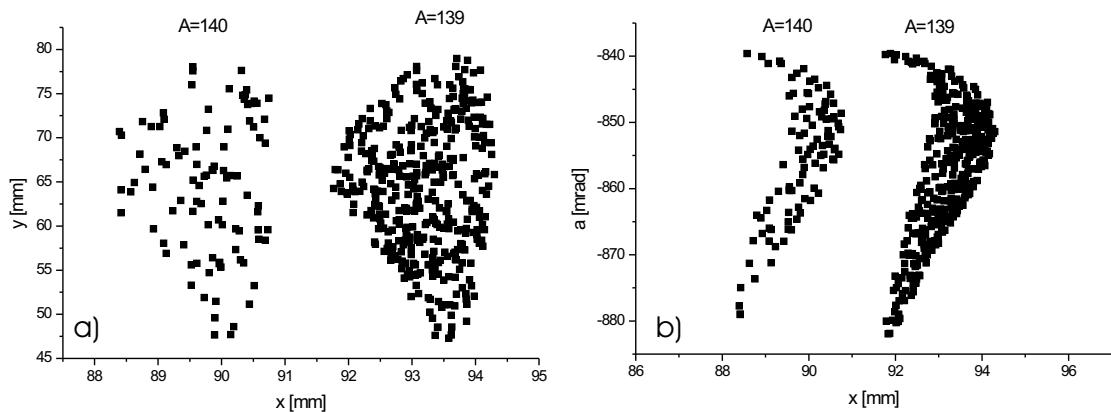


Figure 3.26: Mass resolving power in the focal plane for a) x-y space and b) x-a phase space. It is obvious that the sextupole error is reducing the mass resolving power.

L1 and it was found that the maximum resolution is achieved for a drift length $L_1 = 548 \pm 7$ mm to the electrostatic deflector. The error in the result comes from the uncertainty in determining the x-focus due to a 6.6 mm long waist and from the difficulty in defining the beginning of a curved detector entrance, with a penetration depth of the curve into the deflector body of 8 mm.

The value found with SIMION, however, is 159 mm or 22.5% smaller than the distance suggested by first order calculations for the classic Mattauch-Herzog design. Using the original value of 707 mm the mass resolving power drops below 100, showing that the dependence of the mass resolving power on this distance is quite severe. It is likely that the true value lies closer to 548 mm then

707 mm, since SIMION is probably the trustworthier programme, because the numerical solving of the Laplace equation is the more accurate approach and fringe field treatment is without a doubt more sophisticated. The need for innovative shunt design has shown that fringe fields play a major role for the image aberrations. The shunt design used in the simulation is likely to leave room for improvements on the 10% scale within the simulation environment and is already sufficient to fulfil all requirements. Hence, further improvement of the shunt design and the determination of the optimal L_1 value should be pursued experimentally. Unfortunately, plans to do so have been put on hold due to lack of funding.

Besides the drift length L_1 , there are two other important variables that affect the mass resolution. The electrostatic dipole must deflect by 31.5° . Already 30° reduces the mass resolving power below $m/\Delta m=100$. Also important is that the beam enters the magnet perpendicularly. A deviation of a few degrees increases the image aberrations and therefore reduces the mass resolution. However, because of the non zero emittance it is impossible to form a parallel beam, which will automatically cause image distortion. Nevertheless, the problem could be corrected by a circular pole face, but simulations with such pole faces did not show a noticeable difference.

Finally the mass resolving power can be determined geometrically. From Fig. 3.26 it can be seen that the peak to peak distance between the two masses is 5.8 mm and the full width of one mass is 3.9 mm. With these data, the mass resolving power can be calculated to:

$$\frac{m}{\Delta m} = \frac{5.8}{3.9} 140 = 208.2 \quad (3.15)$$

This is about 33% smaller than the theoretical value. The difference is probably due to higher order corrections, fringe field effects, and remaining energy dispersion from the 90° to 80° change in magnetic dipole angle.

The mass resolving power will be further reduced if a hole in the electrostatic deflector, as shown in Fig. 3.27a, is introduced. A hole like this is required to open a line of sight onto the ion source, which could be monitored in this way, e.g. with a pyrometric temperature measurement, for optical position control of the source or coupling in a laser for operation as a laser ion source.

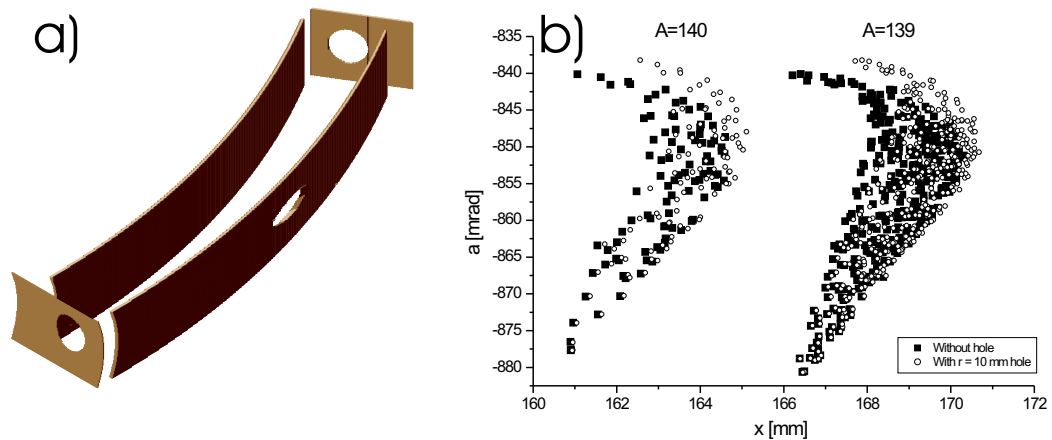


Figure 3.27: Influence of a hole in the electrostatic deflector as shown in a). Mass resolving power in the non-hole case is compared to the situation with a 20 mm diameter hole.

Fig. 3.27b) shows the influence of a 20 mm diameter hole on the mass resolving power of the mass pre-separator. The full width of a single mass increases to 4.3 mm, while the distance between the two mass peaks reduces to 5.7 mm resulting in a reduced mass resolving power:

$$\frac{m}{\Delta m} = \frac{5.7}{4.3} 140 = 185.6 \quad (3.16)$$

Nevertheless, this would still be above the required value, but reduces the safety margin for additional deviations between simulation environment and experimental reality. The effect can be reduced by the use of a smaller hole or covering the hole with a transparent but conducting material. Possible materials would be zinc oxyfluoride [53], semiconducting glass [54] or a wire grid.

For the selection of two masses at the slit system some flexibility in the mass ratio of heavy to light beam is desired, since it is very unlikely, that two experimentalists will always demand beams with a mass ratio of 1.5 as given by the fission fragment mass distribution peaks. Therefore, the possibilities to vary this ratio with the ion optical system by adding a steering capability to the slit system (see also Chapter 6) have been investigated. With a plane plate capacitor (plate distance 3 mm) as steerer in the focal plane of the magnet, masses of ± 5 u around the peak value can be deflected to the following lenses allowing the mass ratio to be chosen from 1.34 to 1.67. To complete the parallel shift of the beam initiated by the focal plane deflector it has been found very useful to have an additional steerer in front of the lenses. With a more sophisticated steerer in the focal, plane having parabolic electrodes (minimum distance 3 mm), it was possible to deflect beams in a mass range of ± 12 u without losing particles, which corresponds to a mass ratio range from 1.21 to 1.86 and even higher mass deviations being possible if some beam loss is accepted. With 50% beam loss a mass difference of ± 24 u becomes available, which is already more than the mass difference between the peaks (46 u). While this feature is obviously not recommended for the experiment it shows what can be done in the controlled simulation environment.

A summary of the three available options is given in Table 3.5.

Table 3.5: Possible mass ratios for two different steerer types. Voltage 1 applied to the focal plane steerer and voltage 2 to the steerer in front of the lenses. Next to the available mass ratios, the loss of intensity is given.

Type	Range	Voltage 1 [V]	Voltage2 [V]	Ratio	Loss
Plate	± 5 u	<600	<1600	1.34-1.67	0%
Parabola	± 12 u	<1200	<3400	1.21-1.86	0%
Parabola	± 24 u	<1900	<4800	0.98-2.36	<50%

Conclusion

In summary of this section it can be concluded that a mass separator setup suited for the special needs at MAFF has been found. Image aberrations due to second order effects have been traced down and reduced to an acceptable level by using curved shunts at the electrostatic deflector. The mass resolving power has been affected by these effects and is reduced to 208.2, which is still above the required minimum resolution. However, it must be kept in mind that the resolution depends linearly on the ion source emittance and the radius of the electrostatic deflector. If for some reason the emittance doubles the mass resolving power is reduced by half.

The possibilities of varying the mass ratio of the transmitted beams have been studied and found to be quite extensive if steering voltages are applied to the slit system and some follow up steerer. For this purpose a curtain like slit structure (see also Chapter 6) with two moving slits with added steering capabilities is proposed.

A third beam line from the pre-separator would not be an ion optical problem, since the previous two are already identical. The curtain like slit system could have three gaps, that can be moved freely around.

3.1.3 Transport to beam coolers

This section is concerned with the transport of the mass separated beams towards the ion beam coolers, with the ion optical elements used in each of the two beam lines being similar from the separator to the cooler. Nevertheless, the major question is, where the best position for the ion beam coolers would be. Three positions are under investigation, each of them with its individual advantages and disadvantages.

a) In the reactor hall just before the beam leaves the building.

Advantages

- The differential pumping of the beam cooler could function as a separator between the radiation controlled area (of concern for the TÜV) and the experimental area. Whatever would be done to the vacuum on either side, during normal operation or malfunction, could not have any impact on vacuum on the other side of the cooler.

- Emittance growth up to the beam cooler would be at a minimum.
- Ground level in the East Building is possibly higher than in the reactor hall. The beam cooler could be used to compensate this without emittance growth.

Disadvantages

- The beam cooler would be furthest away from the high resolution mass separators.

- Additional ion optics would be needed after the cooler, giving way to emittance growth.

b) In the East Building just before the mass separators.

Advantages

- No beam optics between the cooler and HR-separator will reduce emittance growth to the absolute minimum.

- Highest possible resolution of the mass separator.

Disadvantages

- Worst possible emittance enters the cooler. Likely lower transmission through the cooler.

- Most complicated ion optics up to the cooler.

c) In the East Building immediately after the building wall.

Advantages

- Compromise between a and b. Avoids complicated optics and maximum emittance growth

- Preserves some of the original gas shield idea.

Disadvantage

- Some beam transport from cooler to separator is required.

- Reasonable but not maximum separator resolution is maintained.

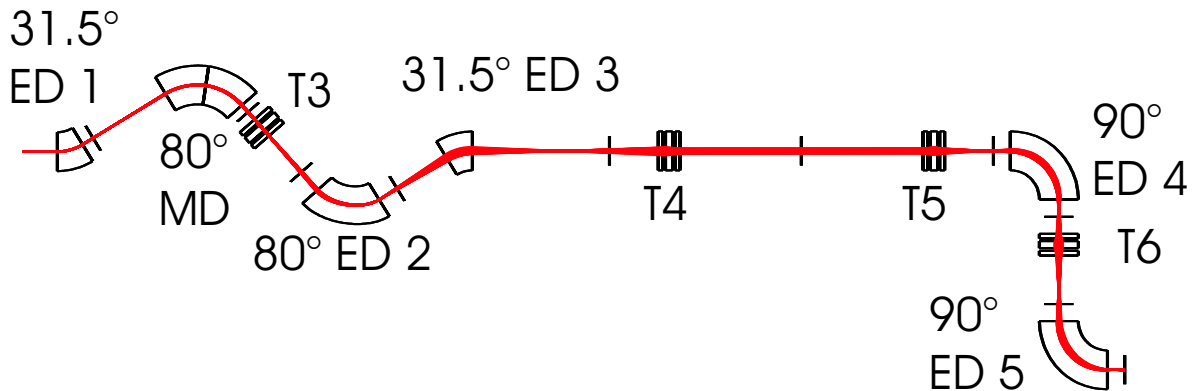


Figure 3.28: COSY simulation for 2nd and 3rd section. Two electrostatic deflectors are used to mirror the first pair and make the system symmetric. A pair of triplets is used to transport the beam into the East Building, where another series of 90° deflections is made.

As shown in Fig. 2.12 solution b) is realized by also maintaining some goals of option a). Nevertheless, the other options have been investigated as well.

Option a) and b) can be studied in a simplified beam line as shown in Fig. 3.28, where COSY has been used for 1st and 2nd order calculations. The properties of the ion beam after triplet T5 correspond to the first possible beam cooler position still inside the reactor building, while the two additional 90° deflectors have been added to study their influence on beam quality if the beam cooler shall be placed in front of the high resolution mass separator, in the east building.

In order to guide the beam out of the experimental hall, the beam must be re-aligned with the first section and the opening in the reactor wall. Three approaches for re-alignment have been studied. Whereby the first two options rely on another set of antisymmetric electrostatic 80° and 31.5° deflectors mirroring the mass separator deflections, as shown in Fig. 3.28. Depending on the distances between the deflectors a wide or narrow loop is possible leading to two options for this deflection scheme. However, this scheme has two disadvantages: It requires two electrostatic deflectors and consumes a noticeable amount of space.

The third option, as implemented in Fig. 2.12 and shown in the SIMION simulation of Fig. 3.29, is the favorable solution. It requires only one electrostatic deflection just after the mass separator, so that the remainder of the beam-line is straight until the beam leaves the reactor, where another deflection is necessary to avoid the collision with a supporting pillar of the Reactor Building East, which blocks the straight path.

For the third option another doublet (D2) is required immediately after the magnet for y re-focusing, since the following 48.5° deflector has no y-focusing capabilities. Without the doublet the beam diameter would exceed the acceptance of the following ion optic components, where further triplets, with an aperture of 80 mm, are used to guide the beam out of the reactor building. The amount of triplets outnumbers the triplets used in the COSY simulation shown in Fig. 3.28, which is because of fringe field effects and higher order aberrations that cause a growth of the beam diameter and are not fully treated in the shown COSY simulation.

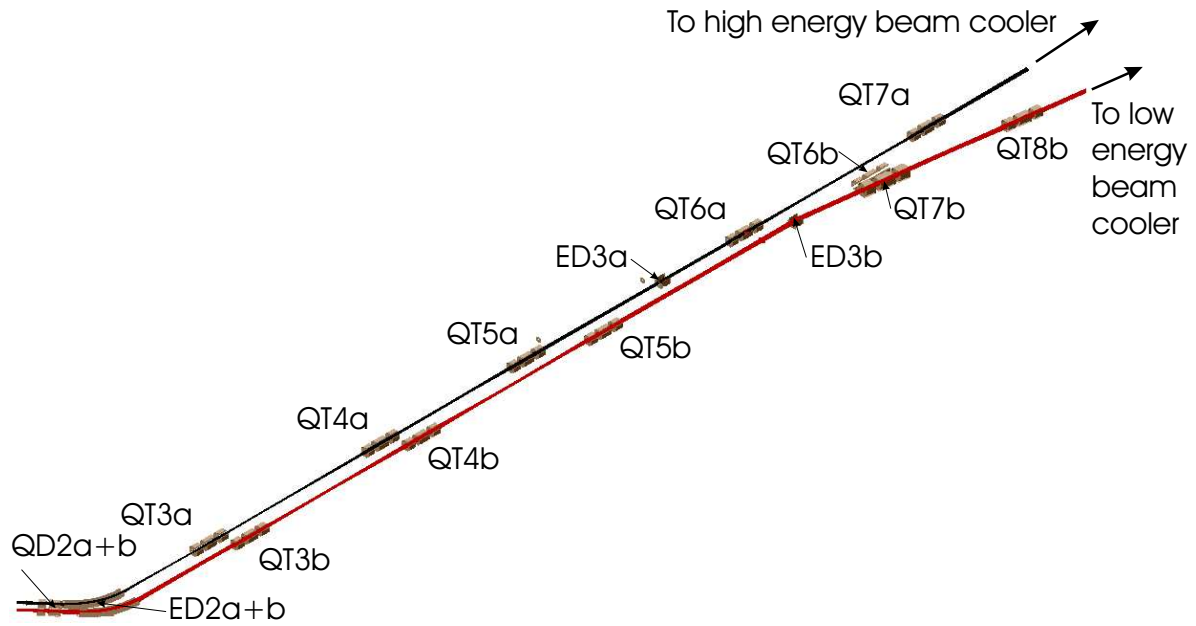


Figure 3.29: SIMION simulation result for a beam transport scenario using only one deflector to re-align the beam with the SR6.

Beam switch

The area between the reactor building and the east building can be used to electrostatically switch the light and heavy mass beam between the dedicated low and high energy beam lines, as well as for a further deflection into the beam coolers. If the two beams are switched it cannot be avoided to cross the beams as shown in Fig. 3.30. The beam size at the intersection point is very large, therefore beam-beam interaction is at its minimum. The 7° deflectors do not need to be removed from the beam path if the opening in the front shunt has a diameter of 80 mm. The deflector downstream of the heavy mass path, however, must be retractable to give way for the switched light mass beam.

Emittance

The emittance evolution behind the mass separator has been studied in detail for the heavy mass branch. The ion optical system for the light mass branch has equal ion optical elements and starting conditions. Therefore, for symmetry reasons, the emittance evolution is comparable to the heavy mass branch, where an emittance growth can be observed in this section. There is not merely a sole cause for this increase, but a combination of various reasons.

Standard quadrupole error As shown in Fig. 3.11, this fringe field aberration causes "ears" that develop on the rim of the phase space diagram, which increase with the amount of quadrupoles passed by the beam, and ultimately lead to a spiral structure, increasing the effective emittance of the beam. This aberration can be reduced, if the aperture of the quadrupoles is increased.

Second order x and a aberration The second order matrix elements $(x|xx)$, $(x|aa)$, $(a|xx)$ and $(a|aa)$ lead to a crescent shaped distortion of the phase space diagram. Hereby, the xx and

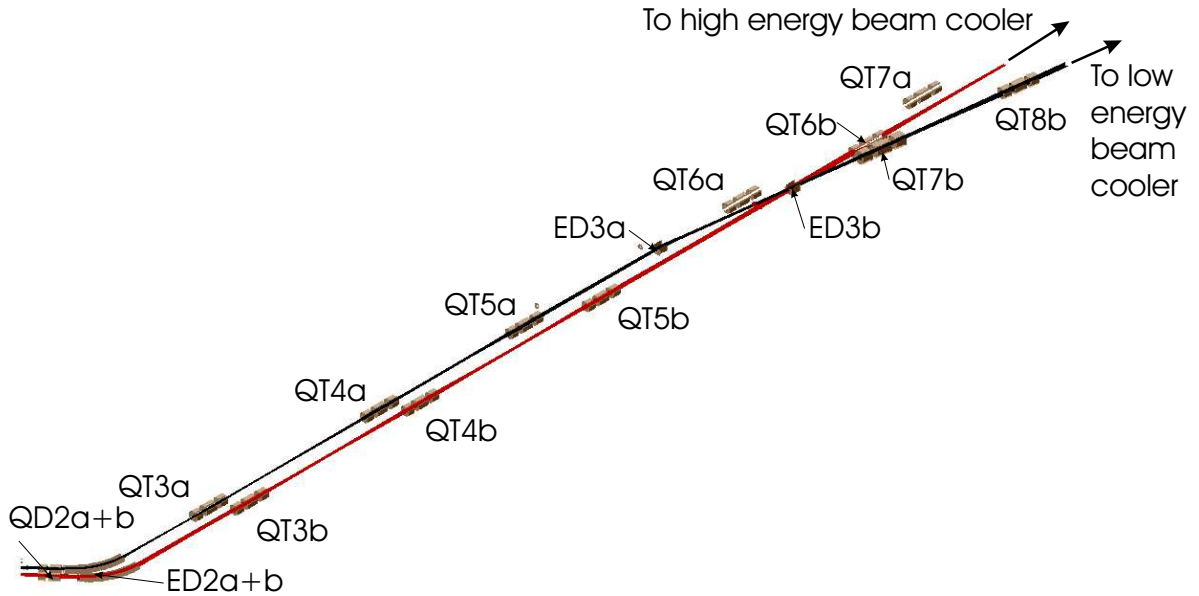


Figure 3.30: Beam switch option installed in the transport section.

aa aberration counteract and can completely cancel each other. While these errors do not increase the phase space area they lead to an increase in the effective emittance.

Energy dependent aberrations As explained in Fig. 3.23, first and second order energy distortion, as well as second order energy-angle distortion cause particles of different energies to occupy different phase space areas and, as a result, the emittance grows.

In Fig. 3.31 the emittance of the heavy mass beam, before the dedicated low energy cooler (right path in Fig. 3.30), is shown. The x -emittance has increased to approximately $28 \pi \text{mm}\cdot\text{mrad}$, that is dominated by the crescent shaped distortion caused by the sextupole error, which can be seen much clearer in the y - b phase space diagram.

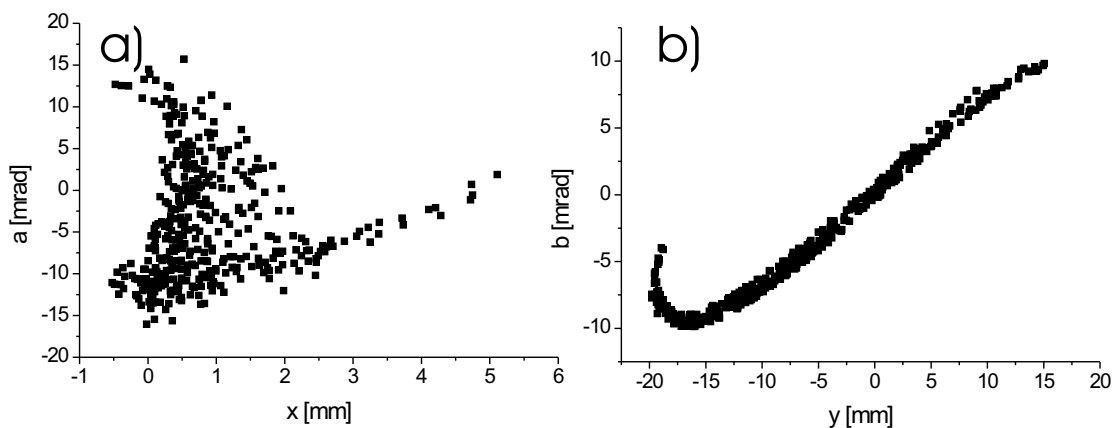


Figure 3.31: Phase space diagram for heavy mass at dedicated low energy beam cooler for a) x - a and b) y - b phase space area. The x -emittance is approximately $28 \pi \text{mm}\cdot\text{mrad}$ and the y -emittance $20 \pi \text{mm}\cdot\text{mrad}$.

For the dedicated high energy beam cooler, Fig. 3.32, (straight path in Fig. 3.30), the situation is a little different. The influence of the sextupole error on x - a phase space diagram is reduced and

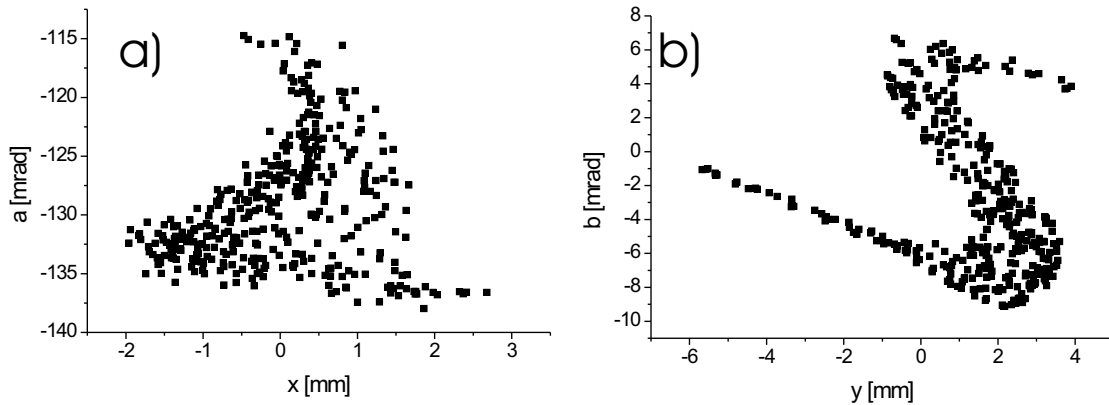


Figure 3.32: Phase space diagram for heavy mass at dedicated high energy beam cooler for a) x-a and b) y-b phase space area. The x-emittance is approximately $15 \pi \text{ mm} \cdot \text{mrad}$ and the effective y-emittance is $35 \pi \text{ mm} \cdot \text{mrad}$.

the x-emittance can be determined to approximately $15 \pi \text{ mm} \cdot \text{mrad}$ for the heavy mass. The y-b phase space diagram, on the other hand is now strongly influenced by higher order aberrations and the standard quadrupole error has caused the ears to grow into a spiral structure.

Conclusion

In conclusion for the third section on the ion optical system it can be stated that a feasible solution for the ion transport to the beam coolers located in the Reactor Building East has been found. A suggestion for a possible switch system offering the possibility to interchange the heavy and light mass beam has been made and the emittance obtained at the positions of the beam coolers is smaller than the acceptance of the coolers.

3.2 Beam Diagnostics

The beam observation system is deeply connected to ion transport for various reasons. In the experimental setup the beam can not be as comfortably observed as in the simulation environment. In account of this, suitable detectors must be placed at points of interest along the beam line:

1. Focus after 1st triplet
2. Focus after 2nd triplet
3. Mass separator object position
4. Mass separator image position
5. Further intermediate foci

Available beam observation methods are:

1. Beam profile monitor

Advantages Approximate beam current and a rough beam profile is determined by turning a metal loop in the ion current resulting in an almost non destructive measurement. Interference with the ion beam can be avoided completely if the loop is positioned perpendicular to the ion beam. With three monitors online measurement of the beam emittance is possible.

Disadvantages No exact current measurement is possible and the monitor will be contaminated by the ion beams. It is also a rather sensitive piece of equipment and less reliable. Also, the shape of the beam profile is not determined in real-time.

2. Grid

Advantages A metal wire grid is inserted into the beam line allowing real-time beam shape and approximate current determination. Emittance measurements with three grids is possible.

Disadvantages The Grid needs to be retractable and no exact current measurement is possible. Nevertheless, the monitor will be contaminated by the ion beams. It is an expensive, rather sensitive piece of equipment and less reliable.

3. Farady cup

Advantages The faraday cup is a simple and reliable device for current measurement.

Disadvantages The measurement is destructive, so that the cup will be heavily contaminated and must be retractable.

4. Segmented iris

Advantages A segmented iris can be placed around the beam allowing a non destructive measurement of the beam shape and the device does not need to be retracted. From different currents on the various segments, the beam position can be determined.

Disadvantages No beam current measurement is possible and the iris will be contaminated.

5. Adjustable Slits

Advantages Slits in x or y can be placed around the ion beam. By adjusting the slit position and measuring the current, the beam diameter can be determined.

Disadvantages No beam current measurement is possible and the slits will be contaminated. Also, some kind of motor is necessary to move the slits.

6. Electrode current measurement

Advantages Additional information can be gathered, by monitoring the electrode currents from all electrodes within the beam line. In this way it can be controlled if the radioactive ion beam collides with an optical element, which can help to avoid unnecessary contamination.

Disadvantages The control system gets more complex.

7. Micro channel plates (MCP)

Advantages The huge possible current magnification allows the detection of single ions with an optical imaging on phosphore screen or electronic readout. Also ion current measurements are possible as well as real time beam shape determination.

Disadvantages Very sensitive equipment, that stops the ion beam. Therefore not suited for radioactive beams and only of limited use for high ion currents.

The layout of the MAFF beam line basically reduces the available options for the different points a lot. At the in-pile positions 1 and 2 only a segmented iris for beam diagnostics is possible. With this it should be possible to adjust beam position and diameter at these points, in order to create a focus.

Point 3 is more complicated, since the exact position for maximum mass resolution is uncertain. The standard solution to fix the position of an x-focus only would be to use an adjustable slit followed by a faraday cup. The focus could be achieved by minimizing beam current on the slits and slit width and also maintaining maximum current on the faraday cup. An alternative, but not feasible option, due to technical difficulties and space restrictions, would be to place three beam profile monitors or grids at this point for emittance measurements, which would give the highest flexibility. The use of only one beam profile monitor or another segmented iris can be a compromise for this point.

For the position in the focal plane after the magnet a further alternative can be considered. It can be expected, that a considerable amount of alkali and earth-alkali elements, from impurities in the source, namely kalium and calcium will be ionized. Having masses in the region of 40 u they would follow a very small radius in the magnet hitting the vacuum chamber wall far away from the lightest fission fragments. Some beam imaging device, e.g. MCPs, can be placed at this position mounted on an additional flange. Now the doublet voltages can be adjusted until the perfect mass resolution is achieved. However, $A=40$ might not be representative enough for the heavier fission fragments. The slit system it self, with a subsequent faraday cup can be used as adjustable slits to optimize the mass resolving power.

For the further intermediate foci, all options are possible, with the deluxe option certainly being the use of grids. However, segmented irises are also possible and much cheaper. Since intermediate foci are not necessarily required it would be sufficient to place the irises directly in front of the multiplets choosing the aperture of the iris to be 70% of the triplet's.

4 Atom distribution

The distribution of radionuclides along the MAFF beam-line is of central importance for the operational modes of MAFF, with respect to normal operation and the assessment of emergency scenarios. Five major questions can be posed, that formulate the most important issues concerning the distribution of radionuclides.

1. Where in the system do radionuclides spread?
2. What kind of radionuclides cause contamination?
3. How much radioactivity is deposited and where?
4. When will the system be re-accessible after the end of a reactor cycle?
5. How does the long term evolution of contamination look like?

At the beginning of this chapter the simulation codes used to address the questions, shown above, are introduced and the obtained results shown. In the last leg, the simulation results will be discussed.

Based on the results obtained in this chapter, a description of the operational modes, under normal and emergency conditions, will be laid out in the next chapter.

4.1 Investigative Tools

For complementary and cross-reference two simulations have been made. For time independent simulations the commercial program MOVAK3D [55] has been used, which was originally developed for conductance simulations of vacuum systems pumped by cryo-pumps and therefore can be used for MAFF as well. MOVAK3D yields a reasonable accurate answer to the first question, but is not capable of simulating radioactive decay.

In order to simulate radioactive decay and answer the remaining questions a custom code has been developed [56], which includes a time dependent Monte Carlo procedure for release and ionization probabilities in the source, radioactive decay of the fission products as well as the element dependent sticking and release probabilities on cold and warm surfaces. In addition, external time dependent actions like actuation of valves, removing the source from the irradiation position, and warm-up of the cryo-panels are included in the code.

Finally, analytical calculations based on the radioactive decay law have been used for further calculations.

4.1.1 Time independent simulations

Time independent simulations have been performed with MOVAK3D, which calculates trajectories of atoms independent of the element in an arbitrary geometry. For the geometry used in the code some simplification have been made to obtain a cylindrically symmetric layout. The simulated volume extends from the vacuum seal on the source side to a point several meters behind the separator, which is referred to as the end-absorber and is a virtual surface that counts the amount of particles leaving the simulated volume. Within the volume all cold surfaces, cryo-pumps and panels are assumed to be fully absorbing, while all other surfaces reflect gaseous particles. During this reflection, particles hitting a wall are re-emitted following a cosine distribution. Stable particles are generated in the source, on a ring shaped surface and are emitted following a cosine distribution. Within the source volume, the particles quickly collide with the source walls, before the manage to leave the volume, subsequently, all memory of the generation process is lost. The escaped particles remain neutral, since the code is not able to consider ionization.

The trajectory calculations take very long and the total computation time invested sums to more than half a year. Therefore, some approximations needed to be made to reduce the computation time. One of which is a straight beam line. While in reality, particles directly from the source are stopped in the multi-purpose unit (MPU), they would hit the end-absorber in the simulation, due to the approximation mentioned above. To prevent this, a beam sized stopper is placed in the beam tube at the position of the MPU to block the straight path. In account of this, it has been confirmed, that the conductance is equal with and without the stopper. Furthermore, the vacuum chamber of the magnet is replaced by a cone giving credit to the growing volume of the magnet chamber. Finally, the cryo-pumps' absorbing surfaces are simulated as a cylinder mantel, with a surface equal to the cryo-pump inlet flange cross-section. Most of the particles will be trapped on either one of the cryo-panels or in one of the cryo-pumps, which are located at positions shown in Fig. 4.1 for the extraction side (A-Side) and Fig. 4.2 for the source side (B-Side).

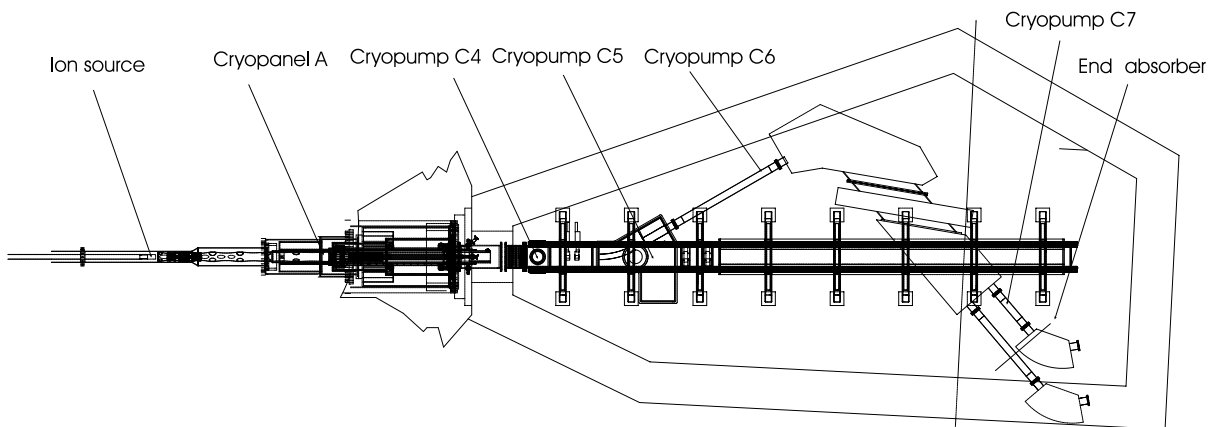


Figure 4.1: Extraction side (A-side) cryo surfaces. Volatile radionuclides can only be absorbed on cryo surfaces. These are provided by the cryo-panels and cryo-pumps labelled in the drawing. The end-absorber is an arbitrary surface absorbing all particles which would leave the simulated volume.

Cryo-pumps C4 to C7 are placed on the A-Side as can be seen in Fig. 4.1, while Cryo-pump C3 is located on the source side (side B), just before the valve, as shown in Fig. 4.2.

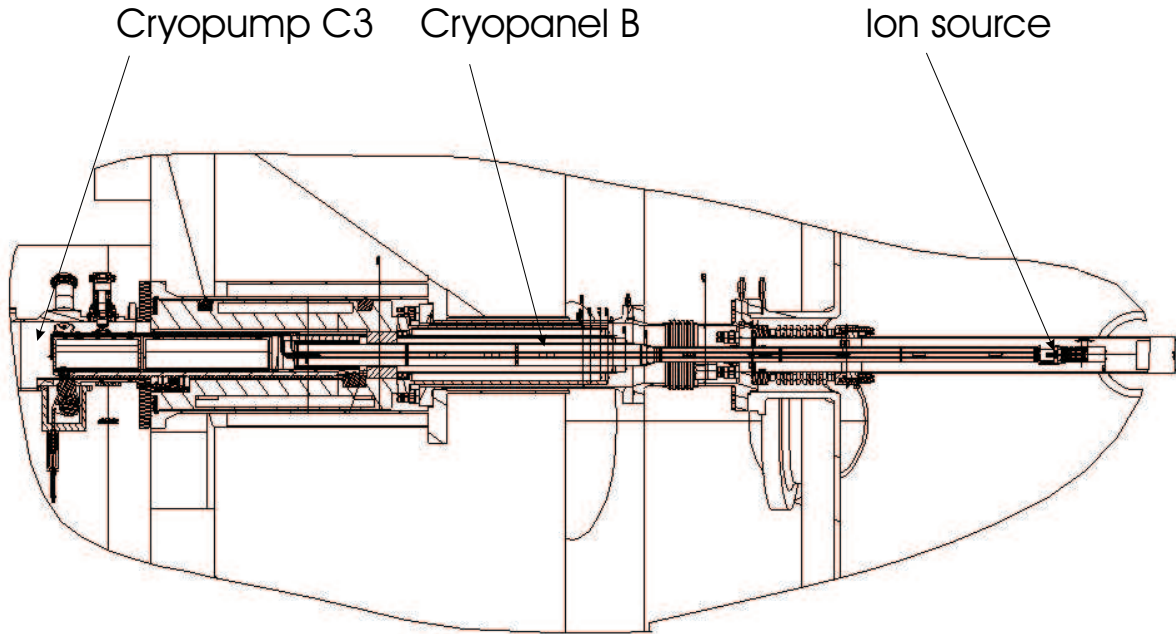


Figure 4.2: Schematics of B-Side of MAFF with indicated source side cryo surfaces. Only one cryo-pump is active at the source side, since the beam line is closed by a valve directly behind cryo-pump C3.

In a first calculation more than 10^6 events were tracked, but none of the particles arrived at the end-absorber, because 99.98% of the particles were absorbed by the cryo-panels. Therefore, in order to obtain the fraction of particles arriving at the end-absorber, a second run was performed with deactivated cryo-panels to allow more particles to reach the end-absorber. From this run, the fraction of particles reaching the end-absorber is calculated to be $9 \cdot 10^{-8}$ and compared to the other results in the summary given in Table 4.1.

Table 4.1: Fraction of particles absorbed at the cryo-pumps C3-C7, the cryo-panels and reaching the end-absorber.

C3	C4	C5	C6	C7	Panel A	Panel B	End-ab.
$1 \cdot 10^{-4}$	$8 \cdot 10^{-6}$	$6 \cdot 10^{-5}$	$4 \cdot 10^{-6}$	$< 4 \cdot 10^{-9}$	0.4	0.6	$9 \cdot 10^{-8}$

On a first glimpse it seems unexpected, that cryo-pump C5 collects more atoms than cryo-pump C4. This is easily explained by the direct neutral current coming from the source hitting the stopper plate placed in the MPU directly in front of cryo-pump C5 as described above. Also not intuitively clear is why cryo-pump C7 collects less atoms than the end-absorber. This is due to the poorer conductance to cryo-pump C7 compared to the end-absorber, which arises from the fact that the cryo surface is not placed immediately at the beam line but at some distance away from it, as it is the case with the actual cryo-pumps.

For additional insights, simulations with a cryo-panel sticking coefficient (the probability of a particle sticking to a given surface) equal to 0.2 only (full absorption corresponds to 1.0) have been performed. It was found that the efficiency of the panels does not strongly depend on the sticking coefficient, because every re-emitted particle has a very high chance of hitting the cold surface again, so that multiple hits are very common, resulting in an exponential decrease of the chance that a particle escapes the cryo-panel.

4.1.2 Time dependent simulations

The time independent simulations have shown, how the radioactive atoms will distribute within the system, while the other four questions still remain unanswered. In order to provide insights to these questions some kind of time dependent calculation is needed, with the most accurate approach certainly being a 3D trajectory calculation, similar to MOVAK3D, with added time dependence. However, no suitable program was available and computation time for a 4-dimensional code would be extensive.

The code used is based on a probability approach [57], where the chance P_i of a particle with the mean velocity \bar{v} hitting a specific area A_i in a volume element V_s per unit time is given by:

$$P_i = \frac{A_i}{V_s} \cdot \frac{\bar{v}}{4} \quad (4.1)$$

The surface elements A_i can be either warm or cold surfaces or openings to neighboring volume elements. A cold surface adsorbs all elements including the volatile elements Br, Kr, I, and Xe with a probability of 100%, while warm surfaces adsorb all but the volatile elements.

The scalar approximation used in the code is an alternative to a time-consuming 3-dimensional treatment of the problem, if P_i is not strongly influenced by the spatial arrangement of the surfaces as it is the case for volume elements with nearly cubic or spherical shapes. In account of this, very long tubes for example have to be subdivided into a series of short elements, the length of which is of the order of the diameter. This concept, however, leads to a too large number of volume elements for tubes with a small ratio of diameter to length. Therefore, very long tubes are simulated in the code by two volume elements, which are connected by a small opening, the area of which is adjusted in such a way that the conductance of the long tube is reproduced. To get reliable results, the simplified MAFF beamline as described above is split into about 60 volume elements. Most of the simplifications mentioned previously have only a marginal effect on the code introduced in this section, since it is only concerned with surface areas.

In addition to the probabilities P_i for the passage of the atoms through the vacuum system, probabilities for creation and diffusion in the source as well as for radioactive decay of the atoms were added to the Monte-Carlo code. The probabilities for the creation are taken from data measured by Rudstam et al. [58] [59] and calculations by Wahl [60]. Diffusion times are taken from tabulated half-lives [58] [59] and decay data are taken from Ref. [61]. Measured release data are available for Zn to Sr and Pd to Ba. The elements Ni and Cu have been observed at ISOLDE and OSIRIS, but no release data have been published. All other elements have not been observed and no release data are known. Finally, surface ionization probabilities have been calculated with the Langmuir equation [29] on a rhenium surface at 2700 K.

In a first step, the functionality of this code was verified by comparison to the MOVAK3D results for stable atoms (N_2). The results are compared in Table 4.2. Set 1 and Set 2 stand for two different sectoring approaches for the same geometry.

It can be seen, that with the Set 1 values the B side pump collects far too few atoms, which is due to an underestimation of the gap width between source trolley and beam tube by a factor of 10. The problem has been fixed in Set 2, but gives an idea about the influence of the geometry.

The ratios S1/M3D and S2/M3D compare the different sectoring sets to the MOVAK3D simulation. If the last value is ignored, the average derivation for Set 1 can be determined to 50% and 30% for Set 2. Therefore, the influence of sectoring within the same geometry is in the order of 20% and it can be found, that the two programs agree within a factor of 2, which is a very pleasant agreement, since for dose rate calculations the order of magnitude is of primary concern.

Table 4.2: Comparison of the absorbed fraction of particles from MOVAK3D and the scalar code. Set 1 and Set 2 represent two different sectoring approaches for the same geometry.

	MOVAK3D	Set 1	S1/M3D	Set 2	S2/M3D
A_{total}	0.4019	0.5818	1.4	0.4826	1.2
A_{panel}	0.4018	0.5817	1.4	0.4826	1.2
A_{pumps}	$1.72 \cdot 10^{-4}$	$5.28 \cdot 10^{-5}$	0.3	$6.61 \cdot 10^{-5}$	0.4
B_{total}	0.5981	0.4182	0.7	0.5174	0.9
B_{panel}	0.5980	0.4182	0.7	0.5172	0.9
B_{pumps}	$1.88 \cdot 10^{-4}$	$9.33 \cdot 10^{-6}$	0.05	$3.23 \cdot 10^{-4}$	1.7

With confidence in the obtained results the calculation is extended to unstable nuclei. Here, the principle of operation of the code is illustrated best by two typical examples of Monte Carlo events. In these examples the time evolution is displayed in a number of subsequent time steps showing the locations of the nuclei of the decay chain from the birth of the fission fragment in the source to the final location of the stable nuclide.

The first example (Fig. 4.3) starts with the primary fission fragment ^{133m}Te , which is released from the hot source as neutral atom into the volume. It sticks to a warm surface and then after the decay to the volatile element iodine moves through the vacuum system until it hits the cold surface of the cryo-panel.

```

step    time    nuclide  location    ....  probabilities for monte carlo  ....
                                     dec1 dec2  war  col  ex1  ex2  ex3  non  ion
1  43.412d  Te133m  ion source  hot    -1   -1
2  43.412d                vol    -6   -7  99*
3  43.412d                warm   82*  18
4  43.436d  I 133    warm    -9
5  43.436d                vol    -4   -6          99*  -3
6  43.436d                A tube i1  -5   -6          -1  71*  27
7  43.436d                A tube i2  -6   -8          50  50*
8  43.436d                A tube i3  -5   -7          6   65*  27
9  43.436d                A panel st -7   -8          5  50  39*  5
10 43.436d                A panel a1 -7   -8          60  32   6*
11 43.436d                A panel a2 -6   -8          31*  68
12 43.436d                cold   97*  2
13 44.332d  Xe133    cold  100*
13 46.626d  Cs133    A panel a2 cold  stable nuclide

```

Figure 4.3: Sample output of time dependent simulation for ^{133}Te . The non-volatile fission fragment is created in the source, decays to volatile iodine and spreads through the vacuum system until collected by the cryo-panel.

In the second example (Fig. 4.4) the fission product first decays to ^{91}Rb , which leaves the source as an ionized atom, before it is guided directly to the slit system by the beam optics, where it decays in three steps to stable ^{91}Zr .

On the left side of the examples the internal time of the actual nuclide is shown for each step, this time records when something happens to the nuclide, e.g. in the first step of example 1, a ^{133m}Te nuclide is produced in the ion source, 43.41 days after the start of the reactor.

The right hand side (Fig. 4.3 and Fig. 4.4) shows the probabilities (in %, -1 means 0.1%) normalized to 100% for the Monte Carlo process:

dec1, **dec2** are probabilities for two alternative decay modes.

war, **col** are the sticking probabilities on warm or cold (cryo-panel, cryo-pumps) surfaces.

step	time	nuclide	location	 probabilities for monte carlo								
					dec1	dec2	war	col	ex1	ex2	ex3	non	ion
1	26.435d	Kr 91	ion source	hot	10*							75	13
2	26.435d	Rb 91		hot	2							3	93*
3	26.435d		A slit sys	cold	100*								
4	26.435d	Sr 91		cold	43*	57							
5	27.109d	Y 91		cold	100*								
5	87.031d	Zr 91	A slit sys	cold	stable nuclide								

Figure 4.4: Sample output of time dependent simulation for ^{91}Kr . ^{91}Kr is created in the ion source but decays to Rb which becomes ionized and is transferred by the ion optics to the slit system, where it decays to stable ^{91}Zr .

ex1, ex2, ex3 are probabilities for escape to adjacent volume elements according to equation 4.1. **non, ion** are the probabilities for the release from surfaces as neutral atoms (non) or as ions (ion). The probability which is selected from the Monte Carlo process is marked with an asterisk (*).

The examples also demonstrate, that the noble gases Xe and Kr, as well as the halogens I and Br are assumed volatile and stick only to cold surfaces. All other elements will stick to any surface they encounter until they decay to something volatile. The time of decay, surface and isotope type are recorded in a 3-dimensional matrix. The time scale in this matrix is typically binned in steps of 1 day for a 10 year simulation or 3 days for 30 years of simulated time. From this matrix the activity of each element on each surface at any time can be determined. The complete set of obtained data is given in Appendix E.

The isotope-specific activity information has also been used for sophisticated shielding calculations, which is part of the code. For this calculations, a spherical symmetry is assumed for the shielding material and a 3-dimensional Monte Carlo method is used to calculate the absorption. Cross sections for the photo-effect have been taken from Ref. [62], for Compton scattering and electron-positron pair production formulas from Ref. [63] have been used. Multiple Compton scattering and pair annihilation are included as well. Fig. 4.6 gives an overview of the textbook values [64] of the shielding performance of some elements for 1 MeV γ -radiation.

To calculate the dose rate, gamma energies and branching ratios are required additionally to the activity for each nuclide. The level schemes for short lived isotopes with a few seconds half-life or less are especially complicated and unimportant for the shielding calculations. They only play a major role during the reactor cycle and a few minutes afterwards. Since the surroundings of MAFF will be inaccessible during this time for reasons of radiation safety anyways, there is no need to implement these nuclides. However, this alters the dose rate calculation for the slit system as shown in Fig. 4.5. If the short lived nuclides would be taken into account the dose rate would start and stay constant at a higher level, but would also drop down more rapidly once the reactor is turned off. Subsequently, the calculation is accurate once the longer living isotopes start to dominate, which happens after two days.

The dose rate has been calculated for energy absorption in water at 1 m distance. The dose rate-constants [64] for water, air and lead are shown in Fig. 4.7.

As a by-product of the simulation, the isotope yields at the mass pre-separator can be obtained, which is nothing else as the amount of isotopes deposited on the slit system per second. For the yields shown in Fig. 4.8 the best values of surface and laser ionization [65] have been used. Some isotopes of interest have very low yields due to low production, ionization and diffusion probabilities. Therefore, the yield is determined in a slightly different way: Low fission probabilities have been scaled up and ionization probabilities are set to 100% at first, so that all isotopes propagate to the slit system. Afterwards, those probabilities have been multiplied by the true production and ionization probabilities and the correct yield is obtained.

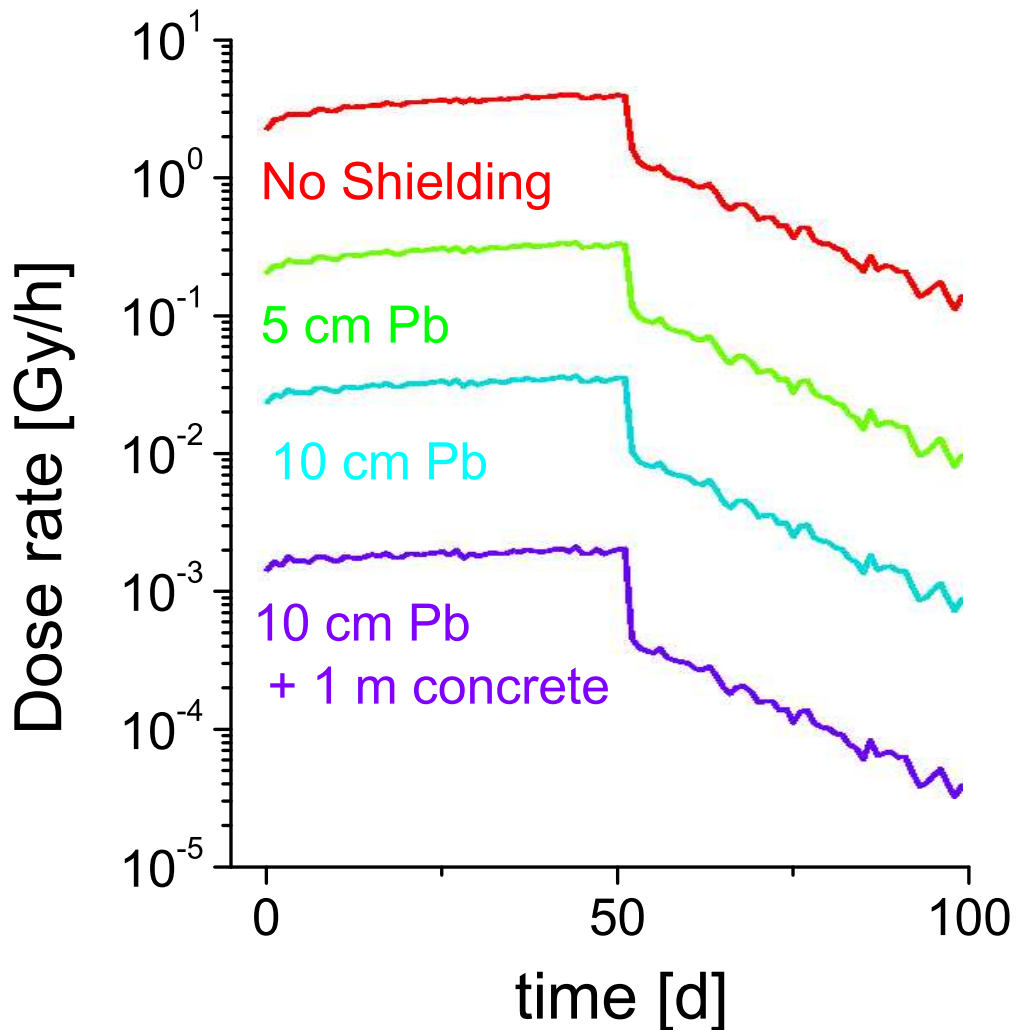


Figure 4.5: Dose rate calculation at the MAFF slit system at 1 m distance. Isotope specific activity information is used as input for a 3-dimensional Monte Carlo code. Photoabsorption, Compton scattering, multiple Compton scattering and pair annihilation are included.

4.1.3 Analytical calculations

The evolution of a radionuclide mixture is described theoretically very accurately by the radioactive decay law. The decay law for successive transformations [66] can be used to reproduce mother-daughter relations up to arbitrary order. For the purpose of this work 9th order has been used, since only very few decay chains have more than 9 consecutive decays. The error made by ignoring higher orders is <0.5%.

For the analytical calculations all fission isotopes and isomers from ^{65}Mn to ^{156}Eu have been taken into consideration. A fission rate of 10^{14} fission/s has been assumed, which is multiplied by the production yields according to the Wahl Z_p model to obtain the in source production yield.

Diffusion of elements out of the source is described by diffusion probabilities measured by Rudstam.

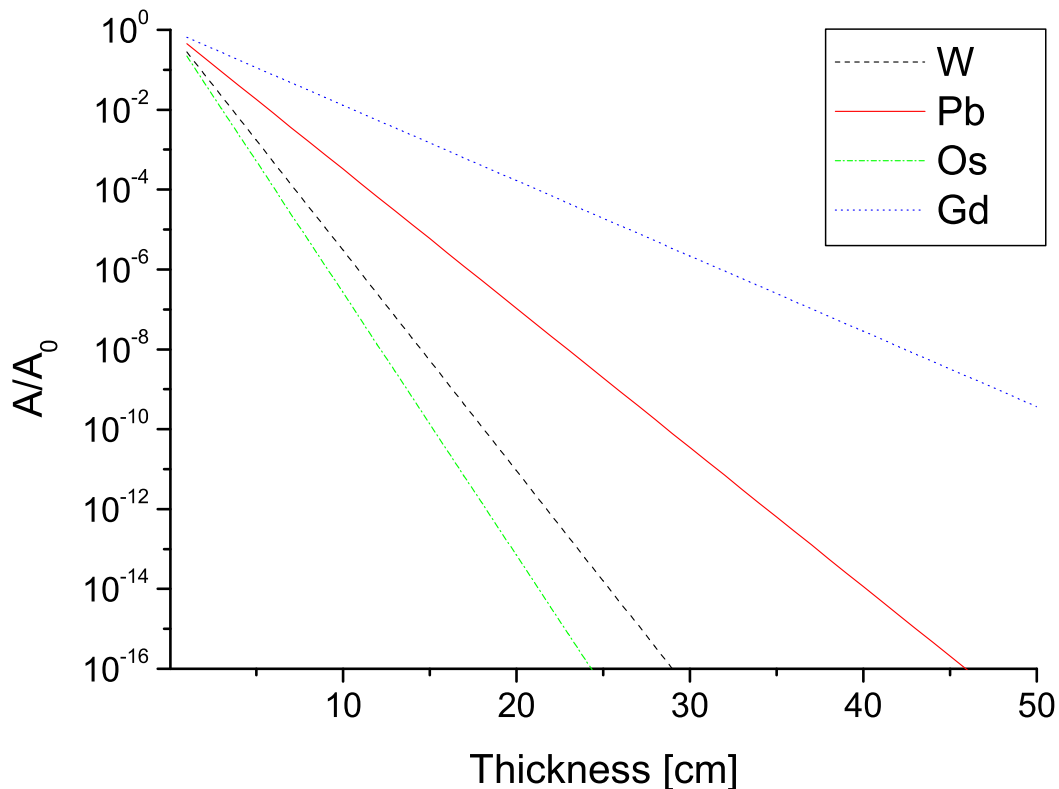


Figure 4.6: Shielding performance for various elements for 1 MeV γ -radiation [64].

Ionization probabilities are calculated with the Langmuir equation.

Those isotopes, which manage to diffuse out of the ion source and get ionized form the ion beam. Those, that only diffuse out of the ion source are not considered any further, while the remaining nuclides decay in the ion source until they form a stable isotope. However, at each intermediate element formed during the decay, there is a certain probability for ionization in which case the ion is counted as a part of the ion beam as well.

This mechanism has been implemented in an MS Excel matrix, which has been designed in a way, that ionization and diffusion can be switched off, so that the maximum or total radioactive inventory can be calculated. Also it can be calculated which parts are volatile, non-volatile and ionized.

Another input parameter to the matrix are production time and decay time. Production time relates to the time a reactor cycle lasts, while the decay time is the amount of time waited for the isotopes to decay.

The matrix contains three different decay schemes. First, there is the very inaccurate scheme with neglected mother-daughter relations.

Secondly, there is a decay scheme, which considers the nuclides remaining in the ion source. This scenario is interesting when calculating the activity, which remains in the ion source.

Thirdly, there is a scenario, which only considers the decay of particles transported by the ion beam. Those particles have been transported as ions out of the ion source and are all stopped at

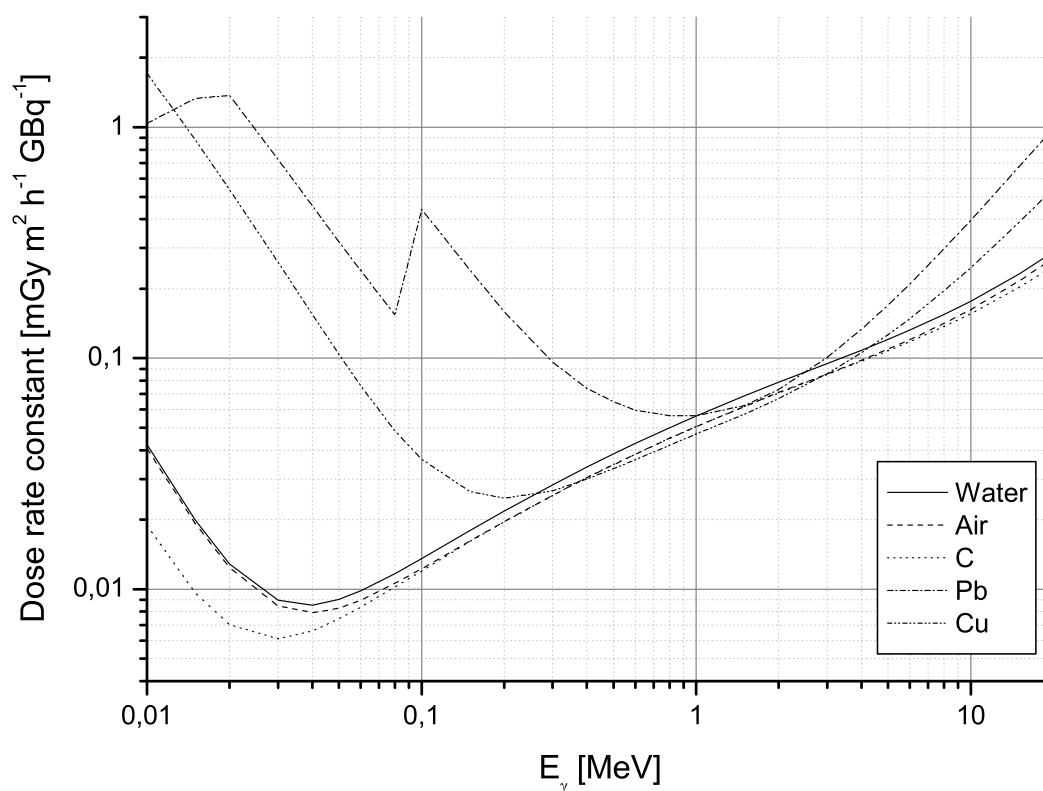


Figure 4.7: Dose rate constants for various elements over a broad energy range [64].

an absorber, e.g. the slit system. In this scenario all isotopes produced as ions during the reactor cycle are taken as a starting point for a subsequent successive transformations decay scheme.

Finally, activities and dose rates (using a dose rate constant) are calculated from the remaining inventory. By default a dose rate constant for absorption of γ -rays with 2 MeV energy in water at 1 m distance, has been used. However, dose rate constant and distance can be adjusted to any other value as suited.

For visualization, isotopes and mass branches are ranked according to their dose rate and put into an automatically reorganizing table.

4.2 Discussion

With the available tools and obtained results many aspects of radionuclide distribution have been investigated and are discussed hereafter. Among the topics of interest are the following items:

- Distribution of ionized isotopes
- Distribution of neutral isotopes
- Formation of volatile compounds
- Formation of aerosols

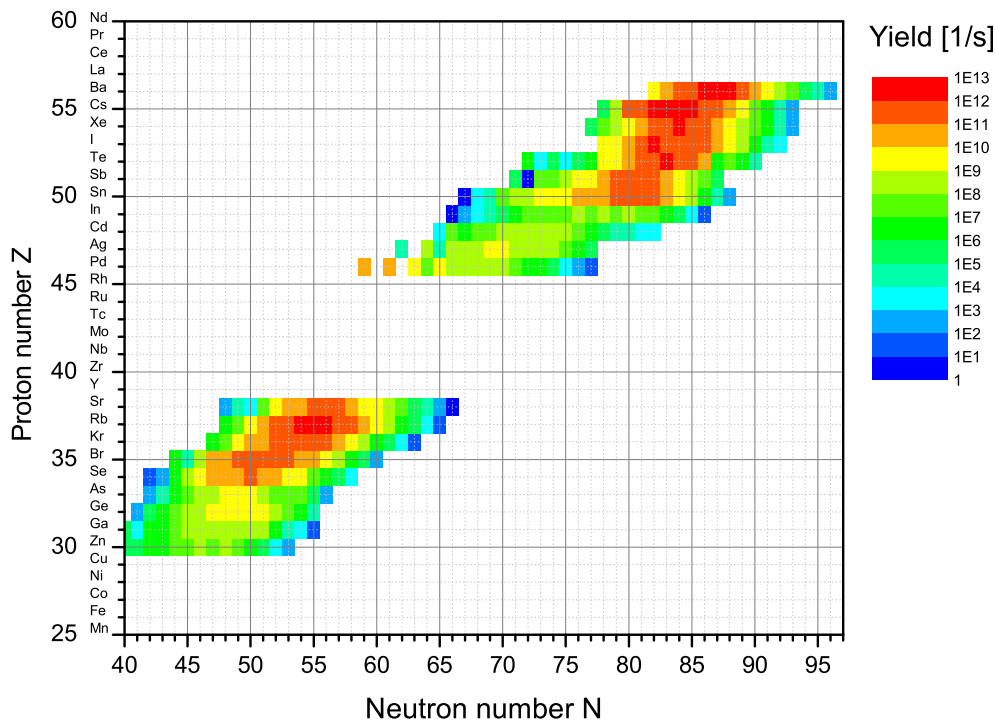


Figure 4.8: Ion yield at slit system, calculated with best values of surface and laser ionization. Measured release probabilities for fission fragments from a graphite matrix have been implemented. The elements Ni and Cu have been observed at ISOL facilities but no release data has been published.

- α -activity
- Volume activity
- Distribution of graphite
- Core radiation

For a better understanding of the following discussions some introductory words should be spent. For the purpose of this investigation radionuclides can be classified according to their half-life in three categories:

Short Isotopes with a half-life of less than a day can be considered short lived. They provide the largest contribution to the dose rate during operation and soon after.

Intermediate Isotopes with a half-life of a few days up to a year keep the dose rate at an elevated level during short pauses, e.g. between reactor cycles.

Long Isotopes with a half-life of more than a year cause long term contaminations, of low activities and dose rates.

Fission fragments decay via β - and γ -radiation. While β radiation is automatically shielded by the vacuum chamber, the highly penetrating γ -particles can pose a health risk to nearby personnel.

The penetration capabilities of γ -radiation depend on the energy of the γ -particles, which is roughly related to the inverse of the half-life. For a typical fission fragment, e.g. ^{137}Cs , the γ -energy is 662 keV.

The general behavior of a radionuclide is given by its volatility and its tendency to become ionized. Fission fragments originating from the ion source can therefore be split into ionized, volatile and refractory particles, as shown in Fig. 4.9, which shows the evolution of the activity ratios beginning at the end of a 52 d reactor cycle. Over time most volatile isotopes decay to non-volatile elements. Activity from ionized particles accounts for ions deposited at a beam dump, which is shown in the figure.

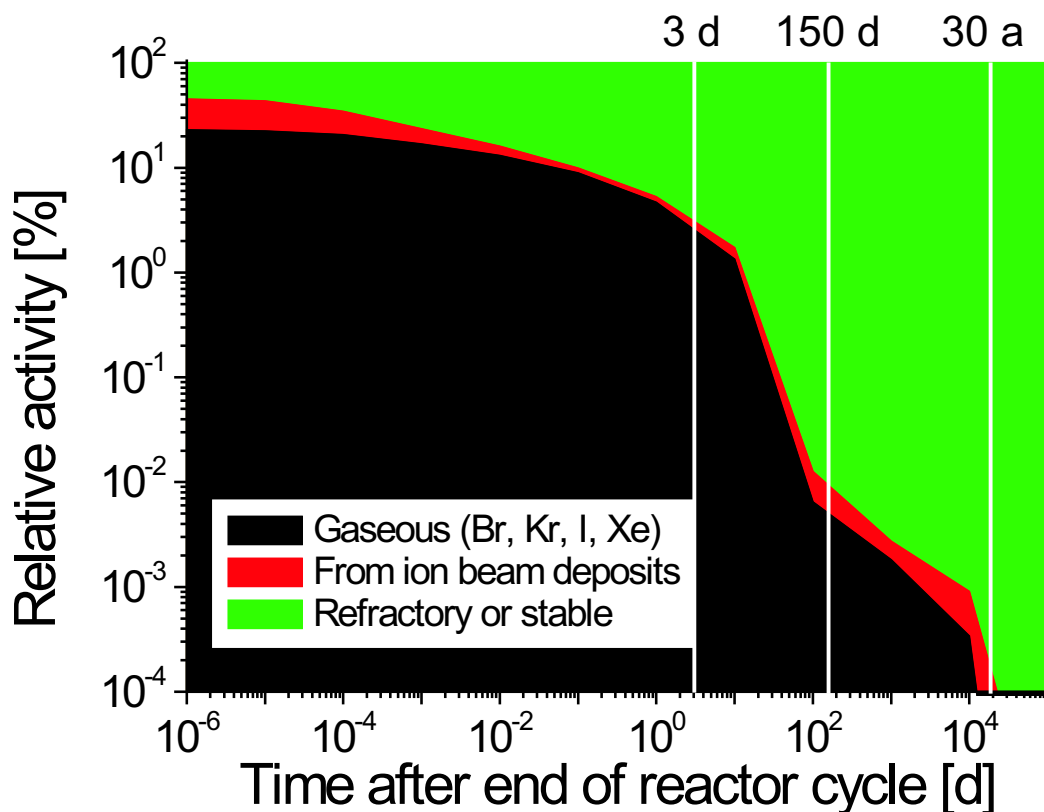


Figure 4.9: Relative percentages of volatile, refractory and ionized particles, which change over time in favor of non-volatile or stable particles. The ratio is independent of the duration of a reactor cycle. After 3 d the cryo-panels are regenerated, after 150 d the decay tanks are vented and after 30 a the reactor is decommissioned.

It can be seen from Fig. 4.9, that most particles are non-volatile and stay in the ion source. Together with activation of source materials from neutron capture, the ion source is the most radioactive part of MAFF. However, activity originating from activated materials cannot spread out at all.

4.2.1 Contamination by the ion beam

Before the mass pre-separator the potential activity transported by the beam is especially severe since all ions produced by the source are contained within the beam. If the ion beam collides with

any material (e.g. slit system, ion optic elements, beam diagnostic elements, valves, beam dump, target) it will implant the ions deeply and contaminate the material.

Table 4.3 shows the ten isotopes with the highest dose rates seven days after the end of a 52 d reactor cycle, calculated with the third scheme of analytical approach described above. In Table 4.4 the same top ten is given for the mass branches.

Table 4.3: Dose rates from ion beam in 1 m distance for average γ -decay energies of 2 MeV. See text for details.

Isotope	$T_{1/2}$ [d]	Dose [$\mu\text{Sv/h}$]
^{140}La	1.68	$2.4 \cdot 10^5$
^{140}Ba	13	$2.3 \cdot 10^5$
^{89}Sr	50.5	$3.4 \cdot 10^3$
^{137}Cs	10950	$4.8 \cdot 10^2$
^{91}Y	58.5	$2.2 \cdot 10^2$
^{141}Ce	33	$1.6 \cdot 10^2$
^{90}Sr	10585	37
^{90}Y	2.67	31
^{143}Pr	13.6	6.5
^{86}Rb	19	2.7

Table 4.4: Dose rates from ion beam in 1 m distance for average γ -decay energies of 2 MeV. See text for details.

Mass	Dose [$\mu\text{Sv/h}$]
140	$4.7 \cdot 10^5$
89	$3.4 \cdot 10^3$
137	$4.8 \cdot 10^2$
91	$2.2 \cdot 10^2$
141	$1.6 \cdot 10^2$
90	68
143	9.1
86	2.7
95	1.5
144	0.9

4.2.2 Ion gas collisions

Not only can ions collide with hardware parts but also with residual gas atoms, where charge exchange or scatter processes result in ion loss, which will eventually collide with walls and contribute to the contamination of the beam tubes. In order to estimate the amount of particles lost in collisions with residual gas SRIM2003 simulation for 30 keV Ba ions passing through air under various pressures have been performed and indicated that for an air pressure of 10^{-6} hPa the loss rate is 10^{-7} per meter.

At this loss rate, the contribution of the ion beam to contamination before the slit system will be $50 \text{ nSv h}^{-1} \text{ m}^{-1}$. The dose rate is given for a decay period of 7 d. Decay period describes the time between the end of a reactor cycle and the accessing of the experimental facilities. During operation the level will be in the magnitude of $1 \mu\text{Sv/h}$.

Behind the slit system the dose rates will be even lower, since only two mass branches will be transported to the experiments.

4.2.3 Neutral isotopes

The non-volatile fission products, which leave the source with a kinetic energy corresponding to the source temperature of 2700 K, will cool down quickly due to wall interactions and finally stick to the wall in the vicinity of the ion source. If they decay to one of the four volatile elements (Xe, Kr, I, Br) they will start spreading again until they are trapped on one of the cryo surfaces, where they might decay to non-volatile elements. Subsequently, during the regeneration of these cryo surfaces only the volatile elements will be released. In case of cryo-panel regeneration, which is planned to be performed 3 days after the end of each reactor cycle, the radioactivity is transported to the nearest cryo-pump leading to an activity transfer as can be seen in Fig. 4.10. Xe is collected

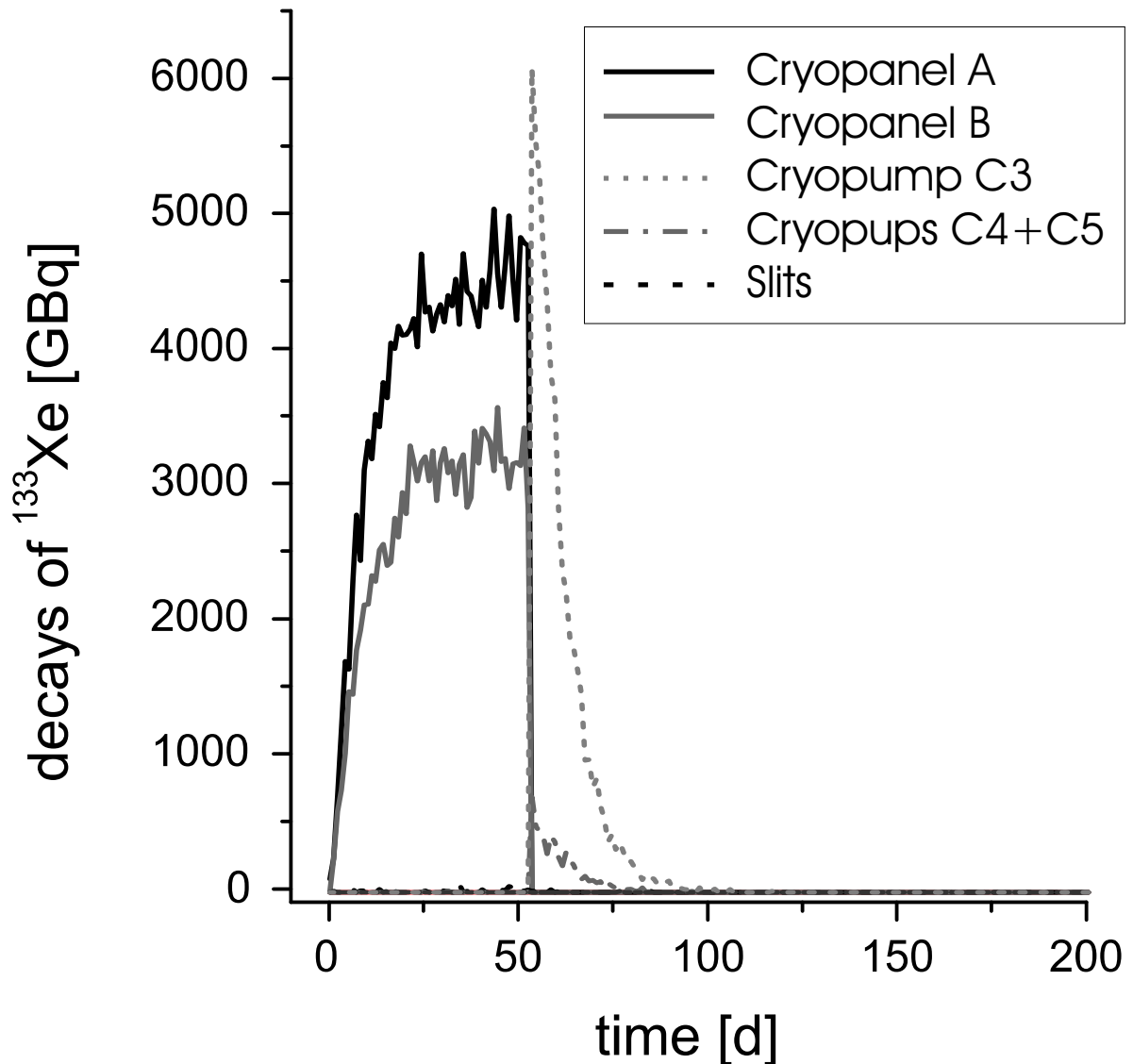


Figure 4.10: Distribution of ^{133}Xe along the beam line. As a volatile nuclide Xe sticks only to cold surfaces. After 55 days the source trolley is removed and the cryo-panels regenerated, resulting in the majority of the activity being gathered on cryo-pump C3.

on the cryo-panels during the reactor cycle of 52 days, until three days after the shutdown the panels are regenerated and most of the atoms are transferred to cryo-pump C3 on the B-side, which is then collecting the dominant part of the activity, since the source trolley is removed at this time and thus the beam tube offers a high conductance in this direction.

Once the cryo-panels are regenerated and the activity has been collected in the pumps, the corresponding gate valves are closed and the cryo-pumps are regenerated. During this process the radioactivity is transported towards one of two decay tanks by the dry-roughing pumps, which do not introduce any hydro-carbon contamination into the vacuum volume or the decay tanks. There are two decay tanks on the A and B-side, for a total of four tanks. Each tank will be filled over 3 reactor periods, while the material in the other tank is given 3 periods ($>150d$) time to decay.

Since only the four volatile elements Xe, Kr, I, Br, are released from the cryo-pump or cryo-panel, only those elements will be found in the decay tanks and might be released from the vacuum system due to an air leak in case of an emergency scenario. Tables 4.5 to 4.8 list all relevant isotopes of these elements and the corresponding activities at the end of a reactor cycle (52d) as well as 2.5 days and 150 days after the end of the cycle assuming that no new activity is produced in the meantime.

Table 4.5: Activity from Kr isotopes at the end of a reactor cycle (after 52 d) A_{52d} , 2.5 d later $A_{+2.5d}$ and 150 d later A_{+150d} under the assumption, that no new activity is added.

Isotope	$T_{1/2}$	A_{52d} [Bq]	$A_{+2.5d}$ [Bq]	A_{+150d} [Bq]
^{83m}Kr	1.83 h	$5.3 \cdot 10^{11}$	0	0
^{85m}Kr	4.48 h	$1.3 \cdot 10^{12}$	$1.2 \cdot 10^8$	0
^{85}Kr	10.76 a	$2.6 \cdot 10^9$	$2.6 \cdot 10^9$	$2.5 \cdot 10^9$
^{87}Kr	76.3 m	$2.6 \cdot 10^{12}$	$1.6 \cdot 10^{-2}$	0
^{88}Kr	2.84 h	$3.4 \cdot 10^{12}$	$1.5 \cdot 10^6$	0
^{89}Kr	3.18 m	$4.4 \cdot 10^{12}$	0	0
^{90}Kr	32.3 s	$4.6 \cdot 10^{12}$	0	0
Kr total		$1.7 \cdot 10^{13}$	$1.2 \cdot 10^8$	$2.5 \cdot 10^9$

Table 4.6: Same as Table 4.5 for Br isotopes.

Isotope	$T_{1/2}$	A_{52d} [Bq]	$A_{+2.5d}$ [Bq]	A_{+150d} [Bq]
^{83}Br	2.4 h	$5.4 \cdot 10^{11}$	$1.6 \cdot 10^4$	0
^{84f}Br	6 m	$9.6 \cdot 10^{11}$	$8.9 \cdot 10^{-23}$	0
^{85}Br	2.87 m	$1.3 \cdot 10^{12}$	0	0
^{86}Br	55.1 s	$1.8 \cdot 10^{12}$	0	0
^{88}Br	16.3 s	$1.9 \cdot 10^{12}$	0	0
Br total		$6.5 \cdot 10^{12}$	$1.6 \cdot 10^4$	0

These numbers should be compared to the yearly legal limits for the FRM-II as summarized in Table 4.9, with the daily limit being 1% of the year-round total. If the inventory of Kr, and Xe is compared to the critical value, it can be seen that there is no danger to exceed the legal limits with Kr isotopes, since after 2.5 days, when the cryo-panels are regenerated, the inventory is already well below the daily limit. However, for Xe the situation is less relaxed. During the regeneration of the panels the inventory is above the yearly limit due to ^{133}Xe . However, after 150d decay the activity drops well below the limit and a release at this time is harmless.

Table 4.7: Same as Table 4.5 for I isotopes.

Isotope	$T_{1/2}$	A_{52d} [Bq]	$A_{+2.5d}$ [Bq]	A_{+150d} [Bq]
^{129}I	$1.6 \cdot 10^7$ a	$3.6 \cdot 10^3$	$3.6 \cdot 10^3$	$4.1 \cdot 10^3$
^{131}I	8.02 d	$2.8 \cdot 10^{12}$	$2.3 \cdot 10^{12}$	$6.8 \cdot 10^6$
^{132}I	2.3 h	$4.3 \cdot 10^{12}$	$2.5 \cdot 10^{12}$	$6.0 \cdot 10^{-2}$
^{132m}I	83.6 m	$2.7 \cdot 10^{10}$	$2.9 \cdot 10^{-3}$	0
^{133}I	20.8 h	$6.6 \cdot 10^{12}$	$9.2 \cdot 10^{11}$	0
^{133}I	9 s	$1.7 \cdot 10^{11}$	0	0
^{134}I	52 m	$7.6 \cdot 10^{12}$	$7.9 \cdot 10^{-8}$	0
^{134m}I	3.5 m	$5.7 \cdot 10^{11}$	0	0
^{135}I	6.61 h	$6.0 \cdot 10^{12}$	$1.1 \cdot 10^{10}$	0
^{136}I	84 s	$2.8 \cdot 10^{12}$	0	0
^{136m}I	45 s	$1.7 \cdot 10^{12}$	0	0
I total		$3.2 \cdot 10^{13}$	$5.8 \cdot 10^{12}$	$6.8 \cdot 10^6$

Table 4.8: Same as Table 4.5 for Xe isotopes.

Isotope	$T_{1/2}$	A_{52d} [Bq]	$A_{+2.5d}$ [Bq]	A_{+150d} [Bq]
^{129m}Xe	8.89 d	$9.3 \cdot 10^3$	$7.5 \cdot 10^3$	$2.1 \cdot 10^{-2}$
^{131m}Xe	11.9 d	$2.0 \cdot 10^{10}$	$2.0 \cdot 10^{10}$	$1.1 \cdot 10^7$
^{133}Xe	5.25 d	$6.6 \cdot 10^{12}$	$5.5 \cdot 10^{12}$	$2.0 \cdot 10^4$
^{133m}Xe	2.19 d	$2.0 \cdot 10^{11}$	$1.3 \cdot 10^{11}$	$7.6 \cdot 10^{-10}$
^{135}Xe	9.1 h	$8.0 \cdot 10^{11}$	$1.4 \cdot 10^{11}$	0
^{135m}Xe	15.3 m	$1.3 \cdot 10^{12}$	$1.8 \cdot 10^9$	0
^{137}Xe	3.83 m	$5.9 \cdot 10^{12}$	0	0
^{138}Xe	14.1 m	$5.9 \cdot 10^{12}$	0	0
Xe total		$2.1 \cdot 10^{13}$	$5.8 \cdot 10^{12}$	$1.1 \cdot 10^7$

Table 4.9: Legal emission limits for various radionuclides for the FRM-II [67].

Agent	Yearly limit [Bq]
Noble gases	$2 \cdot 10^{13}$
Aerosols ($T_{1/2} \geq 8d$)	$2 \cdot 10^6$
^{131}I	$1.8 \cdot 10^8$
^{14}C	$2 \cdot 10^{10}$
^3H	$3 \cdot 10^{12}$

The situation for halogens is comparable. There is no long-living Br isotope, which leads to no remarkable radioactive inventory after 150 days. Iodine on the other hand has two long-living isotopes, ^{129}I and ^{131}I . However, only the latter is responsible for noteworthy amounts of activity, so that at the end of a reactor cycle the inventory is above the limit but decays rapidly within 150 days leaving only amounts that can be released safely.

Overall, it can be stated, that the activities caused by decay of Xe, Kr, I, and Br do not cause any concerns. However, there might be problematic decay products, which will be discussed hereafter. According to calculation with the Z_p model after A. Wahl[60], the more abundant Xe isotopes are ^{135}Xe to ^{142}Xe .

- ^{135}Xe decays to ^{135}Cs with a very long half-life of $2 \cdot 10^6$ a. Fortunately, it decays with β -radiation only.

- ^{136}Xe is stable.
- ^{137}Xe is short lived and decays to the long lived nuclide ^{137}Cs ($T_{1/2}=30.17$ a). During the 2.5 days between the end of the reactor cycle and the regeneration of the cryo-panels ^{137}Xe will be completely decayed. At this time the total activity originating from ^{137}Cs is $2 \cdot 10^{10}$ Bq. The majority of the produced ^{137}Cs (99.98%) will remain on the cryo-panels. The rest (0.02%) will be distributed among the various cryo-pumps, none of the Cs will reach the decay tanks.
- ^{138}Xe (14.1 m) and its daughter ^{138}Cs (32.2 m) are short lived and decay to stable Ba.
- ^{139}Xe (39.7 s), its daughter ^{139}Cs (9.3 m) and granddaughter ^{139}Ba (83.06 m) are short lived and decay to stable La, before cryo-panels or pumps are regenerated.
- ^{140}Xe (13.6 s) and its daughter ^{140}Cs (63.7 s) are short lived and decay to ^{140}Ba (12.75 d) and ^{140}La (40.3 h). After 2.5 days the total activity from one reactor cycle is $5 \cdot 10^{12}$ Bq for Ba as well as for La. This distributes along the beam-line according to Table 4.1. Because of the half-life, there will be no significant buildup of activity caused by these isotopes. None of the mentioned Ba or La isotopes will reach the decay tanks.
- ^{141}Xe (1.7 s) decays via short lived daughters (^{141}Cs (25 s), ^{141}Ba (18.3 m), ^{141}La (3.93 h)) to ^{141}Ce (32.5 d). This half-life is in the order of one reactor cycle. The total ^{141}Ce activity produced during one reactor cycle, and 2.5 days decay time, is $4 \cdot 10^{12}$ Bq distributed along the beam-line according to Table 4.1. ^{141}Ce decays to stable ^{141}Pr . None of the ^{141}Ce atoms will reach the decay tanks.
- ^{142}Xe (1.24 s) decays via short lived daughters (^{142}Cs (1.7 s), ^{142}Ba (10.7 m), ^{142}La (92.5 m)) to stable ^{142}Ce .

The less abundant isotopes with $A > 142$ are produced with individual yields $Y < 5 \cdot 10^{-4}$ atoms/fission. Since all daughters of Xe are non-volatile, they will only leave the ion source as atoms unless they are produced by decay from Xe outside the source. With the decreasing individual yield for heavy Xe isotopes the chance of finding its daughters outside the source decreases and the activity caused by these isotopes can be neglected in comparison with other sources of radiation.

Iodine decays to xenon, which has been discussed above.

Krypton is produced with individual yields $Y > 1 \cdot 10^{-4}$ atoms/fission for $A < 95$. The resulting decay chains are discussed in the following:

- ^{85}Kr is long lived (10.76 a) and decays to stable ^{85}Rb . It will eventually be regenerated in the decay tanks where it will build up to activities $< 8 \cdot 10^9$ Bq.
- ^{86}Kr is stable.
- ^{87}Kr decays to ^{87}Rb ($4.8 \cdot 10^{10}$ a), which decays without γ -emission.
- ^{88}Kr decays via ^{88}Rb (17.8 m) to stable ^{88}Sr .
- ^{89}Kr decays via ^{89}Rb (15.2 m) to long lived ^{89}Sr (50.5 d). ^{89}Sr favors β -decay to ^{89}Y ground state. Branching ratio to ^{89m}Y (16 s) is only $9.6 \cdot 10^{-5}$. Resulting γ activity is in the MBq range. ^{89m}Y will distribute along the beam-line as shown in Table 4.1, but will not reach the decay tanks.

- ^{90}Kr decays via ^{90}Rb (4.3 m) to ^{90}Sr (28.6 a). The latter decays without γ radiation to ^{90}Y (64.1 h). Populated by ^{90}Sr , the activity of ^{90}Y saturates at $2 \cdot 10^{10}\text{Bq}$. ^{90}Y favors β -decay to ^{90}Zr ground state (99.9885%). It will distribute along the beam-line as shown in Table 4.1, but will not reach the decay tanks.
- ^{91}Kr decays via ^{91}Rb (58s) and ^{91}Sr (9.5h) to ^{91}Y (58.5 d). ^{91}Y favors β -decay to ^{91}Zr ground state. The branching ratio to ^{91m}Zr (0.17 ps) is only $3 \cdot 10^{-3}$. The resulting γ activity is in the GBq range. ^{91m}Zr will distribute along the beam-line as shown in Table 4.1, but will not reach the decay tanks.
- ^{92}Kr decays via short lived daughters (^{92}Rb (4.5 s), ^{92}Sr (2.71 h), ^{92}Y (3.54 h)) to stable ^{92}Zr .
- ^{93}Kr decays via short lived daughters (^{93}Rb (5.8 s), ^{93}Sr (7.45 m), ^{93}Y (10.1 h)) to long lived ^{93}Zr ($1.5 \cdot 10^6$ a). ^{93}Zr decays by β -emission with a branching ratio of 95% to ^{93m}Nb (16.13 y). It emits very soft 31 keV γ radiation to the stable ground state. It will distribute along the beam-line as shown in Table 4.1, but will not reach the decay tanks.
- ^{94}Kr decays via short lived daughters (^{94}Rb (2.7 s), ^{94}Sr (74 s), ^{94}Y (18.7 m)) to stable ^{94}Zr .

Bromide decays to krypton which has been studied above.

For the volatile elements one can conclude, that they do not pose a danger to the environment or people as long as the described operation procedures are enforced. It must be added, however, that elemental Br and I are chemically very active substances and it is very unlikely to find them unbound. It is even doubtful that they are volatile at all. Nevertheless this was assumed throughout all calculations for the sake of conservatism. Furthermore, it has been shown that the decay products ^{90}Y , ^{91m}Zr , ^{137}Cs , ^{140}Ba , ^{140}La and ^{141}Ce lead to noteworthy amounts of γ radiation sources on the cryo-pumps. The most dominating γ -radiator that will reach the decay tanks is ^{85}Kr . Its activity in the decay tanks can be observed with γ spectroscopy and serve as an indicator for the radioactive fill level of the tank.

4.2.4 Volatile compounds

Besides the volatile elements, there is the possibility of forming volatile compounds, e.g. oxides, and hence creating a volatile radioactive substance from an otherwise non-volatile radionuclide. A list of known compounds is given in Table 4.10 and continued in Table 4.11 [68]. It is highly unlikely that these compounds can be formed under vacuum condition, but their formation might be possible in case of air intake into the system. Since the amount of fission fragments is very small, it is highly unlikely that compounds, with more than one fission fragment are formed. Within the tables melting points are listed for reasons of completeness, but the concept of melting can hardly be applied to individual fission fragments. For some compounds only a melting point is listed in Table 4.10, which means, that they disintegrate before they evaporate. For other compounds only a decomposition point is listed, meaning that they disintegrate before they melt. Compounds without boiling, melting or decomposition temperature have been observed but no data are available. The boiling temperatures serve as an indicator for the vapor pressures. Compounds with high boiling points, have a very low vapor pressure, and thus can not be considered volatile. With these constraints in mind only the compounds of iodine and tellurium remain as possible candidates for volatile compounds. Iodine has already been discussed and a summary of longer lived tellurium isotopes is given in Table 4.12, where it can be seen, that the Te activity is comparable to the Kr activity, which is below the legal limits.

Table 4.10: List of volatile compounds of Sr, Y, Zr, Nb, Sb and Te, their melting point T_m , boiling point T_B and decomposition point T_D .

Element/Compound	T_m [K]	T_B [K]	T_D [K]
Sr	1050	1655	
SrH ₂ solid (s)			1323
SrO(s)	2803/2938	3273	
SrO ₂ (s)			488
Sr ₃ N ₂ (s)			
Y	1799	3609	
Y ₂ O ₃		704	
YO			
YO ₂			
Zr	2128	4682	
ZrO ₂	2950/2983		
ZrN	3233		
Nb	2750	5017	
NbO	2210		
NbO ₂	2173		
Nb ₂ O ₅	1733/1758		
NbN	2573		
Sb	903	1860	
SbO			
SbO ₂			
SbH ₃	185	256	
Sb ₂ O ₃	928	1518	
Sb ₂ O ₄ (s)			
Sb ₂ O ₅ (s)			653
Te	723	1261	
TeO			
TeO ₂	1006	1518	
TeO ₃	973	1703	

4.2.5 Aerosols

Another way to create volatile activity from non-volatile radionuclides is the formation of aerosols. Aerosol is a very general term applied to all suspensions of solid or liquid particles in a gas, e.g. air. Typical aerosol dimensions reach from 1 nm to 100 μm , with the average diameter being 0.1 μm . The limit set by the European Commission [69] [70] for average aerosol content, smaller 10 μm , is 50 $\mu\text{g}/\text{m}^3$.

To calculate the actual number of aerosols per cubic meter, it is necessary to estimate their density. Since the ion source is graphite loaded it seems reasonable to use the density of carbon, which allows to calculate the amount of aerosols for different radii, e.g. at 1 nm radius $5 \cdot 10^{18}$ aerosols can be calculated, but it must be kept in mind that this number reduces with the third power of the radius.

Under vacuum conditions the gas can sustain less aerosols compared to ambient pressure, which is reflected in the calculations by assuming a linear dependence on the pressure level. MAFF will be operated at a pressure of 10^{-6} hPa, which is nine orders of magnitude below ambient pressure.

Table 4.11: Same as Table 4.10 for I, Cs, Ba, Ce and Pr.

Element/Compound	T_m [K]	T_B [K]	T_D [K]
I	387	457	
IO ₂			
IO ₃			
I ₂ O ₄ (s)			403
I ₂ O ₅ (s)			573
I ₄ O ₉			348
Cs	302	944	
CsH(s)			443
CsO ₂	873/705		
Cs ₂ O	763		
Cs ₂ O ₂	863		
Ba	1000	2143	
BaH ₂ (s)			1473/948
BaO	2246/2186	2273	
BaO ₂ (s)			723
Ba ₃ N ₂ (s)			1273
Ce	1068	3633	
CeH ₂ (s)			
CeO ₂	2673		
Ce ₂ O ₃	2503		
CeN	2830		
Pr	1208	3563	
PrO ₂ (s)			623
Pr ₂ O ₃ (s)	2573		

Table 4.12: Tellurium isotopes.

Isotope	$T_{1/2}$	A_{52d} [Bq]	$A_{+2.5d}$ [Bq]	A_{+150d} [Bq]
^{127m} Te	109d	$7.4 \cdot 10^6$	$7.3 \cdot 10^6$	$2.8 \cdot 10^6$
¹²⁷ Te	9.35h	$1.2 \cdot 10^{11}$	$8.3 \cdot 10^{10}$	$2.7 \cdot 10^6$
^{129m} Te	33.6d	$8.7 \cdot 10^{10}$	$8.4 \cdot 10^{10}$	$4.0 \cdot 10^9$
¹²⁹ Te	69.6m	$5.8 \cdot 10^{11}$	$5.4 \cdot 10^{10}$	$2.6 \cdot 10^9$
^{131m} Te	30h	$3.1 \cdot 10^{11}$	$7.8 \cdot 10^{10}$	0
¹³¹ Te	25m	$2.6 \cdot 10^{12}$	$1.7 \cdot 10^{10}$	0
¹³² Te	76.3h	$4.2 \cdot 10^{12}$	$2.5 \cdot 10^{12}$	$5.8 \cdot 10^{-2}$

Subsequently, it is assumed that the amount of aerosols sustained under vacuum is reduced by the same amount.

An aerosol by itself, however, is not radioactive. To form a radioactive aerosol, a radionuclide must bind to an aerosol particle. A list of radionuclides, which must be taken into account for aerosol formation is given in Tables 4.13 and 4.14 for refractory elements, which will stay in the ion source even at 2700 K and volatile elements. The noble gases have not been taken into account here, since they form no compounds.

The probability of a radionuclide clustering to an aerosol is very small. Using geometrical cross section considerations a mean free path of over 40 m can be calculated for a radionuclide before

Table 4.13: Refractory fission fragments with half-life of 8 d or more are potential candidates for formation of dangerous aerosols. See Table 4.5 for explanation of columns.

Isotope	$T_{1/2}$ [d]	N_{52d}	A_{52d} [Bq]	A_{+150d} [Bq]
⁹¹ Y	58.5	$2.0 \cdot 10^{19}$	$2.7 \cdot 10^{12}$	$4.6 \cdot 10^{11}$
⁹³ Zr	$5.48 \cdot 10^8$	$2.8 \cdot 10^{19}$	$4.0 \cdot 10^5$	$4.0 \cdot 10^5$
⁹⁵ Zr	64	$2.2 \cdot 10^{19}$	$2.8 \cdot 10^{12}$	$5.5 \cdot 10^{11}$
⁹⁵ Nb	35	$4.9 \cdot 10^{18}$	$1.1 \cdot 10^{12}$	$9.5 \cdot 10^{11}$
⁹⁹ Tc	$7.67 \cdot 10^7$	$2.5 \cdot 10^{19}$	$2.6 \cdot 10^6$	$2.8 \cdot 10^6$
¹⁰³ Ru	39.35	$8.8 \cdot 10^{18}$	$1.8 \cdot 10^{12}$	$1.3 \cdot 10^{11}$
¹⁰⁶ Ru	373.6	$1.7 \cdot 10^{18}$	$3.7 \cdot 10^{10}$	$2.8 \cdot 10^{10}$
¹²⁵ Sb	985.5	$1.2 \cdot 10^{17}$	$9.4 \cdot 10^8$	$8.4 \cdot 10^8$
¹²⁶ Sb	12.4	$2.7 \cdot 10^{14}$	$1.7 \cdot 10^8$	$8.3 \cdot 10^4$
¹⁴¹ Ce	33	$1.5 \cdot 10^{19}$	$3.8 \cdot 10^{12}$	$1.6 \cdot 10^{11}$
¹⁴⁴ Ce	284	$2.3 \cdot 10^{19}$	$6.4 \cdot 10^{11}$	$4.5 \cdot 10^{11}$
¹⁴³ Pr	13.6	$9.1 \cdot 10^{18}$	$5.4 \cdot 10^{12}$	$2.9 \cdot 10^9$
¹⁴⁷ Nd	10.98	$2.9 \cdot 10^{18}$	$2.1 \cdot 10^{12}$	$1.6 \cdot 10^8$
¹⁴⁷ Pm	956.3	$6.7 \cdot 10^{18}$	$5.7 \cdot 10^{10}$	$7.3 \cdot 10^{10}$
¹⁵¹ Sm	33945	$4.5 \cdot 10^{17}$	$1.1 \cdot 10^8$	$1.3 \cdot 10^8$
Total:		$1.7 \cdot 10^{20}$	$2.0 \cdot 10^{13}$	$2.8 \cdot 10^{12}$

Table 4.14: Same as Table 4.13 for volatile aerosol candidates.

Isotope	$T_{1/2}$ [d]	N_{52d}	A_{52d} [Bq]	A_{+150d} [Bq]
⁸⁹ Sr	50.5	$1.5 \cdot 10^{19}$	$2.4 \cdot 10^{12}$	$3.1 \cdot 10^{11}$
⁹⁰ Sr	10585	$2.6 \cdot 10^{19}$	$2.0 \cdot 10^{10}$	$2.0 \cdot 10^{10}$
¹²⁶ Sn	$8.56 \cdot 10^7$	$2.0 \cdot 10^{17}$	$4.3 \cdot 10^4$	$4.3 \cdot 10^4$
¹²⁷ Te	109	$5.6 \cdot 10^{15}$	$1.2 \cdot 10^{11}$	$2.8 \cdot 10^6$
¹²⁹ Te	33.5	$3.7 \cdot 10^{17}$	$8.7 \cdot 10^{10}$	$4.0 \cdot 10^9$
¹²⁹ I	$6.21 \cdot 10^9$	$2.6 \cdot 10^{18}$	$3.6 \cdot 10^3$	$4.1 \cdot 10^3$
¹³¹ I	8	$2.8 \cdot 10^{18}$	$2.8 \cdot 10^{12}$	$6.8 \cdot 10^6$
¹³⁵ Cs	$1.10 \cdot 10^9$	$3.6 \cdot 10^{18}$	$3.4 \cdot 10^4$	$3.7 \cdot 10^4$
¹³⁷ Cs	10950	$2.7 \cdot 10^{19}$	$2.0 \cdot 10^{10}$	$2.0 \cdot 10^{10}$
¹⁴⁰ Ba	13	$9.1 \cdot 10^{18}$	$5.7 \cdot 10^{12}$	$1.7 \cdot 10^9$
Total		$8.7 \cdot 10^{19}$	$1.1 \cdot 10^{13}$	$3.6 \cdot 10^{11}$

it collides with a residual gas atom at vacuum pressure. Therefore, aerosol-radionuclide collisions are very rare.

In a conservative assumption aerosols might somehow manage to acquire a complete monolayer of radionuclides on their surface. The amount of radionuclides that can cluster to an aerosol can be derived by simple geometric considerations, assuming both partners to be spherical. Since there are always unfilled volumes between spheres an additional correction factor must be added, assuming closest packing.

Combining all of the above, but the cluster probability, the maximum activity sustainable by aerosols per m^3 can be derived. The obtained activities have been normalized by the yearly allowance of $2 \cdot 10^6$ Bq, and plotted in Fig. 4.11.

Fig. 4.11 demonstrates, that even for the smallest aerosol diameters, immediately after the end of a reactor cycle the activity from aerosols is small compared to the threshold. Additional safety margins arise from the facts that typical aerosols have $0.1 \mu m$ radius and not 1 nm (safety

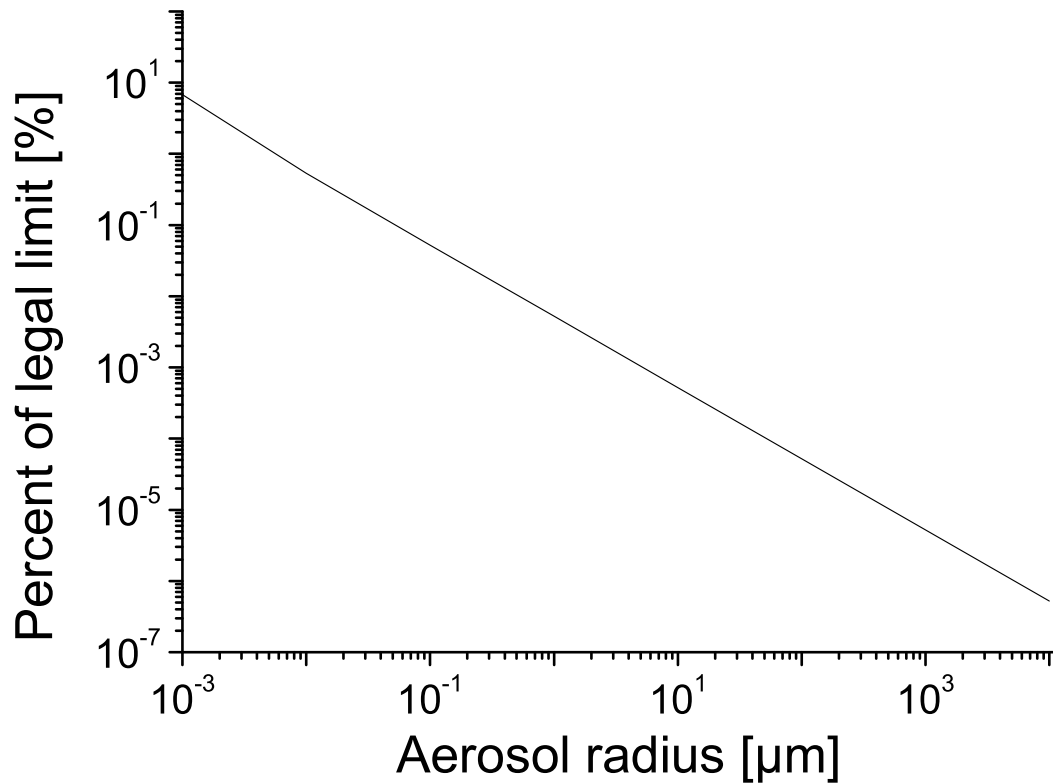


Figure 4.11: Expected aerosol activity compared to legal limit for different aerosol diameters.

factor: $8 \cdot 10^{-3}$), that the reactor has an aerosol filter installed (10^{-5}) and the decay time of 150 d (10^{-1}). Combining all three gives a final safety factor of $8 \cdot 10^{-9}$.

4.2.6 α Activity

Special consideration is necessary for α activity coming from uranium and plutonium produced from ^{238}U by thermal neutron capture and β -decay. Both elements can be implanted in the slit system due to diffusion of uranium out of the graphite matrix, subsequent ionization and ion-beam transport. An uranium inventory of 1.2 g (99.9% enriched ^{235}U) corresponds to $3.1 \cdot 10^{21}$ uranium atoms. Because of the small amount of uranium in the matrix compared to carbon it is justified to assume the same release rate W for uranium as for graphite [71]:

$$W = 0.077 \cdot p \sqrt{\frac{M}{T}} \left[\frac{\text{g}}{\text{cm}^2 \text{s}} \right] \quad (4.2)$$

This gives a release rate of $4.11 \cdot 10^{-7} \frac{\text{g}}{\text{cm}^2 \text{s}}$ for mass number $A=12$, temperature $T=2400$ K and graphite vapor pressure $p=7.5 \cdot 10^{-5}$ Pa. The relevant area is the 2 mm diameter hole in the rhenium cylinder of the ion source. Therefore the release rate is 0.057 g/50 d. The surface ionization probability for uranium of 0.162% is used for plutonium as well, for the purpose of this estimate. For 100 fissioned ^{235}U atoms, 16 are converted to ^{236}U by thermal neutron capture. Disregarding decay the isotope ratio at the slit system is calculated to the values shown in Table 4.15.

Table 4.15: Ratio of isotopes decaying by α -radiation at the slit system.

Percentage	Isotope
97.6%	^{235}U
2.3%	^{236}U
0.1%	^{238}U
$6.2 \cdot 10^{-5}\%$	^{239}Pu
$1.9 \cdot 10^{-6}\%$	^{240}Pu

Using the well known half-lives and disregarding decay over 150 reactor cycles one finds rather low activity after one reactor period and even after 30 years of operation, as listed in Table 4.16.

Table 4.16: α Activity on the slit system from uranium and plutonium released from the ion source as uranium.

Isotope	After 50 d	After 30 a
^{235}U	0.35 Bq	52 Bq
^{236}U	0.25 Bq	37 Bq
^{238}U	56 μBq	8.4 mBq
^{239}Pu	0.01 Bq	1.5 Bq
^{240}Pu	0.7 mBq	0.1 Bq

Even from this coarse estimate it can be seen, that α -activity caused by uranium or plutonium is very small compared to β -activity created by fission fragments. The contribution from plutonium is so low, that 99% enriched ^{235}U would be sufficient.

4.2.7 Activity from delayed neutrons

The excitation energy of some neutron rich fission fragments can be high enough that neutron decay is an alternative to β -decay. Those neutron rich fission fragments are short lived and usually decay with high energy γ -radiation. Table 4.17 gives an overview of isotopes emitting delayed neutrons.

It can be seen from Table 4.17 that $T_{1/2}$ is in the magnitude of 1 s. Delayed neutron radiation is therefore of no concern to radiation safety once the reactor is turned off.

4.2.8 Volume activity

Finally activity in the volume itself shall be considered caused by volatile or non-volatile radionuclides emitted from the source, which have not been trapped yet. A reasonably conservative estimate for this amount can be made by comparing the time an atom spends travelling compared to the total time a reactor cycle lasts. Most atoms travel some milliseconds. Therefore 1 s seems a quite reasonable upper limit. Comparing 1 s to 52 days (4.5 Ms) gives a fraction of $2.2 \cdot 10^{-7}$ in the volume, which is comparably low.

A similar amount can be derived for the activity contained in the ion beam. At 30 keV beam energy, the average ion has a velocity of 200 km/s. At this speed ions spend only $5\mu\text{s}$ in the beam tube. It is obvious that this contribution is small compared to the volume activity caused by radionuclides in the residual gas.

Table 4.17: List of delayed neutron radiators among fission fragments. $BR_{n-decay}$ gives the branching ratio for neutron emission.

Isotope	$T_{1/2}$	$BR_{n-decay}$
^{82}Ga	0.6 s	0.2
^{87}Br	55.6 s	0.02
^{88}Br	16 s	0.06
^{89}Br	4.38 s	0.13
^{90}Br	1.92 s	0.25
^{91}Br	0.54 s	0.09
^{93}Kr	1.29 s	0.02
^{94}Kr	0.208 s	0.06
^{93}Rb	5.85 s	0.01
^{94}Rb	2.66 s	0.1
^{95}Rb	0.348 s	0.08
^{96}Rb	0.201 s	0.14
^{97}Rb	0.170 s	0.25
^{98}Rb	0.119 s	0.14
^{102}Sr	0.068 s	0.05
^{102}Y	0.30 s	0.06
^{102m}Y	0.36 s	0.06
^{123}Ag	0.30 s	0.55
^{132}In	0.20 s	0.06
^{135}Sb	1.71 s	0.2
^{136}Sb	0.82 s	0.32
^{137}Te	2.7 s	0.03
^{137}I	24.5 s	0.06
^{138}I	6.53 s	0.05
^{139}I	2.29 s	0.1
^{140}I	0.60 s	0.14
^{141}I	0.43 s	0.6
^{143}Cs	1.78 s	0.02
^{144}Cs	1.00 s	0.03
^{145}Cs	0.56 s	0.12

4.2.9 Graphite

The evaporation of graphite from the source is an unavoidable contaminant. As calculated in one of the preceding subsections from equation 4.2 the amount of evaporated graphite sums to 57 mg per reactor cycle. However, due to solid angle restrictions in the source, by the extraction electrodes (opening hole of 6 mm diameter 12 mm away from the rhenium cylinder) only 15% of the carbon atoms manage to leave the source. In a first approximation the carbon will homogeneously distribute on the surfaces between the extraction electrode and the segmented acceleration electrode with an area of about 1 m² leading to a surface coating of 0.8 $\mu\text{g}/\text{cm}^2$ after one reactor cycle corresponding to a 40 nm thick carbon layer.

The specific resistance of graphite is 8 $\Omega\text{mm}^2/\text{m}$ [72](at 293K). Applied to a 1 cm long and 1 cm wide strip with a layer thickness of 40 nm, this corresponds to a resistance of $\approx 200 \Omega$.

It is quite clear, from this very basic deliberations, that already after one reactor cycle a conducting layer of graphite will cover everything surrounding the ion source, which includes especially the

segmented acceleration electrode. In account of this, great care has to be taken in the design of that part to avoid the covering of insulators with carbon. A possible solution could be to support the segments only from behind and at the outer rim.

4.2.10 Core radiation

As a neutron source, the FRM-II reactor core is radiating high amounts of neutron and γ -radiation.

The **neutron** spectrum has a thermalization level of 84%, which leads to problems with neutron capture for many materials. Since the SR6 is a through-going beam tube it is impossible that neutrons are moderated on-axis. Therefore, a direct neutron current out of the SR-6 cannot be expected. Detailed calculations are under way and not part of this work.

The in-pile components will be constructed from neutron transparent materials like Ti and Al, to avoid neutron activation. In addition it is planned to further reduce the activation by installing a strong neutron absorber at the first beam waste in the lens trolley.

Since the SR6 is not looking directly onto the reactor core it is also impossible that γ -rays propagate from the core, out of the SR6, to the experimental hall in a direct line. For the absorption of those γ -rays a 1 m long lead block is planned on the rear end of the lens trolley, which has a long bore in the center, with very small diameter for the ion beam to pass. Therefore resulting in a very small conductance for vacuum pumping. Without this lead block, conductance would be good enough to enable pumping of in-pile vacuum in case of a cryo-panel failure.

For radiation protection this lead block is not necessary, since no direct γ -rays can be expected, the following A-side components are very well shielded with concrete, and the MAFF cave is off-limits during reactor operation anyways.

4.2.11 Summary

Radionuclides created in the fission source can spread by the ion beam and as volatile elements (Br, Kr, I, Xe). The contribution of aerosols or oxides can be neglected.

The spread out elements create centers of contamination at points hit by the ion beam and on the cryo surfaces. It has been shown that certain masses in the ion beam carry a high amount of radioactive inventory and should be stopped at the slit system to prevent propagation to the experiments.

Multiplying the distribution of atoms from the source, as shown in Table 4.1 with the total dose rate available at the end of a 52 d reactor cycle, respectively 7 d later gives the dose rate values as shown in Table 4.18. The dose rate values for the slit system have been obtained using the Excel matrix.

4.3 Measurements

The MAFF project is not only creating and containing radionuclides but it is also placed in a radiation field. Especially the source side in the neutron guide tunnel is subject to enhanced γ and neutron radiation. The latter come from the nearby neutron guides, they can activate components of the MAFF beamline and accelerate aging of components. The neutron guides, their supporting structures and the walls of the neutron guide tunnel are also subject to activation by neutron

Table 4.18: Dose rates at centers of contamination.

Position	After 52 d	After 52 d+7 d
	[μ Sv/h]	[μ Sv/h]
Cryo-pump C3	14127	682
Cryo-pump C4	1130	55
Cryo-pump C5	8476	409
Cryo-pump C6	565	27
Cryo-pump C7	0.57	0.03
Cryo-panel A	$5.70 \cdot 10^7$	$2.7 \cdot 10^6$
Cryo-panel B	$8.50 \cdot 10^7$	$4.1 \cdot 10^6$
End-absorber	12.7	0.6
Slit System	$1.1 \cdot 10^5$	$4.8 \cdot 10^5$

capture. A process that already has created a background of γ -radiation, which restricts access to the tunnel.

Knowledge of the γ and neutron fields in the tunnel is interesting for further design of the MAFF B-side. Therefore, measurements of both fields have been performed in cooperation with the FRM-II radiation safety department.

4.3.1 γ -Radiation in the neutron guide tunnel

Seven days after the third regular reactor cycle the neutron guide tunnel was accessed and the γ field measured in two ways, as summarized in Fig. 4.12. First, radiation dose was measured on many positions within the tunnel in order to get a spatial distribution of the γ field. Finally, on selected positions with low dose rate (positions 1 to 5) a detailed γ spectrum was recorded. A sample spectrum is shown in Fig. 4.13b). The dose rate measurements from Fig. 4.12 have been used to generate a map for the area between the first neutron guide and the wall, as shown in Fig. 4.13a). For better understanding the coordinate system is also shown in Fig. 4.12. The map has been created by applying a quadratic fit in x direction and a linear fit in y, as shown in Fig. 4.14. With the fit functions a matrix has been generated and used to create the map. It can be seen from the map, that the dose rate drops at least 2 orders of magnitude from the reactor towards the far wall, so that electronics placed at this position have a much higher survival probability. The extrapolation towards 0, however, must be treated with care.

In Fig. 4.15a) the measured activity of all identified radionuclides are shown, for various positions. It is striking that ^{40}K has only been identified at position 1, which does not mean, that the isotope has not been measured elsewhere, but the data were simply insufficient for a quantitative analysis, as it was the case for the ^{58}Co line at position 3. Also worth mentioning is the decreasing activity from position 4 to position 5, while from the dose rate measurements an increase was expected. However, the fact that the germanium detector used, records less counts is due to an increased dead time of the detector, which obviously has been misjudged by the detector electronics. The measurement has been repeated 33 days later. A comparison of the two measurements for position 2 and 3 is given in Fig. 4.15b). For comparison and verification the expected activity based on the decay properties of the radionuclides as shown in Fig. 4.16 is also given. The comparison shows, that all isotopes are identified correctly and ^{58}Co is the only isotope where the agreement with the expectation is not 100% perfect. The existence of the ^{58}Co line is also somewhat surprising

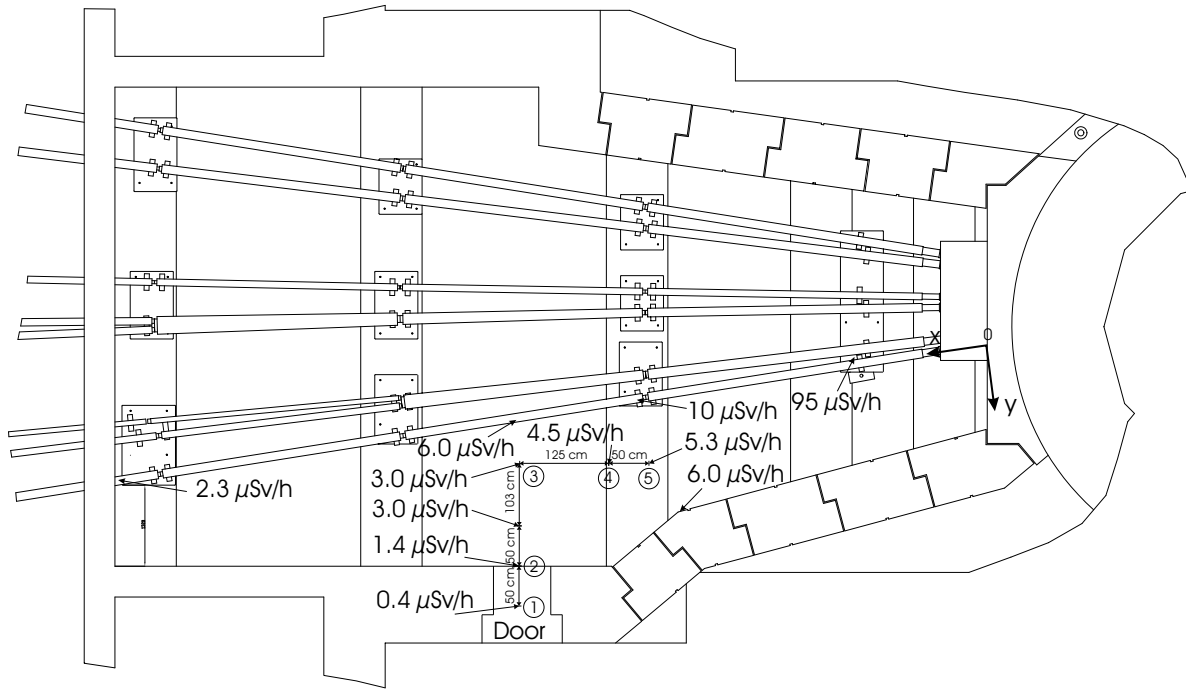


Figure 4.12: Obtained dose rates from measurements in the neutron guide tunnel seven days after the end of the third regular reactor cycle. Numbers in circles mark positions where detailed γ spectra have been taken.

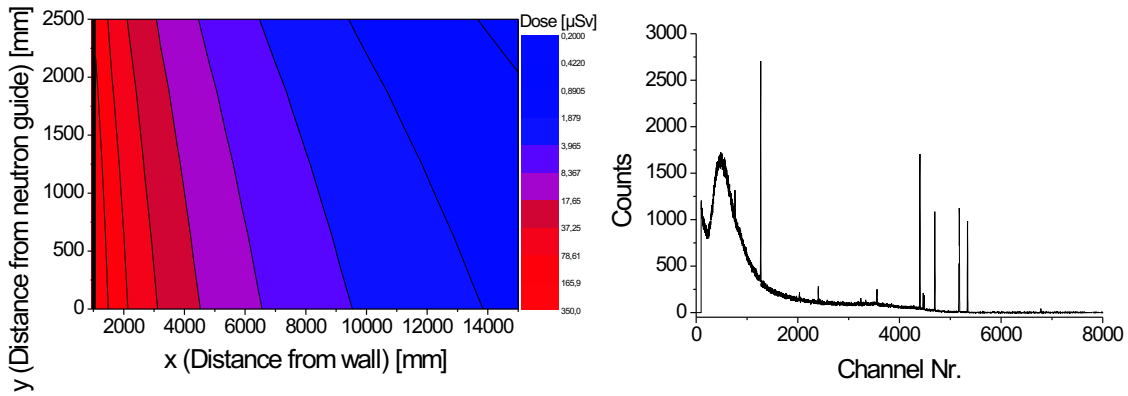


Figure 4.13: a) Dose rate distribution between neutron guide 1 and door. b) Sample γ spectra for position 2.

since it is a neutron deficient isotope and cannot be created by neutron capture. The most likely explanation is the following reaction,



using fast neutrons. At the FRM-II, the ratio of fast neutrons to thermal neutrons, in the neutron guides, is 1:4. In order to realize the measured ^{58}Co quantities, with fast neutrons, a cross-section of ≈ 200 mb would be required, which is supported by total cross-sections, deduced from Ref. [73], for $^{58}\text{Ni}(n,p)^{58}\text{Co}$ reactions, as shown in Fig. 4.17.

An overview of likely sources for the observed isotopes is given in table 4.19.

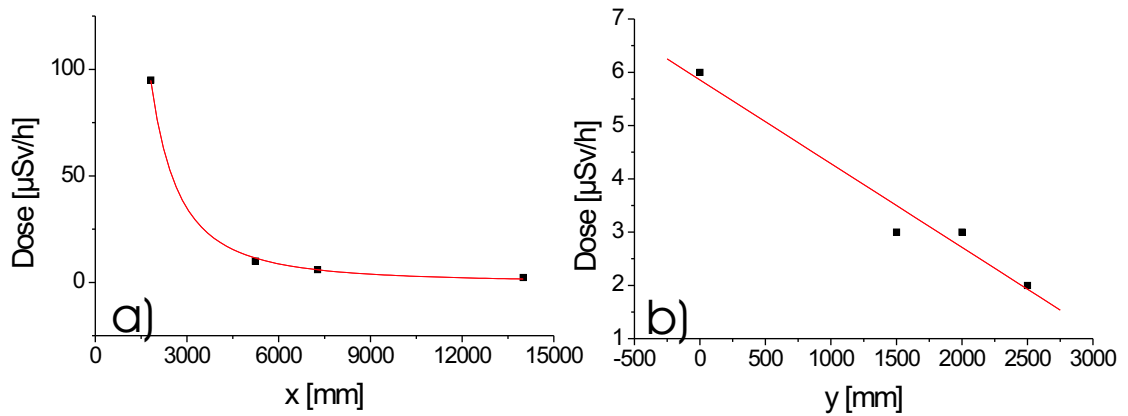


Figure 4.14: Fits for dose rate distribution parallel (y) and perpendicular (x) to the first neutron guide.

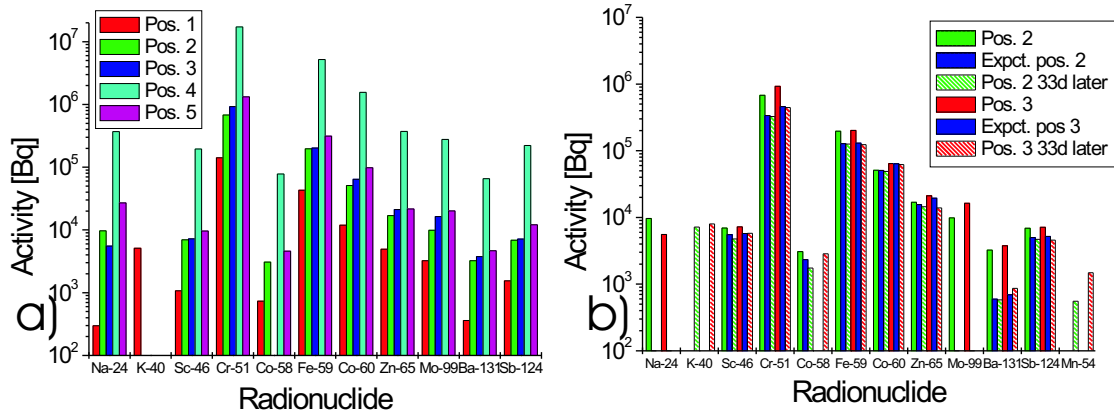


Figure 4.15: a) Measured γ activity on all positions of Fig 4.12 for identified nuclides. Initial activities of position 2 and 3 are compared in b) with the calculated and measured activities 33 d later. The comparison shows, that nuclide identification is correct.

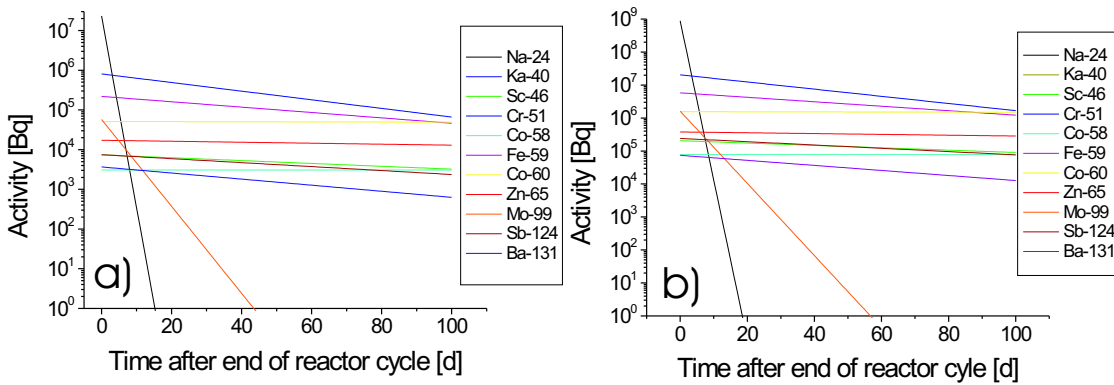


Figure 4.16: Time dependent γ activity at a) position 2 and b) position 4.

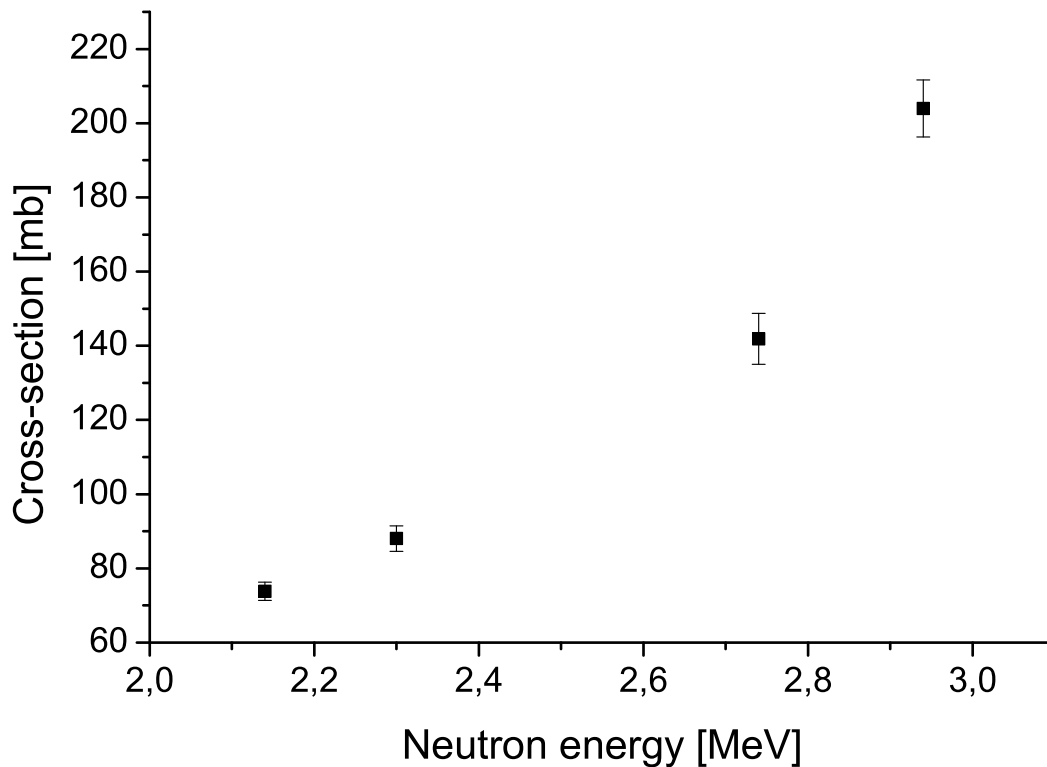


Figure 4.17: Total cross-sections for $^{58}\text{Ni}(n,p)^{58}\text{Co}$ reactions at different neutron energies, deduced from Ref. [73].

It can be seen that once the contribution from Na has decayed radionuclides from steel components are responsible for the majority of the activity. The use of steel as a material is therefore disfavored for MAFF.

4.3.2 Neutron radiation in the neutron guide tunnel

For more accurate prediction of the neutron induced γ -activity of possible MAFF components, some knowledge is required about the neutron field inside the neutron guide tunnel especially in the dedicated MAFF area. Therefore, the neutron flux was measured during the 5th reactor cycle at locations as indicated in Fig. 4.18. The odd numbers represent positions on top of neutron guide #1, samples placed at even numbers are in alignment with the SR6.

The half-life of ^{198}Au ($T_{1/2}=2.6943$ d) is very well known, which makes it a very favorable material for the neutron flux measurement. However, this time is rather short compared to the length of one reactor cycle. ^{198}Au activity is therefore only recording the neutron flux during the last days of the reactor cycle.

An integral neutron flux measurement is achieved by measuring the ^{60}Co ($T_{1/2}=5.272$ a) activity after one reactor cycle.

The activity is measured with the same germanium detector as described in the previous subchapter. The determined specific activity for gold and cobalt samples in each position are summarized

Table 4.19: Possible sources for identified isotopes.

Isotope	$T_{1/2}$	Possible source
^{24}Na	14.96 h	NaCl in the concrete of the surrounding walls. A Cl line is not expected.
^{40}K	$1.3 \cdot 10^9$ a	Common impurity.
^{46}Sc	83.82 d	Relative measured abundance of $9 \cdot 10^{-6}$ compared to ^{59}Fe suggests it is an impurity. Sc is typically used in vapor lamps. Possibly it is used in the neon lamps installed in the neutron guide tunnel.
^{51}Cr	27.7 d	Component of stainless steel. Typically in the order of 10%
^{58}Co	70.86 d	Possible reaction product from ^{58}Ni as described in equation 4.3. Ni is a major part in steel alloys.
^{59}Fe	44.5 d	Steel.
^{60}Co	5.272 a	From ^{59}Co , which is a stainless steel impurity. Relative measured abundance 0.1%.
^{65}Zn	244.3 d	Possibly form ZnO based paint or Zn galvanized iron structures.
^{99}Mo	66 h	Stainless steel contains up to 5% Mo. Relative abundance is determined to 0.1%.
^{124}Sb	60.3 d	Relative measured abundance of 2.6%. Used in cable insulation, flame proof paint and various alloys.
^{131}Ba	11.5 d	Barium is used in paint and for rubber manufacturing.

in Table 4.20, where one can see, that gold and cobalt samples have not always been placed at the same location.

Table 4.20: Specific activity of neutron detectors after irradiation with neutrons in the neutron guide tunnel. Gold and cobalt samples are not always placed in the same locations.

Position	Gold [Bq/ μg]	Cobalt [Bq/g]
1	9.69	29364
2	0.160	12040
3	2.87	-
4	0.154	5725
5	0.719	2405
6	0.067	3211
7	0.41	1367
8	0.036	1794
9	0.024	-
10	0.213	-
11	-	929

From the specific activities A_s , the neutron flux Φ can be calculated according to equation 4.4:

$$\Phi = \frac{A_s}{\sigma \cdot N(0)_s \cdot (1 - \exp(\frac{-\ln 2 \cdot t}{T_{1/2}}))} \quad (4.4)$$

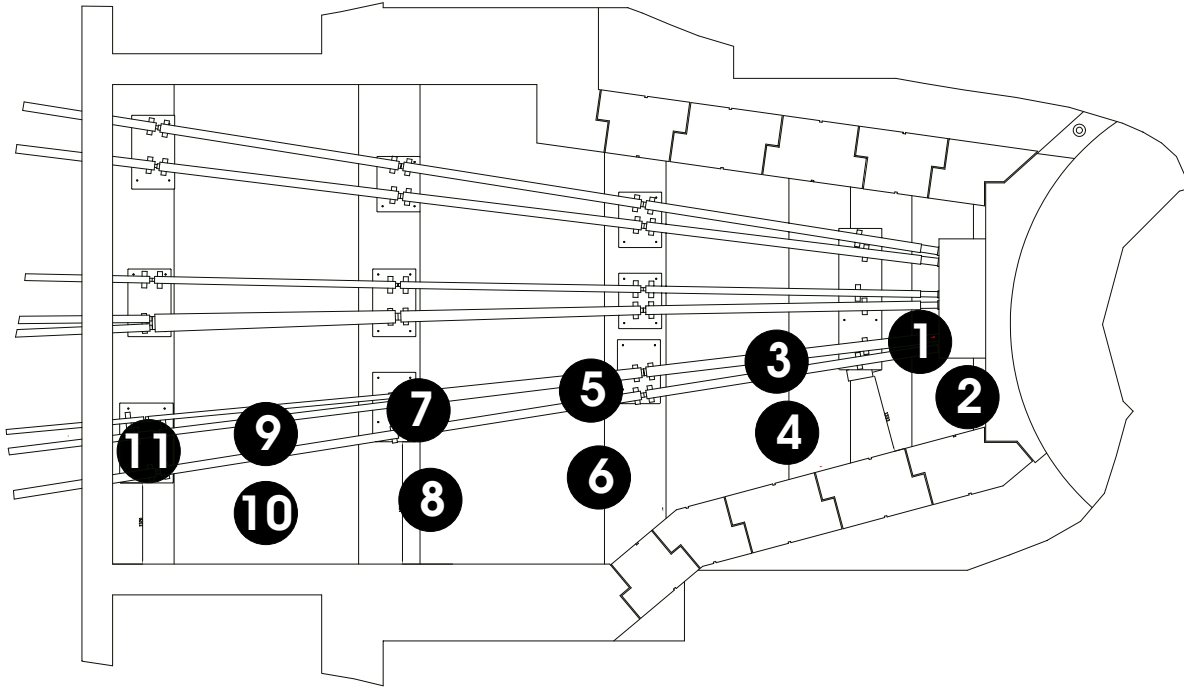


Figure 4.18: Positions used for placement of Au and Co samples for neutron flux measurement in the neutron guide tunnel. Odd numbers are on top of neutron guide #1. Even numbers are placed in alignment with the SR6.

With neutron capture cross section σ and half-life $T_{1/2}$. The results are summarized in Table 4.21.

Table 4.21: Neutron flux for irradiation position for gold and cobalt samples.

Position	Gold [$\text{n cm}^{-2}\text{s}^{-1}$]	Cobalt [$\text{n cm}^{-2}\text{s}^{-1}$]
1	$3.2 \cdot 10^7$	$4.1 \cdot 10^6$
2	$5.3 \cdot 10^5$	$1.7 \cdot 10^6$
3	$9.5 \cdot 10^6$	-
4	$5.1 \cdot 10^5$	$8.0 \cdot 10^5$
5	$2.4 \cdot 10^5$	$3.4 \cdot 10^5$
6	$2.2 \cdot 10^5$	$4.5 \cdot 10^5$
7	$1.4 \cdot 10^6$	$1.9 \cdot 10^5$
8	$1.2 \cdot 10^5$	$2.5 \cdot 10^5$
9	$8.0 \cdot 10^4$	-
10	$7.1 \cdot 10^5$	-
11	-	$1.3 \cdot 10^5$

From all data points obtained, only gold at position 10 does not fit into any systematics. Either the measurement for this sample has been faulty or it is a hint to a leak in neutron guide #1, which is directed towards position 10. Whatever the cause, this point is omitted during the following systematic analysis.

The results from cobalt analysis indicate a lower neutron background, which is not unexpected, since the cobalt measurement represents the average flux over the whole reactor cycle. The reac-

tor, however, is not continuously operating at maximum power.

The neutron flux distribution along neutron guide #1 and in alignment with SR6 have been independently fitted for gold and cobalt samples, using equation 4.5.

$$\Phi(x) = \Phi_0 \exp\left(\frac{-\ln 2 \cdot x}{x_{1/2}}\right) \quad (4.5)$$

With the neutron flux $\Phi(x)$ at position x , Φ_0 , the neutron flux at position $x=0$ and $x_{1/2}$ the half-distance. The fit function and parameters are shown in Fig. 4.19 for cobalt and Fig. 4.20 for gold. Figures a) correspond to the situation on the neutron guide.

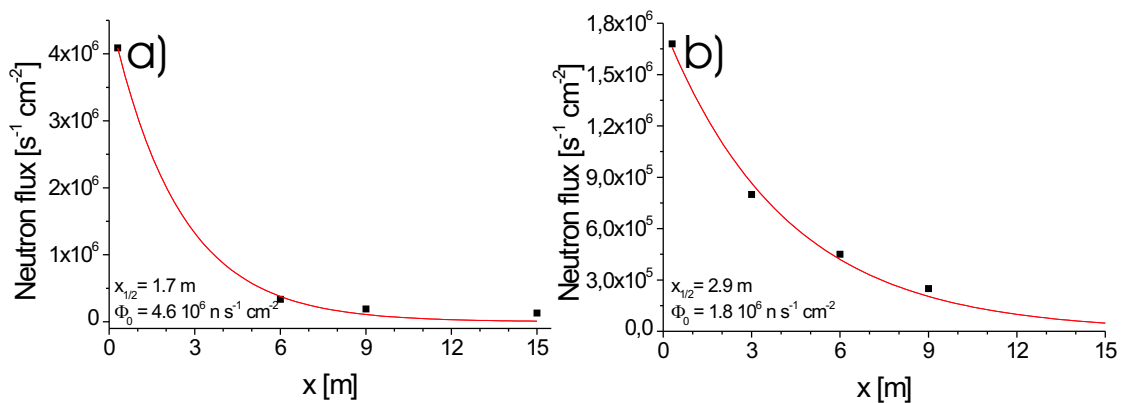


Figure 4.19: Development of the neutron flux as measured with cobalt samples. a) on the neutron guide, b) in alignment with SR6.

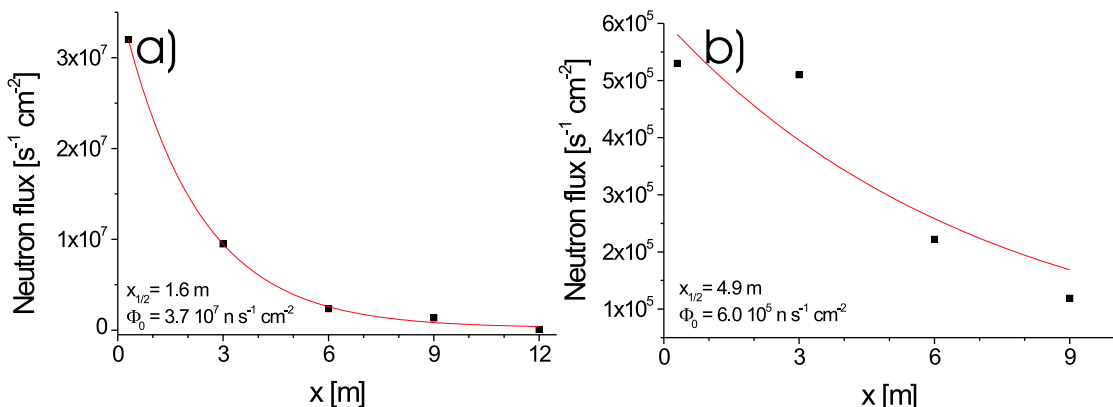


Figure 4.20: Development of the neutron flux as measured with gold samples. a) on the neutron guide, b) in alignment with SR6.

The knowledge of the neutron flux can be used to calculate the degree to which certain materials will be activated due to neutron capture. Hereby, the comparison between aluminum and stainless steel is in the focus of interest. Both materials are suitable for the construction of the vacuum vessels and one of them will be the material used at MAFF for most components. Table 4.22

Table 4.22: γ -Activity and dose rate caused by a neutron flux of $3.2 \cdot 10^7 \text{ n cm}^{-2}\text{s}^{-1}$ over a period of 150 reactor cycles of 52 d each in a stainless steel sample of 1 kg (81.1% Fe, 0.01% Co, 2.5% Ni, 14% Cr, 0.01% V, 0.23% C, 1% Si, 1% Mn, 0.045% P, 0.03% S, 0.01% Mo). Dose rate is given at the end of the last cycle and 7 days later.

Components	γ -Dose [mGy/h]	γ -Activity after 7 d [Bq]	γ -Dose after 7 d [mGy/h]
Fe-54	0	0	0
Fe-58	$2.04 \cdot 10^{-3}$	$9.13 \cdot 10^5$	$1.83 \cdot 10^{-3}$
Co-59	$2.29 \cdot 10^{-3}$	$1.14 \cdot 10^6$	$2.28 \cdot 10^{-3}$
Ni-58	0	0	0
Ni-62	0	0	0
Ni-64	$2.28 \cdot 10^{-4}$	$9.73 \cdot 10^{-16}$	0
Cr-50	$7.21 \cdot 10^{-2}$	$3.03 \cdot 10^7$	$6.06 \cdot 10^{-2}$
Cr-54	$8.84 \cdot 10^{-4}$	0	0
V-51	$3.70 \cdot 10^{-4}$	0	0
C-13	0	0	0
Si-30	$4.59 \cdot 10^{-5}$	$1.14 \cdot 10^{-15}$	0
Mn-55	$9.33 \cdot 10^{-2}$	$1.17 \cdot 10^{-12}$	0
P-31	0	0	0
S-34	0	0	0
S-36	$1.66 \cdot 10^{-8}$	0	0
Mo-98	$1.36 \cdot 10^{-6}$	$1.16 \cdot 10^2$	$2.32 \cdot 10^{-7}$
Mo-100	$4.60 \cdot 10^{-13}$	0	0
Total	$1.71 \cdot 10^{-1}$		$6.47 \cdot 10^{-2}$

and 4.23 show the activities and dose rates expected from typical stainless steel and aluminium components.

Within the tables, only γ -activity has been taken into account. The dose is calculated with a dose rate constant of $0.3 \text{ mGy m}^2\text{h}^{-1}\text{GBq}^{-1}$, corresponding to 3 MeV photon energy [64], in 0.5 m distance. Aluminium is the favored material for vacuum components, because of the Cr and Co content in stainless steel.

Table 4.23: γ -Activity and dose rate caused by a neutron flux of $3.2 \cdot 10^7 \text{ n cm}^{-2} \text{ s}^{-1}$ over a period of 150 reactor cycles of 52 d each in a aluminum sample of 1 kg (99% Al, 1% Si, 0.06% Cu, 0.05% Ti, 0.04% Zn, 0.76% Mg, 0.47% Mn, 0.33% Fe, 0.05% Cr, 0.01% Pb, 0.005% Sn). Dose rate is given at the end of the last cycle and 7 days later.

Components	γ -Dose [mGy/h]	γ -Activity after 7 d [Bq]	γ -Dose after 7 d [mGy/h]
Al-27	$3.25 \cdot 10^{-1}$	0	0
Si-30	$4.59 \cdot 10^{-5}$	0	0
Cu-63	$1.22 \cdot 10^{-3}$	$6.36 \cdot 10^1$	$1.27 \cdot 10^{-7}$
Cu-65	$2.63 \cdot 10^{-4}$	0	0
Ti-50	0	0	0
Zn-64	$8.82 \cdot 10^{-5}$	$4.32 \cdot 10^4$	$8.65 \cdot 10^{-5}$
Zn-68	$3.86 \cdot 10^{-5}$	4.18	$8.36 \cdot 10^{-9}$
Zn-70	$1.29 \cdot 10^{-7}$	$6.94 \cdot 10^{-12}$	0
Mg-26	$4.91 \cdot 10^{-5}$	0	0
Mn-55	$4.39 \cdot 10^{-2}$	$5.48 \cdot 10^{-13}$	0
Fe-54	0	0	0
Fe-58	$8.29 \cdot 10^{-6}$	$3.72 \cdot 10^3$	$7.43 \cdot 10^{-6}$
Cr-50	$2.58 \cdot 10^{-4}$	$1.08 \cdot 10^5$	$2.16 \cdot 10^{-4}$
Cr-54	$3.16 \cdot 10^{-6}$	0	0
Pb-208	$4.78 \cdot 10^{-9}$	$6.78 \cdot 10^{-16}$	0
Sn-112	$8.82 \cdot 10^{-8}$	$4.23 \cdot 10^1$	$8.45 \cdot 10^{-8}$
Sn-120	$1.78 \cdot 10^{-7}$	$8.88 \cdot 10^1$	$1.78 \cdot 10^{-7}$
Sn-122	$1.13 \cdot 10^{-7}$	$5.47 \cdot 10^1$	$1.09 \cdot 10^{-7}$
Sn-124	$1.27 \cdot 10^{-7}$	$3.84 \cdot 10^1$	$7.67 \cdot 10^{-8}$
Total	$3.71 \cdot 10^{-1}$		$3.11 \cdot 10^{-4}$

5 Operational modes

In addition to mechanical safety features a well considered concept of operation is necessary for a safe operation of MAFF. This concept was developed under a series of basic premisses listed in the following:

1. Prevent unauthorized release of radiation
2. Maintain accessibility of the MAFF equipment for maintenance
3. Minimize possibilities for negative feedback on FRM-II operation
4. Achieve a high availability of MAFF

Ad 1): At MAFF, the foremost interest is protecting the environment, population, and the personnel involved from volatile activity. This is achieved by a series of operational methods, installed safety features and protective functions in the control system.

Ad 2): During the maintenance period of the FRM-II, it is desired to access the MAFF cave for maintenance, repairs or upgrades. This is possible, if areas with increased activity, so called *hot spots* (e.g. slit system) are equipped with lead shielding.

Ad 3): The risk of negative feedback of MAFF on reactor operation must be reduced to an absolute minimum to avoid any impact on reactor operation and on other experiments. To minimize this risk, all MAFF components and control system are designed in a way that only very few scenarios exist, which interfere with reactor operation.

Ad 4): Although, the availability of the MAFF system is of no safety relevance users and operators are still interested in a reliable machine with a low down-time.

Having these premisses in mind it should be easier to understand the following operational modes.

5.1 Start-up Phase

Prior to the start-up phase, two other phases must be completed, with the first one being the **testing phase**. Here the complete MAFF beam-line, from the B-side up to the slit system on the A-side will be assembled and tested on a mock-up. In this way it will be confirmed that all components function according to specifications.

In the following **installation phase** the mock-up is disassembled and all MAFF components are moved to the reactor for re-assembly. Now, several tests are performed to ensure, that no components were damaged during relocation. However, all beam related components cannot be completely tested during the installation phase since an ion beam is required, which is not available until the start-up phase begins.

The **start-up phase** is composed of several steps, which are outlined below and explained in the following.

1. Evacuation
2. Stable beam testing
3. Step by step increase of uranium content

Ad 1): As part of the radiation protection scheme it is planned to maintain vacuum at all times, and break it only in case of emergency or for necessary maintenance work. Because of the pressure difference, the vacuum system will function as an additional barrier against radiation release, since all leaks will lead to a gas-flow into the system. The vacuum quality will be monitored with pressure gauges and a pressure increase will serve as an indicator for a vacuum breach.

Ad 2): For stable beam testing, a standard ion source with heat shields, but without uranium content will be inserted into the reactor. In order to avoid neutron induced activation of the source trolley at this early point, tests with stable beams (e.g. K or stable Cs) should be performed during a reactor shutdown. It is the aim of this tests to verify the functionality of ion optical system and beam diagnostics components. For better testing of the mass separator and subsequent beam optics other alkali metals can be added to the ion source. As long as only stable beams have been used, it will still be possible to modify the source trolley if some problems are encountered during the start-up phase. Once the ion optical system works well, some experience with beam steering can be gained. This expertise will be required to minimize contamination of vacuum components due to collisions with the ion beam during steering.

Ad 3): After it has been verified, that the ion optics and beam diagnostics are functional, an uranium loaded ion source with heat shields can be used. The aim of this step is to confirm the calculation for the radionuclide inventory, its distribution, and subsequent shielding calculations.

For safety reasons a very low uranium content of approximately $10 \mu\text{g}$ is used in the beginning. With this inventory it is possible to operate safely, even with the cryo-panels turned off. Starting from this very low amount of uranium, the content can be increased in steps of one or two orders of magnitude, over a period of three to six reactor cycles, until the fission rate of 10^{14} fissions per second is reached. At each step the following measurements will be performed:

- Activities and dose rates at *hot spots*.
- Radioactive inventory transported to the decay tanks.
- Achieved fission rate by yield measurements.
- Measurement of cryo-panel efficiency (optional).

Depending on the measurements, shielding material can be added if necessary, the decay period adjusted or operation procedures modified. The following items have to be adjusted potentially:

- Shielding material at *hot spots*.
- The decay period in the decay tanks
- Number of decay tanks

The start-up phase will be finished once a fission rate of 10^{14} fission per second has been reached and the four basic premisses are still fulfilled.

5.2 Normal operation

Normal operation relates to the operational modes beginning after the start-up phase until the decommissioning of the experimental facility and the reactor approximately 30 years later. From the radiation safety point of view the following rules must be applied to concur with the basic premisses.

1. Maintain vacuum at all times
2. Regenerate cryo-panels and cryo-pumps at each reactor stop
3. Store volatile activity in decay tanks prior to release
4. Shield *hot spots*
5. Stop undesirable mass branches at slit system

The MAFF control system is a centralized and unified software tool, exercising control over all MAFF components. Several logical interconnections will be implemented in the control system in order to avoid handling mistakes (e.g. opening a vacuum valve to air pressure). In relation with the control system four terms will be used frequently hereafter. An *automatic* action relates to something the control system does when a certain trigger has occurred (e.g. regenerating the pumps when the reactor is turned off). Automatic functions can be disabled by the user. A *protective* action is similar to an automatic function in the way that it is automatically performing an action based on a certain trigger (e.g. giving an alarm, when vacuum level reaches a threshold) or preventing an action by the user (e.g. opening a vacuum valve to air pressure). A protective function is password protected to avoid unauthorized modifications. A *remote* action corresponds to a remotely issued command by the user (e.g. opening a certain valve). Finally, there are *manual* actions, which require the user to manipulate some device on site by hand.

5.2.1 Maintaining vacuum at all times

As mentioned previously, maintaining vacuum at all times plays an important role to prevent radiation release. All leaks will lead to gas flow into the system at first, resulting in an increase in vacuum pressure. This pressure increase is monitored by redundant (multiple devices of the same kind) gauges distributed along the vacuum system. These measurements will trigger certain *protective* actions if one of the pressure levels mentioned in Table 5.1 is reached.

Table 5.1: Protective pressure levels.

Level No.	Pressure	Action
1	10^{-4} hPa	Optical warning
2	1 hPa	Optical warning and sound, protective actions

Level 1 will lead to an optical on-screen warning, requiring the attention of the operator. At this time the operator can use the installed rest gas analyzers to identify the source of the pressure increase and take measures as described in the emergency operation section.

Level 2 will give an optical warning and corresponding sound. Protective functions will automatically close all vacuum valves and shut down all voltages to the ion optical components, hence disabling the ion beam. The system is now in the safest possible mode. If the pressure increase

is due to an external leak additional manual actions depending on the situation may be required. See the emergency operation section for details.

5.2.2 Regeneration of cryo surfaces

Volatile particles are absorbed on cold surfaces, like cryo-pumps and cryo-panels. The storage capacity of those cryo devices is somewhere between 100 and over 100,000 times higher than the expected gas load from ion source, surface outgassing and very minor leaks. Once the capacity limit is reached, the cryo-device will no longer be able to absorb additional particles and must be regenerated. During this process the device is warmed up, volatile particles are released from the surface and the storage capacity is restored. If the gas load would be the only concern, regeneration intervals, at MAFF, could be very long. However, radionuclide inventory, and hence activity, build-up much faster. To minimize the radioactive inventory in the vacuum system it is useful to regenerate the cold surfaces at each opportunity, which is given at each stop of the reactor.

The regeneration is an *automatic* action triggered by the reactor-off signal. To avoid vacuum loss, not all pumps can be regenerated simultaneously. Therefore only every other pump will be regenerated at a time, resulting in two regeneration steps. First the regeneration of the even numbered cryo-pumps will be completed followed by the odd numbered cryo-pumps. Further information on this automatic functions are given in the control system description, where the following basic steps will be explained in more detail:

1. Closing of B-side heavy vacuum valve and A-side H-stack
2. Regeneration of A and B cryo-panels
 - a) Turning off He-cryo-pump-system
 - b) Warming up cryo panels (passive process)
 - c) Released elements are collected by pumps C3 and C4
3. Regeneration of even numbered cryo-pumps
 - a) Closing cryo-pump gate valve
 - b) Switch cryo-pump compressor off
 - c) Waiting for cryo-pump to warm up (optional: active heating)
 - d) Starting regeneration roughing pumps
 - e) Evacuating roughing-vacuum lines into decay tanks
 - f) Opening cryo-pump fore-vacuum valve
 - g) Released elements are transported to decay tanks
4. Cooling of even numbered cryo-pumps
 - a) Cryo-pump gate-valve is closed, fore-vacuum valve open
 - b) Evacuate cryo-pump to crossover pressure
 - c) Switch cryo-pump compressor on
 - d) Close fore-vacuum valve
 - e) Evacuate cryo-pump volume to beam line vacuum quality

- f) Open gate-valve
- 5. Regeneration of odd numbered cryo-pumps (see 3.)
- 6. Cooling of odd numbered cryo-pumps (see 4.)
- 7. Switch roughing-pumps off
- 8. Open B-side heavy vacuum seal and A-side H-stack

With this procedure the amount of volatile elements in the vacuum system is reduced to the absolute minimum and cannot exceed the activity produced in one reactor cycle.

5.2.3 Storage in decay tanks

The volatile activity produced in one reactor cycle is too high to be released to the atmosphere right away. Br, Kr, I, and Xe sum to approximately $8 \cdot 10^{13}$ Bq, at the end of a 52 d reactor cycle, which is slightly above the yearly legal limit of $2 \cdot 10^{13}$ Bq for noble gases. However, for the release to atmosphere the daily limit of $2 \cdot 10^{11}$ Bq must be observed. Therefore, it is necessary to store the volatile elements in decay tanks for some time.

In detail the decay tank filling and release scheme looks as follows:

1. Fill Tank I for 150-180 reactor days (days of reactor operation)
2. Fill Tank II for 150-180 reactor days, while inventory in Tank I decays
3. Measure ^{85}Kr activity in Tank I with mobile γ -spectrometer
4. Release activity of Tank I to KLA 70
5. Fill Tank I for 150-180 reactor days, while inventory in Tank II decays
6. ...

Ad 1, 2 and 5): It has been shown in the previous chapter, that for a decay time of 150 d the activity reduces to $2.5 \cdot 10^9$ Bq dominated by the decay of ^{85}Kr , which is very well below the daily limit. Therefore, an increase in the decay tank inventory by a factor 2 (e.g. 300 instead of 150 collected reactor days) will not cause any severe problems. Even an increase by a factor of 10 would be tolerable. A protective function of the control system takes track of the number of reactor days (day when the reactor is in operation) regenerated in each decay tank. The variation in the number of days regenerated into a tank is necessary to ensure that the release of a decay tank coincides with a maintenance period of the FRM-II.

Ad 3): Prior to release, the activity in the decay tanks can be measured manually with a germanium γ -ray detector, looking for the strong ^{85}Kr γ -line.

Ad 4): If the measured activity is within legal limits, the activity in the tank can be released via the reactor exhaust vent KLA 70. This release can happen during one day or be stretched over a complete maintenance period.

By applying this decay scheme it is physically impossible to violate the legal limits for radiation release. Also a large safety margin (factor 80) is achieved.

5.2.4 Shielding of hot spots

The activity carried by the ion beam is a noteworthy fraction of the total activity, as shown in the previous chapter. At locations where the beam loses intensity, contamination by the ion beam will occur and a hot spot will be created. Table 5.2 gives an overview of possible hot spots and estimates on the beam percentages lost.

Table 5.2: Overview of possible hot spots along the beam line

Percentage	Location
Pre slit system	
93-100	Slit System
<1	Ion optic components
<1	Beam diagnostics
Post slit system	
80	Beam cooler
<20	High resolution mass separator
<2	Charge breeder
<0.4	Post accelerator
<1.6	Beam dump, target

For the values behind the slit system one must keep in mind, that only two mass branches are transported towards the experiments and radioactive inventory is reduced.

The mentioned hot spots will be shielded according to the expected radiation levels. In-pile components are shielded by the biological shield of the reactor itself, while components in the experimental hall up to the slit system will be shielded by concrete similar to the concrete shields of the neutron guides in the experimental hall. For the slit system a 20 cm thick lead shield will be used. Components following the slit system must be shielded during operation, but no shielding is required to access these components after 7 days decay time have passed, as shown in the previous chapter, if certain mass branches are omitted from passing the slit system.

5.2.5 Stopping undesirable mass branches

As shown in Table 4.4 certain mass branches carry an exceptionally high activity and should be stopped at the slit system to avoid long term contamination of the following components and allow easy shielding and high accessibility of those areas.

The masses considered for omitting are given in Table 5.3.

Table 5.3: Overview of mass branches considered for omitting. The given dose rates are calculated for a γ -ray energy of 2 MeV.

Mass	Element	Half-life	γ -Energy	Dose [μ Sv]
140	La	40.272 h	1596 keV	$2.4 \cdot 10^5$
140	Ba	12.75 d	537 keV	$2.2 \cdot 10^5$
89	Sr	50.5 d	909 keV	$3.4 \cdot 10^3$
137	Cs	30.17 a	662 keV	$4.8 \cdot 10^2$
91	Y	58.5 d	1205 keV	$2.8 \cdot 10^2$
141	Ce	32.5 d	145 keV	$1.6 \cdot 10^2$

Mass 140 should be stopped at the slit system in any case. The combination of two *intermediate* lived elements is causing a very high dose rate, which would prohibit accessing the components downstream of the slit system during maintenance periods.

Mass 89 should be stopped at the slit system for the same reason as mass 140.

Mass 137 will build-up a severe long term contamination due to its long half-life. Already after the first cycle the dose rate caused by ^{137}Cs would probably be too high.

Mass 91 has a moderate half-life as well. Even though it causes a very small dose rate compared to mass 140 it is probably not acceptable.

Mass 141 is dominated by a γ -ray energy of 145 keV, which is very much overestimated by a value of 2000 keV as used for the dose rate calculations in Table 5.3. A recalculation of the dose rate for 145 keV is resulting in a dose of 14 $\mu\text{Sv/h}$, which most likely does not pose a problem. Mass 141 should therefore **not** be omitted.

Mass 90 has not been listed in the table because no γ -radiation is emitted in the decay of these nuclei, as explained in detail in the neutral elements subsection in Chapter 4.

To assure that no forbidden mass gets through the slit system a γ -spectrometer can be used to identify beam particles. The identification best takes soon after the slit system and will only be performed every time a new mass is selected. It would not take place continuously.

5.3 Maintenance procedures

Maintaining the MAFF system is important to ensure long term safety and reliability of the system. No maintenance is planned or possible during reactor operation, due to the distribution of fission fragments along the beam line. Additional challenges arise for maintaining components in, or in the vicinity of the vacuum system where γ -radiation from the decay of fission fragments can cause elevated dose rates at certain locations (see Table 4.18 and 5.2 for possible hot spots). Additionally it is of interest for the maintenance procedure, whether or not the vacuum system is opened, thus resulting in four maintenance scenarios as summarized in Table 5.4. Explanations on how these scenarios can possibly be resolved are given in the following.

All maintenance procedures will be performed in close collaboration with the radiation safety department, which decides for each individual case, what kind of protective measures are required to ensure the safety of the environment and personnel involved. Maintaining radioactive materials at the FRM-II is not a problem unique to MAFF, but is performed regularly, e.g. during repairs at the stainless steel neutron guides.

Table 5.4: Summary of possible maintenance scenarios.

	Cold spot	Hot spot
Outside vacuum	1)	2)
Inside vacuum	3)	4)

Ad 1): Away from hot spots the expected dose rates is well below 1 $\mu\text{Sv/h}$. Operations outside of the vacuum system can take place without any additional safety precautions.

Ad 2): At a hot spot, γ -radiation will cause a dose rate similar to the dose rates listed in Table 4.18. This dose rate is dominated by the elements with intermediate half-life, which is, according to

Table 4.3, 500 times higher than the most active long living isotope ^{137}Cs . To ease maintenance close to hot spots, outside the vacuum system, lead shields are installed at the hot spots aiming to reduce the dose rate below $10 \mu\text{Sv/h}$. This can be achieved with the relatively moderate amount of 5 to 6 cm of lead. With this precautions maintenance close to the hot spots is possible.

Ad 3): If the vacuum system needs to be opened to exchange or repair equipment (e.g. pressure gauge), only the vacuum section with the broken device needs to be vented (e.g. with helium). Personnel will be familiar with the device and well trained to ensure the shortest possible exchange time. During the exchange of parts away from hot spots γ -radiation is of no concern. However, there is a very small probability that local air pressure variation will lead to media exchange from the vented vacuum system. Also it can be supposed that very small amounts of radionuclide are dissolved in the gas and might leave the vacuum system in this way. However, this effect is most likely below the detection limit. Additional safety precautions, such as dusk respirator masks are not necessary.

Ad 4): The increased amount of non-volatile fission fragments implanted in the surfaces of a hot spot increase the dose rate from γ -radiation and also enhances the risk of radionuclide release, as described in 3). Again it will be necessary to deploy well trained personnel and seal exposed areas quickly. The additional use of convection shields and suction techniques, as used for maintenance of the neutron guides, will reduce the possibilities of radionuclides spreading outside of the vacuum system to an acceptable level. In case of increased γ -activity the use of protective gloves or clothing will be advised by the radiation safety department in agreement with regulations.

Special attention must be payed to the more complex and highly activated components: Ion source, source trolley, lens trolley and slit system.

If repairs on the **source trolley** are required (expected maintenance interval 30 a), the trolley can be moved into the source trolley's transport container and removed from the neutron guide tunnel as shown in Fig. 2.8. Neutron capture of impurities in the trolleys materials causes a dose rate of 1 mSv/h per kg material in 0.5 m distance, dominated by ^{50}Cr activation, for a maximum neutron flux of 10^{11} n/s (see also Table 4.23). For a trolley weight in the order of 100 kg, the total dose rate is below 100 mSv/h . Neutron absorbing materials will be installed at the trolleys to reduce material activation during operation, however their efficiency has not been quantified at this time, hence worst case, with no neutron shielding is assumed.

The transport containers will be equipped with 12 cm of lead shielding reducing the dose rate by $7 \cdot 10^{-5}$ (1 MeV average γ -ray energy) to a final dose rate of $7 \mu\text{Sv/h}$ in 0.5 m distance. This container has a weight of 7.2 t. Within the container the trolley can be transported to a *hot cell* or storage area.

It would be possible to equip the source trolley with up to 15 cm of lead for a total reduction of $6 \cdot 10^{-6}$ and a mass of 9.9 t.

For the **lens trolley** (expected maintenance interval 30 a) a similarly shielded transport container exists (12 cm Pb, $m_{\text{Pb}}=9.6 \text{ t}$). However, it is not connected permanently to the vacuum system and will only be attached if needed. Due to the contamination of the trolleys it is unlikely, that they will be repaired, instead they will be replaced by a new one.

The same holds true for the **slit system** (expected maintenance interval 30 a). The vacuum chamber of the slit system will be equipped with the means to connect a transport container for the slit system. The slit system will be moved in this shielded container and be replaced by a new one.

A routine maintenance operation is the replacement of the used **ion source**. The dose rate of the burned-up source 3 d after the end of a 52 d reactor cycle is in the order of 18 Sv/h in 0.5 m

distance. With a 20 cm lead shield the dose rate reduces by 10^{-7} (1 MeV average γ -ray energy) to $1.8 \mu\text{Sv/h}$. The lead container of this size has a weight of 1.9 t.

5.4 Emergency operation

MAFF does not only need a safety concept for normal operation but also for various *abnormal working conditions* and *hazardous incidents* as an earthquake and an air plane crash. Additionally, it is always supposed that any single device may suffer from spontaneous failure, which can be supposed for any component for unknown reasons. The safety concept takes this events into account and outlines solutions. Due to the uniqueness of each failure it is impossible to give a detailed recipe for any of them. However, all failures can be categorized according to the matrix given in Table 5.5.

Table 5.5: Simple failure matrix categorizing different leak scenarios

	Minor leak	Major leak
Air	0	1
Water	0	1
He	0	1

A **minor leak** is defined as a leak with a leak rate smaller than the pumping speed of the system. Depending on the size of the leak, pumping can continue for a variable time. For very small leaks it is possible that no pressure increase is detected. In order to detect those leaks it is necessary to run the installed mass spectrometers once per reactor cycle and look for increased He, water, and nitrogen partial pressures in the rest gas.

A leak is considered very minor, if the time during which pumping can continue is larger than the regeneration interval of the cryo-pumps. A very minor leak has no influence on the operational vacuum and the operation of MAFF can continue undisturbed. Therefore, there is no need to discuss very minor leaks in detail.

A **major leak** is given, when the pumping speed is insufficient to pump the leak for sufficient time to administrate counter measures (see below) or when the leak rate is larger than the pumping speed. Those leaks lead to a very fast flooding of the vacuum system with media and to subsequent media exchange. Major air leaks lead to very unfavorable situations, as shown below. Therefore, appropriate precautions are undertaken to reduce the risk of severe leaks. These precautions lead to certain requirements (hereafter indicated in bold face) for certain parts of the facility.

- A section that is required to be **standing** after an outside influence must not collapse or be seriously deformed.
- A section that is required to be **standing with integrity** has to meet all the above requirements and conserve the barrier function against radioactivity release.
- A section classified as **functional** has to meet all the above requirements and be able to fulfill all its additional functions.

Independent of the cause, in the worst case, an incident will always result in one of the scenarios shown in Table 5.5, which will be discussed hereafter. Once a pressure threshold as listed in Table 5.1 is reached and a leak is detected the operator has the following possibilities:

- Use the two installed mass spectrometers to identify the leak media.
- Close valves to separate different vacuum sections or cryo-pumps.
- Use different pressure readouts as an indicator for the location of the leak.

With these measures it is possible to get an idea about the size of the leak, identify the leak media, and isolate the location. In case of a minor leak the operator has the additional option, to reduce the radionuclide inventory by regenerating cryo-panels and pumps.

5.4.1 Helium leak

A helium leak can occur at the cryo-panels or pumps. Both devices will be designed to be functional after earthquakes and plane crashes. Therefore it can not be supposed that they will fail during one of these incidents. However, one of them might fail during regular operation.

A **minor leak** at a cryo-pump or panel will quickly be detected, since the pumping capacity of the cryo-pumps for helium is very low (0.3 bar·l per pump) and the panels do not pump it at all. Therefore, a helium leak at one of the pumps will quickly lead to an increase in pump temperature accompanied by an increase in vacuum pressure, as soon as the capacity limit of the pump is reached. The pump with the actual leak can be identified by the higher vacuum pressure detected by the pumps vacuum gauge. Subsequently, the defect pump will be isolated and replaced. Operation with one less pump is not crucial for MAFF because of the high safety factor in pump capacity and pumping power.

Replacing the cryo-panels in case of a leakage is a major endeavor and would not be undertaken if the leak can be pumped until the scheduled regeneration of the cryo-pumps. A failure of cryo-panel B would not be a problem for radiation safety, since in this case all activity would be collected by cryo-panel A or cryo-pump C3 (radionuclides cannot escape, on the B side, since the heavy vacuum seal is closed during operation). However, in this case cryo-pump C3 would collect an increased amount of activity and could not be maintained easily anymore. Therefore, an isolation of pump C3 will be necessary in case of cryo-panel B failure. If cryo-panel A fails, operation could continue if the conductance to the ion source is sufficiently high and operational vacuum at the source can be maintained. However, without cryo-panel A operational the radionuclide inventory in the A-side cryo-pumps would increase by the efficiency of the cryo-panels and require more shielding for the pumps as well as a more complicated maintaining scheme due to the increased dose rate. Therefore, in case of a failure of cryo-panel A the reactor needs to be turned off and the ion source removed before reactor operation can continue.

A **major leak** can be caused in the event of a severe instantaneous failure of one of the cryo systems. This will lead to a helium shock wave travelling through the system with high velocity. There are various approaches for determining the velocity of this shockwave, but it is clear that it cannot be faster than the speed of sound. However, there are two possible velocities for comparison: The speed of sound in helium under standard conditions is 971 m/s compared to 332 m/s in air. A typical fast DN100 valve needs 15 ms to close, which requires a safe distance from the helium leak of up to 14.6 m if the highest speed is assumed. For MAFF the agreement reached with the safety authorities, so far, was to use the velocity of sound in air under normal conditions, requiring a safe distance of 5.2 m.

For a more detailed analysis Torricellis Law [72] can serve as a starting point. The law describes the effusion of an incompressible substance through an opening in a container. The substance with the density ρ in the container, under the relative pressure $p_{overpressure}$, with respect to the pressure outside the container, effuses with the velocity v :

$$v = \sqrt{\frac{2 \cdot p_{\text{overpressure}}}{\rho}} \quad (5.1)$$

The volume ΔV of substance exhausted in a time interval Δt through an opening area A is given by:

$$\Delta V = A \cdot v \cdot \Delta t \quad (5.2)$$

The pressure dependent density is:

$$\rho = \frac{pM}{RT} \quad (5.3)$$

with the molar mass M , the universal gas constant R , and temperature T .

Assuming that at $t=0$, N_0 particles are in the Volume V_0 under the pressure p_0 , the particle change dN can be calculated according to equation 5.2 to:

$$dN = -v(t) \cdot A \cdot \frac{\rho(t)}{M} \cdot dt \quad (5.4)$$

The time dependent components are:

$$\rho(t) = \frac{m(t)}{V_0} = \frac{N(t) \cdot M}{V_0} \quad (5.5)$$

$$v(t) = \sqrt{\frac{2 \cdot (p(t) - p_{\text{out}})}{\rho(t)}} \quad (5.6)$$

with p_{out} being the pressure outside the volume V_0 , the time dependent pressure is:

$$p(t) = \frac{N(t)RT}{V_0} \quad (5.7)$$

From equations 5.5, 5.6 and 5.7 the exhaust velocity can be calculated to:

$$v(t) = \sqrt{2 \left(\frac{kT}{M} - \frac{p_{\text{out}} V_0}{M \cdot N(t)} \right)} \quad (5.8)$$

Combining 5.8, 5.5 and 5.4 yields:

$$\frac{dN}{dt} = -\frac{A}{V_0} \sqrt{\frac{2}{M} (RTN(t)^2 - p_{\text{out}} V_0 N(t))} \quad (5.9)$$

The solution for this differential equation is rather complicated. The situation can be simplified by assuming the outside pressure to be zero. This is possible since it leads to a more conservative estimate. Doing so, greatly simplifies the differential equation to:

$$\dot{N} = -\beta N \quad (5.10)$$

with

$$\beta = \frac{A}{V_0} \sqrt{\frac{2RT}{M}} \quad (5.11)$$

The solution is:

$$N(t) = N_0 \exp(-\beta \cdot t) \quad (5.12)$$

Using a diameter of 15 mm for the opening hole in the H-valve stack (see Fig. 1.2) during regular operation and a volume of 300 l, as well as a homogeneous distribution of room-temperature helium within the volume, the fraction of helium leaking out in 15 ms can be calculated to:

$$1 - \frac{N(t = 15 \text{ ms})}{N_0} = 9.8 \cdot 10^{-3} \quad (5.13)$$

If helium travels at maximum velocity of 971 m/s to the fast valve it takes about 6 ms to get there. Taking this time into account the leak time reduces to 9 ms. This leads to a leak of:

$$1 - \frac{N(t = 9 \text{ ms})}{N_0} = 5.8 \cdot 10^{-3} \quad (5.14)$$

Due to the estimates made above, the real value will be even smaller. The leak into the first volume also must occur through some kind of hole. If the cryo-panel had a 15 mm diameter hole, some similar fraction would leak into the 300 l volume in 15 ms. From this fraction $5.8 \cdot 10^{-3}$ would leak into the outside beamline. Even with no assumptions made for the cryo-panel hole, the fraction is small. It also must be remembered that it is not supposed that a cryo-panel break will happen during a hazardous incident, which could destroy other parts of the beamline, therefore the remainder of the system, which is not affected by a failure of a cryo-panel, will be intact and the above fraction is not released to the outside world, but to another part of the beamline, which was under vacuum up to the failure.

It also must be added, that the amount of activity transported beyond the fast valve is not dominated by the fraction of helium that leaks out, but by the amount of radionuclides that can be sustained in the helium. The dominating mechanism for sustaining heavy fission fragments in helium will be atomic collisions between gas atoms and fission fragments, resulting in a Brownian Motion of the fission fragments. It is clear that the amount of particles that can be sustained in this way depends on the mass of the particles, with heavier particles being more likely to separate from the gas than lighter ones.

The amount of fission fragments of different mass soluble in helium is not known, but can roughly be estimated from the amount of water that can be sustained in helium. Industrial helium is produced absolutely free of water in a cryogenic process. Once filled in bottles, for transport, water adhering to the container walls will dissolve in the helium until an equilibrium, at 5 ppm, is reached. For the fission fragments this equilibrium will be attained at a smaller ratio, since they are much heavier than water.

For the problem of radioactivity dissolved within helium it is therefore conservative to assume, that less than $5 \cdot 10^{-6}$ fission fragments per escaped helium atom can be transported. Therefore no dangerous amount of activity could be released in this way.

5.4.2 Water leak

A water leak can occur from the light or heavy water pool of the reactor into the through-going zircalloy beam tube. The beam tube has a lifetime larger than the reactor and is designed to withstand earthquakes and aircraft crashes. It is the first barrier against pool water loss and is not supposed to crack during a hazardous incident, but it might fail during normal operation.

A **minor leak** will be pumped very well by the cryo-pumps and panels. Each cryo-pump can pump water until the pump volume is filled with ice. At an advanced stage the ice layer will increase the thermal conductance to the cold head of the pump and temperature will increase. A very minor leak will therefore most likely be detected by a routine scan with the mass spectrometer. With a larger leak the pressure will increase up to the partial water vapor pressure and water vapor will start to condensate until the beam-line between the heavy vacuum seal and the H-stack is filled with water.

A **major leak** will fill the beam-line up to the H-stack much faster and no reduction of the radionuclide inventory will be possible. Therefore, fission fragments will dissolve in the water and spread to the reactor pool via media exchange. This scenario is a minor version of a similar scenario involving the reactor fuel element. During the partial breaking of the fuel element fission fragments are dissolved in water as well. The precautions for this scenario are sufficient to cover the MAFF scenario as well, since the amount of radionuclide inventory in the MAFF source is small compared to the considered broken part of the reactor fuel element.

A very severe water leak will occur during the hypothetical steam bubble explosion in the reactor core. In this case the zircalloy tube of SR6 will be destroyed, the shockwave will destroy the rupture disks (see Fig. 1.2) and water will pour out until the slow valves after the supply sections close. This scenario is not unique to MAFF and a steam bubble explosion is physically impossible for this type of reactor. Therefore no further measures to prevent its consequences are installed.

5.4.3 Air leak

An air leak can result from damaged beam tubes and seals or gaskets. A degeneration of gaskets and seals is not possible since all seals are metallic. Possible damage to the beam tube on the other hand could come from falling equipment. To reduce the risk of an air leak the beam tube on the A-side is *standing with integrity* after earthquake and aircraft crash up to the fast He valve, while the rest of the system only needs to be *standing* after a hazardous incident.

Minor air leaks are identified by an increased nitrogen partial pressure in the mass spectrum. Air leaks have the potential threat of filling the complete system with air, achieving a pressure equilibrium leading to subsequent media exchange with the possibility of radionuclide release into the MAFF cave. For a minor leak the inventory of volatile elements can be reduced to almost zero, by regeneration of the cold surfaces. In addition separating the vacuum sectors minimizes the flooded volume and depending on the location of the leak it can be possible to fix the leak before the system is flooded. Normally, this will not be possible and a partial flooding of the system must be accepted and the leak repaired.

A **major leak** does not leave the opportunity to reduce the radionuclide content, therefore media exchange will happen and volatile nuclides might escape. Since most volatile nuclides are located either on the cryo-panels or on the cryo-pumps only a leak on the pump housing or at the beam-line between the reactor wall and the first vacuum wall would be problematic. The probabilities for leaks in those areas are reduced by constructive measures (e.g. double barrier construction of sensitive components, like bellows and feedthroughs).

For repairs of air leaks safety procedures, similar to those for maintenance and repairs on neutron guides, must be applied.

5.4.4 Summary

A summary of the probabilities of the different media leaking-in and the severeness of such events are explained below and summarized in Table 5.6 with severity classes as explained in Table 5.7 and occurrence classes as given in Table 5.8.

The probabilities for a **helium leak** are very small due to the applied constructive measures. The detection scheme is very sensitive with respect to a helium leak and very early detection of very small leaks is possible. The consequences towards radiation safety, resulting even from an extensive He leak, are very minor. Negative feedback to the reactor exits only in case of a cryo-panel failure, where the reactor must be shut down until the source trolley is removed. However, no radiation release out of the vacuum system is possible and consequences towards the availability of MAFF are acceptable.

A **water leak** must be considered unlikely since it can only happen during a spontaneous failure of components designed for a lifetime of over 30 a. The consequences would lead to a flooding of the SR-6 between the heavy vacuum seal on the B-side and the H-stack on the A-side. Reactor operation could not continue and the beam tube must be exchanged. There will be additional release of fission fragments, which is covered by countermeasures already installed in the reactor. Even though the consequences of a water leak are severe, MAFF does not lead to an increased probability for this events, nor are any new scenarios introduced, which are strictly MAFF related.

Air leaks are potentially dangerous since they can lead to release of volatile fission fragments. The possibility of air leaks is reduced by massive constructive efforts. If the air leak happens despite that, isolation of the leaking sector and reduction of the radioactive inventory offer possibilities to reduce the amount of radiation release to the absolute minimum.

Table 5.6: Detailed failure matrix categorizing different leaks according to location, media, leak type T (minor (0), major (1)) occurrence class O, severity class for safety S, environment E, availability A, and possibility of feedback to reactor operation F.

Location	Media	T	O	S	E	A	F	Comment
Cryo-pump	He	0	2	0	0	0	0	
Cryo-pump	He	1	0	0	0	2	0	
Cryo-panel A	He	0	2	0	0	0 or 2	0	Depending on conductance
Cryo-panel A	He	1	1	0	0	3	1	
Cryo-panel B	He	0	2	0	0	0	0	
Cryo-panel B	He	1	1	0	0	2 or 3	0	Depending on conductance
SR6	H ₂ O	0	0	0	0	3	0	
SR6	H ₂ O	1	0	0	1	3	0	
Reactor	H ₂ O	1	0	2	2	4	1	Steam bubble explosion
Supply section	air	0	1	1	1	2	1	
Supply section	air	1	0	2	2	3	1	
Cryo-pump	air	0	1	1	1	2	0	
Cryo-pump	air	1	0	2	2	2	0	
Vacuum system	air	0	1	0	1	2	0	
Vacuum system	air	1	3	0	1	2	0	Partial flooding for repairs

Table 5.7: Severity classes as used in Table 5.6

Severity class	Bodily injury (safety)	Environment damage (environment)	Effect on availability (availability)
0	No bodily injury	No damage to environment	No damage to equipment
1	Minor injury with no lasting effect	Moderate damage with no lasting effect	Damage of small size equipment (several hours)
2	Serious injury	Serious damage but may be corrected	Damage to large equipment (several days)
3	Potential victim	Serious and durable damage	Damage to very large items (several weeks or month)
4	Major accident with potentiality of several victims	Ecological catastrophe	Massive destruction of facilities

Table 5.8: Occurrence classes as used in Table 5.6

Occurrence class	Class name	Example
0	Unlikely	Multiple failures
1	Very rare	Pipe leakage
2	Rare	Equipment failure
3	Possible	Operator error
4	Frequent	Normal operation

6 Slit system

The slit system behind the mass pre-separator is the beam stop for all ionized fission fragments aside from those two masses selected for further transport towards the experiments. The slit system is the hot spot with the third highest dose rate deposited within the beam line, next to the cryo-panels and the ion source. Due to the restricted space in this area it is planned to contain these radionuclides on the slits in order to minimize the volume that needs to be surrounded by shielding material. The slit system requires adjustable slits, to vary the mass ratio between the two selected mass peaks, since the following ion optics are fixed in place. As explained in Chapter 3 an additional steering capability is required, which is implemented into the slit system by designing the slits as electrostatic deflectors, resulting in a curtain like structure as shown in Fig. 6.1.

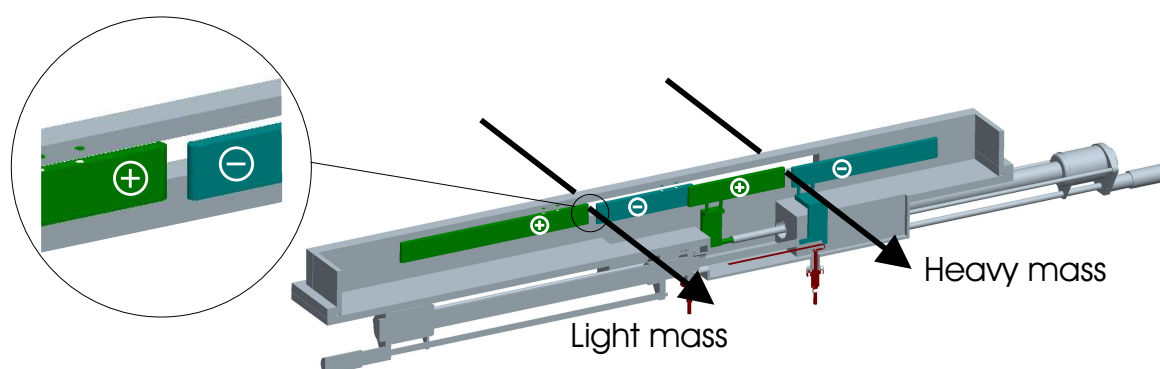


Figure 6.1: Schematic drawing of the slit system. Inspired by a curtain, the slit position can be variably adjusted and a steering capability is added by applying voltage onto the slits.

The key issue for the radioactivity distribution is whether or not activity implanted in the slit system will be released due to sputter effects. The extend of sputtering has been studied in simulations with SRIM2003 [74] and in test experiments using a 30 keV ion beam. Both approaches went hand in hand but will be introduced here in steps.

6.1 Simulations

Simulations were performed with SRIM2003, studying at first a 30 keV ion beam impinging on a copper target and the behavior of other materials in later simulations, the results of which are listed in Table 6.1. The use of iodine as a beam has multiple advantages, which will be explained later.

From Table 6.1 can be seen, that there is a relation between sputter yield (ion range) and target density (surface binding energy). Obviously smaller density and higher surface binding energy reduce the sputter yield and favor deeper ion penetration. While combination of both is giving carbon the advantage (over aluminium), but carbon is an ill defined system, since there are many forms of it. However, the sputter yield of the substrate is of smaller interest compared to the

Table 6.1: Iodine with 30 keV beam energy is impinged on various target materials. Target density ρ and target surface binding energy B_s are given. Resulting sputter yield Y_s , energy E_s of the sputtered atoms together with range R and lateral straggle S of incoming ions are noted.

Target	ρ [g/cm ³]	B_s [eV]	Y_s	E_s [eV]	R [Å]	S [Å]
Cu	8.92	3.52	11.4±0.2	32.1±0.6	82	33
Al	2.70	3.36	3.61±0.04	44.6±0.4	202	55
Ti	4.52	4.89	2.89±0.09	69±2	146	49
C	2.25	4.41	1.73±0.05	40.1±1.2	208	34
Fe	7.87	4.34	6.9±0.2	41.3±1.2	87	33
Pb	11.34	2.03	18.2±0.5	91±3	115	66

sputter yield of the implanted ions. From the first experiment with iodine on copper the ratio of iodine to copper in the target was found to be 1:45 and was entered into the simulation by creating an alloy with 97.9% copper and 2.1% iodine. The sputter yields for this alloy are given in Table 6.2, where the ratio of copper sputter yield to iodine sputter yield of 27.6 ± 0.5 will be of interest for later comparison with the experiment.

Table 6.2: Iodine beam on copper-iodine alloy, as Table 6.1.

Beam	E_{kin} [keV]	Target	Y_s	E_s [eV]	R [Å]	S [Å]
Iodine	30	copper (97.9%)	10.75±0.09	31.78±0.27	83	34
Iodine	30	iodine (2.1%)	0.389±0.003	29.68±0.25	83	34

The next step was the investigation of how the sputter yields are varying for the different fission fragments implanted into the slits. For this investigation alloys consisting of 50 parts aluminum and one part each, of the selected fission fragments, were irradiated in the simulation with a 30 keV iodine beam. Fission fragments from Ni to Sm have been taken into account and the results for sputter atom yield and sputter atom energy are shown in Fig. 6.2 and 6.3.

From Fig. 6.2 it can be seen that the sputter yield varies between 0.08 and 0.4, that means that every incoming iodine ion releases 0.08 to 0.4 fission fragments. In the final slit system, however, incoming ions and sputtered ions will have the same mass, since the masses are separated in space after the mass pre-separator. In order to get a better understanding of the influence of the incoming particle, the simulation has been repeated for four aluminum alloys with appropriate beams, as summarized in Table 6.3.

Table 6.3: Same as Table 6.1 for aluminum alloy.

Beam	E_{kin} [keV]	Target	Y_s	E_s [eV]	R Å	S Å
Nickel	30	Ni (2.1%)	0.069±0.002	85±3	246	96
Zirconium	30	Zr (2.1%)	0.073±0.002	41.2±1.2	218	75
Iodine	30	I (2.1%)	0.152±0.005	24.7±0.7	205	61
Samarium	30	Sm (2.1%)	0.173±0.005	21.8±0.7	208	57

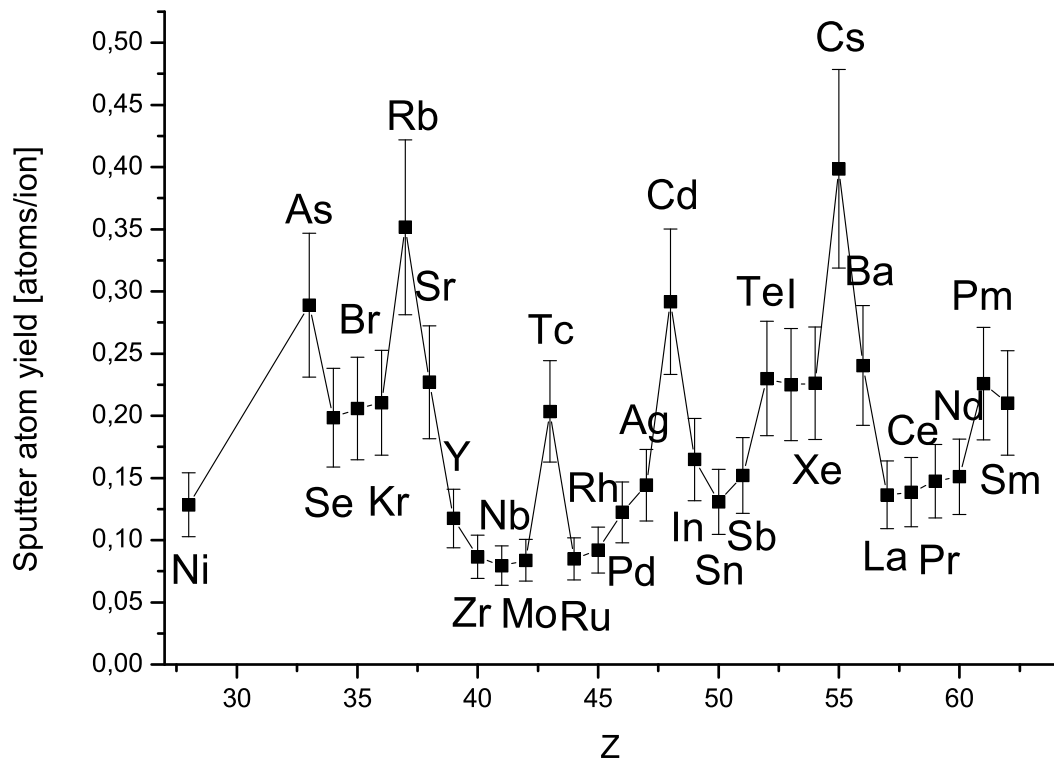


Figure 6.2: Simulated sputter atom yields caused by a 30 keV iodine beam impinging on an aluminum target with traces of elements from Ni to Sm.

Comparing the values with the data from the iodine on aluminum alloy simulations it can be seen, that the sputter yields used for Fig. 6.2 are systematically larger than values listed in Table 6.2, giving a more conservative sputter yield.

The results in Fig. 6.2 and Fig. 6.3 show that the simplification made leads to a conservative estimate of the sputter yields and further simulations can be made using this simplification. However, the simulations show, that over time up to 40% of the implanted ions will be released back into the magnet chamber, where they will collide with the chamber wall at some point. To achieve the deepest possible implantation of sputtered fission fragments the chamber should be manufactured from aluminum. For the sputtered elements marked in gray in Fig. 6.3 the penetration depth into aluminum is given in Table 6.4 listing values between 5 to 10 atomic layers with one atomic layer in aluminum corresponding to about 25 nm.

To increase the knowledge on the circumstances needed to release these implanted atoms by a second atom that hits the same spot (secondary sputtering), further simulations were performed. In a first very conservative approach, a 30 nm layer of aluminum followed by a 4 μm alloy of nickel was used as a target material for a 200 eV iodine beam. The resulting secondary sputter yield for Ni was $(3.4 \pm 0.1) \cdot 10^{-3}$. In a slightly more reasonable approach the nickel was replaced by an alloy consisting of 50 parts aluminum and 1 part nickel. This reduces the secondary sputter yield to $(1.49 \pm 0.05) \cdot 10^{-4}$. Studying an even more realistic setup, e.g. 10 \AA deep implanted Sr under similar conditions as above the sputter yield is $< 10^{-6}$. From this probability can be seen, that the chances for secondary sputtering are small compared to primary sputtering. Therefore, it

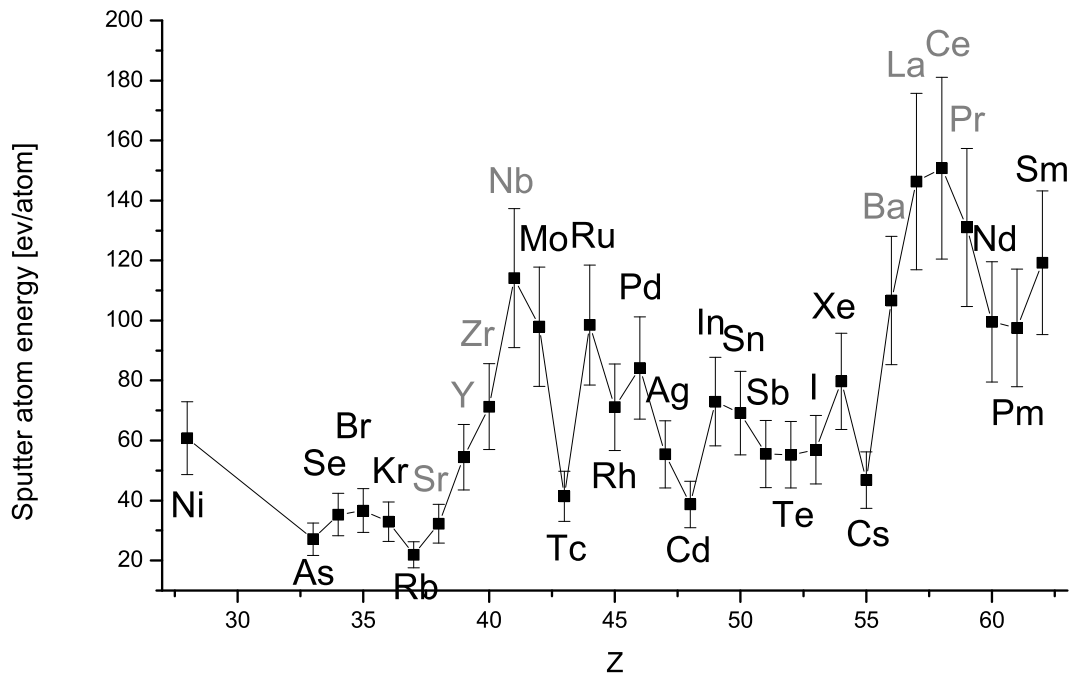


Figure 6.3: Energies of atoms sputtered by a 30 keV iodine beam from aluminum alloy with traces of fission fragments. For elements marked in gray, the penetration depth of the sputtered atoms into aluminum is given in table 6.4.

Table 6.4: Penetration depth of sputtered atoms into aluminum target.

Beam	Energy [eV]	Ion Range [atomic layers]
Strontium	30	4.4
Yttrium	54	5.2
Zirconium	72	5.6
Niobium	114	6.8
Barium	107	8.4
Lanthanum	147	9.2
Cerium	151	9.6
Praseodymium	132	9.2

can not be expected that secondary sputtering will increase the distribution of radionuclides on a significant level.

From the simulations it is clear, that corrosion of the slit system caused by sputtering will lead to the release of implanted radionuclides in the magnet chamber. Simulations also show that it is unlikely that this re-implanted nuclides will be sputtered a second or third time. However, the amount of primary sputtered atoms is already undesirably large, and measures should be taken to reduce the sputter yield into the magnet chamber by three orders of magnitude.

The easiest way to restrict the movement of sputtered atoms is a reduction of the solid angle, which can be achieved in a one step or multi step layout, with a one step layout consisting of a

simple horizontal slit, just large enough for the ion beam to pass through. In a multi step layout many of these slits can be stacked for enhanced performance.

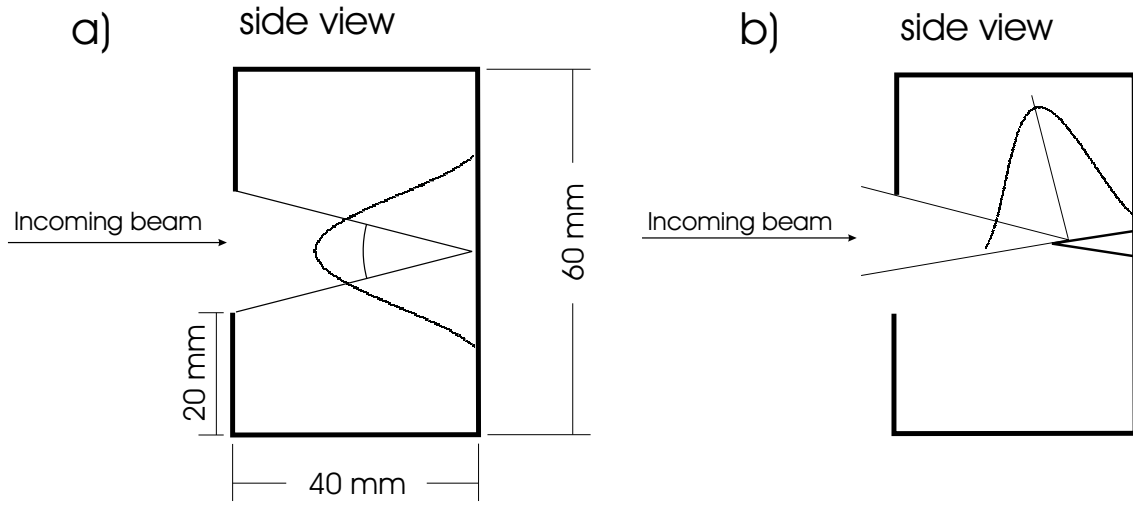


Figure 6.4: Layout for a slit system aiming to reduce the sputter yield. The layout shown in a) exploits solid angle reduction only. The layout shown in b) takes advantage of the distribution of sputtered atoms, which are released following a cosine distribution.

Figure 6.4a) gives an example how a one step solid angle reduction can look like. The design shown reduces the opening angle by 75% in the flat geometry, which is not even one order of magnitude and demands further steps.

Sputtered atoms are released following a cosine distribution, as included in Fig. 6.4. The exact shape of the distribution is likely to be some inflated cosine distribution favoring the zero degree angles [75]. The simplest functions having this properties are a cosine or cosine-square distribution, which are compared in Fig. 6.8. Since the majority of the atoms is obviously emitted perpendicularly to the surface it is intriguing to study the effects of an inclined surface.

In Fig. 6.5 a schematic drawing of an inclined wedge shaped structure is given with various labels added. The values a , b and c are given by the chosen geometry. In the special case shown, b and c are equal but this is not a necessity. The sputtered atoms can leave the structure only within the angle ω , which increases if a is fixed and e is very small or large. Therefore there must be an intermediate minimal value for ω , which can be derived from geometric considerations:

$$\begin{aligned}
 \omega &= \alpha + \beta \\
 \tan \alpha &= \frac{c}{e} = \frac{b-y}{a-d} \\
 \tan \beta &= \frac{b-y}{d} \\
 \Rightarrow \omega &= \arctan\left(\frac{(b-y) \tan \alpha}{a \tan \alpha - b + y}\right) + \alpha
 \end{aligned} \tag{6.1}$$

For a central hit with $y=0$ the equation simplifies to:

$$\omega = \arctan\left(\frac{b \frac{c}{e}}{a \frac{c}{e} - b}\right) + \arctan \frac{c}{e} \tag{6.2}$$

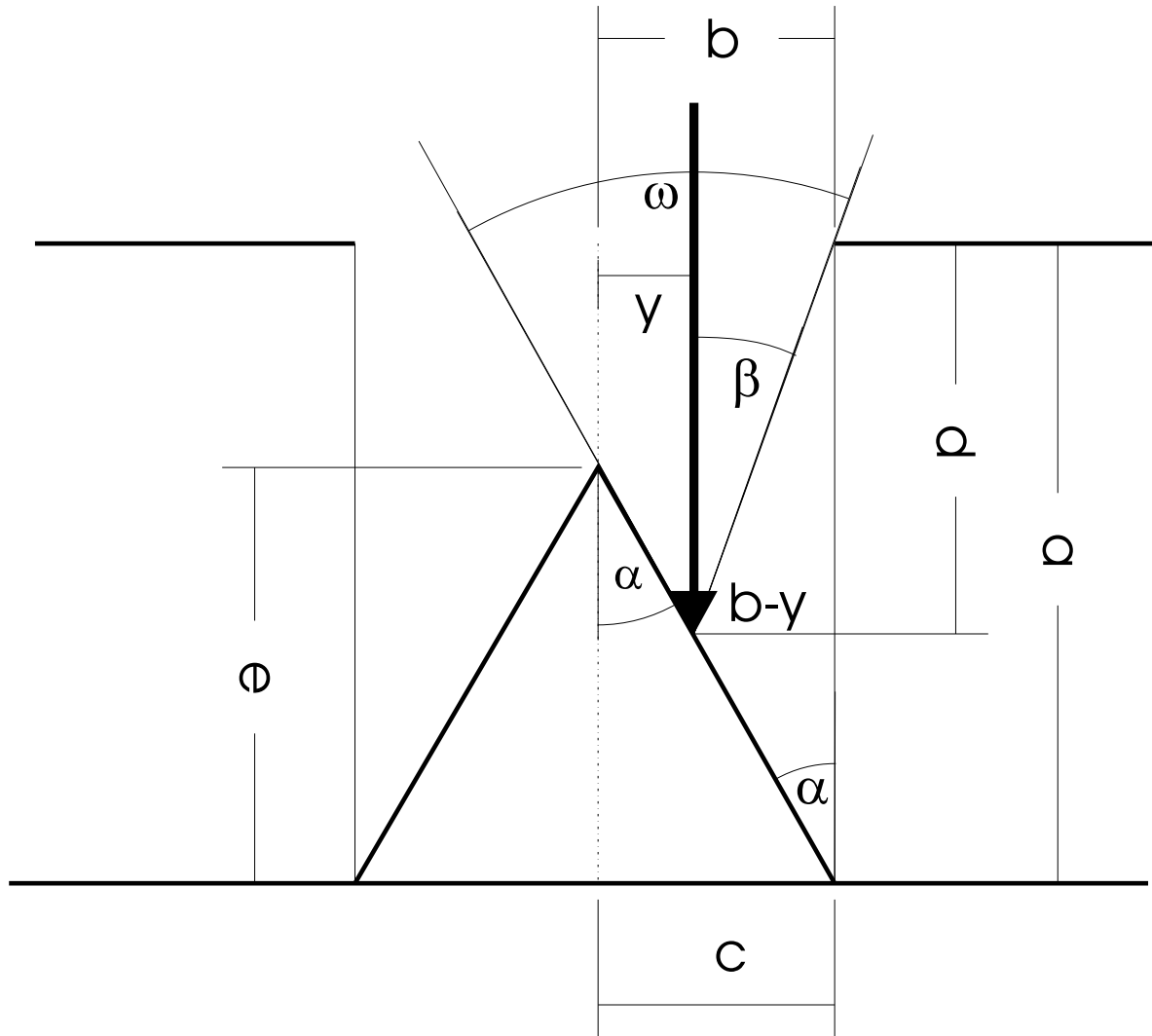


Figure 6.5: Dimensioning of a single wedge as used in calculations.

The obvious disadvantage of one wedge with a broad base is, that e needs to be large in order to get a steep angle. This problem can be solved by using many wedges with small base, as illustrated in Fig. 6.6.

Here the wedge number n needs to be introduced as a new parameter. The formula for ω can be calculated in a similar way:

$$\omega = \arctan\left(\frac{c(b - (2nc))}{e(y + 2nc - c) + ca}\right) + \arctan \frac{c}{e} \quad (6.3)$$

For $y=0$ and $b=c$ equation 6.2 and 6.3 are identical. In Fig. 6.7 a number of graphs are shown for various parameter values leaving only a and b fixed to $b=10$ mm, since the half beam size at this point is slightly smaller than 8 mm, and $a=40$ mm, the depth of the slit system.

From Fig. 6.7 it can be seen that one big wedge is clearly the poorest solution, whereas wedges with larger base are clearly outperformed by smaller ones, whereby $c=2$ mm was the smallest machineable half width and $e=13$ mm seems to be the best height, judging from the full line graph in Fig. 6.7. Comparing ω with a cosine-square distribution as done in Fig. 6.8 it can be seen, that without a wedge, 30.5% of the sputtered particles make it past the opening back into the magnet

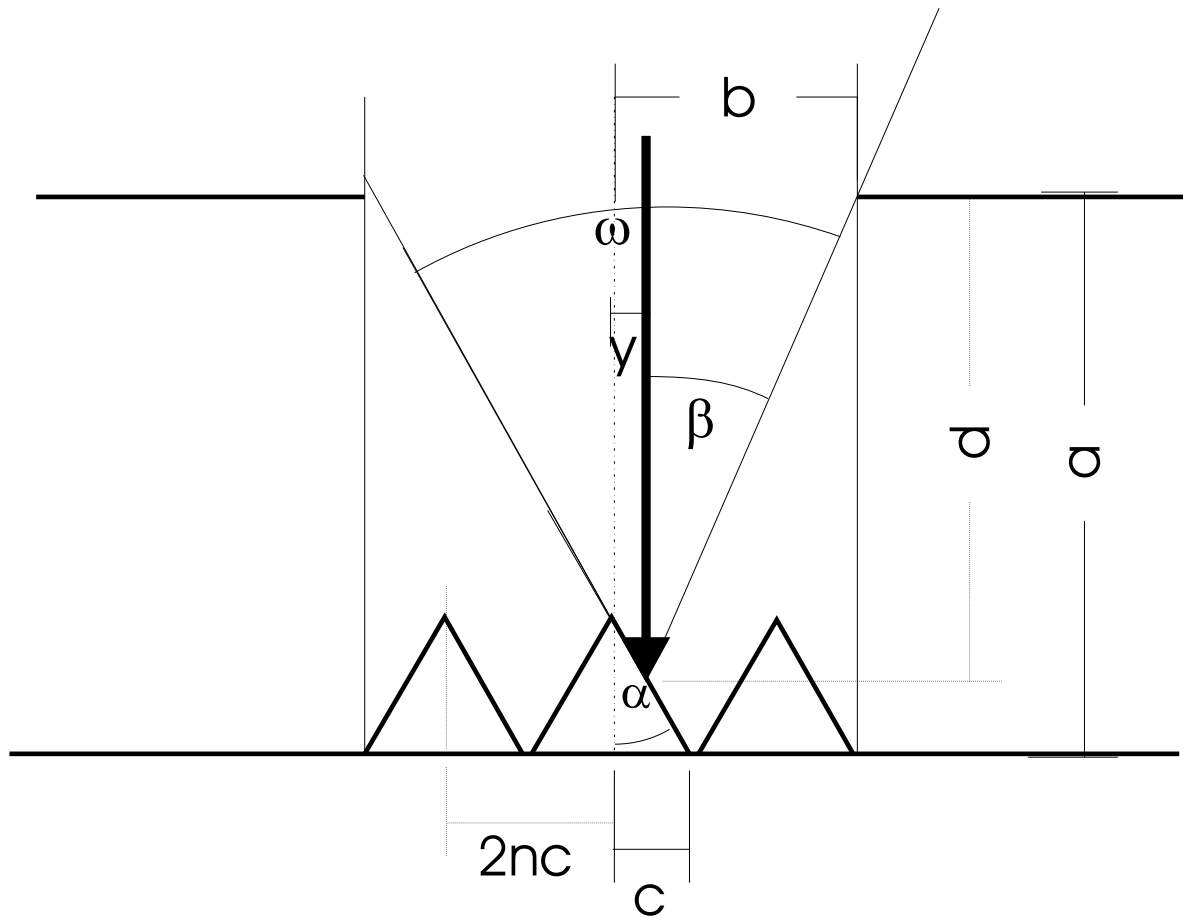


Figure 6.6: Dimensioning of multiple wedges as used in calculations.

chamber. With one big wedge this amount instantly reduces to 14.3%. For the small wedges, based on the full line graph, the released percentage is 2.6%, which is a promising result.

After the experiment described in Section 6.2 it was realized, that there is an increase in the sputter yield with increasing impact angle. For 30 keV iodine on copper simulations with SRIM2003 for different impact angles have been performed and are shown in Fig. 6.9. Judging from Fig. 6.9 it appears therefore doubtful if the wedge structure is actually improving the situation.

6.2 Experiments

In order to validate the simulation results, experimental proof is sought. In the experiment the incoming ion current as well as the number and species of sputtered atoms must be measured. From Fig. 6.4 the basic layout of the experimental setup is already given and the test slit system mounted on a DN100 flange is shown in Fig. 6.10, with the inner dimensions of the box being 50·50·30 mm³.

For ion current measurement, the box is designed as a Faraday cup, what for the front is electrically insulated against the rest of the box, so that a suppression voltage of -150 V can be applied to the front for secondary electron suppression leading to more accurate current measurements. The current is recorded over the course of the experiment and the total ion charge and hence the number of incoming ions can be determined from the integral current.

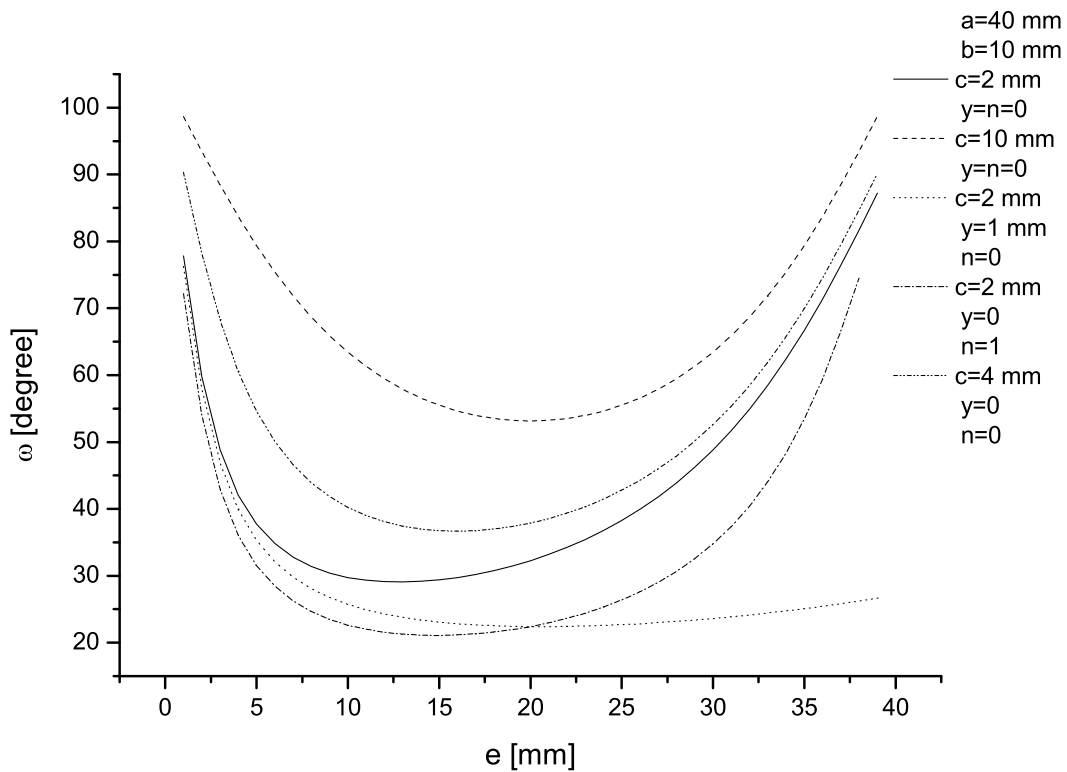


Figure 6.7: Dependence of ω on various geometrical parameters.

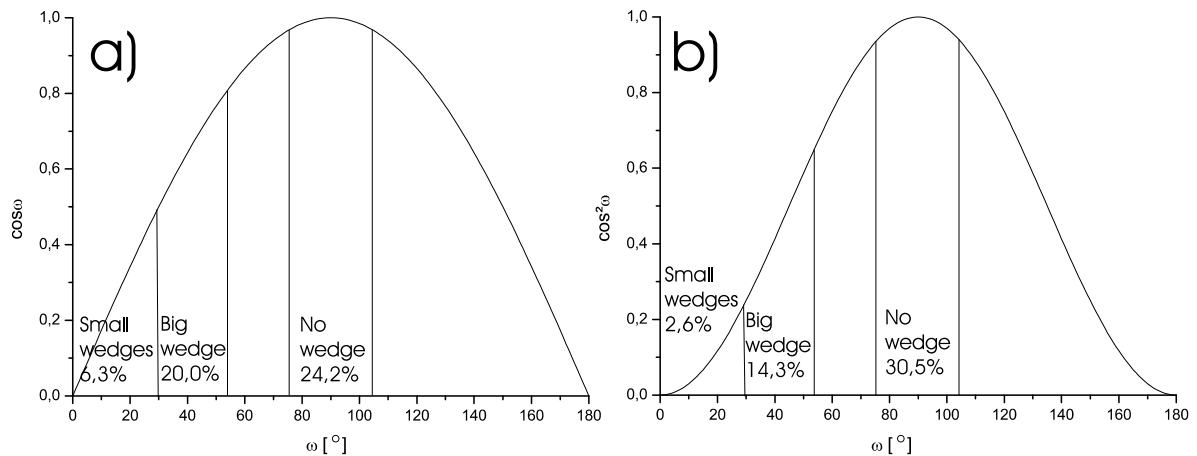


Figure 6.8: Released percentage of sputtered atoms following a) a plain cosine distribution and b) a cosine square distribution. The areas bordered by the vertical lines represent the fraction of the total number of particles sputtered into the magnet chamber. This fraction is given in percent for three different scenarios.

To determine the amount and species of sputtered atoms, that would leave the slit system, the opening is covered by a silicon wafer with a 3 mm hole for the ion beam to pass through, which also functions as a catcher for the sputtered iodine and copper ions. The surface coating of the wafer is analyzed after the experiment with Rutherford Back Scattering (RBS) at Forschungszentrum Rossendorf (FZR). The choice of copper as a target, iodine as beam and silicon as catcher material

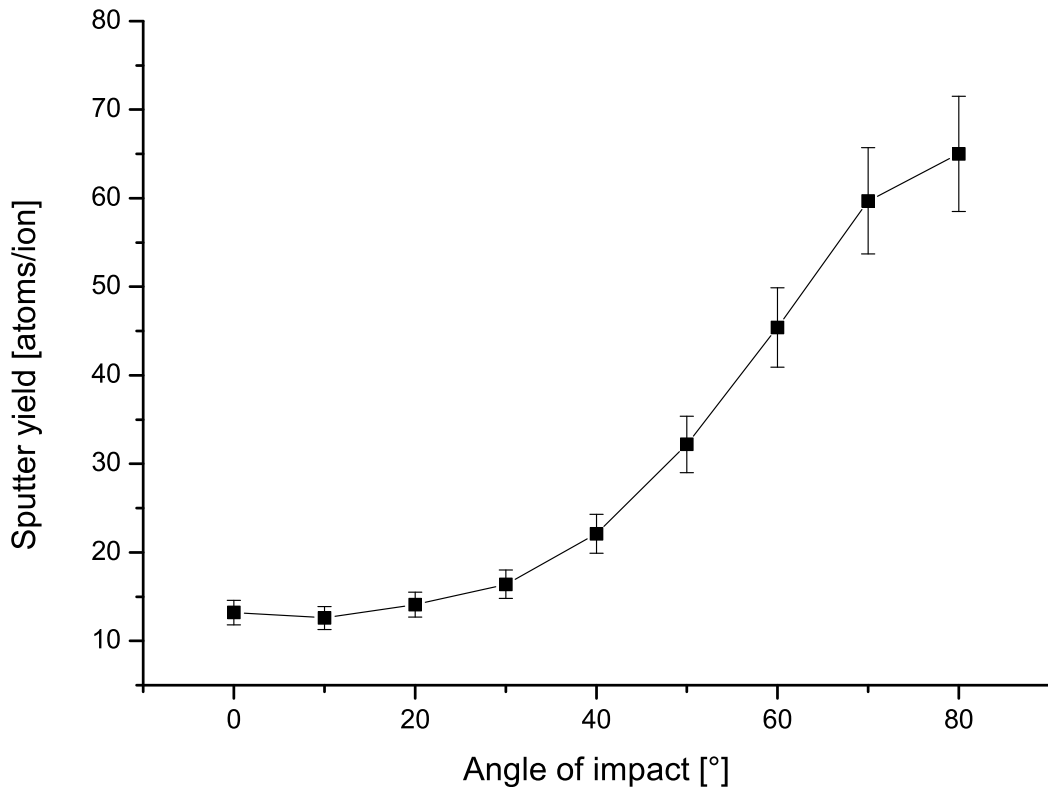


Figure 6.9: Dependence of the sputter factor on the impact angle for 30 keV iodine beam on copper.

was greatly influenced by the idea of keeping the analysis simple, because there is a large difference between the atomic masses of those elements, hence they are easy to distinguish with RBS. During the analysis a cross, with the hole in the center, was scanned with screened points in 3 mm distance from each other in both directions.

The iodine beam was provided by the ion source test stand of the Maier-Leibnitz-Laboratory (MLL), on which setup a systematic overview is given in Fig. 6.11. The ion source used, was a negative-ion source, similar to the source used at the MLL tandem accelerator. For a negative-ion source, iodine has some practical advantages, as it is easy to produce negative ions and it has only one stable isotope leading to no losses after mass separation. The iris and opening hole in the silicon wafer skim the beam, which makes for a quite parallel beam on the target. Furthermore the ion current on the target is maximized by adjusting einzel-lens-2. The current on the target was typically $3 \mu\text{A}$ as can be seen from a typical current in time development over one hour as shown in Fig. 6.12.

The first series of experiments was devoted to the comparison of a flat target to a multi-wedge structure, as introduced in the previous section and shown in Fig. 6.13, with five copper wedges, that covered the whole entrance area.

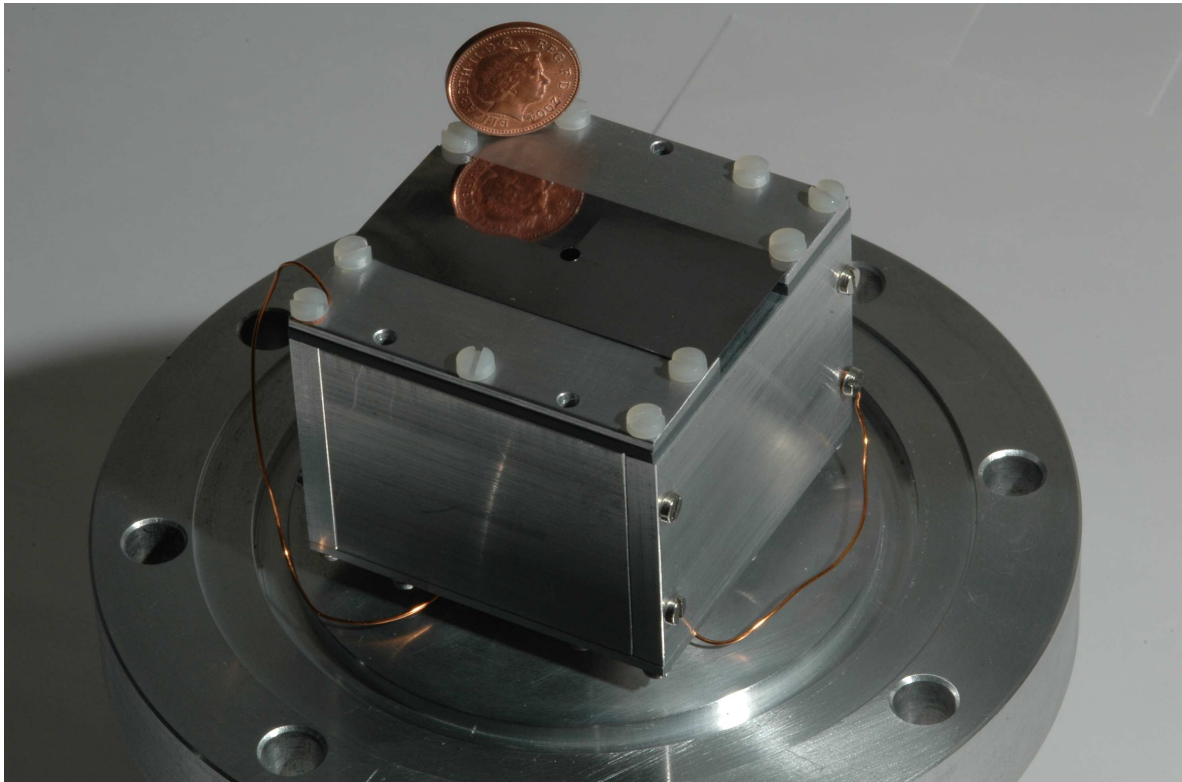


Figure 6.10: Photograph of the experimental setup for sputter yield measurement. The box can operate as a Faraday Cup for current measurement. The opening slit is covered with a silicon wafer, as a collector for the sputtered atoms, with a small hole for the ion beam.

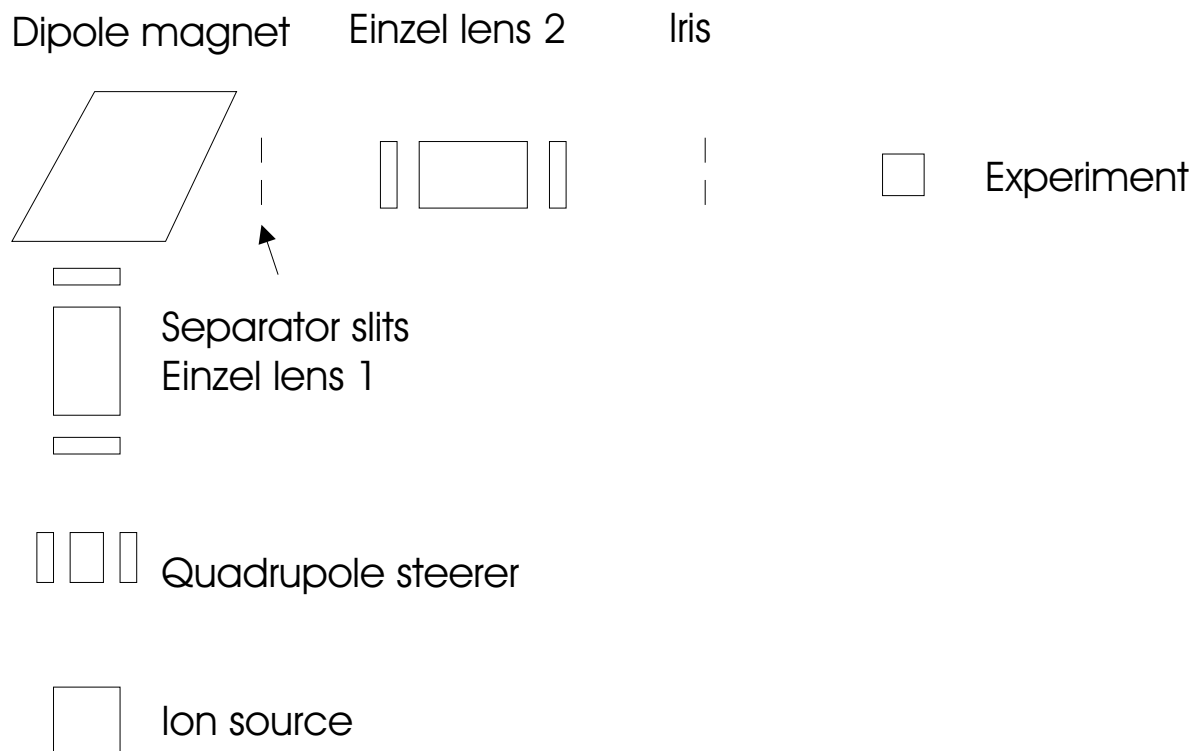


Figure 6.11: Systematic drawing of the MLL ion source test stand as used for the experiment. A nearly parallel beam is obtained by the iris and the subsequent hole in the silicon wafer.

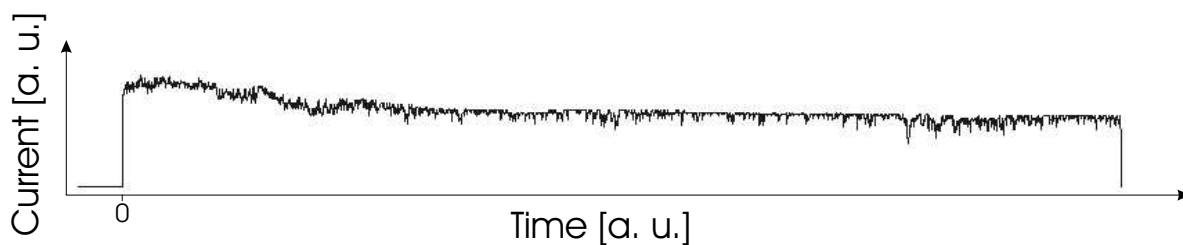


Figure 6.12: Typical ion current development in time.

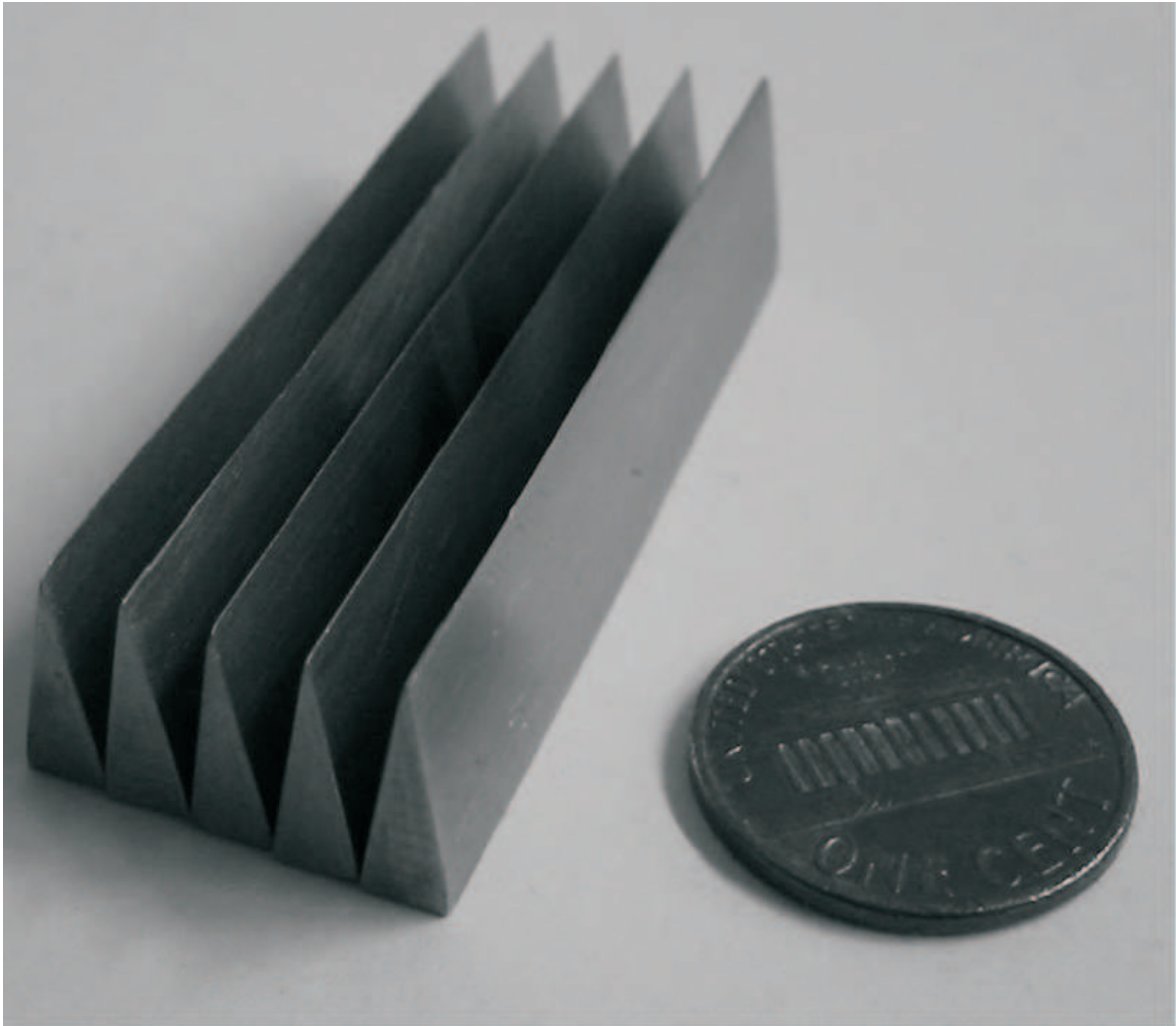


Figure 6.13: Photograph of the wedge structure used in the experiment. Individual wedges have a base of 4 mm and are 13 mm high.

The wedge structure was irradiated with the iodine beam for about one hour, as can be seen from Table 6.5 together with other irradiation conditions, e.g. the amount of incoming ions, which is enough to sputter a few thousand atomic layers of copper.

Table 6.5: Irradiation conditions for flat and wedge targets.

Target	Time	I_{max}	Q_{total}	Collected ions
Flat	3679 s	3.08 μA	$1.09 \cdot 10^{-2}$ C	$6.79 \cdot 10^{16}$
Wedges	3811 s	3.39 μA	$1.06 \cdot 10^{-2}$ C	$6.63 \cdot 10^{16}$

Additionally, the structures have been weighed before and after irradiation to a relative accuracy of 10 μg , in order to determine the amount of sputtered atoms from the mass loss by calculating the ratio of lost mass (sputtered atoms) to incoming ions. With this method, the sputter yield can be determined to 21 ± 1 for the flat target and 57 ± 3 for the wedges, assuming a 5% error for time and mass measurements and discarding uncertainties from the current measurement. On a first glimpse the obtained results support the hypothesis of increasing sputter yield with increasing impact angle. However, only 30.5% for the flat and 2.6% for the wedge target exit the slit system if the sputtered atoms follow a cosine distribution. Taking this percentages into account leads to an effective sputter yield of 6.4 ± 0.3 for the flat geometry and 1.48 ± 0.08 for the wedges, therefore favoring the wedge structure. However, this very rough estimate is not element sensitive.

The more accurate RBS results are shown in Fig. 6.14 to 6.17 with statistical errors. The data have been fitted with polynomials approximating the cosine distribution to second order. This procedure is working very well for the flat target, as shown in Fig. 6.16 a) and b) as well as in Fig. 6.17 a), where only one runaway point, which have their origin in a variation of the surface coating, is reducing the fit quality. Variations in the surface coating can be caused by inhomogeneities in the silicon wafer, affecting the release of material during RBS, or by actual fluctuations in the surface coating caused by an inhomogeneous intensity distribution in the impinging iodine beam. The distribution shown in Fig. 6.17 b) for the iodine distribution in y-direction is lacking visible systematics, because the silicon wafer broke during the RBS analysis of this sample leading to unphysical results as seen in Fig. 6.17 b).

Comparing FWHM of the iodine distribution in Fig. 6.16 to the copper distribution it can be seen that the FWHM for iodine is lower. However, the FWHM of the copper distribution reduces when comparing x- to y-direction, but the reduction is within errors.

The fit quality for the wedge structure is visibly reduced and FWHM is varying, which is expected since the measurements lack a common base of comparison. The wedges are non symmetric in x- and y-direction, so that a different angular distribution for copper and iodine in the same direction in space is not surprising considering their different atomic mass and origin (beam vs. target).

From the fitted functions the total amount of particles implanted into the silicon was determined by,

$$N = \int_{x=-25}^{x=25} \int_{y=-10}^{y=10} f(x) \cdot g(y) dy dx \quad (6.4)$$

with $f(x)$ and $g(y)$ being the fit functions in x- and y-direction. For the iodine distribution in y-direction on the flat target a reasonable fit was not possible, therefore the x-distribution was used in this case for both x- and y-direction, that is possible, because on a symmetric target the function describing the sputter distribution for x and y should be identical, only the integration limits are different. Dividing equation 6.4 by the number of incoming ions gives the sputter yield for copper and iodine, as shown in Table 6.6, with statistical errors, which do not include uncertainties from the beam current measurement. Assuming that the derivation is the same for

both measurements, they can be compared within the given errors. These errors, however, are much larger if a comparison to other experimental data or the SRIM2003 calculation is desired.

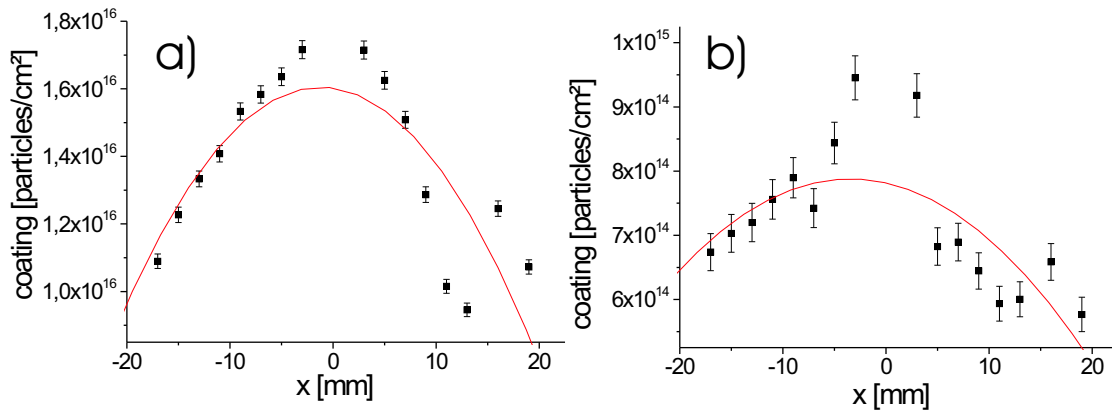


Figure 6.14: a) Copper and b) iodine sputter distribution with wedge target.

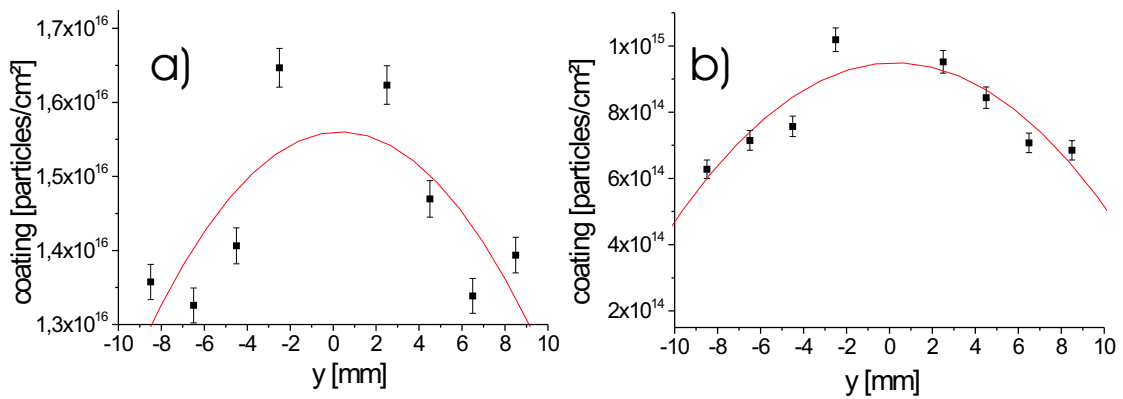


Figure 6.15: a) Copper and b) iodine sputter distribution with wedge target.

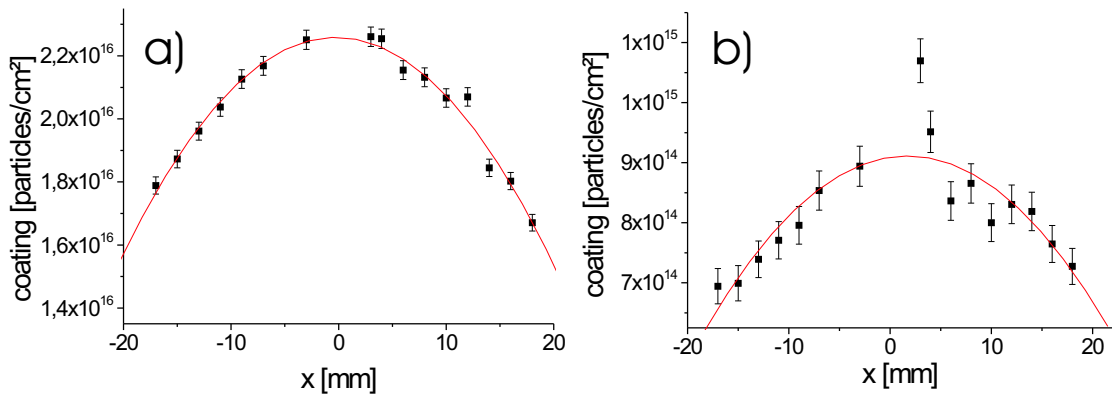


Figure 6.16: a) Copper and b) iodine sputter distribution with flat target.

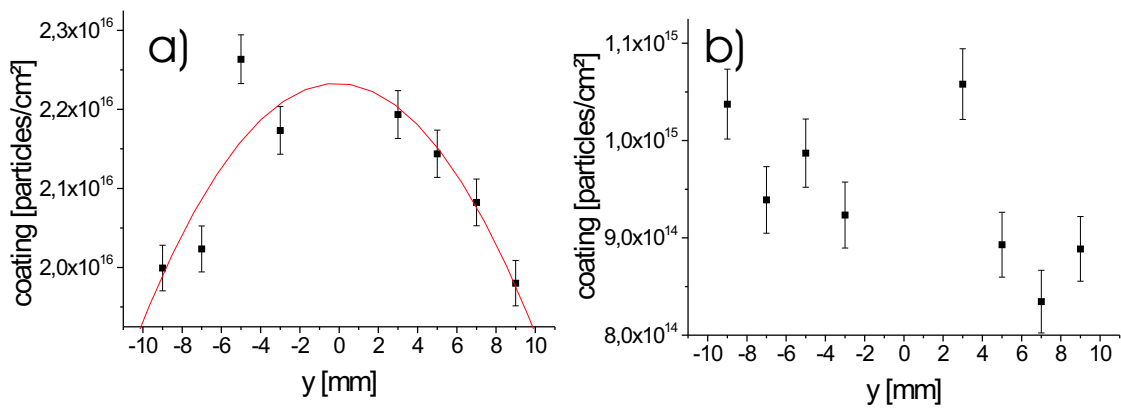


Figure 6.17: a) Copper and b) iodine sputter distribution with flat target.

Table 6.6: Effective sputter yield for flat and wedge targets.

	Flat (sim)	Flat (exp)	Wedges (exp)
Copper (substrate)	2.69 ± 0.02	2.6 ± 0.2	1.7 ± 0.02
Iodine (beam)	0.097 ± 0.001	0.109 ± 0.003	0.094 ± 0.002

The sputter yields for copper compare reasonably well with the sputter yields estimated from the mass loss measurements. The agreement with the solid angle corrected simulation results is almost perfect for the flat target using the plain cosine distribution. The ratio of copper to iodine sputter yield predicted by SRIM2003 was 27.6 ± 0.5 , the experimental value for the flat target is 23.9 ± 2.6 . Iodine sputter yields are in the order of 0.1, for both flat and wedge structure. However, the iodine sputter yield on the wedge target is 8.6% smaller compared to the flat structure, which is not a significant improvement. The increasing sputter factor with inclined angle of impact and the effect of the cosine distribution seem to mostly cancel each other. Therefore, the wedge structure does not provide the expected reduction of sputter yield and new approaches are necessary.

The first idea is to further exploit the wedge structure. As discussed in the previous subchapter, a smaller wedge base is advantageous, but was limited by manufacturing capabilities. A classic razor blade is very similar to a wedge with extremely small base. They are readily available, 22 mm high, 43 mm long and 0.1 mm thick. Therefore two setups with razor blades have been under investigation, with the first exploiting the micro wedge idea, using the cutting edge of the blade as a wedge. In this setup, 50 blades are stacked next to each other, hence this configuration is called Mach50 in the style of another razor blade product. However, the problem with this setup is, that the blades are 22 mm high resulting in an unfavorably large solid angle, because the cutting edge is rather close to the slit. However, a machining of the ultra hard and brittle material was not desirable. Nevertheless, the distance to the catcher material could have been maintained by increasing the depth of the box, but with the future implementation of the slit system at MAFF in mind a 70 mm deep system would not be suitable.

The second razor blade experiment was a stack of 12 blades, with a distance of 0.5 mm in between the blades and accordingly labelled Mach12. This design is based on a solid angle reduction, where the ions passing through the blades will sputter on the copper back and the small opening angle of 1.3° will leave only a 0.7% chance of escape. However, the chance of an incoming particle hitting a razor blade edge is 16.7%, which might dominate over the other factors.

The third setup is taking an entirely different approach to the subject. One of the simulation results has shown, that low target density and high surface binding energies are reducing sputter yield. The element forming the strongest surface bonds is carbon, that is available in various forms, with one of them being POCO [76] foam, which has a density of only 0.4 g/cm^3 and is therefore a good candidate for a very low sputter yield. In addition it has an advantageous open porosity of 58% [26].

Irradiation conditions for all three target configurations are given in Table 6.7. The results of the

Table 6.7: Irradiation conditions for Mach12, Mach50 and POCO targets.

Target	Time	I_{max}	Q_{total}	Collected ions
Mach12	3600 s	$2.8 \mu\text{A}$	$1.22 \cdot 10^{-2} \text{ C}$	$6.78 \cdot 10^{16}$
Mach50	3033 s	$3.8 \mu\text{A}$	$0.86 \cdot 10^{-2} \text{ C}$	$4.99 \cdot 10^{16}$
POCO	3500 s	$3.3 \mu\text{A}$	$1.19 \cdot 10^{-2} \text{ C}$	$6.88 \cdot 10^{16}$

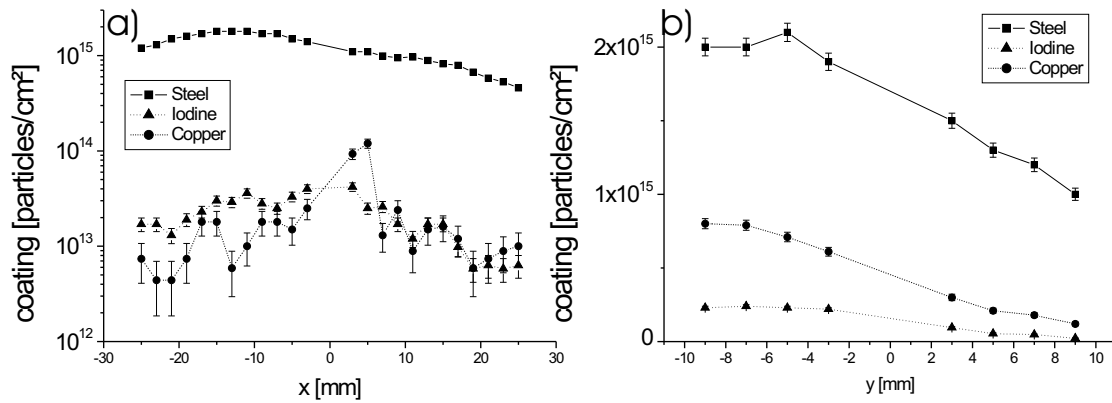


Figure 6.18: Sputter distribution for Mach12 experiment.

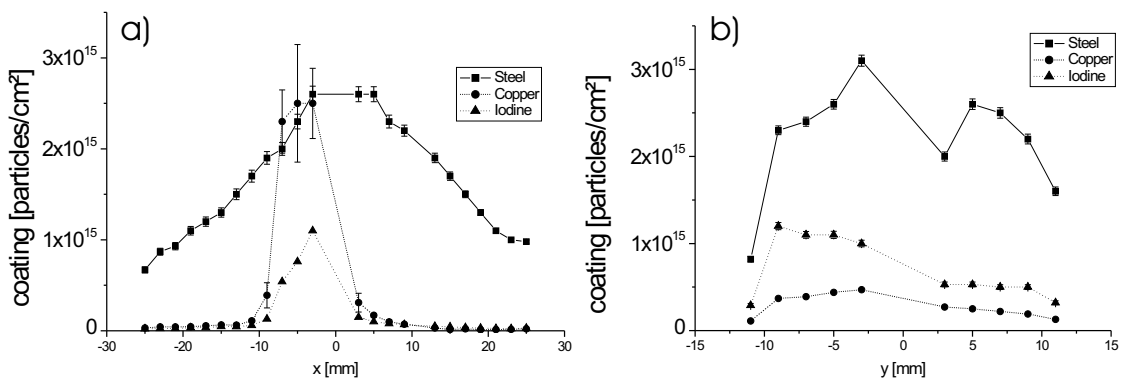


Figure 6.19: Sputter distribution for Mach50 experiment.

RBS analysis for the two razor blade experiments are given in Fig. 6.18 for Mach12 and Fig. 6.19 for Mach50.

Results for Mach12 look very reasonable. The x-distribution, perpendicular to the razor blade stack is symmetric, the vast majority of particles is linked to steel (chrome, iron, nickel), copper and iodine are sputtered significantly less, with copper having a higher peak value than iodine. For y direction, the distribution is not symmetric, which is possibly due to misalignment of the blades or a non central hit of the ion beam, so that one end of the y-direction has been favored resulting in a distribution as seen in Fig. 6.18b). Despite the lack of symmetry it can be seen, that the difference between copper and steel sputtering is approximately a factor of two and much lower than in x-direction due to no solid angle restrictions by the blades.

The surface coating distributions of the experiments with Mach12, Mach50 and POCO target follow no longer a cosine distribution. On account of this a different approach for the determination of the sputter yield is required. In addition it is striking, that in all three samples, the y-yield peaks at a much higher value compared to the x-yield. The missing particles in x have possibly escaped through the entrance hole for the beam. Therefore, for the interpretation of the RBS analysis, the x-yield is normalized and multiplied with the y-yield in a way to form a matrix describing the surface coating all over the silicon wafer. This matrix is shown in Fig. 6.20 for the Mach12 iodine yield.

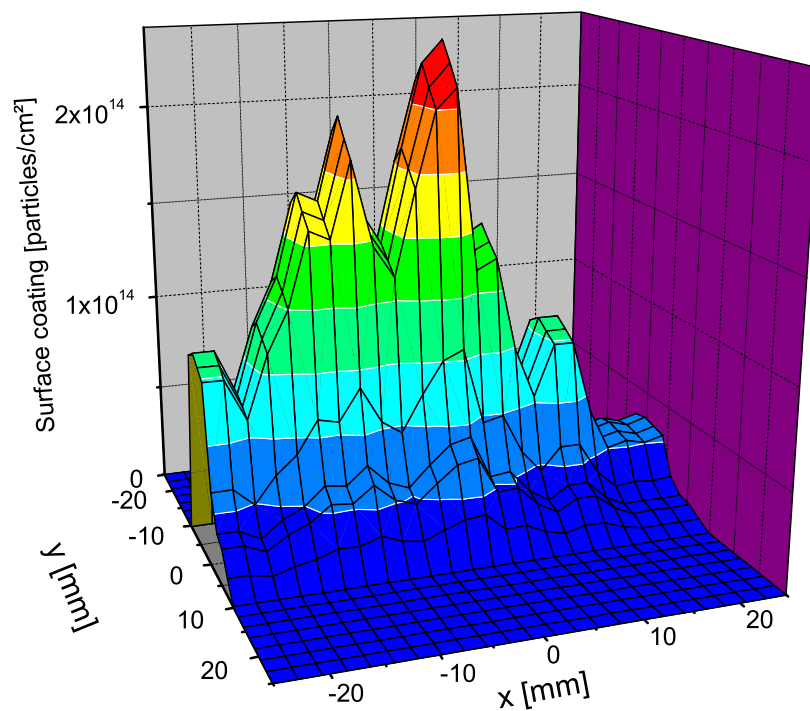


Figure 6.20: Iodine sputter matrix for Mach12 experiment.

The matrix can be integrated to determine the amount of particles collected on the silicon. Integrating the Mach12 matrix gives a result of $6.3 \cdot 10^{14}$ particles. Dividing this by the amount of incoming particles results in a sputter yield of 0.0092 ± 0.0003 , where the given statistical error is very small similar to the previous sputter yields and the systematic error from the current mea-

surement would be about 50%. The same analysis method can be used for the steel and copper sputter yield, giving the results summarized in Table 6.8.

Table 6.8: Effective sputter yields for Mach12.

	Mach12 (expected)	Mach12 (experiment)
Copper (substrate)	0.024 ± 0.002	0.0103 ± 0.0003
Steel (substrate)	0.38 ± 0.17	0.141 ± 0.004
Iodine (beam)	0.007 ± 0.003	0.0092 ± 0.0003

The expectations listed in Table 6.8 come from calculations based on sputter yields obtained from previous measurements or simulations, which have been combined with solid angle restrictions and the reduction expected from the plain cosine distribution.

Also interesting is the sputter matrix for copper shown in Fig. 6.21a), where all sputtered copper must come from the bottom below the razor blades. Five peaks in x direction are clearly visible and two more start forming towards the edges, which does perfectly coincide with the seven expected peaks from a beam spot slightly larger than 3 mm. A spot of that size would cover seven valleys formed by the blades and therefore result in seven peaks with decreasing amplitude from the center. Another strange coincidence of peaks is found in correlation of the copper distribution with the iodine distribution, especially for positive x-values, best seen in Fig. 6.18a). However, there is a strong argument opposing this conjecture: The solid angle limitations by the razor blades do not allow the image of the beam spot area to grow to more than 5 mm diameter and it is therefore more likely, that the structure is formed by chance.

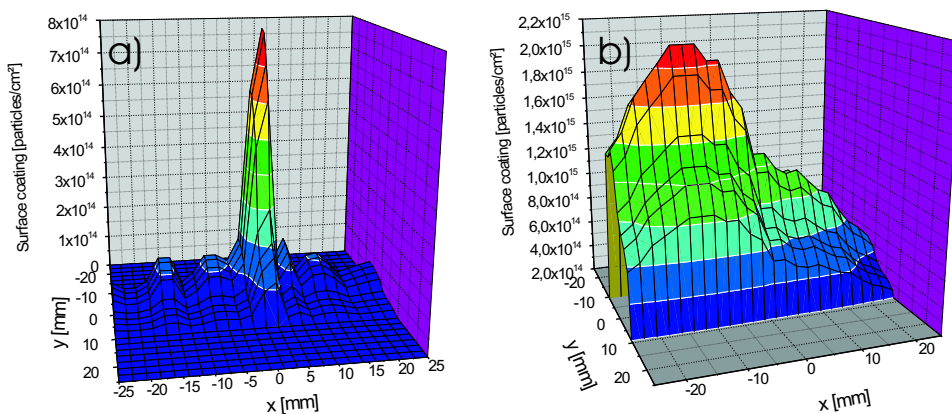


Figure 6.21: Mach12 sputter matrix for a) copper and b) steel. The copper matrix shows a clear substructure with five clearly visible peaks and two more beginning towards the edges.

A projection for the expected Mach50 results can be made from the Mach12 sputter yields. For Mach50, there is no copper yield expected, since the copper surface should not be visible to the beam and the steel sputter yield should increase, because in Mach12 only 16.7% of the surface is steel in comparison to a 100% at Mach50. Therefore, the yield should increase to 0.84. For the same reason, iodine sputter yield should increase to 0.055. However, a detailed analysis of the Mach50 target is more complex, since 15% of the beam, based on a visual impression, missed the razor blade stack. A measurement of the partial beam spot on the copper shows that 17% of the

total beam spot missed the razor blades. This explains why the copper peak is almost as high, as the steel peak and off center by a couple of millimeters. Subsequently, the sputtering of iodine is also enhanced by this effect.

From the flat target a sputter factor for copper of 2.6 ± 0.2 is known, but at the Mach50 stack, the solid angle for the release of copper is only $9.9^\circ \pm 1.4^\circ$. This argument together with the assumed cosine distribution suggests a sputter yield of 0.038 ± 0.014 for copper. Evaluation of the sputter yield analog to the Mach12 analysis reveals a sputter yield of 0.05 ± 0.02 , which is within reasonable agreement with the predicted value, so that the latter value can be used, to determine the percentage of particles collected from the 17% area in question to $1.9 \pm 0.6\%$. Using this percentage and the sputter yield for iodine from the flat target as previously determined, the total number of iodine particles sputtered from the copper surface can be determined to $1.033 \cdot 10^{14}$. Now, this particles can be subtracted from the total amount of sputtered iodine particles ($9.9622 \cdot 10^{14}$) and hence giving the number of iodine particles sputtered from steel. Dividing this by the number of ions hitting the blades gives a sputter yield of 0.022 ± 0.001 . Furthermore, the sputter yield for steel can be calculated by dividing the total number of steel atoms sputtered by the number of ions hitting the steel. The results obtained for the Mach50 stack are summarized in Table 6.9.

Table 6.9: Effective sputter yields for Mach50.

	Mach50 (expectation)	Mach50 (experiment)
Steel (substrate)	0.84 ± 0.02	0.37 ± 0.01
Iodine (beam)	0.055 ± 0.002	0.022 ± 0.001

About the results shown in Table 6.9 two things are unexpected. The sputter yields are smaller than expected, but are within systematic errors, that come from the current measurements with a faraday cup, which should be accurate to approximately 50%. The smaller sputter yields can possibly be explained if the steel alloy used for the razor blades has better sputter properties compared to iron. Also the micro wedge structure of the razor blades can play a role but not to this magnitude. Solid angle arguments ($\omega = 33^\circ$) and sputter factor increase with inclined surface (86°) should lead to worse results compared to the wedge structure. This assumptions was confirmed with SRIM2003, resulting in a sputter yield increase by a factor of 6 for hardened steel (66% Fe, 14% Cr, 18% Ni, 2% C).

The second interesting fact is, that iodine sputter yield is in the order of the Mach12 experiment. After correcting for the solid angle disadvantage, which gives a factor of two, since the Mach50 edge is 18 mm away from the opening but could have been 40 mm if the blades would have been cut, the two results are similar. This is not that surprising after the projections from the Mach12 experiment, but yet another hint on the possibly superb sputter properties of the alloy used for razor blades.

Finally, the RBS analysis of the POCO target is shown in Fig. 6.22, indicating very promising results. The amount of iodine found on the silicon wafer is close to the detection limit of the RBS setup. Hence, the gathered statistics are small and only positive x- and y-axis have been scanned resulting in the symmetric figures. Furthermore, a measurement of the carbon coating of the silicon wafer cannot be done to a reasonable accuracy with RBS. As with the copper target, seven peaks can be counted in Fig. 6.22a). No link to any geometry can be constructed for the POCO target which makes it even more likely that the structure is an artefact caused by the RBS analysis.

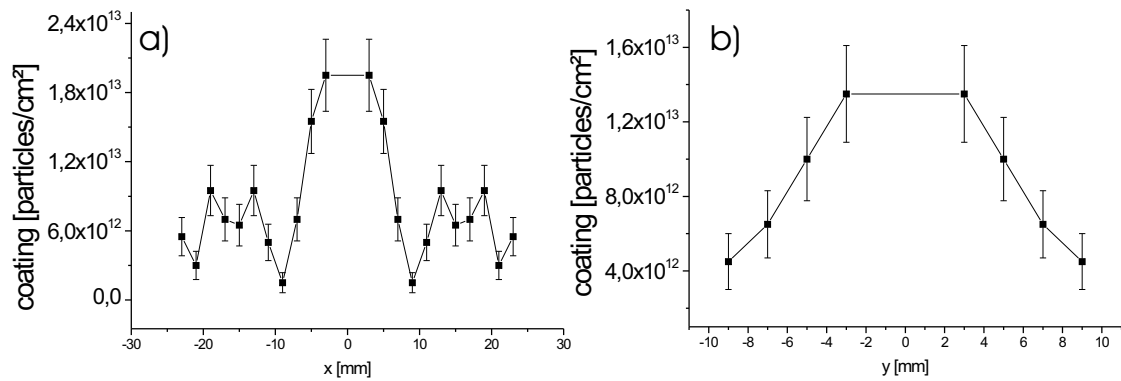


Figure 6.22: Sputter distribution of POCO target for iodine in a) x- and b) y-direction.

Using the same integration method as for the Mach12 and Mach50 targets results in $4.668 \cdot 10^{13}$ collected particles. Dividing by the ion current gives a sputter yield of $6.8 \pm 1.8 \cdot 10^{-4}$ and is therefore below the envisaged sputter yield of 0.1%. The iodine sputter yields for all tested target materials are summarized in Table 6.10.

Table 6.10: Summary of effective iodine sputter yields for all tested target materials.

Target	Iodine sputter yield
Flat	$(1.09 \pm 0.03) \cdot 10^{-1}$
Wedges	$(9.4 \pm 0.2) \cdot 10^{-2}$
Mach12	$(9.2 \pm 0.3) \cdot 10^{-3}$
Mach50	$(2.2 \pm 0.1) \cdot 10^{-2}$
POCO	$(6.8 \pm 1.8) \cdot 10^{-4}$

6.3 Conclusion

In conclusion it can be found, that the low density carbon foam clearly outperformed the structures based on geometric considerations and should be used for the construction of the slit system. Simulations performed with SRIM2003 hinted already in this direction and are supported by this result. Therefore, it can be expected that the use of lower density carbon materials will further reduce the sputter yield as shown in Fig. 6.23, where the dependence of carbon sputter yield on the carbon density for incoming 30 keV iodine beam is plotted. Since the correlation is linear, a gain of a factor 2 in density will lead to the same change in sputter yield. Therefore, it can be stated, that the sputter yield measured for the POCO foam is probably the best, that can be achieved with a reasonable material. Subsequently, a sputter yield reduction by a factor of 10.000 or more seems not likely from today's point of view.

More elaborated geometric considerations, e.g. a pincushion, extending the razor blade idea in 2 dimensions are tempting to try, but are not as promising as the carbon foam. From the various carbon foams available POCO has been chosen because it was already in stock from past studies and offered a low density. However, for the construction of the slit system another foam of similar density but better machining properties will be advantageous.

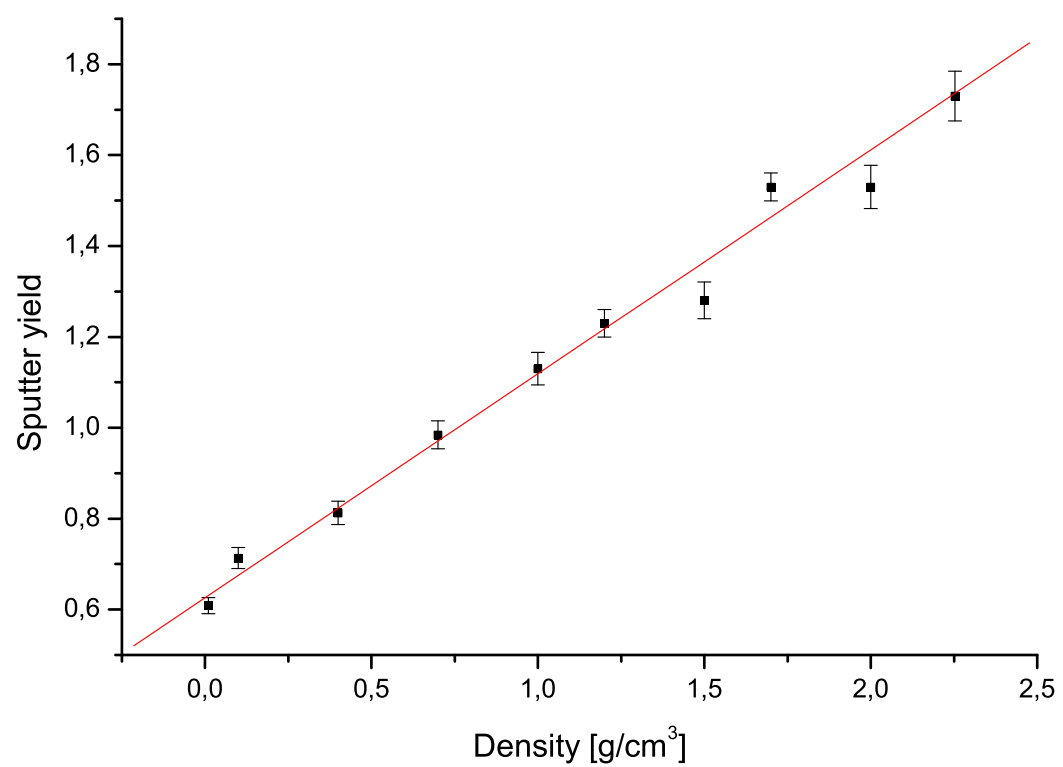


Figure 6.23: Sputter yield for carbon depending on carbon target density. Density of POCO foam is 0.4 g/cm^3

7 Technical investigations

This section is devoted to the technical investigations of several MAFF components undertaken in the past years. During this time two key components considered crucial for the realization of MAFF have been build and tested. At first the electrostatic quadrupole triplet was investigated as the primary ion optical element, which is therefore of central importance for the beam transport. Also, the mass of the first triplet in the lens trolley defines the bending of the beam tube due to gravitational influence. Secondly, the endeavor of constructing one of the trolley prototypes has been undertaken, where the feasibility of many concepts has been studied.

7.1 Quadrupole triplet

In addition to the ion optical requirements, elaborated on in Chapter 3, the quadrupole lenses must be temperature resistant up to 600 K and operate under strong neutron and gamma radiation, with the latter two requirements being especially true for the first triplet very close to the source.

7.1.1 Design specifications

The requirement for a mass-reduced design of the triplet is met by using a low density metal as well as reducing the triplet to the minimum amount of components with spare material taken off wherever possible. This leads to a layout of the pole shoes with circular surface as shown in the technical drawing in Fig. 7.1 and the photograph of the triplet prototype in Fig. 7.2. It can be seen, that the different pole shoes only vary in length, with the middle quadrupole being 15 cm long and the others 10 cm.

The maximum temperature, that the triplet can withstand, is limited by the electrical insulators, where macor has been used for the prototype, which is a machinable glass ceramic of various compounds (46% SiO₂, 17% MgO, 16% Al₂O₃, 10% K₂O, 7% B₂O₃, 4% fluorides), that slowly loses its insulating properties until it becomes conducting at temperatures of ≈ 1300 K. In account of that it will be replaced by Al₂O₃ in the final version, which is even more temperature stable. The metallic parts of the triplet prototype are constructed from aluminum and weight 2.2 kg. To achieve a higher temperature stability, the first triplet (expected operational temperature 600 K) will be constructed from titanium (melting point $T_{Ti} = 1941$ K compared to $T_{Al} = 933$ K) with a mass of less than 3.7 kg if the higher elasticity of titanium compared to aluminium is utilized and less material is used. Neutron induced activation is not a problem for either material, since only short lived isotopes can be produced. The five stable Ti isotopes have only small neutron capture cross-sections (0.18 b to 7.9 b), the first β^- unstable isotope has no known neutron capture properties and decays with a half-life of 5.8 min to stable ⁵¹V, with in turn low neutron capture cross-section (4.9 b). Following the capture chain upwards, the first unstable and long lived isotope found is ⁵⁹Fe after 9 consecutive neutron capture and β -decay processes. The situation for aluminum is similar. It has a low neutron capture cross-section (0.23 b) as well and the resulting isotope has no known neutron capture cross-section and decays to stable silicon, which

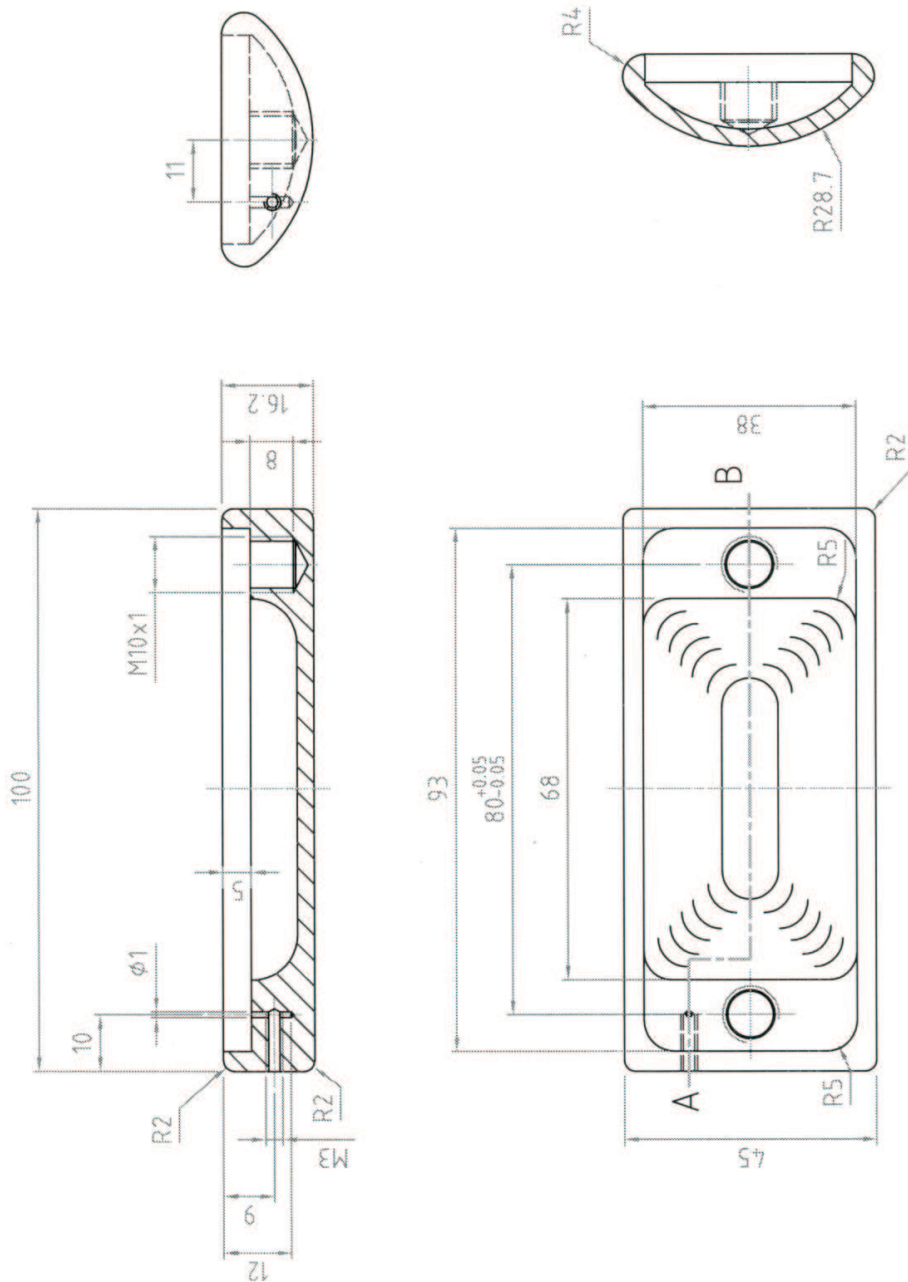


Figure 7.1: Technical drawing of the triplet prototype pole shoe. Pole shoes for the outer quadrupoles are identical, the middle one is 15 cm long. The pole shoes are hollowed out as much as possible for weight reduction.

is a common part of aluminium alloys. The first long lived unstable isotope reached is ^{32}P after 5 consecutive neutron captures and β -decays, but ^{32}P decays without γ -rays. The first γ -radiator created after this is ^{38}Cl , with a half-life of 37.18 min, requiring 11 capture and β -decay processes. Activity coming from oxygen (in Al_2O_3) is small due to the low amount of oxygen in the material and the very low neutron capture cross-section of ^{18}O ($160 \mu\text{b}$).

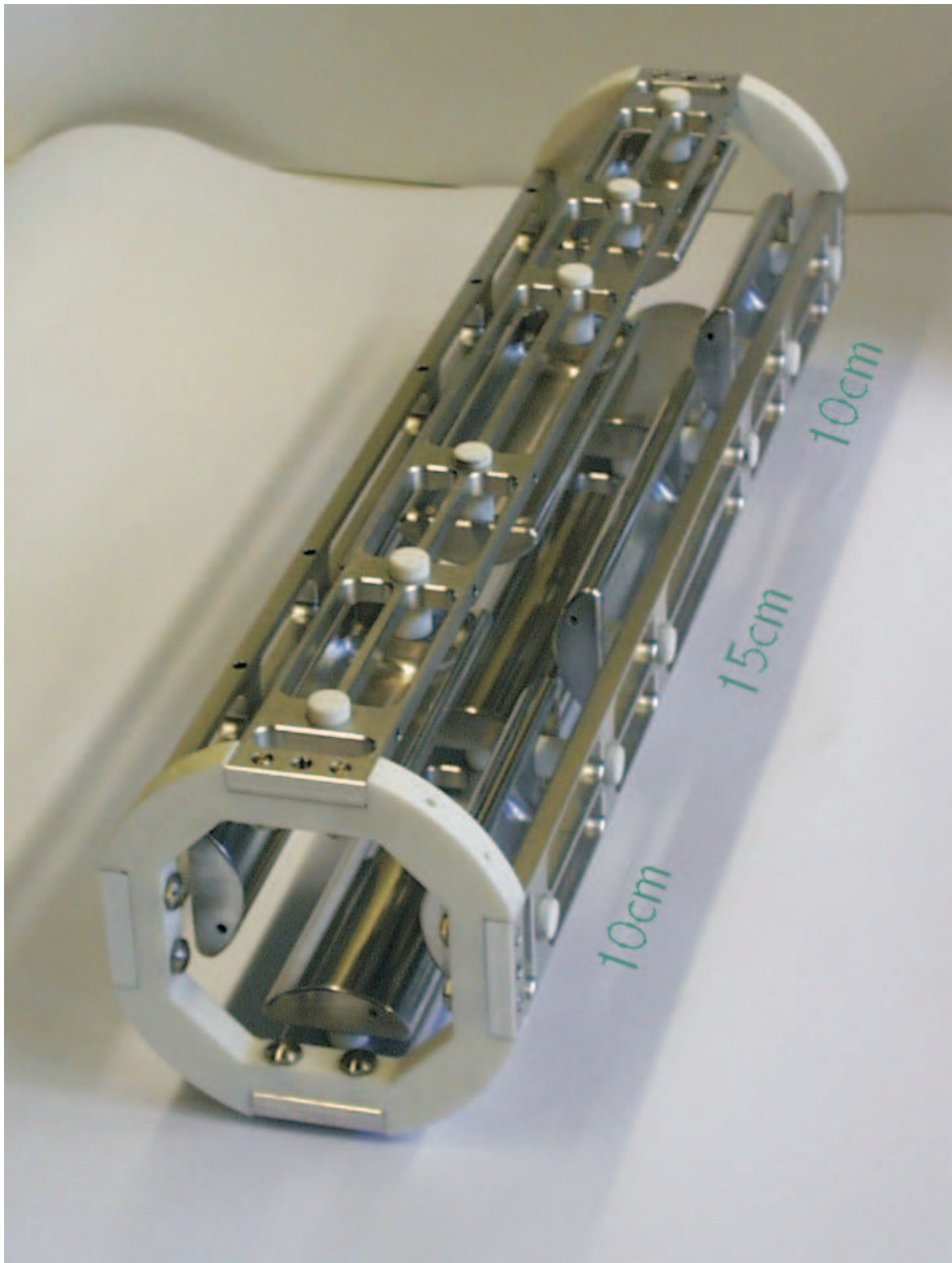


Figure 7.2: Picture of the assembled triplet prototype, where the consequently applied lean design and different pole length can be seen.

Mechanical alignment of the triplet is done by eight set screws, four at each end of the device. Wires for the electrodes are also connected by set screws, but no cable guides are included in the prototype.

7.1.2 Tests

The tests of the triplet have been performed at the MLL ion source test facility, with a 30 keV copper beam, in an experimental setup shown in Fig. 7.3, where the quadrupole triplet is followed by the emittance measurement unit (EMI) or a phosphore screen placed behind a glass viewport. Among the tested subjects are several mechanical and ion optic properties:

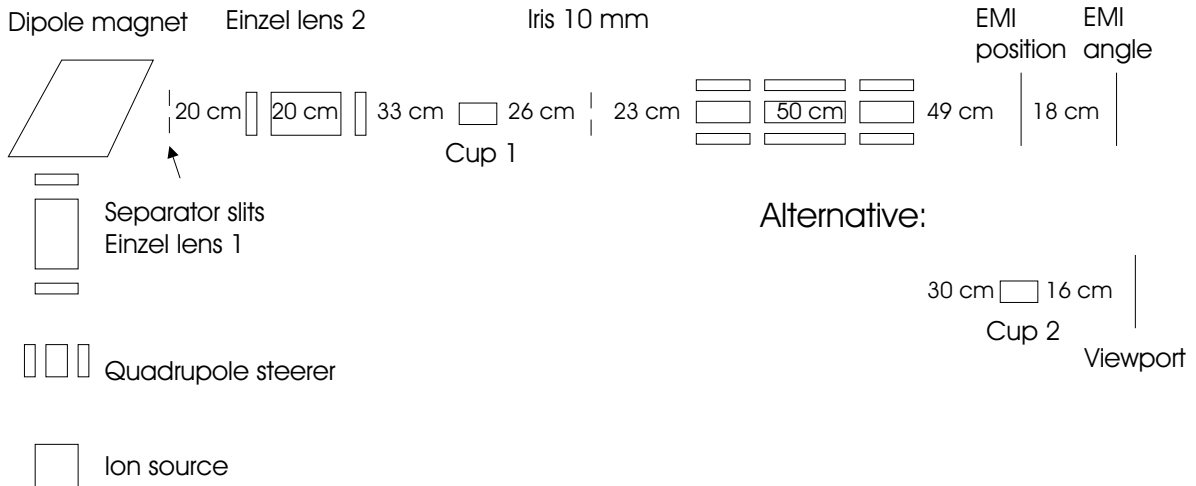


Figure 7.3: Schematic setup for the triplet test. Two alternative beam observation systems have been available for visual observation and emittance measurement.

1. Alignment of the triplet electrodes
2. Mounting of the triplet in the beam tube
3. Electric connection of the electrodes
4. Electric feedthroughs
5. Steering capabilities
6. Offset correction
7. Emittance growth
8. Focus shape

The triplet was cleaned and assembled with special attention towards the alignment of the electrodes. Assembly went smooth, without any free play at the macor aluminium interfaces. However, the brittle insulator material handles stress rather poorly and tends to break easily if some force is applied. The friction force between macor and aluminum was quite strong so no screws would have been necessary to hold it together. All twelve electrodes can be adjusted separately. To get them well aligned, an acrylic glass rod with 5 cm diameter was inserted and the electrodes were fixed in place along the rod, which was centered by a centering device. The electrode insulators also had no play, which was advantageous, since this play also limits the accuracy of the alignment process.

The 50 cm long triplet was centered into a 80 cm long DN150 tube and transverse alignment was done using the set screws. However, access to the screws was already tricky with the relatively

short tube, and is very likely impossible for a longer tube, as foreseen in the final setup. It was tried to confirm correct transverse alignment by measuring the electrode distance to the walls, which was rather complicated as well and hindered by the restricted space in the tube. Final alignment was exact to approximately ± 1 mm. For future alignment some appropriate crosshairs should be available for perfect optical alignment. Also, for the final setup on the lens trolley, transverse adjustment with setscrews will no longer be feasible and standard screws should be used instead to adjust the position from outside of the beam tube, which requires eight threads in the correct positions of the beam tube. This comes with the additional advantage, that the triplet is fixed in place.

The electrical connections for every electrode needed to be placed. Since the triplet design does not incorporate any wiring, an improvised wiring was used. For the future it would be best to go directly from the triplet to the outside of the beam tube, where cable guides are foreseen. As in the simulations, the central quadrupole was connected individually, while the electrodes of the outer quadrupoles are connected in pairs (bottom-top, left-right), which required eight individual power supplies.

Voltage feedthroughs into the vacuum system are needed to connect the electrodes to the power supplies. When the tests were performed it was still assured that high pressure resistant feedthroughs for MAFF are required, which can stand up to 6 bar. The feedthroughs used and tested here are specified for this pressure. Unfortunately the largest multi-feedthrough available at the time had only seven connectors, hence requiring two of them, one placed on each side of the triplet. The allocation of connectors is given in Fig.7.4, where the feedthrough labelled with A has connectors for the nearest and central quadrupole, while the unlabelled second feedthrough, referred to as B connects the remaining quadrupoles. These special feedthroughs come with special cables and connectors as well, so it was necessary to built an adapter box for the connection to the power supplies.

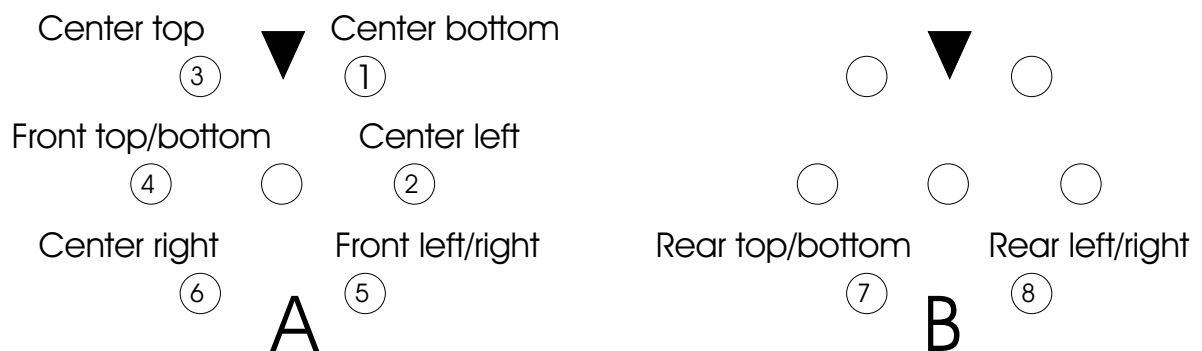


Figure 7.4: Allocation of connectors for the triplet prototype test. The black arrow marks a groove at the connectors.

The feedthroughs and corresponding connectors are rigid and worked reliable, no handling problems have been encountered. However, on the vacuum side contacts are very close to each other and some care was required to avoid short circuits.

The four ion optical tests were performed in a series of over 300 emittance measurements. The EMI (device for the measurement of beam emittance) used was build in an earlier thesis [77], but nevertheless lacked a manual, which has been written as Appendix A of this thesis and represents the status of the device at the time of the experiments. The EMI's principal of operation is straight forward: First a parallel deflection of the incoming beam is made followed by a 0.1 mm wide slit. The deflection voltage is related to the parallel offset, allowing the determination of the x or y position. Behind the slit is another single deflector for an angular deflection followed by a second

0.1 mm slit and a Faraday cup. From the voltage at this deflector the angle can be determined and related to the cup current. The position of the slits is marked in Fig. 7.3. Either x or y emittance can be measured by turning the setup by 90° .

The triplet tests were performed in parallel to the tests of a new ion source. Some tests with the ion source, using a phosphorus beam, were performed before the triplet tests could start. The ion source test showed, that the emittance of the ion source depends on the extraction voltage, and was best for 6 kV. Also the relative position of the source material to the extraction electrode was influencing the emittance as shown in Table 7.1. From this point on, the 8 mm position was used. However, burn-up of target material, over 18 days of source operation, resulted in a subsequent slow emittance increase.

Table 7.1: Beam emittance is influenced by the relative position of the source material to the extraction electrode.

Target distance	Emittance
8 mm	32π mm·mrad
10 mm	53π mm·mrad
12 mm	82π mm·mrad

The first measured property of the triplet was the transmittance. For this purpose, the alternative setup with the second faraday cup behind the triplet was used. The beam current was maximized on cup 1, by adjusting the focus of the second einzel lens. In a second step the triplet voltages were adjusted in order to maximize the current on cup 2. The currents on cup 1 and 2 were measured to $1.8 \pm 0.9 \mu\text{A}$ and $2.3 \pm 1.2 \mu\text{A}$, respectively. Uncertainties for the ion current are very large, since the cups were not equipped with secondary electron suppression. However within the error margin the transmittance could be as high as 100%. The voltages used to achieve the transmission were 20 V/1111 V/850 V.

It is striking, that the voltages applied to the first quadrupole are almost zero, which is related to the beam offset. Due to some inevitable misalignment between the beam axis and the triplet axis the beam enters the triplet at some not well defined position, leading to a severe deflection of the beam if some significant voltage was applied to the first multipole. Cross checking with SIMION simulations showed, that a deviation of 1° over the given distance leads to similar results. The observed effects of the three quadrupoles (QP1 to QP3) are:

QP1: Negligible y focusing, strong y steering.

QP2: x focusing, very strong y defocusing

QP3: y focusing

Two conclusions can be drawn from these results. Firstly, it is possible to correct an unknown beam offset due to misalignment. Secondly, the center quadrupole might not be the best choice for steering. In this case steering on the first quadrupole would have been favorable. Therefore, the final layout should offer the option to connect the steering power-supplies to any of the quadrupoles. However, steering on the first quadrupole could not be tested in this setup because the EMI had to be returned to CERN.

In the next step it was attempted to achieve a point to point focusing. The idea was to create a focus at cup 1 using einzel lens 2. Afterwards, the triplet is used to create a focus as small

as possible on the phosphor screen. With triplet voltages of 50 V/600 V/510 V a small focus with $x=3$ mm and $y=1$ mm was achieved, which is not a round focus, as expected from a triplet. However, this is of little concern, since two einzel lenses are manipulating the beam before the triplet. Tests with the deactivated triplet showed, that it is impossible to get a round beam from the einzel lens to start with.

Emittance measurements with the point to point focus showed an emittance of 20π mm·mrad for the activated and five times more for the deactivated triplet. This can only be explained if the transmittance through the triplet is not 100%. For the case of a point to point focusing this assumption could be confirmed. The faraday cup has an active diameter of 25 mm, allowing only a very coarse focus. The beam grows from here on and illuminates the majority of the triplet rather soon until it is cut towards the end by the electrodes of the last quadrupole, where it left physical beam marks. The effect is possibly enhanced by the offset, and the following y defocusing in the second quadrupole. This would suggest a cut in y -direction, which is also supported by the shape of the focus.

At this time, the iris has been introduced to get a parallel, well defined beam. With deactivated triplet a 1:1 image on the phosphore screen was achieved. For triplet voltages of 100 V/200 V/200 V parallel to parallel imaging could be reached. For slightly higher voltages 100 V/300 V/300 V some focusing was possible, while higher voltages again lead to beam losses. Emittance pictures with activated and deactivated triplet for the latter set of voltages are shown in Fig. 7.5. At a later time in this test series extensive emittance measurements were conducted leading to an emittance of $40.4 \pm 0.4 \pi$ mm·mrad for deactivated triplet and $45.0 \pm 0.8 \pi$ mm·mrad with triplet. The emittance increase of $11 \pm 3\%$ is most likely due to standard quadrupole aberration and compares well with the results observed in the SIMION simulations.

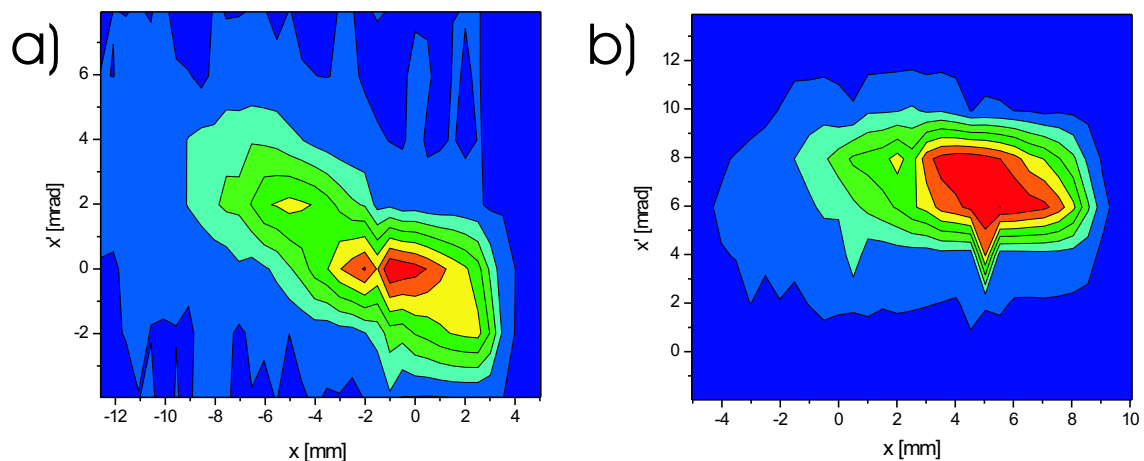


Figure 7.5: Measurement of the emittance growth caused by the triplet. With the activated triplet b) the phase space distribution is more compact and smoother, but also covers a larger area than in the case a) where the triplet is deactivated. The increase in emittance is due to standard quadrupole error and agrees well with simulations.

In conclusion the triplet works within the expectations even with a beam offset, however, some improvement is still needed. The capability to align the triplets within the beam tube should be added during the re-design. The electric wiring can be perfected and steering possibilities should be made available for each quadrupole.

7.2 Lens Trolley

Lens and source trolley are the heart of the MAFF I setup enabling the production and extraction of rare isotopes. Both trolley are similar in design, especially concerning the trolleys bodies and the traction system. A failure of this system could result in a trolley blocking a safety valve, which is not tolerable. Therefore the traction system of the trolley and everything related, like the adjustment system for the trolleys and the lock for securing the trolleys in their final positions, must be well designed and tested.

Along with the trolley comes a supporting structure. It is planned to use the supporting structure, lens trolley and parts of the traction system later on in MAFF, if the tests proof successful. To avoid concerns from the TÜV, detailed material tracing has been performed for all crucial components.

7.2.1 Design specifications

General requirements

As with many other components, the trolleys must be rigid and operational after a hazardous incident. They are placed within the reactor walls and will be activated by thermal neutrons. The body of the trolley, which is under investigation, is manufactured from stainless steel with a very low cobalt content. With respect to neutron activation steel is less favorable than aluminum or titanium, since ^{58}Fe with a natural abundance of 0.28% can be converted to ^{59}Fe ($\sigma=1.3$ b), which has an intermediate half-life of 44.5 d.

Safety regulations demand, that the trolley and the support structure are operational after a hazardous incident. The definitions of a hazardous incident, such as an air plane crash or an earthquake, require the components to withstand additional acceleration forces of 10 m/s^2 in any direction, which will be achieved by appropriate dimensioning of the structures.

Supporting structure

An overview of the planned prototype is given in Fig. 7.6. The supporting structure is constructed from standard steel. Profiles for slot nuts are used on top and bottom to connect the stilts. Those profiles have an unified structure, well suited to mount additional equipment, e.g. cable trays or compressed-air piping. The support structure can be bolted to the ground by two screws on either side of the stilts, also two additional counter screws are available to level the structure.

Propulsion system

Since nothing can be connected to the through going beam tube SR6 itself, all equipment must be installed on the trolleys. To move them in and out, e.g. for repairs or exchange of the ion source, a reliable and vacuum compatible propulsion system is required. Part of the propulsion system is mounted on the trolley's body, which is made from stainless steel and will be loaded with lead blocks, to simulate the additional weight of the lead shielding. Also a standard stainless steel tube (139.7 mm outer diameter, 3 mm wall thickness) will be mounted on the trolley's body to simulate the weight reduced beam tube. During its movement, the trolley is supported by eight rolls and a guiding channel at one end, simulating the guide in the reactor plug. A drawing of the rolls installed in the Breaker-plate-section is shown in Fig. 7.7. One roll guides the trolley and prevents transversal movement, while the second roll has no restriction in transverse movement

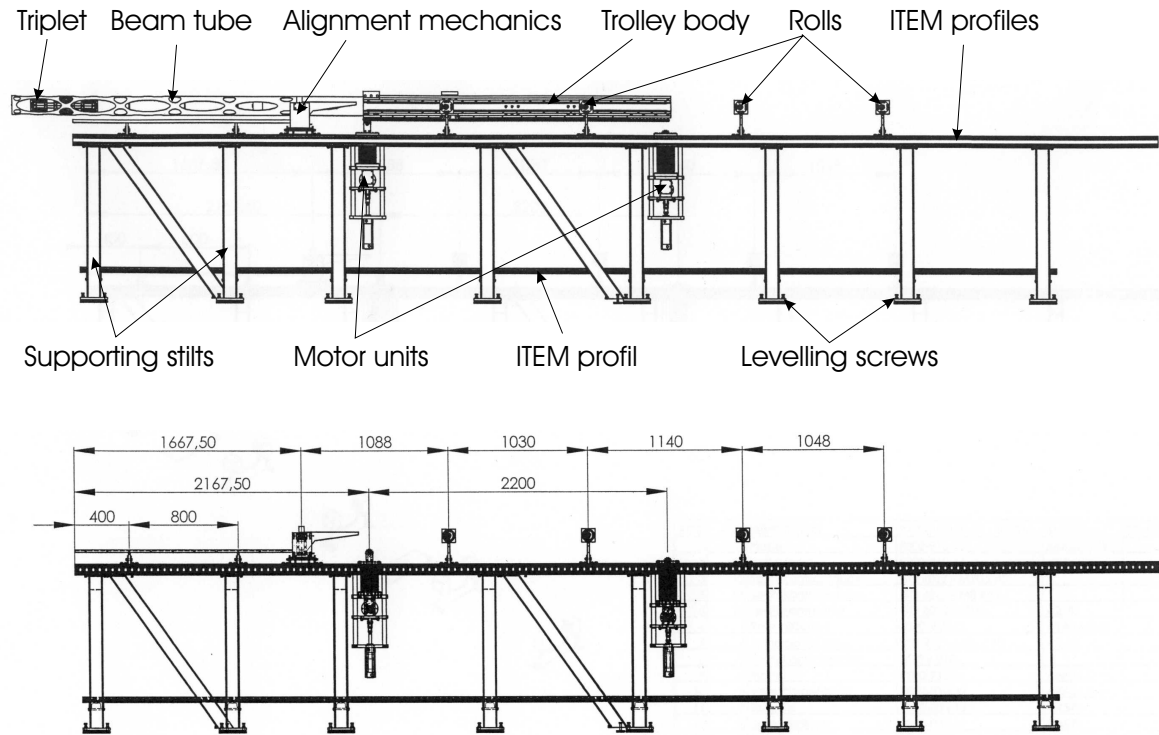


Figure 7.6: Test setup for the trolley prototype. The supporting structure is the same as in the original layout. All motor units and rolls are at the original place.

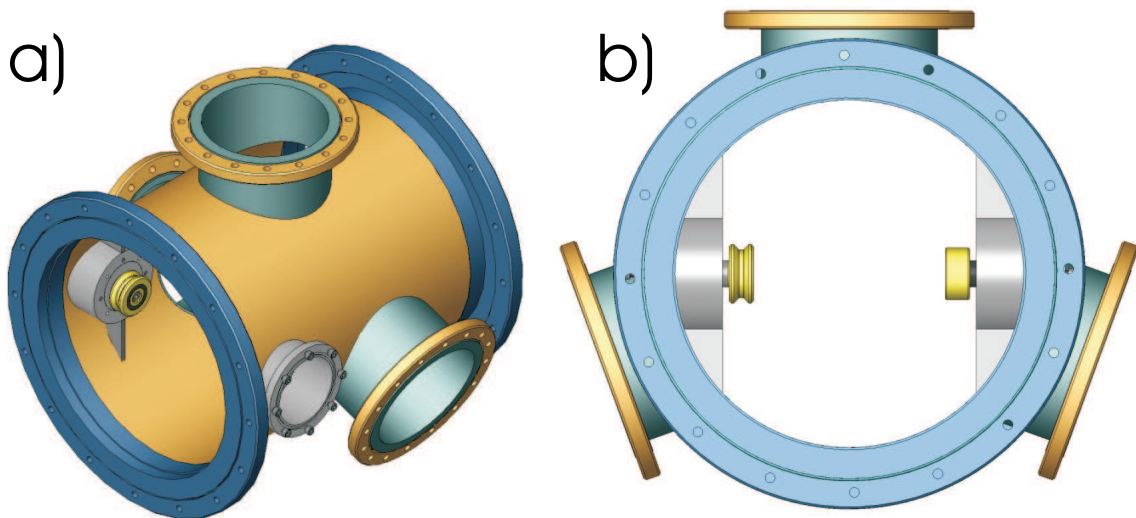


Figure 7.7: Breaker-plate-section with integrated rolls for the trolley.

and is for support only. Therefore accurate alignment in transverse direction is only necessary for one roll.

To move the trolley, cog wheels of the motor units engage a chain, mounted on the bottom of the trolley's body, and move the trolley. Two kinds of motor units have been used in this investigation, a retractable and a fixed one. The retractable units, as shown in Fig. 7.8, are advantageous closest to the reactor, where neutron capture might activate the cog wheels extending into the beam tube. Further downstream, where neutron induced activation is no problem anymore, the simpler fixed units might be more reliable and cheaper. Special problems arise for the motor units in combination with the safety requirements, since they require a mechanical vacuum feedthrough from the electric

motor on the air side to the cog wheels on the vacuum side. On account of this, a special coupling solution is required, which offers a safe and reliable vacuum feedthrough. Currently there are two solutions under investigation. The first, a magnetofluid coupling, is using a persistent shaft pivoted by a magnetic fluid, which in turn is restrained in its movement by magnetic fields from permanent magnets. Every magnetofluid coupling has a redundant barrier system guaranteed to withstand several bars of overpressure. As a more expensive alternative, a magnetic coupling can be used to transmit the moment of torque from the air-side to the vacuum-side, which are completely separated. This has the disadvantage that the transmitted moment is limited to 10 Nm by the strength of the magnetic coupling, which is, however, sufficiently high.

A third option is the *tumbling bellows sealed rotational feedthrough*, as outlined in Ref. [78], which is using bellows as a vacuum seal. While this system is absolutely radiation resistant it has the disadvantage of stressing the bellows with a transversal motion, hence increasing the risk of spontaneous failure.

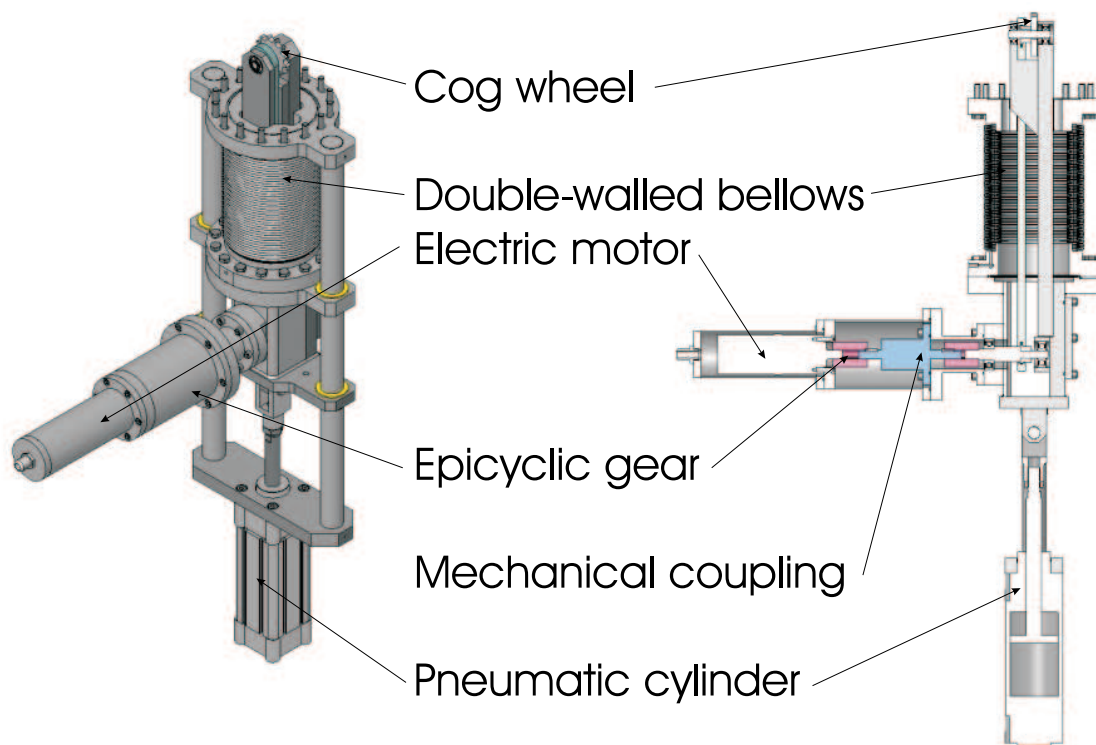


Figure 7.8: Schematic drawing of the retractable motor unit, which has a retractable cog-wheel, while the other tested motor unit is non retractable.

Adjustment system

The purpose of the adjustment system is to position the inserted trolley relative to the surrounding beam tube. Exact positioning of the trolleys is required to align both, source trolley and lens trolley, to each other. From the inner diameter of the SR6 (155 mm) and the outer diameter of the lens trolley beam tube (139.7 mm) a maximum displacement for the tip of the trolley of ± 7.6 mm can be calculated. Consequently, the adjustment system has been designed to achieve a displacement of up to ± 8 mm.

The adjustment system, consists of two parts. First, there is the forward point of support consisting of two ball-bearing-supported balls at the front end of the body, on which the body rolls through the reactor plug. With the actual adjustment system at the rear end of the trolley, as shown in Fig. 7.9 and 7.10, the trolley can be moved in horizontal and vertical direction.

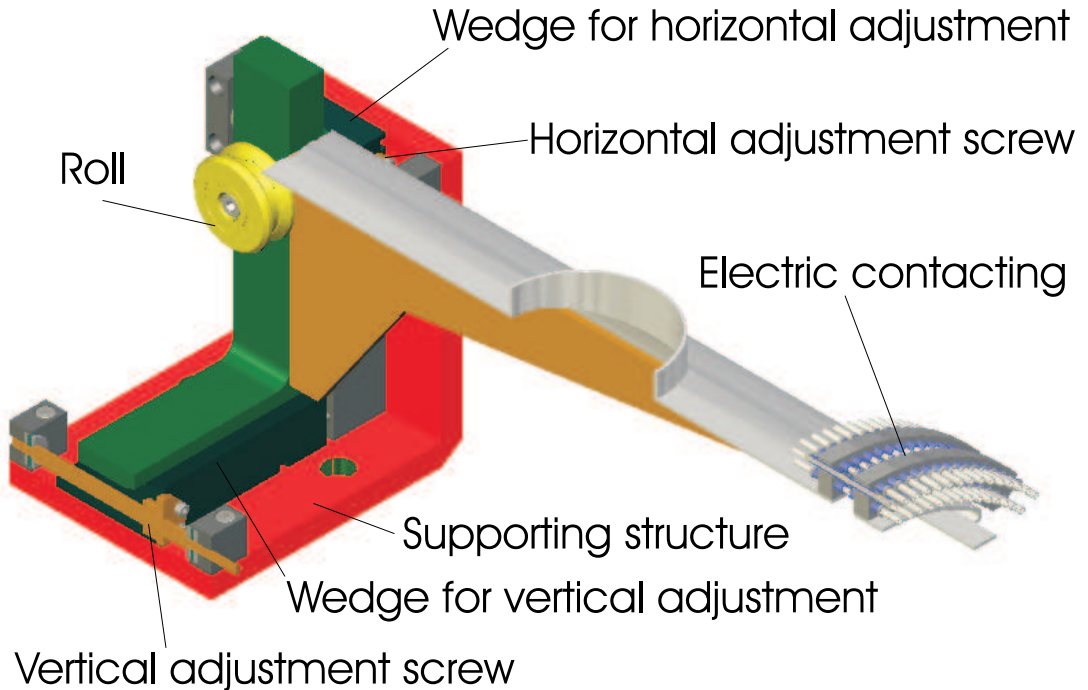


Figure 7.9: Technical drawing of the adjustment system. A small movement in vertical or horizontal direction is translated, by the long lever, into a larger movement of the trolleys tip.

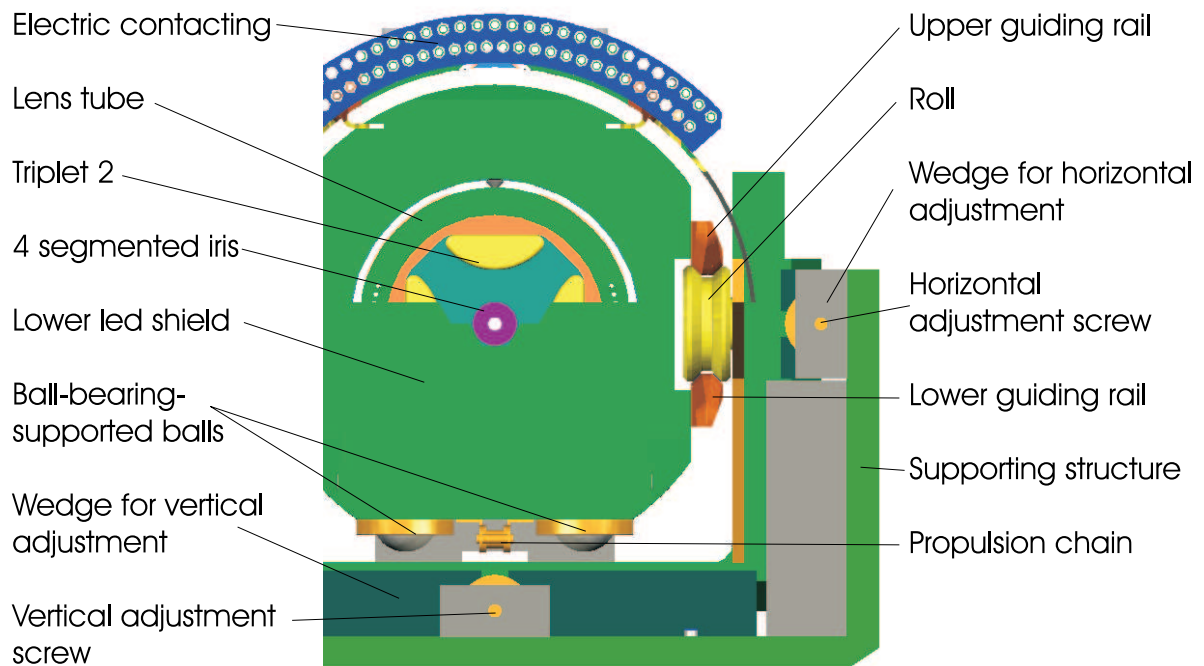


Figure 7.10: Cut through the adjustment system including the lens trolley. The rails mounted on the trolley roll on rolls installed in the adjustment system, while a second support is given by the ball-bearing supported balls.

The horizontal and vertical displacement is achieved by wedges, adjusted by fine thread screws, which are manually operated in the test setup, but can be coupled to a motor for remote operation. The wedges convert their longitudinal motion to a transversal movement of the trolley body, which is pivoted around the fulcrum resulting in a much larger movement of the trolley's tip in the opposing direction. Thus a small change at the adjustment system is translated by the long lever to a larger change at the tip of the trolley. This kind of angular adjustment of the trolley is ideal to compensate a downward bend of the beam tube mounted on the trolley, although a parallel displacement capability would be favorable to compensate an offset between both trolleys. However, if excellent manufacturing precision is achieved for the in-pile components, the tube bending is considered the dominating problem for the alignment of the trolleys.

Electrical connection

The ion optical components and beam diagnostics elements mounted on the lens and source trolley require power connections. While on the source trolley only five connectors for voltages of 200 to 30,000 V are needed, the lens trolley must be equipped with 52 connectors suited for voltages of up to 2000 V. Therefore, the investigations within this work have been focused on the more complex lens trolley connectors, which are shown in the technical drawing of the proposed solution in Fig. 7.11. The connectors mounted on the trolley are fixed, while the ones on the adjustment system are spring loaded.

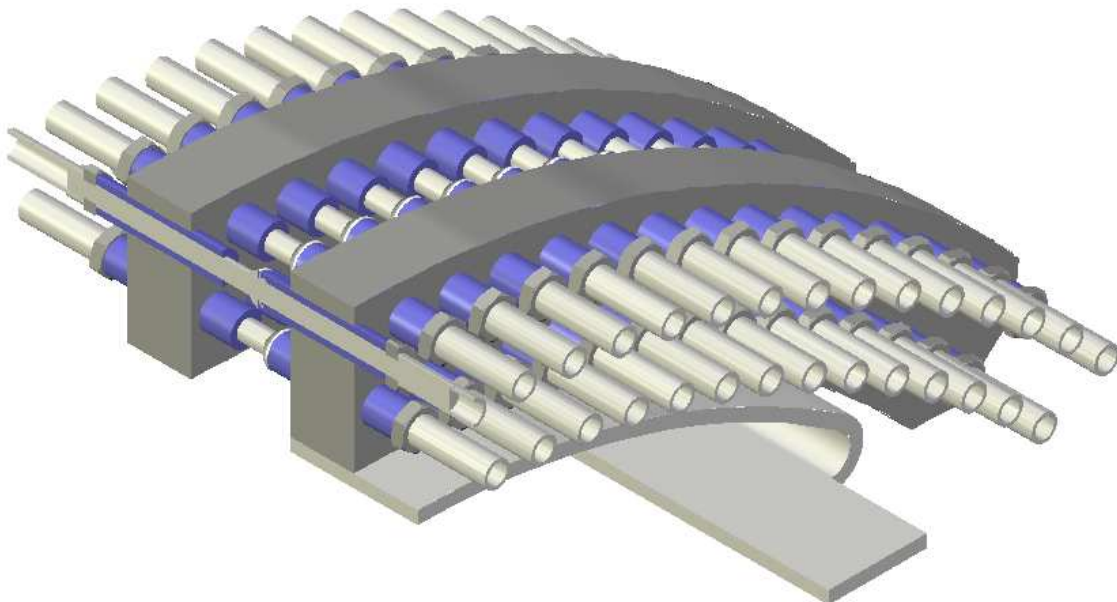


Figure 7.11: Technical drawing of electrical connectors. 52 steep pins are pressed on an equal number of spring loaded pins.

Each array consists of all equal pins, as shown in the close up technical drawing in Fig. 7.12, made from steel. In the final version the pins will be coated with gold to reduce surface degrading. In addition the tips of the pins are round allowing to compensate small misalignments between the trolley and the adjustment system.

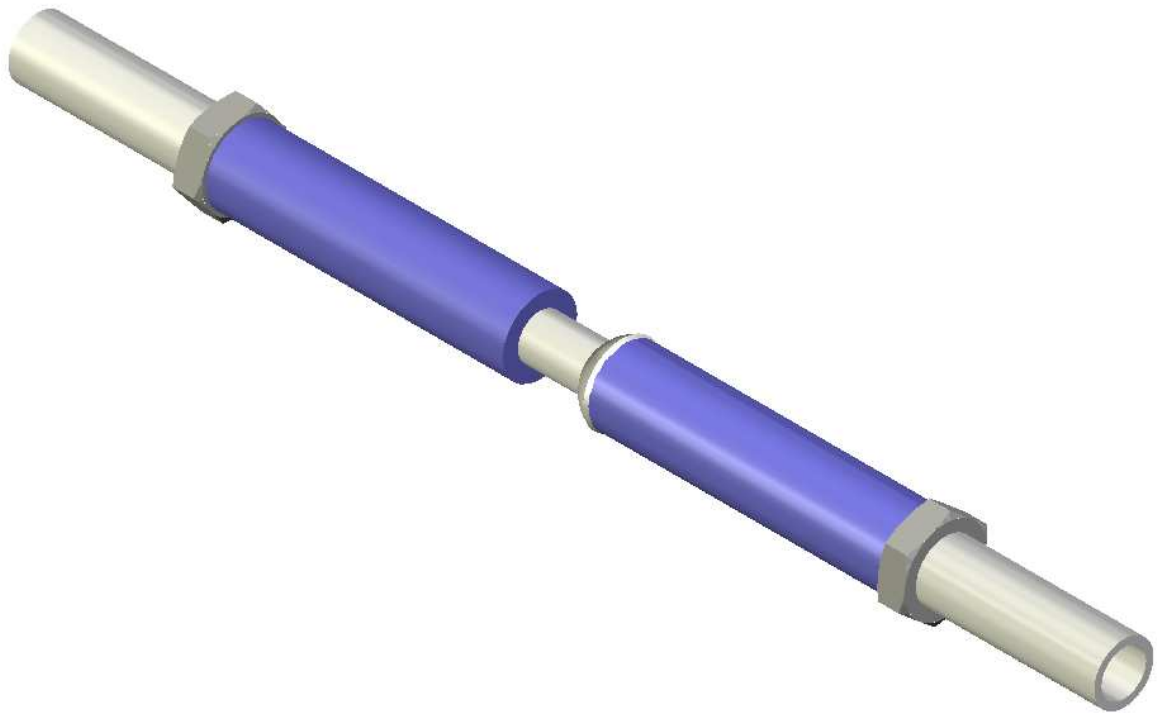


Figure 7.12: Close up view of a pair of connectors. The tips of the connectors are round to be able to compensate small misalignments.

Locking system

During operation of the reactor it must be ensured, that either trolley cannot leave its position and damage parts of the reactor by unpredicted movements. To guarantee this, a locking system is required, which is achieved by a massive bolt locking the trolley. The bolt, as shown in the drawing of the supply section (Fig. 7.13), is moved in by an electric motor from a top side connection.

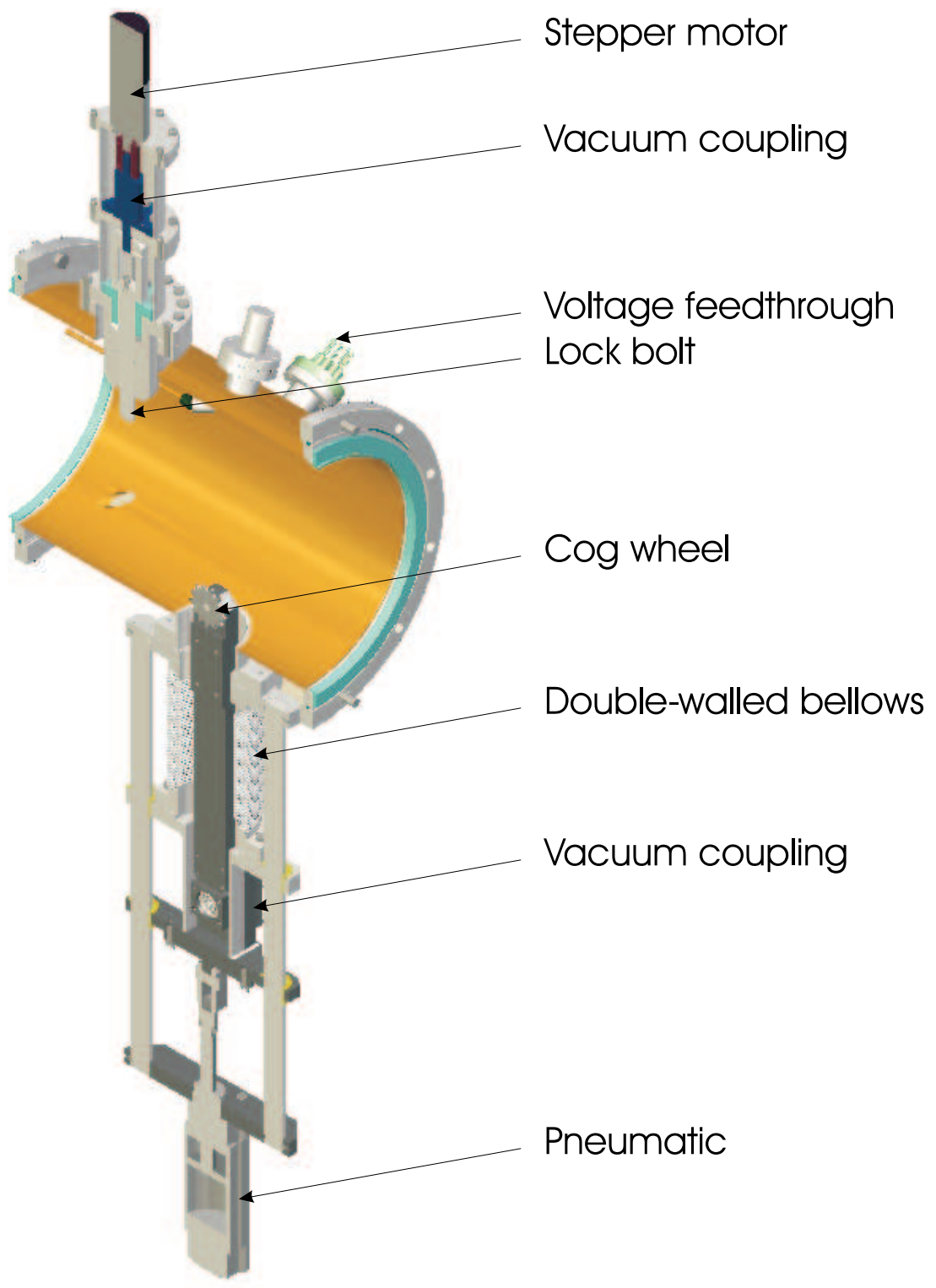


Figure 7.13: Technical drawing of the supply section including the locking mechanism.

7.2.2 Tests

Supporting Structure

During the assembly process of the supporting structure as shown in Fig. 7.14, it was found to be complicated to level the structure without the use of sophisticated optical equipment. Nevertheless, the levelling principle provided the necessary flexibility. However, in the final assembly step it became apparent that the lower cross-ties of the stilts have a varying position from the top cross-ties, so that unfortunate arrangement of the stilts generated a problem with the mounting of the lower profile. Yet, this problems can be avoided in a future re-assembly by choosing an appropriate stilt order or shims.

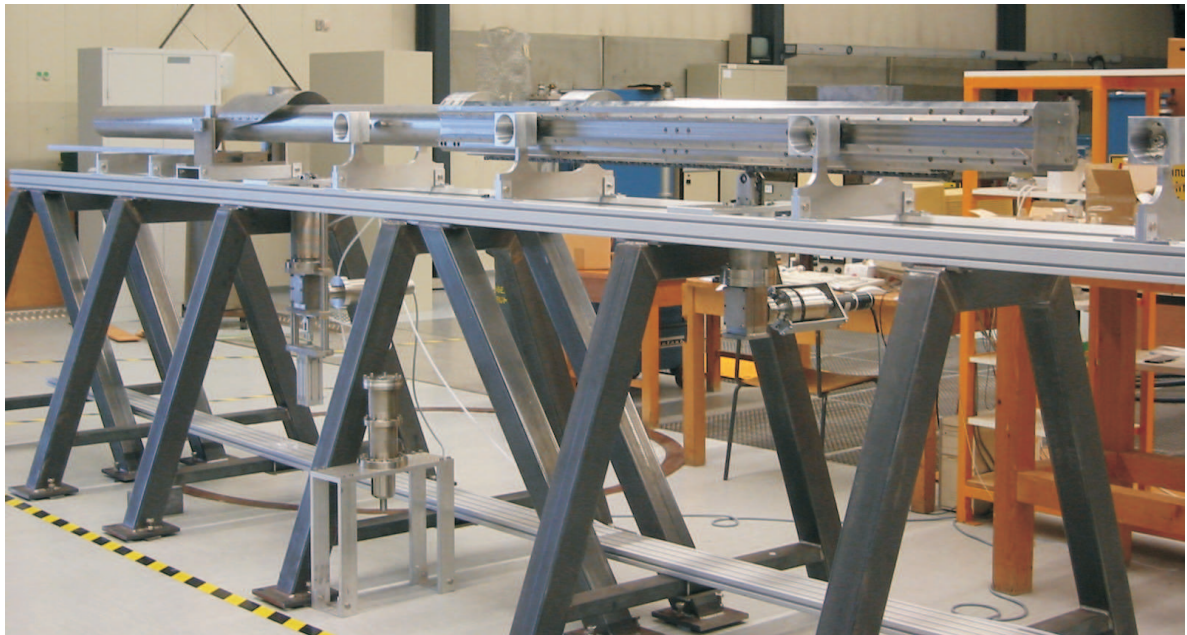


Figure 7.14: Picture of lens trolley prototype as assembled in the location provided by the MLL.

In order to test its stability, the complete assembled structure was hooked up by the hall crane and raised above ground for some seconds, where the structure supported itself and no problems with the trolley movement, due to disturbed alignment, could be found afterwards. This experience can serve as an indication for the structural integrity of the supporting structure and its capability to withstand the additional forces caused by supposed earthquakes and air craft crashes.

Propulsion system

A) Alignment of the rolls

Four pairs of rolls for the trolley transport are mounted on aluminum supports, as shown in Fig. 7.15, simulating the situation inside the beam tube. The rolls can be adjusted in longitudinal and vertical direction, offering the options to correct the few remaining alignment errors after the supporting structure has been levelled, so that the trolley moves smoothly over the rolls. It has been found that the propulsion system, due to mechanical tolerances, can compensate a misalignment of up to 0.4 mm in the rolls.



Figure 7.15: Picture of aluminum support structure, with guiding rolls, simulating the situation in the beam tube.

B) Transmission point

At the transmission point the trolley is handed from one motor unit to the next. There have been concerns that the cog wheels and the chain on the trolley's body might jam during the engagement process, however, the tests showed that the transmission works very smooth and that the cog wheels have enough play to adjust their position as required to perfectly mesh with the chain, as shown in Fig. 7.16.

In order to arbitrarily cause a jam, the cog wheel was aligned in a way to provoke a collision with the chain. As a result the trolley either stops after the collision (and makes a fine transmission on a second try) or continues on its way after some rumbling. In both cases no problematic consequences could be observed.

In a series of 100 tests, this kind of jam could not be observed in case both motors are running at the transmission time. In case one motor is off at the time, this problem has been observed in one case.

In Fig. 7.17 the motor current for both motors is plotted over the stepper motor position. Stepper motors operate with an oscillating current, with a frequency as noted in Table 7.2, which explains the broad current distribution. At positions of increased friction, a small spike can be seen indicating increased power consumption. A major spike occurs at the end when the motor is stopped. It is striking that spikes can only be seen in the backward direction, from front to rear. This is due to a slight misalignment, requiring the trolley to be moved very slightly up, which is not interfering



Figure 7.16: Picture of cog wheel engaging the transmission chain. Due to the pointed teeth of the cog wheel it meshes very smoothly with the chain.

with the trolley's speed as can be seen in the linear time-position relation as shown in Fig. 7.18. From this figure it can also be seen, that it takes 530 s to move the trolley one way, with motor settings as in Table 7.2.

C) Comparison of motor units

Two different motor concepts have been tested, as shown in Fig. 7.19 and Fig. 7.20. Both performed equally well during all tests involving the propulsion system. It must be noted however, that the fixed motor has only mechanical tolerances to compensate alignment problems and variations in the distance between chain and cog wheel as the center of mass moves to and from the supporting rolls during the movement of the trolley. It happens in about 2% of the cases that the force on the cog wheel applied by this effect is sufficient to stop the motor for a moment. A restart of the motor is necessary before the transport can continue.

Table 7.2: Settings of stepper motor parameters as used in the test setup.

Parameter	Setting
Start-/stop-frequency	400 Hz
Run-frequency	2000 Hz
Ramp gradient	5000 Hz/s
Emergency stop factor	0
Stop current	0.2 A
Run current	1 A
Boost current	4 A

The retractable motor on the other hand does not have this problem. The pneumatic system intrinsically compensates the vertical movement of the trolley, but leads to different problems. If

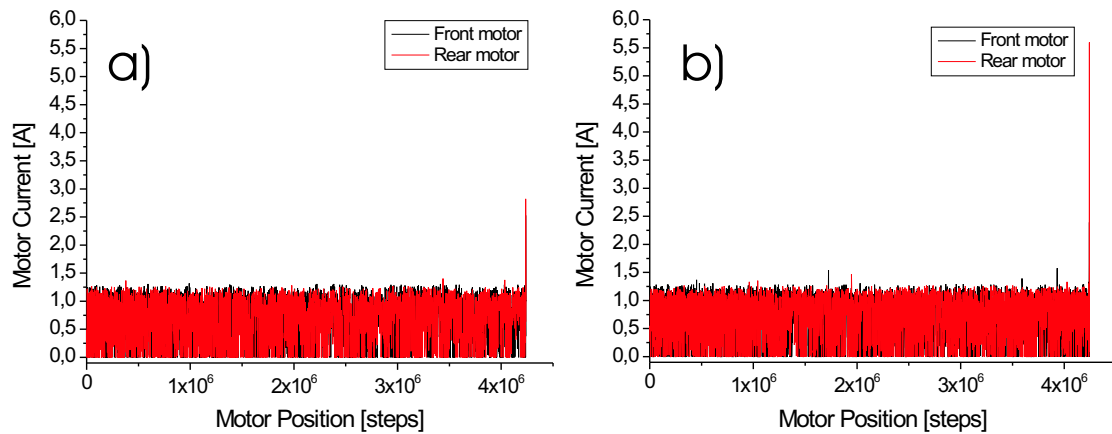


Figure 7.17: Evolution of current consumption of front and rear stepper motor if the trolley is moved from a) rear to front and b) front to rear.

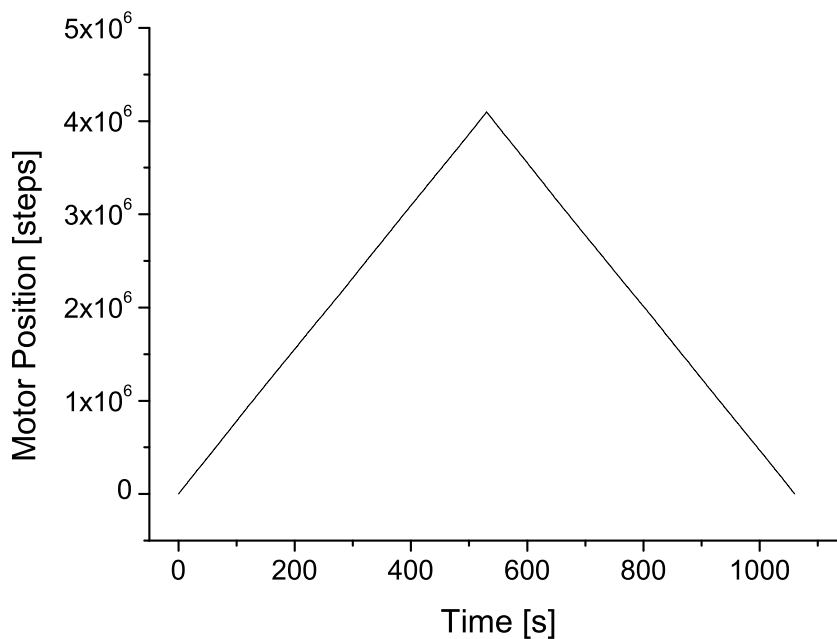


Figure 7.18: Time-position relation for stepper motors.

the motor is pushed up when the trolley is above the motor, it might happen that the cog wheel and chain hit tooth on tooth. This possibility has been investigated for the cases of a spinning and a resting cog wheel prior to engagement. In case of a resting cog wheel the mentioned error with resulting jam of the system has been observed with a probability of $6.0\% \pm 0.6\%$. However, the jam could always be resolved by disengaging the cog wheel and starting over.

In the second case with the wheel spinning the mentioned jam could be observed in $4.0\% \pm 0.4\%$ of the cases. However, there was a rather high possibility of $11.0\% \pm 1.1\%$ that the motor stopped after the spinning wheel engaged. In the case the wheel jammed and it was necessary to disengage

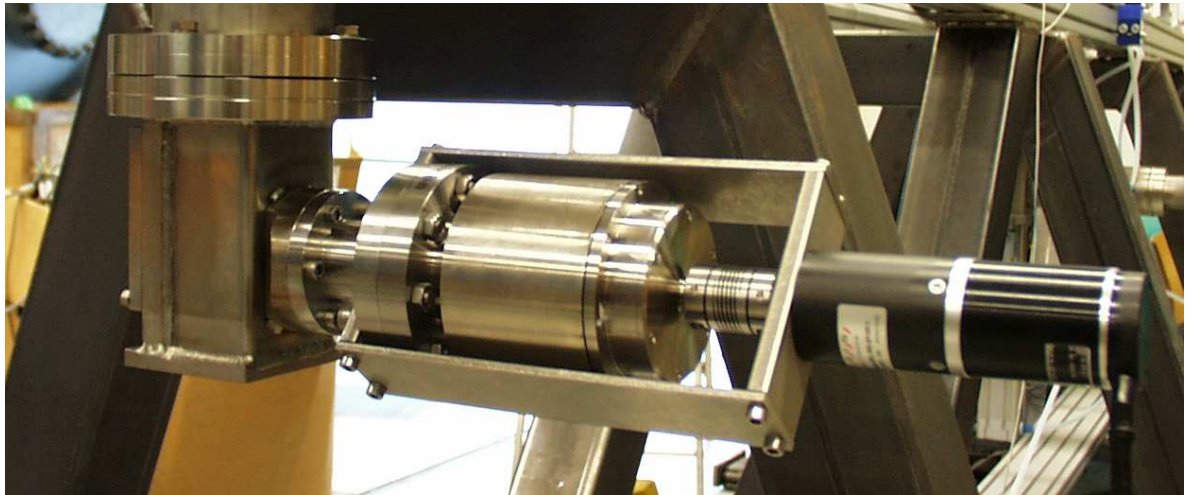


Figure 7.19: Picture of the fixed motor unit. The black cylinder to the right is the stepper motor. The massive stainless steel cylinder within the brackets is the housing of the magnetic coupling.

the wheel and start over. In the cases, when the motor stopped it was sufficient to restart the motor. In any case the situation could be resolved remotely.

Both motor unit designs work equally well under reliability and functionality perspectives. The decision which one to choose in the final layout can be based on cost and radiation protection demands.



Figure 7.20: Picture of the retractable motor unit. The stepper motor is encased in the smaller stainless steel cylinder to the right. The larger cylinder contains the magnetofluid coupling. A bellows and a pneumatic cylinder are required for retracting of the motor.

Adjustment system

First tests of the adjustment system, as shown in Fig. 7.9, revealed that the wedges cannot be moved once they have to support the weight of the trolley, because static friction was underestimated during the design and a re-design, as shown in Fig. 7.21, was necessary. The problem

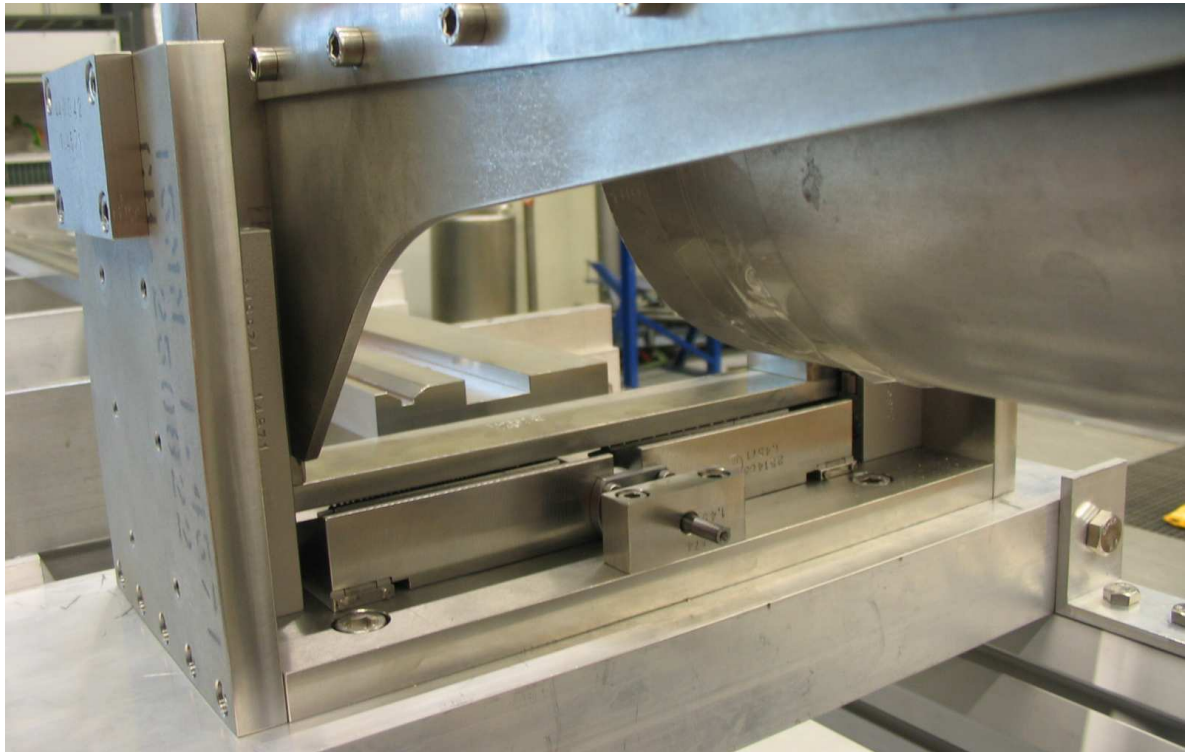


Figure 7.21: Picture of the adjustment system. The wedge for vertical adjustment can be seen at the lower side of the picture.

was solved by supplying all friction surfaces with ball or needle roller bearings, which significantly reduced friction, so that the adjustment system could be operated and the primary questions can be addressed: How exact can the trolley be adjusted and is there a hysteresis to the system?

To determine the hysteresis curve, Fig. 7.22, a laser was mounted on top of the beam tube, projecting a point onto a sheet of paper. Minimum, maximum and central point have been marked on the sheet for later analysis. The adjustment system has been cycled several times to gather multiple data points. However, during all measurements it was found that the three points coincide within the accuracy of the measurement, which is determined by the size of the laser spot and the distance from the end of the trolley.

Fig. 7.22 shows that no significant hysteresis can be reported and it is possible to adjust the tip of the trolley to an accuracy of 0.7 mm, limited in the first place by the accuracy of the position sensor, not by the mechanics. The active range of the adjustment system was determined to only ± 7.6 mm, which is somewhat less than the design value, because it was avoided to move the wedges up to the limit stop. Doing so caused problems with seizing of the wedges, which can be solved in the final version with the use of limit switches.

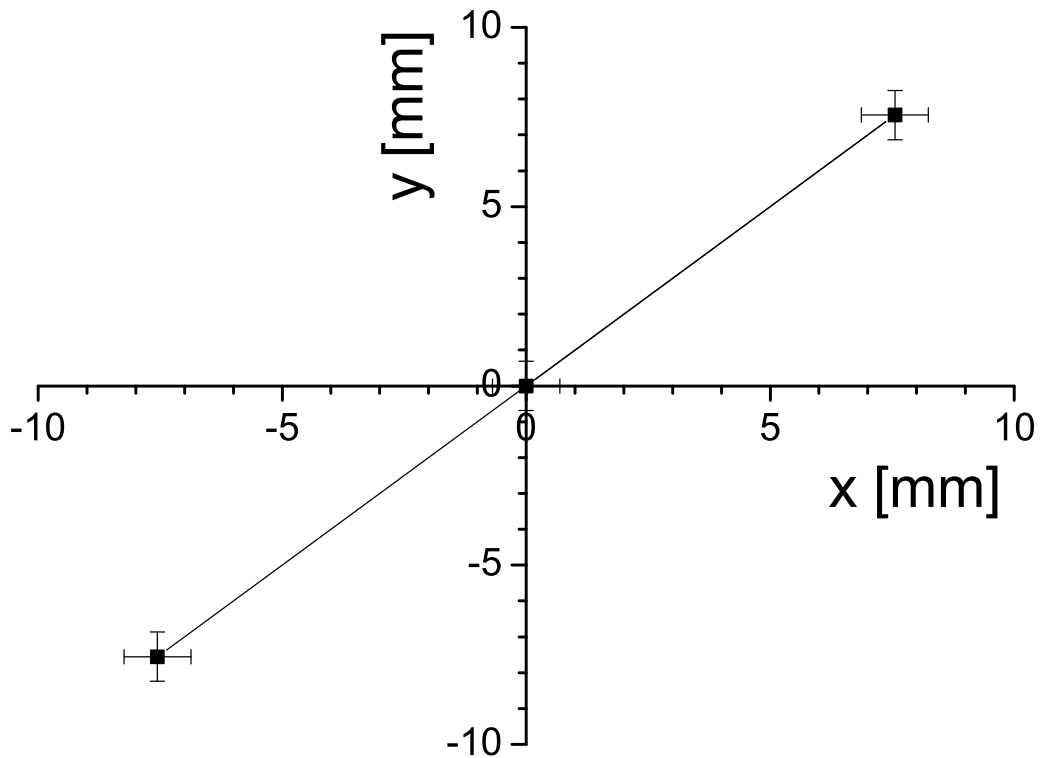


Figure 7.22: Hysteresis curve of the adjustment system.

Electric connections

Contact pins for electric connections, as shown in Fig. 7.12, have been manufactured from steel rivets with aluminum-oxid sleeves. The elasticity of the spring loaded pins have been verified in over 1000 compression cycles, where the springs showed no signs of wearing down. A picture of

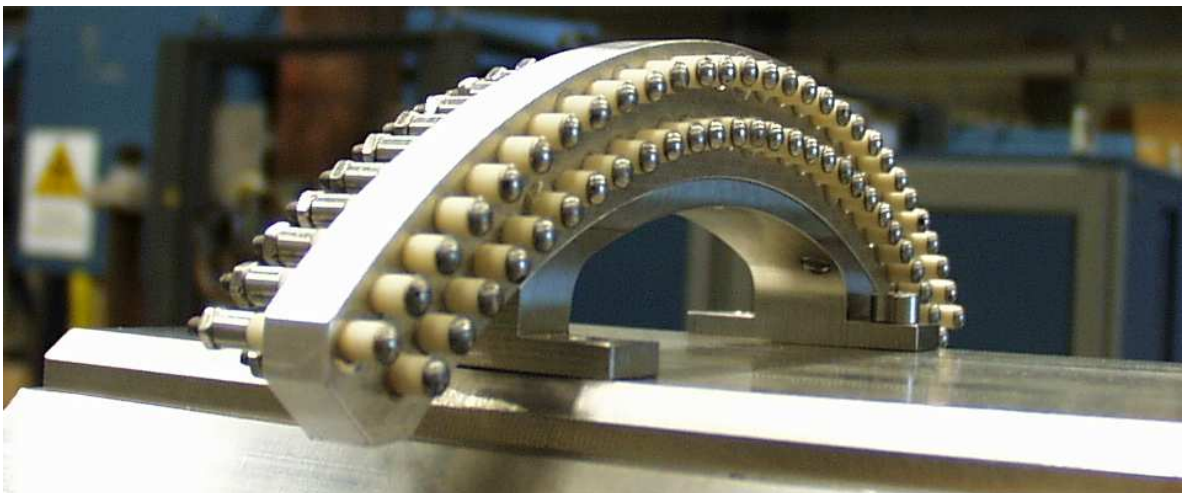


Figure 7.23: Picture of assembled structure of fixed pins. Pins are manufactured from steel rivets and aluminum-oxid sleeves.

the assembled structure of fixed pins, mounted on the lens trolley is shown in Fig. 7.23. During the assembly it was found, that the inner diameter of the sleeves was not very accurately machined. Approximately 40% of the rivets did not fit into the sleeves smoothly. This problem could be solved with an overhead of produced sleeves and selecting only functional ones.

Mechanically this simple construction proofed very durable and reliable. The electrical properties are pleasant as well. The transition resistance is in the order of 1Ω .

7.3 Material analysis

7.3.1 Vacuum greases

The rolls used for the trolley transport are commercially available and not designed for vacuum use. For the tests it would be sufficient to use the rolls as is, but for later use the factory provided default-grease has to be exchanged by something more suitable for the vacuum environment. Various potentially suitable materials as a grease replacement for use in UHV have been investigated. In a first step the default grease has been removed using a 24 h hexan bath followed by 15 minutes ultra-sonic cleaning in iso-propanol.

The re-greased bearings have been tested for vacuum compatibility in a small vacuum chamber. The chamber was pumped to high vacuum ($5 \cdot 10^{-6}$ hPa) and than vented with dry nitrogen, the sample was inserted and the chamber pumped again. The results of this pumping tests are shown in Fig. 7.24 and explained in the following:

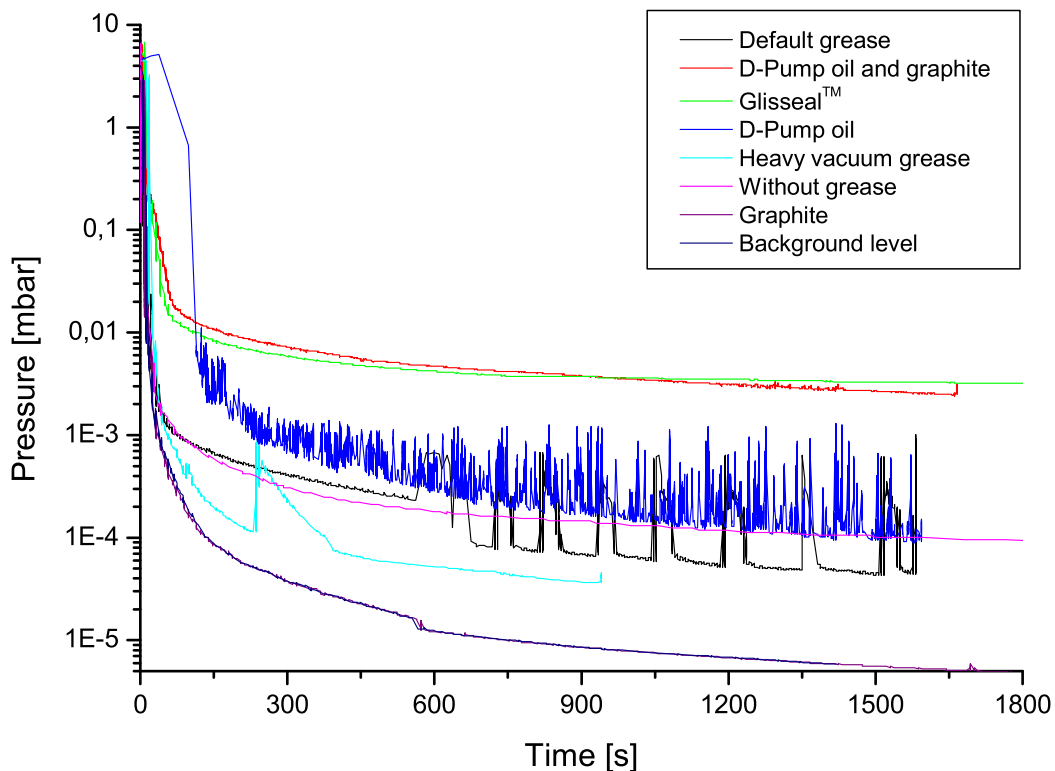


Figure 7.24: Results of vacuum compatibility test for various grease replacements in comparison to the background vacuum achieved with an empty chamber.

Default grease The factory standard lubricant is a carbon based grease. The bearing rolls smooth but cannot be spun. As seen in Fig. 7.24 at a pressure of $3 \cdot 10^{-4}$ hPa serious outgassing effects set in resulting in some spikes in the pressure progression resulting in a minimal achieved pressure of $5 \cdot 10^{-5}$ hPa. Therefore the material is not suited for UHV.

Heavy vacuum grease The university's standard vacuum grease is this silicon based lubricant. It has a much lower viscosity than the default grease, nevertheless the bearing rolls smooth but

cannot be spun. The pumping test shows no outgassing spikes and the pressure converges to $4 \cdot 10^{-5}$ hPa. Also, this material is therefore not suited for UHV.

GlissealTM The lubricant of choice in chemistry is a carbon based grease of similar viscosity and spinning properties as the default grease, but far worse vacuum properties. The pressure converges rather quickly without any outgassing spikes to $3 \cdot 10^{-3}$ hPa, which makes it the worst material tested.

D-Pump oil Carbon based oil used in diffusion vacuum pumps (Santovac 5 manufactured by Monsanto), which has a very high viscosity similar to edible oil. As a result the bearing rolls very comfortable and can be spun. During the pumping procedure, the oil generates outgassing spikes with a high frequency, possibly due to air bubbles enclosed during the greasing process. The series of bubble explosions distributes the oil among the vacuum chamber. Because of this and the achieved pressure of $9 \cdot 10^{-5}$ hPa the oil is not suited for UHV.

Graphite This graphite is better described as incompressible carbon powder. The bearing can initially be turned rather hard. After some time the bearing jams and cannot be turned unless extensive force is applied, which seems not to be a problem in the test setup, where the graphite lubricated bearing moves similar to all other bearings. In addition, the comparison with the background level shows, that carbon is the only contestant that is suited for UHV.

D-Pump oil and graphite With a combination of diffusion pump oil and graphite powder as a lubricant the bearing functions not as smooth as the D-pump oil bearing but works rather well. Vacuum wise the properties are not the average of its ingredients but far worse. No outgassing spikes appear but the final pressure of $2 \cdot 10^{-3}$ hPa is not competitive.

Without grease Without any lubricant the bearing can be spun very well but tends to cant occasionally. About 30% of the cleaned bearings jammed rather quickly without grease. Surprisingly the achieved vacuum of 10^{-4} hPa after 30 minutes pumping is poor compared to the vacuum reached with graphite and heavy vacuum grease. After pumping for 48 h a pressure of $4.3 \cdot 10^{-6}$ hPa can be reached. This suggests some minor outgassing from the ball bearing itself, possibly from some plastic parts required to support the balls. In case of using vacuum grease and in part graphite these parts are probably covered with lubricant and outgassing is reduced.

Background level corresponds to the vacuum quality achieved with an empty vacuum chamber.

In conclusion graphite provides the desired vacuum compatibility and works sufficiently well as a lubricant in the tested application. Nevertheless, additional approaches like ceramic ball bearings or friction bearings are still interesting and should be considered further.

7.3.2 Gadolinium

In a reactor environment or at another facility, where thermal neutrons are produced, the life-time of most electronics and permanent magnets is degraded by neutron radiation. The capabilities of thermal neutrons to activate otherwise stable materials followed by subsequent β -decay, changes the elemental composition of materials, which weakens the crystal structure, so that all materials become glassy after extended irradiation with thermal neutrons. Also neutron induced γ -radiation should be avoided if possible. These problems are not unique to a reactor experiment, but also apply to commercial power plants and spent fuel elements, where delayed neutrons cause a problematic amount of neutron radiation.

A cheap material, with superior neutron absorption properties, which can easily be handled and manufactured with standard equipment would be very interesting, not only to neutron physicists.

Currently boron based compounds like Boral or boron-carbide are used for neutron absorption. However, boron forms some toxic compounds, is rather expensive, and complicated to machine. The use of boron alloys is therefore limited to very sensitive areas where shielding of neutron radiation is absolutely necessary and requires extensive amounts of boron if shielding of high neutron fluxes is required.

Neutron capture properties of gadolinium

Naturally occurring gadolinium has a 63 times larger capture cross-section for thermal neutrons compared to boron. It is a hardly investigated rare earth material with the highest thermal neutron capture cross-section of any known element. Seven isotopes occur naturally with ^{155}Gd and ^{157}Gd offering the supreme capture properties. As seen in Fig. 7.25 even a 0.03 mm thick gadolinium sheet can absorb the complete thermal neutron flux of the FRM-II. However, the high absorption rate also consumes the isotopes in question rather quickly as illustrated in Fig. 7.26, where the evolution of the isotope composition is shown for a Gd sample irradiated with a neutron flux of $10^{12} \text{ n s}^{-1}\text{cm}^{-2}$. It can be seen, that the isotopes offering a high absorption cross-section are quickly converted to other Gd isotopes, while Neutron capture on the heaviest Gd isotopes and subsequent β -decay creates low impurities of Tb and Dy isotopes, which in turn absorb neutrons and created further Dy isotopes. Finally, the conversion of isotopes with a low neutron capture cross-section to high cross-section isotopes stabilizes the total cross-section at 43 b as shown in Fig. 7.27. Depending on the applied neutron flux, saturation is reached after a couple of weeks or years.

General properties of gadolinium

Gadolinium is the most stable of all lanthanides and silvery white, when freshly cut. Within days the surface oxidizes and turns dark grey with a metallic luster. It reacts very slowly with water or moist air. In the experiments performed no reaction with water was observed. However, in the long term it will eventually oxidize under the presence of water, the oxidized surface will spall off, and expose more material to oxidation, so that the oxidation process will start over. During this oxidation process H_2 is formed as a by product, which might ignite potentially and makes gadolinium a fire hazard if exposed to water.

Gd crystallizes in a hexagonal closest packing (hcp), α -structure, until it changes to body-centered cubic (bcc), β -structure, at 1508 K, before it finally melts at 1585 K.

Nothing is known of the toxicity of gadolinium. No unpleasant side effects of gadolinium handling can be reported in this work.

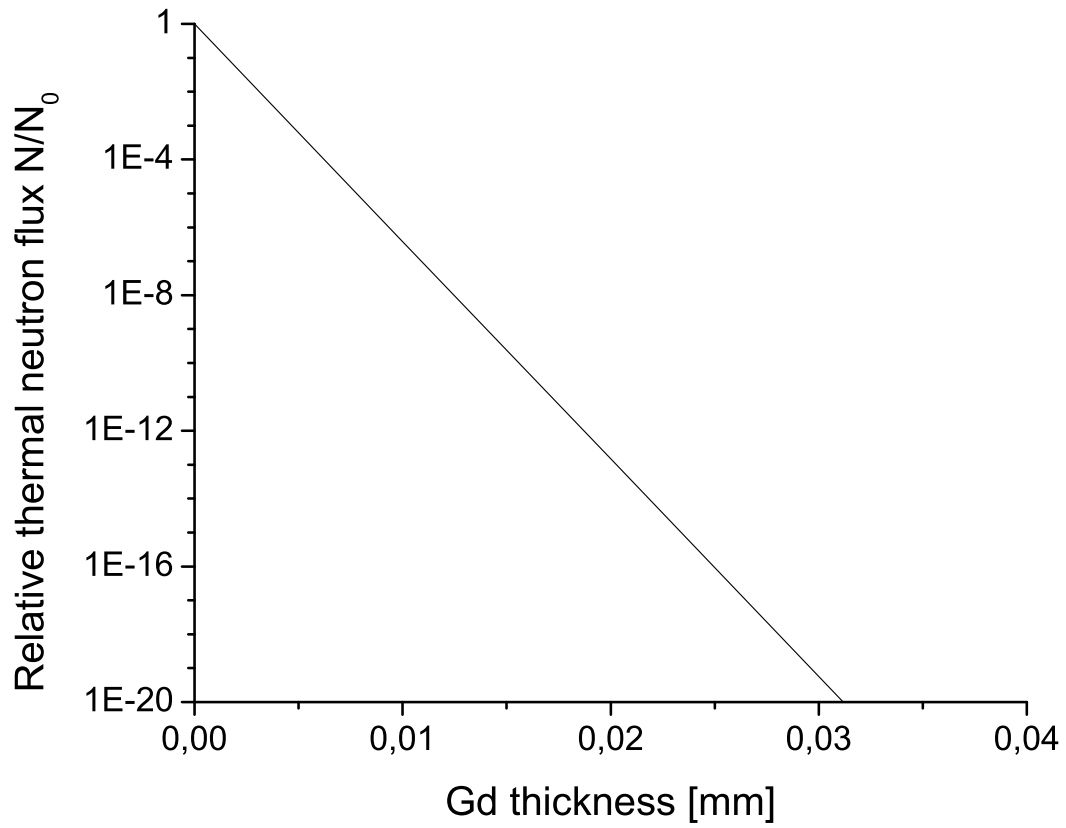


Figure 7.25: Range of thermal neutrons in gadolinium. 0.3 mm thick Gd reduces the neutron flux by more than 20 orders of magnitude.

Gadolinium-oxide is mostly used in the glass industry to adjust the refractive index of the glass. Furthermore it is used as a contrast agent in medicine.

Material testing

A small sample (some kilograms) has been difficult to obtain, since it is usually traded by the tons. From an US-vendor, 4.5 kg Gd originating from China could be obtained. Delivery time was approximately 1 month, however, it took more than a year to find a vendor, who did actually deliver. The vendor claims the composition as listed in Table 7.3. The obtained sample is a cylindrical cast material. A first inspection already showed many obvious sinkholes. Comparing the density of our sample with the literature value suggested that approximately 5% of the volume are air bubbles.

The following steps have been performed with the sample to qualitatively investigate the material properties:

Lathing As expected from a rare earth metal it produced many sparks during the process. Otherwise no problems have been reported from the mechanics. Fig. 7.28 shows the lump material after lathing. The largest crater on top has preserved the original coloring.

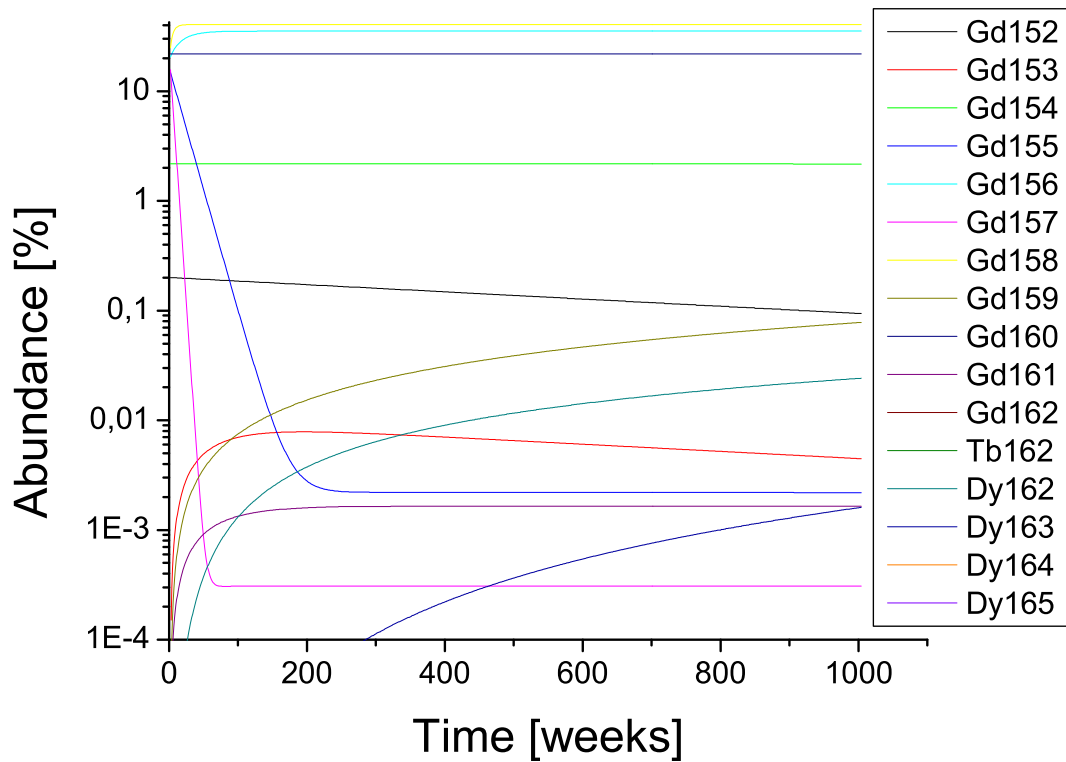


Figure 7.26: Under the influence of a high neutron flux (here $10^{12} \text{ n s}^{-1} \text{ cm}^{-2}$) the isotope composition of the irradiated Gd changes as shown.

Table 7.3: Composition of the gadolinium as provided by the vendor.

Compound	Percentage
Gd	99.56
La	0.02
Ce	0.03
Pr	0.035
Nd	0.026
Sm	0.010
Si	0.021
C	0.018
Ca	0.045
O	0.012
W	0.01

Sawing Cylinders of 3 mm height could be sawed off. During the process the surface smeared and needed to be lathed afterwards to flatten it again.

Milling The obtained pieces could be milled down to 0.2 mm without any problems. However, the milled material is very brittle and cannot be bent without breaking it. Fig. 7.29 shows the examples of milled materials.

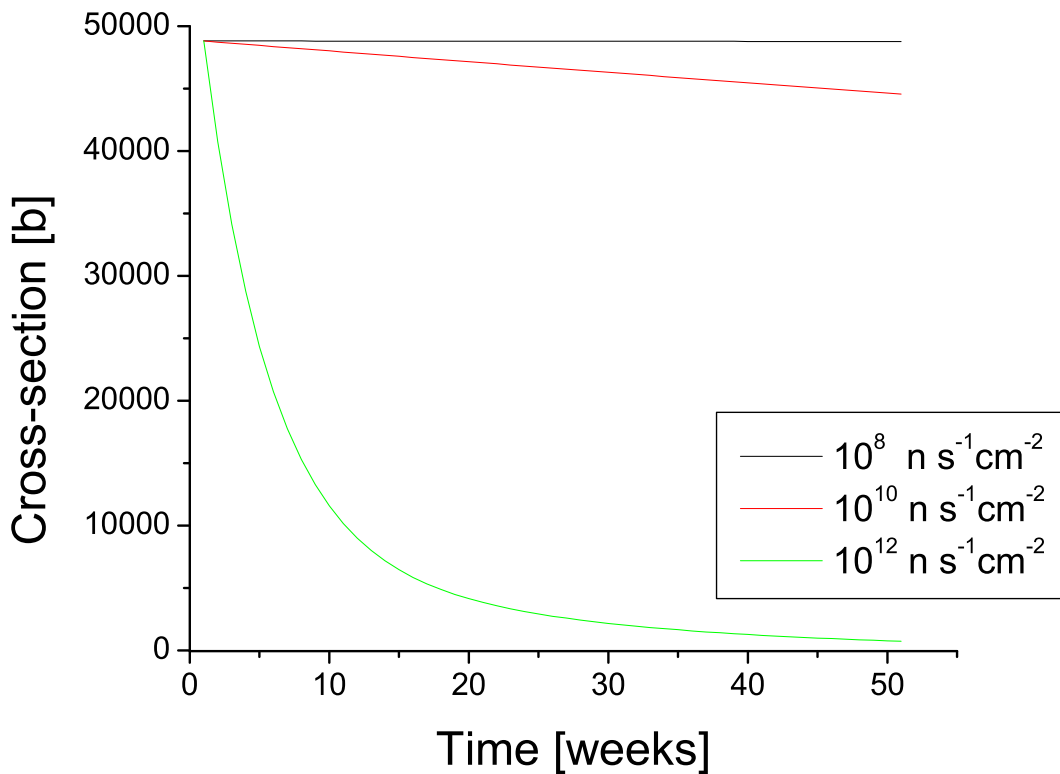


Figure 7.27: Development of Gd neutron capture cross-section under the influence of various neutron fluxes.

Tempering The milled material has been tempered in an electron beam oven. However, a quantitative temperature measurement was not available. Nevertheless, the two samples have been tempered for some time at red heat, a 3rd sample (Fig. 7.30) up to the melting point. The remainders of the 3rd sample can be bent very well without stressing the material too much. The other two samples (Fig. 7.31) are somewhat more flexible than before the tempering but not sufficient.

Welding Two parts of Gd have been successfully welded together using an electron beam (Fig. 7.32). The resulting weld shows no signs of weakness.

Alloying

For a more cost effective machining of gadolinium it would be best if the elasticity of the material could be enhanced. The aim is to be able to bent it by 90° in order to form a right angle. In this case expensive electron beam welding could be avoided.

Based on experience it was first tried to alloy Gd with 30 mass-percent of oxygen free copper, which corresponds to a stoichiometric ratio of 1:1. Both materials have been melted together with an electron gun in a high vacuum oven. The resulting alloy was dark grey with a bronze luster. In order to validate the material properties, GdCu was tried to roll, but the material burst into tiny crumps during the process. An extraordinary hard and brittle material was formed. After consulting



Figure 7.28: Photograph of the Gd lump after turning on a lathe. Largest crater on top preserved original coloring. Cut of sinkholes can be seen as well.

relevant literature [79] [80] [81] it was found that this result had to be expected. According to the *Hume-Rothery* rules the following points define the solubility of two materials forming a solid solution:

Similar atomic radii For complete solubility the difference should not exceed 8%. At a differences of more than 15% solubility is negligible.

Similar lattice structure Identical lattice structure is required for complete solubility.

Similar electronegativity With increasing difference in electronegativity the metallic character of the bond is lost in favor of an ionic bond and solubility is reduced.

Similar valency Identical valency is required for complete solubility of two materials. For different valencies the material with lower valency can dissolve more of the material with higher valency as vice versa.

It is clear that the melting point of either substances must be smaller than the others boiling point. For practical reasons the vapor pressures of both partners should be small as well, since the electron oven used for the alloying process requires high vacuum conditions.



Figure 7.29: Photograph of the Gd after milling. The brittle material shows cracks occasionally.



Figure 7.30: Photograph of the Gd after tempering up to the melting point. The material regained a high flexibility.

Table 7.4 lists the properties of various elements taken into consideration for formation of a binary Gd-alloy. According to *Hume-Rothery* rules the atomic radius of a suitable partner should be between 153 pm and 207 pm, which is true only in case of Pb. However, Pb has very unfavorable thermal and electric properties combined with a not identical lattice structure.

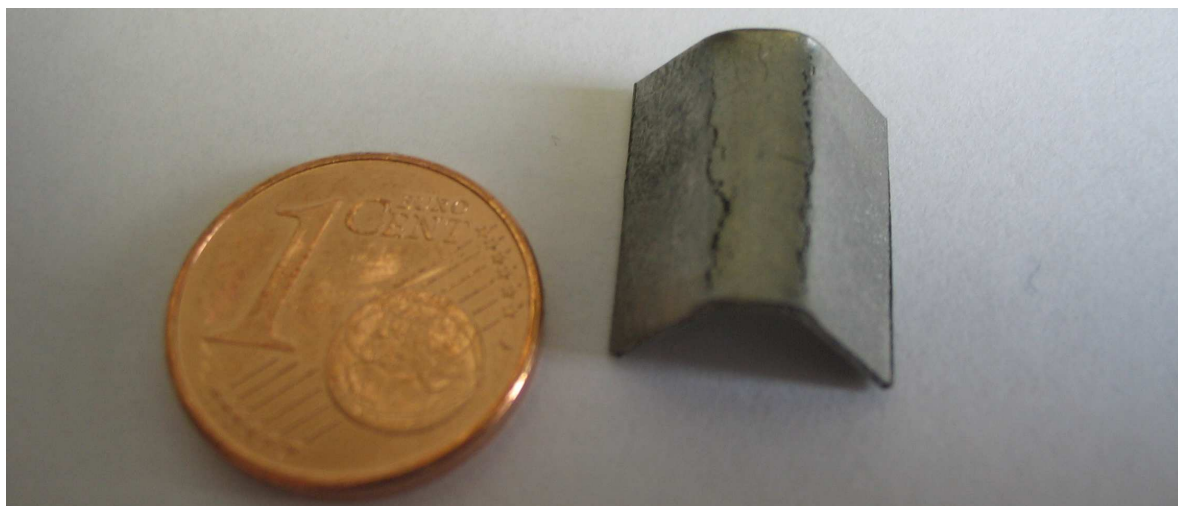


Figure 7.31: Photograph of the Gd after tempering at red heat. The material can be bent without breaking, but cracks occur nonetheless.

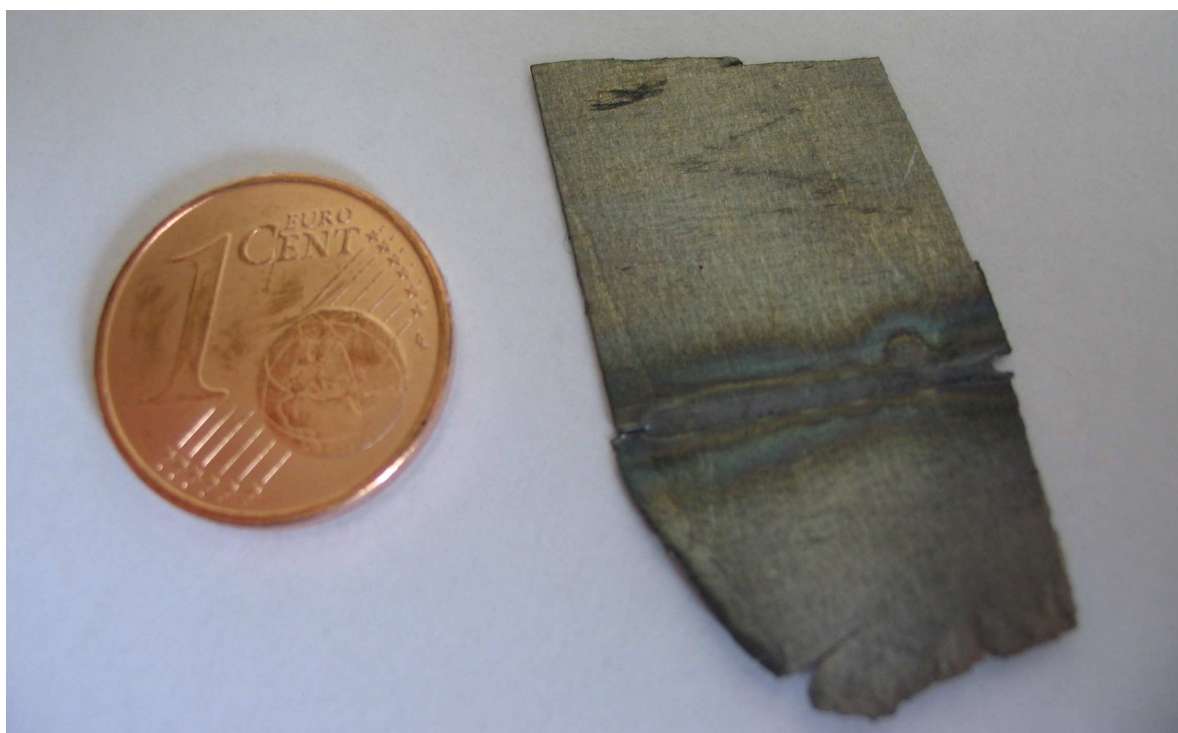


Figure 7.32: Photograph of two Gd samples welded together with electron beam welding.

The overall best agreement is achieved with Ti. However, due to the 22% discrepancy in atomic radii it cannot be expected to dissolve more than 1% in Gd or vice versa. However, the admixture of small quantities can also change the material properties significantly.

7.4 Conclusion

In conclusion many crucial components of MAFF have been successfully tested and important information on the behavior of those components has been collected. The results can briefly be summarized as follows:

Table 7.4: Properties of possible partners for formation of a binary Gd-alloy. Empirical atomic radius r_A , Pauling electronegativity χ_P [82], crystal structure, melting point T_m and boiling point T_b are listed.

	r_A [pm]	χ_P	Electron Configuration	Structure	T_m [K]	T_B [K]
Gd	180	1.2	[Xe].4f ⁷ .5d ¹ .6s ²	hcp	1585	3523
Cu	135	1.9	[Ar].3d ¹⁰ .4s ¹	ccp	1377	3200
Ni	135	1.91	[Ar].3d ⁸ .4s ²	ccp	1728	3186
Mg	150	1.31	[Ne].3s ²	hcp	923	1363
Al	125	1.61	[Ne].3s ² .3p ¹	ccp	933	2792
Pb	180	2.33	[Xe].4f ¹⁴ .5d ¹⁰ .6s ² .6p ²	ccp	600	2022
Sn	145	1.96	[Kr].4d ¹⁰ .5s ² .5p ²	tetragonal	505	2875
Ti	140	1.54	[Ar].3d ² .4s ²	hcp	1941	3560
Mo	145	2.16	[Kr].4d ⁵ .5s ¹	bcc	2896	4912
Co	135	1.88	[Ar].3d ⁷ .4s ²	hcp	1768	3200

In a test of the quadrupole triplet prototype it has been shown, that the concept, of steering the displaced beam back on axis with the triplet, works.

A prototype of the lens trolley, with the option of possible later use at MAFF, has been constructed. A retractable and a fixed motor unit have been constructed and tested. Both devices work equally well in combination with the chain based propulsion system. No problem arising from the use of a chain, mounted on the trolley instead of a spur rack, were encountered. The investigation showed, that small misalignments could be compensated and all occurring errors of the propulsion system could be resolved remotely.

The adjustment system, designed to align lens and source trolley onto each other, exceeded the expectations and showed no sign of hysteresis.

Material investigation have shown, that among the available lubricants graphite is the best solution.

Material properties of gadolinium, as an excellent neutron absorber, have been studied and it was found, that the material can be lathed, sawed, milled, welded (with electron beam), and folded (after tempering). The construction of simple geometric devices (cubes, cylinders), as neutron shields, seems feasible. Alloying gadolinium with copper produced a hard and brittle material unsuited for our purposes. An alternative to gadolinium machining could be coating of pre-machined structures with gadolinium. This might work well at positions, where only a small neutron flux must be stopped and the burn-up rate is acceptable.

The information obtained from prototype construction and tests, as well as from material investigations has been used to modify and adjust the specifications necessary for the MAFF approval process.

8 Summary and conclusion

It is the outcome of this work, that radionuclides at MAFF, whether ionized or neutral, can be handled safely under normal operation and with acceptable impact on radiation safety in case of a system failure.

During this work important parts of the layout and design of MAFF-I have been carefully re-evaluated and the resulting design and concept changes have been explained in Chapter 2. Most of the changes aimed at simplifying the layout and making it more reliable, which required removing some complex functions from the system, while other functions have been disentangled, e.g. to get two simple devices instead of one complex device.

In order to know the ion optical boundary conditions for the design of the extraction side (A-side), the ion transport from the ion source to the beam cooler has been studied in depth relying on the matrix calculation code COSY and the numerical code SIMION7. The major motivation for the detailed simulations came from different obstacles, that arise from the installation of an ion optical system in a fission reactor, which require the ion optical components to be mounted on two trolleys with long self-supporting extensions. The trolleys carrying the source and extraction optics respectively, might not be perfectly aligned with respect to each other, also the extensions will bend due to their weight. The ion beam extraction system described in Chapter 3 compensates the maximum possible offset between the trolleys and a very large bend of the tube before it delivers the ion beam to the mass pre-separator without beam degradation.

The mass pre-separator has been investigated as well and a new solution for a slit system allowing the propagation of multiple mass branches with variable mass ratio has been studied. The possibility to select masses with variable mass-ratio for the experiments is very essential, since it cannot be expected, that experimentalist can always use two masses with a ratio of 1.5. In account of this, a novel solution for the slit system is suggested, proposing to use the slits as electrostatic deflectors and initiate a parallel shift of the beam, which is completed by another set of deflectors in front of the following electrostatic quadrupol doublets. In this way the available mass ratios can be chosen from 1.21 to 1.86, while the ion optics following the slit system can stay in place.

To complete the ion optical simulations, a possible beam transport option, over ≈ 20 m, to the Reactor Building East has been developed. In this section higher order image aberrations started to cause emittance growth and decreased the beam quality. However, the emittance accepted by the beam cooler at the end of this beam transport section set a rather low limit of $36 \pi \text{mm}\cdot\text{mrad}$. Nevertheless, it was achieved to stay below this limiting value. Additionally it was possible to implement an electrostatic beam-switch option, that adds the capability to switch heavy and light mass beam between the different beam coolers, allowing the use of either mass as low energy or accelerated beam.

To assess the potential risks coming from radionuclides produced at MAFF, the distribution of radionuclides within the MAFF beamline and possible consequences for radiation safety, environment and functionality of MAFF have been studied in great detail in Chapter 4 with special

focus on possible escape routes of neutral radionuclides leading to radiation release. Among the routes studied were volatile radionuclides, volatile compounds formed from otherwise non-volatile radionuclides and aerosols formed from radionuclides. The latter were assumed, prior to this work, to carry large amounts of activity, but turned out to pose only an exceptionally minor risk of radiation release under normal operation. In addition to the activity of gaseous agents the radiation levels caused by direct radiation from the reactor core, neutron activation, and fission fragments distributed along the beam line has also been investigated. Based on the outcome of this investigations a simple and coherent concept of operation and emergency response with respect to radiation safety has been developed and is summarized in Chapter 5. Finally, the multitude of emergency scenarios with the possibility of radiation release have been reduced to six basic cases, which are all detected via two pressure thresholds. While the lower threshold, of 10^{-4} hPa, demands the attention of the operator, the higher one, of 1 hPa, will trigger protective functions of the control system, bringing MAFF to a safe mode, where the risk of radiation release is minimized.

Technical investigations of various crucial components have been required to proof the feasibility of the developed concepts. The investigation of the ion optical properties of the quadrupole triplet prototype confirmed the possibility to correct a misalignment of the beam-line and steer the beam. However, it was also discovered, that the decision to have steering capabilities only on the middle quadrupole is insufficient and it is better to have steering possibilities available at all quadrupoles.

To verify various concepts related to the trolleys, the design of the source trolley was pushed to a point, where the construction of a prototype of the lens trolley was possible. This prototype, including the supporting structure, propulsion system, adjustment system and the trolley itself has been constructed from cobalt deficient steel, with the aim to use some of the components later on at MAFF.

Among the tests performed, the propulsion and adjustment system had special importance. The tests with the propulsion system showed, that it works reliably and no failure was observed that could not be resolved by remote operation. For the adjustment system, necessary to adjust both trolleys a re-design was necessary after the first prototype has been constructed, because friction forces have been underestimated and the system did not function at all. However, the re-designed system works well, and allows to adjust the trolleys to the desired accuracy of 1 mm. Both, propulsion and adjustment system, require a lubricant that is suited for vacuum operation in connection with cryo-pumps. Therefore, the vacuum properties of various lubricants have been investigated and it was found, that graphite is the only lubricant meeting the requirements.

Further material investigations have been aimed at studying the mechanical properties of gadolinium, a hardly investigated rare earth material with the highest cross-section for thermal neutron capture of all elements. While it is the ideal neutron absorber little was known about its mechanical properties. If the material could be suitably machined, very thin and highly efficient neutron absorbers could be built to protect electronics in a neutron field from destruction or reduce the activation of sensitive material. For this shielding purpose it is planned to construct housings to protect sensitive materials from the neutrons. It is therefore necessary to manufacture gadolinium into thin sheets, bend or weld them. Therefore gadolinium has been lathed, sawed, and milled to thin sheets, which were too brittle to be bent by 90° , but could be electron beam welded without a problem. In addition it has been found, that the gadolinium sheets could be bent after tempering. Therefore the construction of the desired gadolinium shields seems possible and will be performed in the future.

All these different aspects contribute an important part for the final design of the MAFF system, so that together with the results of other investigations a conclusive layout for MAFF has been established. Based on this layout a successful and safe operation of MAFF can be expected.

A MLL-Emi Manual

A.1 Introduction

The MLL-Emi was designed and constructed during an earlier thesis work by A. Wilfart [86]. This manual describes the status of the Emi at the time the measurements described in this work have been performed. In the mean-time modifications to the device have been applied by M. Schubert.

The Emi is using three electrostatic deflectors and 2 slits to measure the emittance. The beam enters the MLL-Emi and is parallel shifted by the first two electrode pairs. The applied voltage is proportional to the shift. By the following slit only a small line from the beam is selected. This allows to pick a certain position. The adjacent deflector and slit select a specific angle. The voltage applied to the deflector is proportional to the selected angle. A faraday cup after the last slits measures the ion current. In this way the intensity for every position-angle correlation can be determined. By scanning over various positions and angles the complete phase space diagram can be obtained. The whole setup is pivoted and can be turned by 90° in order to measure x-a and y-b emittance.

A.2 List of hardware components

The MLL-Emi is assembled for different parts that are required for a successful operation.

Emi-double-cross This is a CF150 stainless steel double-cross, see Fig. B.2. One side is open for the incoming beam, Fig. B.3. At the opposing side the faraday cup or photomultiplier should be placed. On top of the cross is a knob to turn the Emi for x and y position change. On one side is a glass view-port, one side (usually the bottom) has no flange in order to mount a pump or pumping station. The remaining side has a flange with 4 SHV feedthroughs mounted, see Fig. B.4.

Faraday cup A faraday cup suitable for mounting inside the double-cross was originally manufactured with the MLL-Emi but went missing recently.

Photomultiplier A photomultiplier for low current measurements is available.

Cable Junction This is the cable mess seen in Fig. B.5. It is used to connect the control unit to the PC.

Control Unit The control unit, see Fig. B.6 contains the power supplies for the various deflectors. It has the capability to read back the applied voltage from the power supplies. However, this feature is disabled at the moment.

PC There is a complete PC, including monitor, mouse and keyboard part of the MLL-Emi. The PC runs Windows 2000. The default login is "ladmin". The corresponding password is "ladmin" as well.

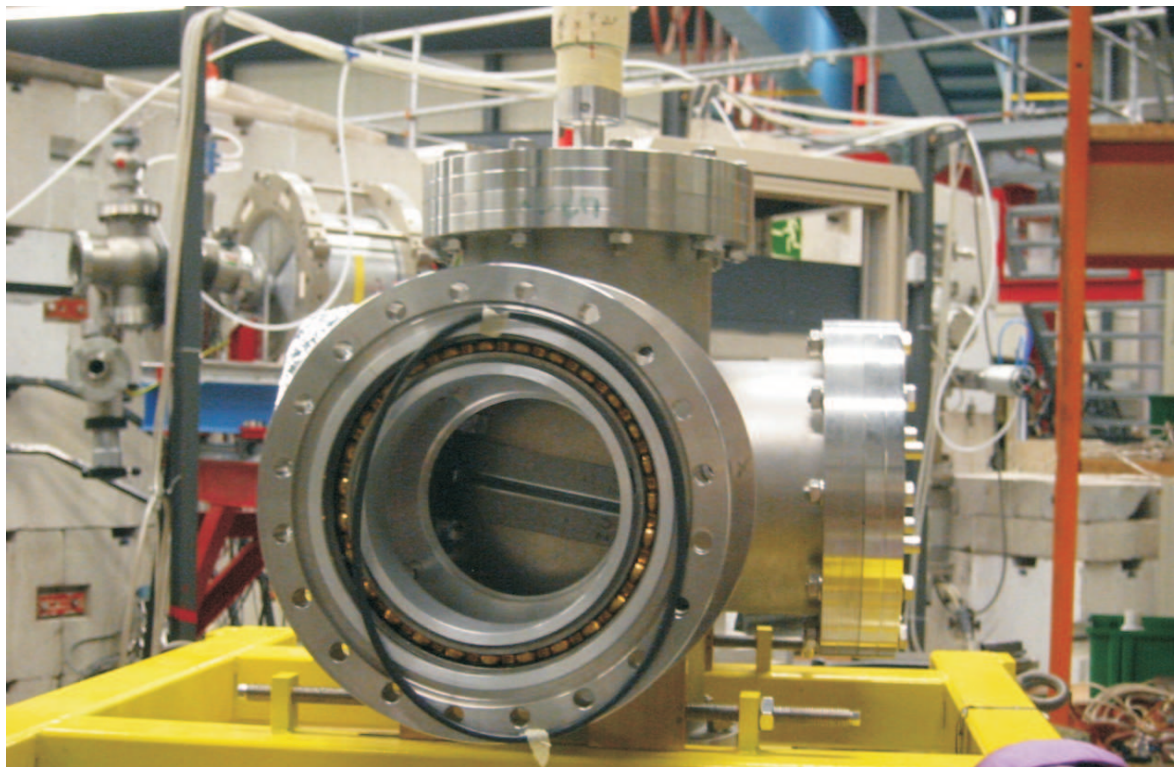


Figure A.1: The MLL-Emi double-cross with the Emi mounted inside View from the back side, where the faraday cup or photomultiplier should be placed.

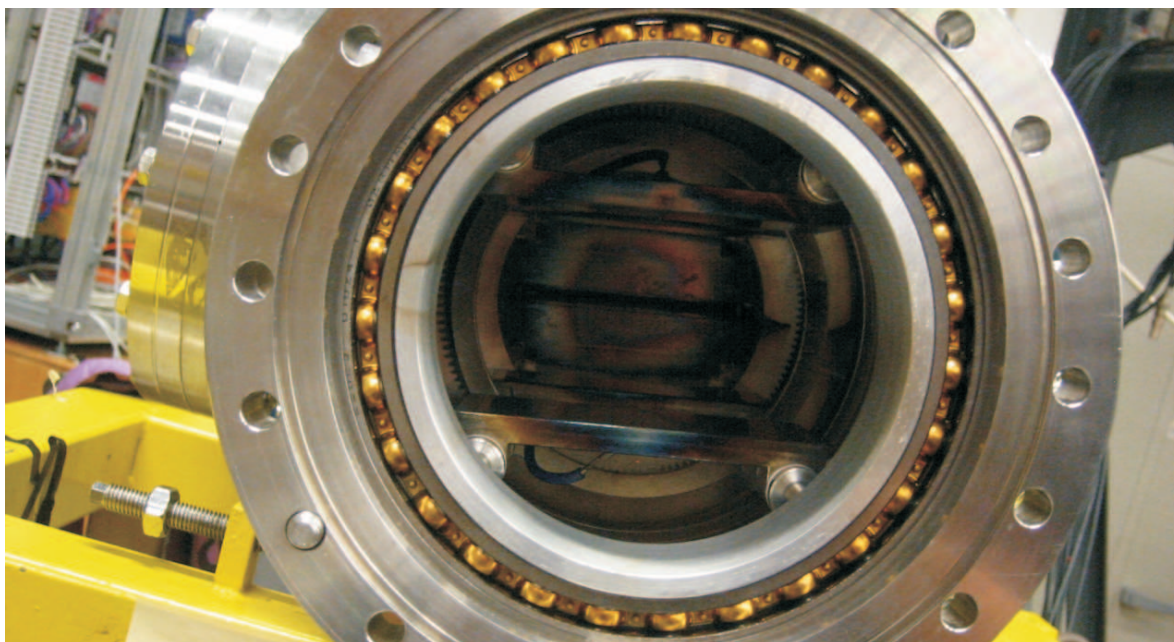


Figure A.2: The MLL-Emi front side for the incoming beam.

Support Stand This yellow steel stand can be varied in height.

SCSI-cable One SCSI-cable to connect the Cable Junction to the PC.

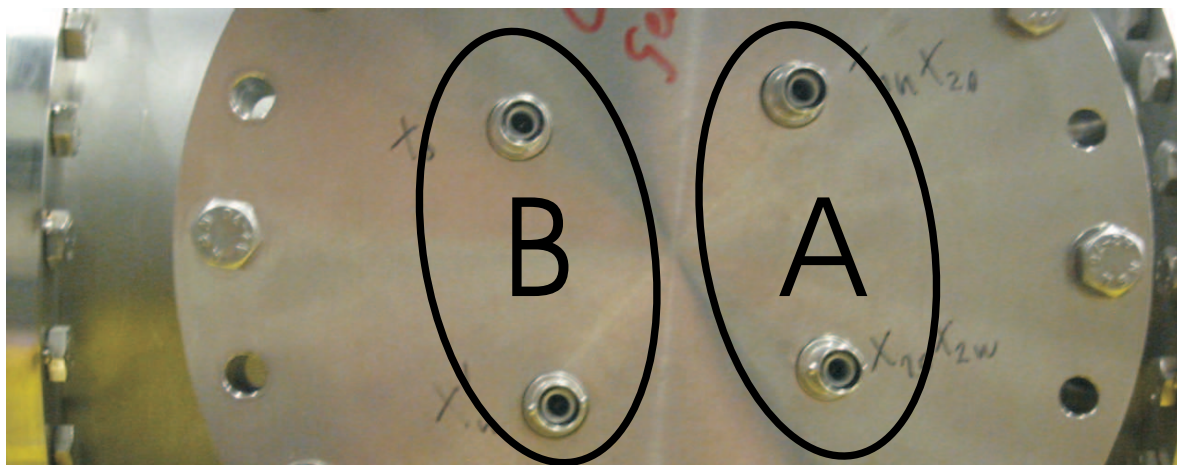


Figure A.3: The MLL-Emi side flange with SHV feedthroughs.

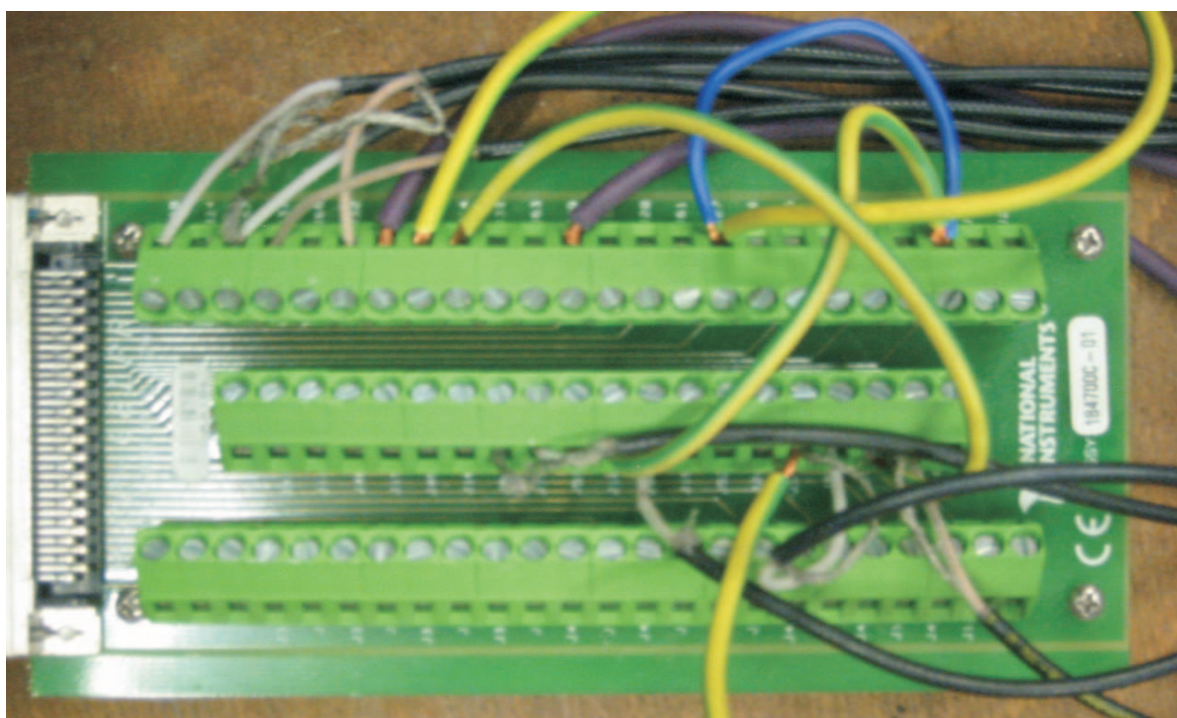


Figure A.4: Cable Junction, connecting the PC with the Control Unit.

A.3 Required software

There should be two kinds of software installed at the PC. The readout runs under Labview. A complete labview program is available. The Labview program requires some hardware drivers to be installed and configured. Documentation on this process has never been written. The current status is documented in Fig. B.7. It is very likely that malfunctions of the voltage readback from the power supplies can be fixed here.

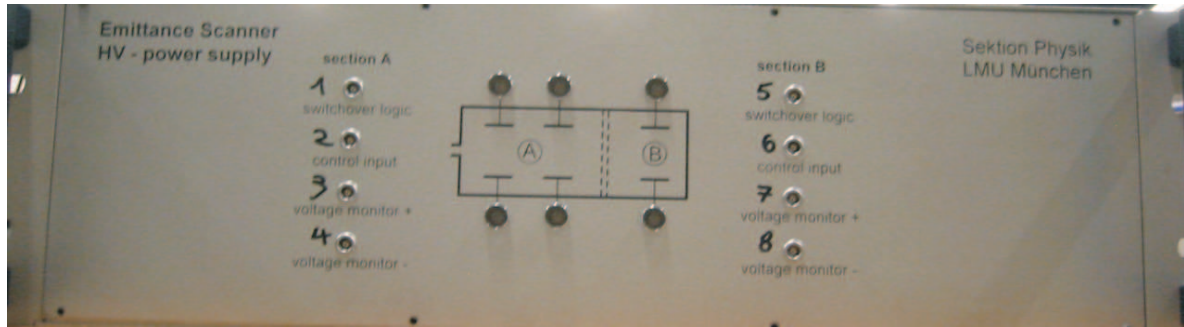


Figure A.5: Front side of the Control Unit. The lemo connectors from cable junction are connected according to the numbers.

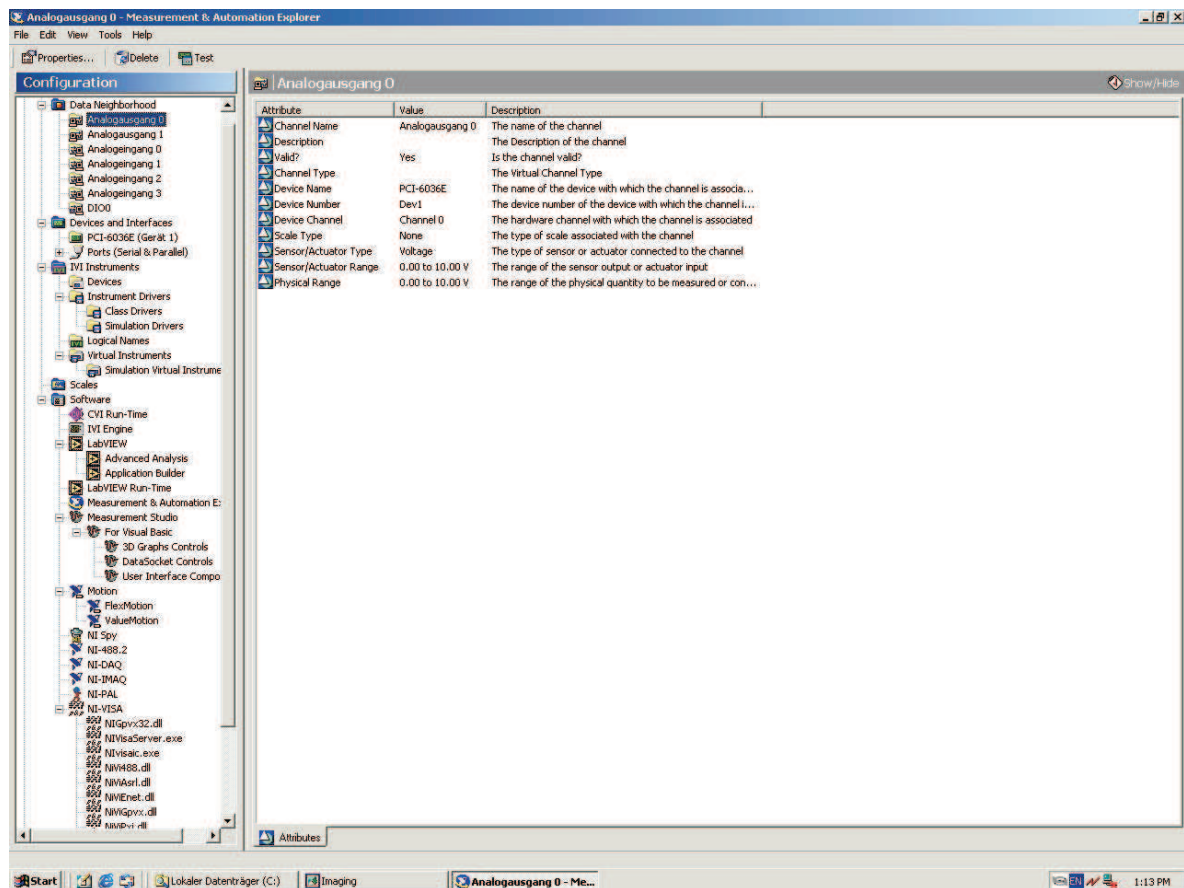


Figure A.6: Main window of the driver config program. The channels in the "data neighborhood" are important. The values assigned to the first channel are shown to the right.

A.4 Assembly Instructions

1. The MLL-Emi-double-cross should be placed on top of the support stand with the knob pointing upwards. The double-cross should be levelled and connected to the beam line in question. A pump or pumping station can be connected to the foreseen flange. The faraday cup or photomultiplier should be installed depending on the expected ion current. A feedthrough flange for the current signal is required to close the emi.

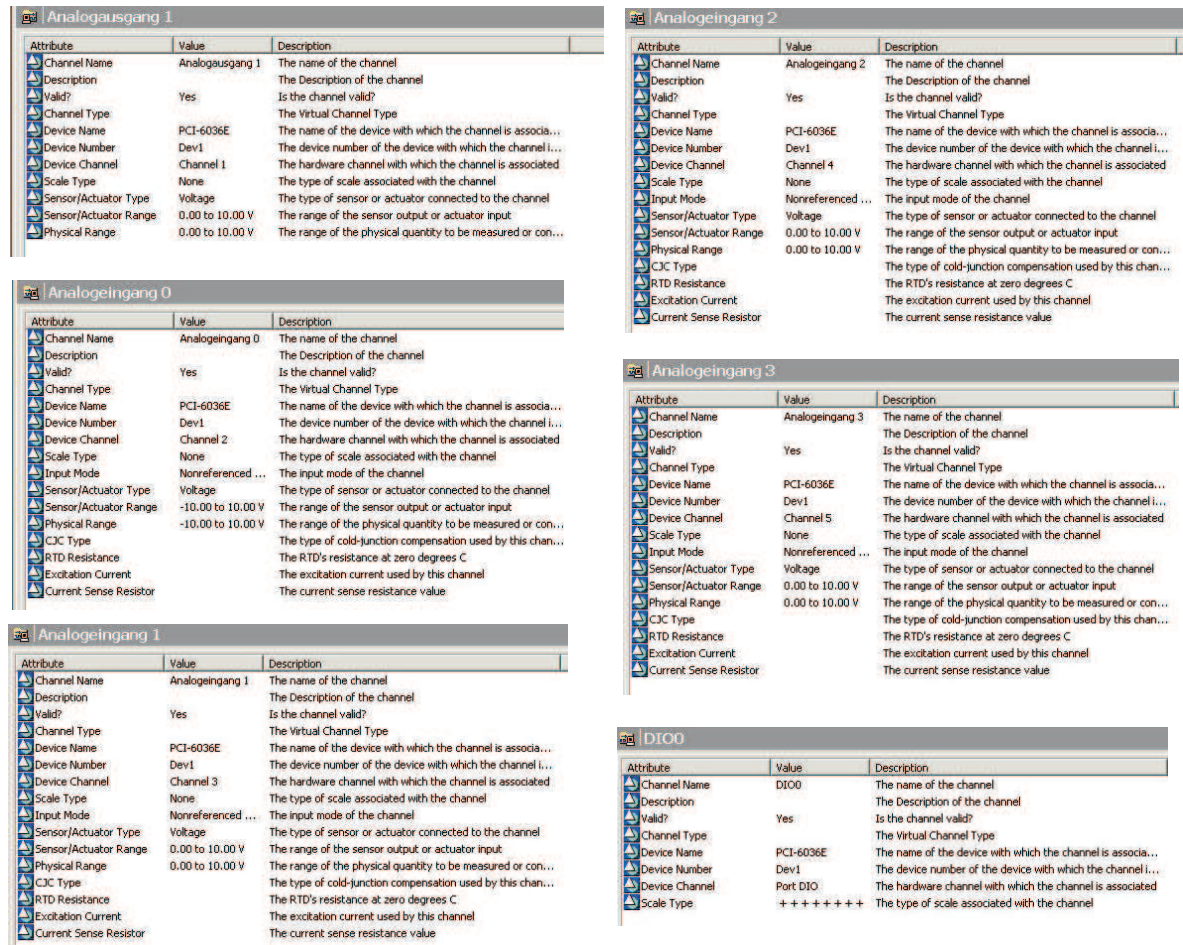


Figure A.7: Screen-shots of configuration of all channels.

2. Connect the x' x' SHV connectors at the EMI with the connectors labelled A on the controll unit. The exact combination does not matter. It only leads to a mirror effect in the emittance picture. Also connect the remaining to connectors to B.
3. Take the Cable Junction and connect the eight lemo connectors to the control unit, following the numbers. e.g. 1 to 1 and so on.
4. Connect the Cable Junction with the PC using the SCSI-cable.
5. Connect the faraday cup/photomultiplier to the ampere meter
6. Use the banana plugs connected to the Cable Junction to connect it to the analogue output of the ampere meter
7. Connect the ground wire of the Cable Junction to the appropriate connector on the back of the control unit.
8. Switch on, the control unit and the PC.

A.5 Measurement

1. Start the Labview program "Emi-meter-4". See Fig. B.9

2. Click the Run button.
3. Enter your beam energy.
4. Adjust the spacial and angular range you want to scan.
5. Adjust the step width you want.
6. Adjust the scanning time per point. This is 400 ms per default. However, this is to low. The power supplies need at least 600 ms to achieve the desired voltages. Good values are between 600 ms and 1000 ms. Once the voltage read-back functions a shorter time can be used.
7. Click Start
8. Tell the programm where you want to save your data
9. Wait until it is done

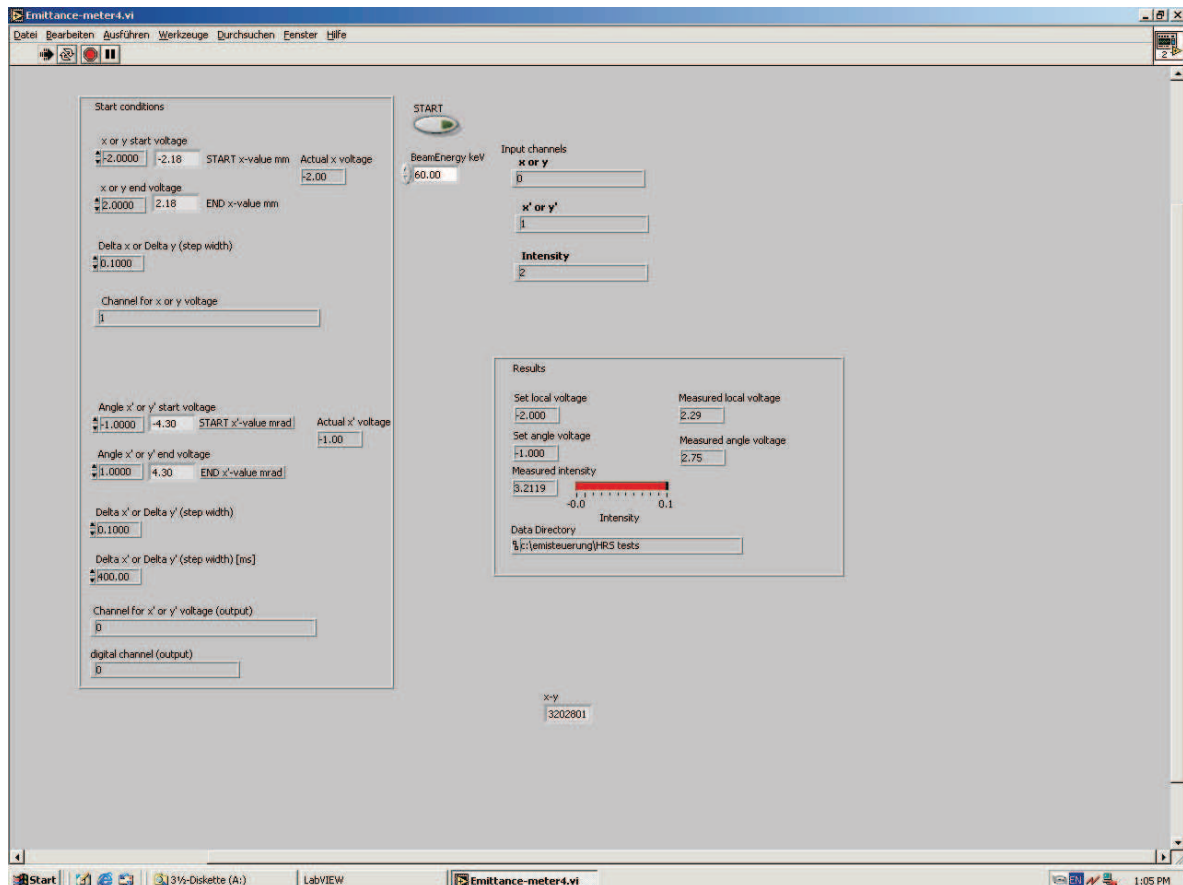


Figure A.8: Screen-shot of control programm for MLL-Emi.

A.6 Output

Five columns are saved in the output file of your choice. The first to contain the set angular voltages for position and angle. In the third and forth column the measured values are noted,

however, these are incorrect until the issue is fixed. The fifth column contains the ion current. Column one, two and five can be used to create a regular matrix using Origin. This matrix can be used for emittance plots.

A.7 General remarks

The MLL-Emi is a reliable, straight forward and easy to use emittance measurement device. However, it has certain limitations. The primary problem is, it takes very long to scan the beam profile. Depending on the detail level required and the waiting time used a measurement can take 10 minutes or more. Instabilities in the beam position or fluctuations in the ion intensity can affect the outcome of the measurement leading to smaller or larger emittances. The best approach depends on the specific setup used, however, it might be better to make a series of coarse, but fast measurements and average over many of those than making one high resolution but slow measurement.

B Mattauch Herzog separator

Original calculations by Mattauch and Herzog do not use the matrix formalism. For better understanding the transfer matrix for the mass separator is derived here.

As shown in Fig. 3.18 the separator consists of a drift length D_1 an electrostatic deflector E and another drift D_2 followed by the magnetic dipole M. Optionally there can be a further drift D_3 after the magnet. In case of the original layout this drift is zero.

The relation between the position vectors \vec{x}_0 at the x focus in front of the separator and \vec{x}_1 in the focal plane x_2 after the magnet can be written as:

$$\begin{pmatrix} x_1 \\ a_1 \\ \delta_k \\ \delta_m \end{pmatrix} = \begin{pmatrix} (x|x) & (x|a) & (x|\delta_k) & (x|\delta_m) \\ (a|x) & (a|a) & (a|\delta_k) & (a|\delta_m) \\ 0 & 0 & 1 & 0 \\ 0 & 0 & 0 & 1 \end{pmatrix} \begin{pmatrix} x_0 \\ a_0 \\ \delta_k \\ \delta_m \end{pmatrix} \quad (\text{B.1})$$

Where x is the distance from the optic axis, a is the angle of inclination towards the optic axis, δ_m and δ_k are the mass dispersion, respectively the energy dispersion.

The transfer Matrix for the whole mass separator T can be obtained by multiplying the transfer matrices for the sub elements D_1 , D_2 , D_3 , E and M.

$$T = D_3 \cdot M \cdot D_2 \cdot E \cdot D_1 \quad (\text{B.2})$$

Matrices for drift length are written as:

$$D_i = \begin{pmatrix} 1 & L_i & 0 & 0 \\ 0 & 1 & 0 & 0 \\ 0 & 0 & 1 & 0 \\ 0 & 0 & 0 & 1 \end{pmatrix} \quad (\text{B.3})$$

The transfer matrix for a radially inhomogeneous Sector Field is slightly more complicated. Depending on the parameter h , which is 0 for magnetic sector field, and 1 for electrostatic sector field,

$$\begin{aligned} h_{magnetic} &= 0 \\ h_{electric} &= 1 \end{aligned} \quad (\text{B.4})$$

the transfer matrix writes as:

$$S = \begin{pmatrix} c_x & s_x & d_x N_k & d_x N_m \\ -s_x k_x^2 & c_x & (s_x/\rho_0) N_k & (s_x/\rho_0) N_m \\ 0 & 0 & 1 & 0 \\ 0 & 0 & 0 & 1 \end{pmatrix} \quad (\text{B.5})$$

with

$$k_x^2 \rho_0^2 = 1 - n_1 + h/(1 + 2\eta_0)^2 \quad (\text{B.6})$$

$$\eta_0 = \frac{1}{2} \left(\frac{1}{\sqrt{1 - \frac{v^2}{c^2}}} - 1 \right) \quad (\text{B.7})$$

$$k_y^2 \rho_0^2 = n_1 \quad (\text{B.8})$$

$$c_x = \cos(k_x \rho_0 \Phi_0) \quad (\text{B.9})$$

$$s_x = \frac{\sin(k_x \rho_0 \Phi_0)}{k_x} \quad (\text{B.10})$$

$$d_x = \frac{1 - \cos(k_x \rho_0 \Phi_0)}{\rho_0 k_x^2} \quad (\text{B.11})$$

$$N_k = \frac{(1 + 2\eta_0)^2 + h}{2(1 + \eta_0)(1 + 2\eta_0)} \quad (\text{B.12})$$

$$N_m = \frac{(1 + 2\eta_0) - h}{2(1 + \eta_0)(1 + 2\eta_0)} \quad (\text{B.13})$$

In the situation at hand n_1 vanishes, v_0 is small compared to c , leading to negligible η_0 . This simplifies the equations, especially N_k and N_m become 1 and 0 for an electrostatic sector field and 1/2 for a magnetic sector field.

Now the matrix multiplication can begin, starting with $E \cdot D1$.

$$E \cdot D1 = \begin{bmatrix} \cos(\sqrt{2}\Phi_e) & \cos(\sqrt{2}\Phi_e)L1 + 1/2 \sin(\sqrt{2}\Phi_e)\sqrt{2}\rho & -1/2 (-1 + \cos(\sqrt{2}\Phi_e)) \rho & 0 \\ \frac{\sin(\sqrt{2}\Phi_e)\sqrt{2}}{\rho} & \frac{-\sin(\sqrt{2}\Phi_e)\sqrt{2}L1 + \cos(\sqrt{2}\Phi_e)\rho}{\rho} & 1/2 \sin(\sqrt{2}\Phi_e)\sqrt{2} & 0 \\ 0 & 0 & 1 & 0 \\ 0 & 0 & 0 & 1 \end{bmatrix} \quad (\text{B.14})$$

In a second step D2 and M can be multiplied:

$$(x|x) = -[-\cos(\Phi_m)\rho_e \cos(\sqrt{2}\Phi_e) + \sin(\sqrt{2}\Phi_e)\sqrt{2} \cos(\Phi_m) + \sin(\sqrt{2}\Phi_e)\sqrt{2} \sin(\Phi_m \rho_m)]/\rho_e \quad (\text{B.15})$$

$$(x|a) = \frac{1}{2} [2L_1 \cos(\Phi_m) \cos(\sqrt{2}\Phi_e)\rho_e - 2\sqrt{2}L_1L_2 \cos(\Phi_m) \sin(\sqrt{2}\Phi_e) - 2L_1\rho_m \sin(\Phi_m) \sin(\sqrt{2}\Phi_e) + \sqrt{2}\rho_e^2 \cos(\Phi_m) \sin(\sqrt{2}\Phi_e) + 2L_2 \cos(\Phi_m) \cos(\sqrt{2}\Phi_e) + 2\rho_m \sin(\Phi_m) \cos(\sqrt{2}\Phi_e)]/\rho_e \quad (\text{B.16})$$

$$\begin{aligned}
(x|\delta_k) &= \frac{1}{2}\rho_m \cos(\Phi_m) - \frac{1}{2}\rho_e \cos(\Phi_m) \cos(\sqrt{2}\Phi_e) \\
&\quad + \frac{1}{2}\sqrt{2}L_2 \cos(\Phi_m) \sin(\sqrt{2}\Phi_e) + \frac{1}{2}\rho_m \\
&\quad + \frac{1}{2}\rho_m \sin(\Phi_m) \sin(\sqrt{2}\Phi_e) - \frac{1}{2}\rho_m \cos(\Phi_m)
\end{aligned} \tag{B.18}$$

$$(x|\delta_m) = \frac{1}{2}(1 - \cos(\Phi_m))\rho_m \tag{B.19}$$

$$\begin{aligned}
(a|x) &= -[\rho_e \sin(\Phi_m) \cos(\sqrt{2}\Phi_e) - \sqrt{2}L_2 \sin(\Phi_m) \sin(\sqrt{2}\Phi_e) \\
&\quad + \sqrt{2}\rho_m \cos(\Phi_m) \sin(\sqrt{2}\Phi_e)]/(\rho_e\rho_m)
\end{aligned} \tag{B.20}$$

$$\begin{aligned}
(a|a) &= -\frac{1}{2}[2L_1\rho_e \sin(\Phi_m) \cos(\sqrt{2}\Phi_e) - 2L_1L_2 \sin(\Phi_m) \sin(\sqrt{2}\Phi_e) \\
&\quad - 2\rho_e \cos(\Phi_m) \cos(\sqrt{2}\Phi_e) \\
&\quad + 2L_1\rho_m \cos(\Phi_m) \sin(\sqrt{2}\Phi_e) + \sqrt{2}\rho_e^2 \sin(\Phi_m) \sin(\sqrt{2}\Phi_e) \\
&\quad + 2L_2\rho_e \sin(\Phi_m) \cos(\sqrt{2}\Phi_e)]/(\rho_e\rho_m)
\end{aligned} \tag{B.21}$$

$$\begin{aligned}
(a|\delta_k) &= \frac{1}{2}[-\rho_e \cos(\Phi_m) + \rho_e \sin(\Phi_m) \cos(\sqrt{2}\Phi_e) + \sqrt{2}\rho_m \cos(\Phi_m) \sin(\sqrt{2}\Phi_e) \\
&\quad - \sqrt{2}L_2 \sin(\Phi_m) \sin(\sqrt{2}\Phi_e) + \rho_m \sin(\Phi_m)]/\rho_m
\end{aligned} \tag{B.22}$$

$$(a|\delta_m) = \frac{1}{2} \sin(\Phi_m) \tag{B.23}$$

For a Mattauch and Herzog mass separator $(x|a)$ and $(x|\delta_k)$ must vanish simultaneously, leading to a focus in energy and x while $(x|\delta_m)$ is non-zero and some mass separation is preserved.

A closer look at equation B.17 reveals that $(x|\delta_k) = 0$ for $\Phi_m = \frac{\pi}{2}$. Using the same angle in equation B.16 all terms with the cosine of Φ_m vanish, and it remains:

$$\begin{aligned}
(x|a) &= 0 \\
L_1\sqrt{2} \sin(\sqrt{2}\Phi_e) &= \cos(\sqrt{2}\Phi_e)
\end{aligned} \tag{B.24}$$

The terms are equal for $\Phi_e = \frac{\pi}{4\sqrt{2}}$ and $L_1 = \rho_e/\sqrt{2}$. With this parameters the transfer matrix simplifies to:

$$T_{MH} = \begin{pmatrix} \rho_m/\rho_e & 0 & 0 & \frac{1}{2}\rho_m \\ \frac{1}{2} \frac{\sqrt{2\rho_e-2L_2}}{\rho_m\rho_e} & \frac{\rho_e}{\rho_m} & -\frac{1}{4} \frac{-2\rho_e+\sqrt{2\rho_e-2L_2}+2\rho_m}{\rho_m} & -\frac{1}{2} \\ 0 & 0 & 1 & 0 \\ 0 & 0 & 0 & 1 \end{pmatrix} \quad (\text{B.25})$$

With the transfer matrix at hand the mass resolving power $\frac{m}{\Delta m}$ can easily be calculated. It increases with $(x|\delta_m)$, but is indirect proportional to the x diameter R in the focal plane, which is given by

$$R = (x|x)2x_0 \quad (\text{B.26})$$

with $(x|x)$ being the x magnification from the transfer matrix and x_0 the initial x derivation from the optic axis. This gives the mass resolving power:

$$\begin{aligned} \frac{m}{\Delta m} &= \frac{(x|\delta_m)}{R} \\ &= \frac{(x|\delta_m)}{(x|x)2x_0} \\ &= \frac{\frac{1}{2}\rho_m}{2\frac{\rho_m}{\rho_e}x_0} \\ &= \frac{\rho_e}{4x_0} \end{aligned} \quad (\text{B.27})$$

C Beam emittance definitions

The beam emittance is a measure for ion beam quality, which describes the phase space occupied by the beam particles [83]. For the purpose of ion optic design the transversal emittance describing the x-x' and y-y' phase space area are of primary interest. The information included in the emittance is the spacial dimension as well as the inclination of the beam at a given position.

For beams of constant energy Liouville's theorem is always obeyed. It states that the phase space volume is invariant. Note, that only the volume is a constant.

For beams of varying energy Liouville's theorem is no longer valid and the emittance changes proportional to:

$$\epsilon \sim \frac{1}{p} \sim \frac{1}{v} \sim \frac{1}{\sqrt{E_{kin}}} \quad (\text{C.1})$$

It is therefore useful to define the normalized emittance as

$$\epsilon_N = \beta\gamma\epsilon \quad (\text{C.2})$$

which does not change with energy, so that Liouville's theorem is now valid for the normalized emittance.

For practical purposes the general emittance definition via the occupied phase space area is not always justified. In many ion optic cases the the beam occupies some elliptic phase space area. This ellipse can be distorted by image aberrations. In this case the emittance as defined above stays constant and will be from here on referred to as *absolute emittance*. The distorted beam however, is usually larger and requires a bigger phase space area. The area of the circumference including the absolute emittance is referred to as the *effective emittance*. Since the way the circumference is drawn can be subject to discussion, Lapostolle [84] was the first to suggest a more mathematic definition.

If a statistical distribution of points is given as in Fig. C.1 the dispersion σ_x^2 and $\sigma_{x'}^2$ of points from the x and x' axis can be calculated. The root mean square, r.m.s. emittance is than defined by:

$$\epsilon_{rms} = 2\sigma_x \cdot 2\sigma_{x'} \quad (\text{C.3})$$

This is for the most common case, where particles of 2σ derivation from the mean are accounted for in the emittance. If a reduction or increase is desired the factor 4 changes to 1 or 9 depending on the desired accuracy. The expression C.3 can be rewritten to:

$$\epsilon_{rms} = 4\sqrt{x^2 \cdot x'^2 - xx'^2} \quad (\text{C.4})$$

This is a rather general definition. For the purpose of consistency a definition based on the transfer matrix coefficients would be better. To achieve this the general definition must be restricted to the common cases of a elliptic phase space.

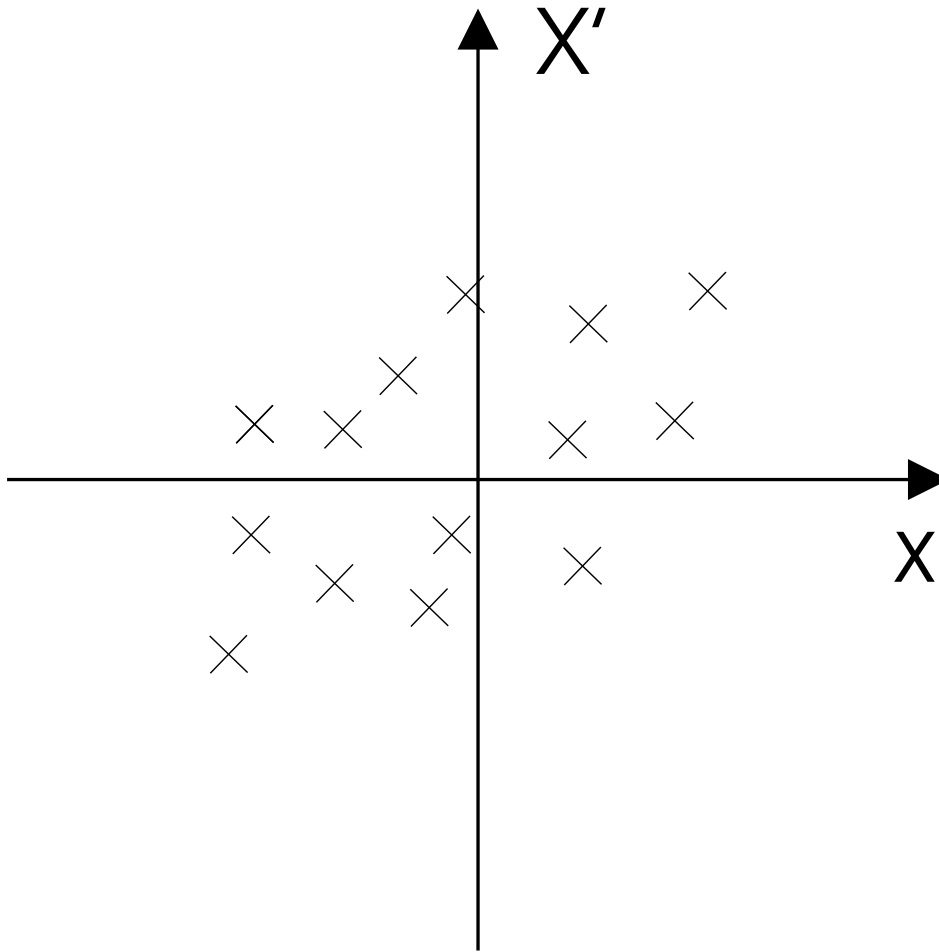


Figure C.1: Statistical distribution of points.

The correlation between two sets of coordinates of an arbitrary trajectory at $t=0$ and $t=n$ is given by the transfer matrix equation:

$$\begin{pmatrix} x_n \\ a_n \end{pmatrix} = \begin{pmatrix} (x|x) & (x|a) \\ (a|x) & (a|a) \end{pmatrix} \begin{pmatrix} x_0 \\ a_0 \end{pmatrix} \quad (\text{C.5})$$

The ellipse area, containing all particles can be parameterized with Twiss parameters, first introduced by Courant and Snyder [85] in 1958, as displayed in Fig. C.2. Using this formalism gives two equations:

$$\epsilon_x = C_0 x_0^2 + 2A_0 x_0 a_0 + B_0 a_0^2 \quad (\text{C.6})$$

$$\epsilon_x = C_n x_n^2 + 2A_n x_n a_n + B_n a_n^2 \quad (\text{C.7})$$

Equation C.5 can be inverted:

$$\begin{pmatrix} x_0 \\ a_0 \end{pmatrix} = \begin{pmatrix} (a|a) & -(x|a) \\ -(a|x) & (x|x) \end{pmatrix} \begin{pmatrix} x_n \\ a_n \end{pmatrix} \quad (\text{C.8})$$

Now, x_0 and a_0 can be inserted into equation C.6. Comparison of the coefficients assigned to $x_n^2, x_n a_n, a_n^2$ leads to a 3x3 matrix for A_n, B_n and C_n :

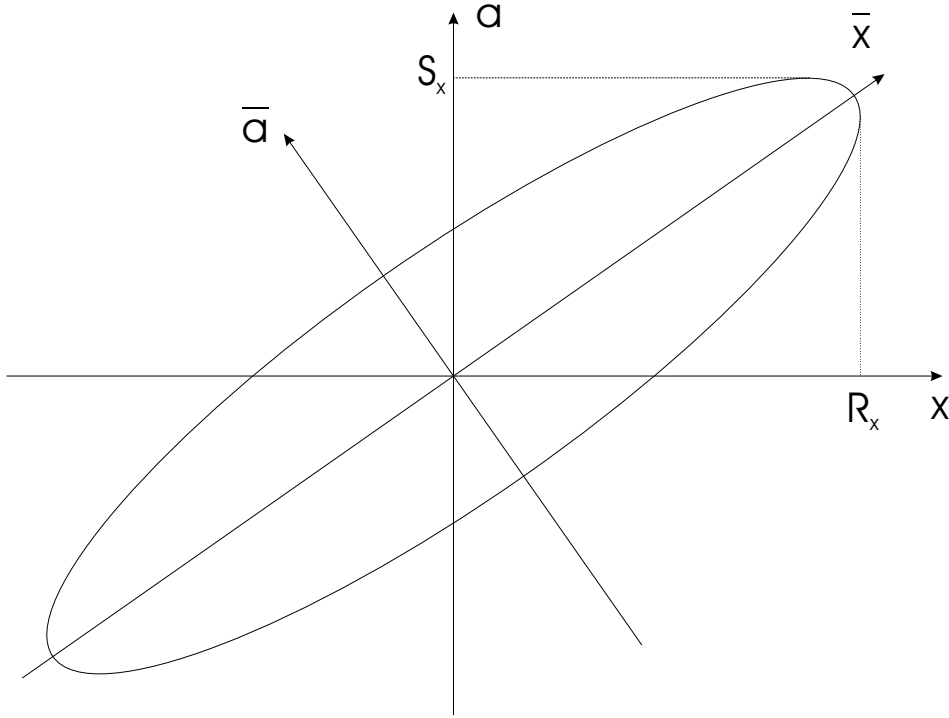


Figure C.2: Ellipse and Twiss parameters.

$$\begin{pmatrix} B_n \\ A_n \\ C_n \end{pmatrix} = \begin{pmatrix} (x|x)^2 & -2(x|x)(x|a) & (x|a)^2 \\ -(x|x)(a|x) & (x|x)(a|a) + (x|a)(a|x) & -(x|a)(s|a) \\ (a|x)^2 & -2(a|x)(a|a) & (a|a)^2 \end{pmatrix} \begin{pmatrix} B_0 \\ A_0 \\ C_0 \end{pmatrix} \quad (\text{C.9})$$

Assuming an upright ellipse at $t=0$ with phase space area $\epsilon_x \pi = x_{00} a_{00} \pi$, $A_0 = 0$ and $B_0 = 1/C_0 = x_{00}/a_{00}$ the matrix equations C.9 can be rewritten to:

$$\epsilon_x B_n = (x|x)^2 x_{00}^2 + (x|a)^2 a_{00}^2 = \sigma_{11} \quad (\text{C.10})$$

$$-\epsilon_x A_n = (x|x)(a|x) x_{00}^2 + (a|a)(x|a) a_{00}^2 = \sigma_{12} \quad (\text{C.11})$$

$$\epsilon_x C_n = (a|x)^2 x_{00}^2 + (a|a)^2 a_{00}^2 = \sigma_{22} \quad (\text{C.12})$$

Already introduced in this equations are the coefficients of the *Sigma-Matrix*. This is a 6x6 matrix from the type

$$\sigma = \begin{pmatrix} \sigma_x & 0 & 0 \\ 0 & \sigma_y & 0 \\ 0 & 0 & \sigma_z \end{pmatrix} \quad (\text{C.13})$$

with σ_x, σ_y and σ_z being the 2x2 *Sigma-Matrices* for the two transverse and longitudinal emittances. According to equation C.10 to C.12 σ_x is defined as:

$$\sigma_x = \begin{pmatrix} \sigma_{11} & \sigma_{12} \\ \sigma_{12} & \sigma_{22} \end{pmatrix} \quad (\text{C.14})$$

From this it is easy to calculate the maximum beam diameter at $t=n$, also referred to as beam envelope:

$$R_{x_n} = \sqrt{\sigma_{11}} = \sqrt{(x|x)^2 x_{00}^2 + (x|a)^2 a_{00}^2} \quad (\text{C.15})$$

Following the same pattern the maximum angle of inclination can be derived as:

$$S_{x_n} = \sqrt{\sigma_{22}} = \sqrt{(a|x)^2 x_{00}^2 + (a|a)^2 a_{00}^2} \quad (\text{C.16})$$

Analogously to equation 3.5 the mass resolving power can be calculated to be:

$$\frac{m}{\Delta m} = \frac{(x|\delta_m)}{R} \quad (\text{C.17})$$

$$= \frac{(x|\delta_m)}{\sqrt{\sigma_{11}}} \quad (\text{C.18})$$

Furthermore the emittance of the beam can be calculated from the Sigma-Matrix via the determinate.

$$\begin{aligned} \epsilon_x &= \sqrt{\det(\sigma_x)} \\ &= \sqrt{\sigma_{11}\sigma_{22} - \sigma_{12}^2} \end{aligned} \quad (\text{C.19})$$

D Matrix elements

Within this chapter, the 1st and 2nd order matrix elements, resulting from COSY infinity calculations, in the geometry as shown in Fig. 3.28 are listed.

Table D.1: First and second order COSY terms after magnet.

	x	a	y	b
x	-1.003726	2.217051	0	0
a	6.82E-06	-0.9963028	0	0
y	0	0	1.184953	0.9634225
b	0	0	6.097728	5.801656
l	0	0	0	0
d_k	1.49E-02	1.590237	0	0
d_m	0.5110985	1.84E-07	0	0
xx	1.687297	0.5694722	0	0
xa	0.8243934	-5.17058	0	0
aa	0.6410728	-1.825146	0	0
xy	0	0	-1.15E-16	0
yy	0	0	0	0
xb	0	0	-3.860977	-3.139157
ab	0	0	3.52E-02	2.86E-02
vb	-3.00E-16	0	0	0
bb	-1.49E-02	-1.590237	0	0
xd_k	0.5839076	-0.5653731	0	0
ad_k	2.089767	-5.195507	0	0
bd_k	0	0	-9.25E-02	0
yd_k	0	0	-5.070712	-3.669954
xd_m	-2.072272	0.496038	0	0
ad_m	0.708263	0.4925167	0	0
bd_m	0	0	-9.25E-02	0
yd_m	0	0	-3.208209	-2.155651
$d_k d_k$	-0.7884798	0.1107753	0	0
$d_k d_m$	-1.120237	0.2480191	0	0
$d_m d_m$	-0.1277747	-1.55E-07	0	0

Table D.2: First and second order COSY terms after ED2.

	x	a	y	b
x	2.584048	6.117032	0	0
a	5.10E-05	0.3871105	0	0
y	0	0	-0.1068103	-0.3406299
b	0	0	2.631119	-0.9714625
l	0	0	0	0
d_k	0.9409361	-7.12E-02	0	0
d_m	-1.315878	-3.553494	0	0
xx	-37.4362	-19.62948	0	0
xa	-7.167689	-5.751867	0	0
aa	-1.86898	-3.887471	0	0
xy	0	0	2.936667	6.80E-16
ay	0	0	0.2582611	0
yy	-0.1136357	-7.54E-02	0	0
xb	0	0	8.723279	1.109887
ab	0	0	0.7333794	-1.01E-02
vb	-0.6481689	-0.4303357	0	0
bb	-0.8858362	0.1078168	0	0
xd_k	-3.539644	-5.699879	0	0
ad_k	-7.923681	-18.22701	0	0
bd_k	0	0	9.017447	2.402342
yd_k	0	0	48.72741	14.20324
xd_m	44.75412	27.82229	0	0
ad_m	1.241067	-3.766077	0	0
bd_m	0	0	-3.311892	-0.5201438
yd_m	0	0	-14.03701	-1.830217
$d_k d_k$	6.566089	15.02677	0	0
$d_k d_m$	6.803494	15.39024	0	0
$d_m d_m$	-11.44355	-4.229113	0	0

Table D.3: First and second order COSY terms after ED3.

	x	a	y	b
x	5.404663	5.486432	0	0
a	-4.21E-06	0.1850211	0	0
y	0	0	-1.6659	-0.3406299
b	0	0	-1.815341	-0.9714625
l	0	0	0	0
d_k	3.514787	1.395479	0	0
d_m	-2.752097	-3.003393	0	0
xx	-305.0215	-120.4581	0	0
xa	-37.9934	-17.68405	0	0
aa	-4.503673	-3.921479	0	0
xy	0	0	6.889154	6.80E-16
ay	0	0	0.4531463	0
yy	-0.4171238	-0.2063395	0	0
xb	0	0	25.07565	1.109887
ab	0	0	1.242899	-1.01E-02
vb	-2.37924	-1.176944	0	0
bb	-3.31253	-1.295429	0	0
xd_k	-84.23679	-26.87643	0	0
ad_k	-20.1985	-17.62034	0	0
bd_k	0	0	21.05651	2.402342
yd_k	0	0	116.7124	14.20324
xd_m	350.5666	143.1428	0	0
ad_m	15.65602	3.891614	0	0
bd_m	0	0	-7.146558	-0.5201438
yd_m	0	0	-26.5606	-1.830217
$d_k d_k$	7.11994	12.47115	0	0
$d_k d_m$	57.46218	26.51886	0	0
$d_m d_m$	-96.75771	-37.98256	0	0

Table D.4: First and second order COSY terms after T4.

	x	a	y	b
x	1.284597	10.28572	0	0
a	2.26E-03	0.796516	0	0
y	0	0	-0.8872552	-1.27238
b	0	0	1.19E-05	-1.127054
l	0	0	0	0
d_k	1.810735	-2.100722	0	0
d_m	-0.6566842	-6.140138	0	0
xx	-204.9133	170.966	0	0
xa	-31.04382	6.147231	0	0
aa	-1.988452	-6.291684	0	0
xy	0	0	30.32129	5.870667
ay	0	0	2.418001	0.3861535
yy	-1.718404	-0.7701407	0	0
xb	0	0	41.42432	20.88875
ab	0	0	2.883446	1.063521
vb	-3.423726	-0.8108962	0	0
bb	-2.034692	1.880421	0	0
xd_k	28.34533	159.375	0	0
ad_k	-0.9436628	-24.85156	0	0
bd_k	0	0	36.20773	28.55852
yd_k	0	0	108.0848	109.0063
xd_m	243.1319	-178.1979	0	0
ad_m	17.01122	-14.85895	0	0
bd_m	0	0	-20.30993	-6.574994
yd_m	0	0	-33.76106	-22.61628
$d_k d_k$	2.267636	76.85671	0	0
$d_k d_m$	-15.33431	-67.23262	0	0
$d_m d_m$	-71.21488	54.98215	0	0

Table D.5: First and second order COSY terms after T6.

	x	a	y	b
x	-2.434182	-8.711423	0	0
a	6.46E-06	-0.4107925	0	0
y	0	0	1.585815	1.936361
b	0	0	-0.3797095	0.1669458
l	0	0	0	0
d_k	-3.522443	-3.846137	0	0
d_m	1.239499	4.901415	0	0
xx	398.2531	469.1708	0	0
xa	60.22564	81.114	0	0
aa	3.820872	8.592148	0	0
xy	0	0	-66.8648	-60.60164
ay	0	0	-5.359826	-4.820587
yy	3.327633	5.054146	0	0
xb	0	0	-87.0142	-84.6991
ab	0	0	-6.188395	-5.837847
vb	6.63391	9.702226	0	0
bb	3.955469	4.565766	0	0
xd_k	5.590684	-107.5728	0	0
ad_k	5.408235	18.41173	0	0
bd_k	0	0	-77.33901	-77.15263
yd_k	0	0	-210.5394	-230.464
xd_m	-472.4244	-570.9454	0	0
ad_m	-33.0675	-38.61373	0	0
bd_m	0	0	44.1117	41.85787
yd_m	0	0	69.22314	69.85866
$d_k d_k$	3.154694	-41.16942	0	0
$d_k d_m$	-5.228066	44.03614	0	0
$d_m d_m$	138.4	166.1981	0	0

Table D.6: First and second order COSY terms after ED5.

	x	a	y	b
x	-2.46786	-11.44662	0	0
a	-1.16E-03	-0.4105995	0	0
y	0	0	5.989965	1.936361
b	0	0	-2.92E-07	0.1669458
l	0	0	0	0
d_k	-2.544431	-7.245493	0	0
d_m	1.257973	6.293982	0	0
xx	249.7902	858.1499	0	0
xa	48.60344	143.1249	0	0
aa	3.613226	12.74955	0	0
xy	0	0	-165.6667	-60.60164
ay	0	0	-14.73348	-4.820587
yy	-0.4021749	6.686763	0	0
xb	0	0	-276.2925	-84.6991
ab	0	0	-19.32914	-5.837847
vb	6.038041	16.79908	0	0
bb	3.954992	8.99903	0	0
xd_k	-158.3465	-145.7236	0	0
ad_k	-0.8710084	22.2369	0	0
bd_k	0	0	-230.5016	-77.15263
yd_k	0	0	-732.7932	-230.464
xd_m	-308.0437	-1037.141	0	0
ad_m	-26.59228	-72.57884	0	0
bd_m	0	0	115.4348	41.85787
yd_m	0	0	226.054	69.85866
$d_k d_k$	-42.45934	-44.36485	0	0
$d_k d_m$	85.41337	61.63976	0	0
$d_m d_m$	92.87062	303.7926	0	0

E Radionuclide distribution

Within this chapter the results of the time dependent simulations, as described in Chapter 4, for isotopes with $T_{1/2} \geq 2$ d are listed. The chapter is ordered according to mass number and proton number, from ^{85}Kr to ^{135}Cs . Each isotope entry starts with the variable *JNUML=* followed by a number, the *chemical symbol* of the element, the *mass of the isotope* and the *half-life* of the isotope. Right of *total=* the total *number of isotopes* produced is given, followed by the resulting *activity* at the end of the reactor cycle. The lines below start with the *name of the surface*, followed by *sum=*, the *number of events* collected on that surface and the corresponding *activity*.

The name of the surfaces consists of an A or B indicating on which side of the source the surface can be found. The capital letter is followed by a short description of the surface, indicating its location and purpose (e.g. Berst 1 Kryo, for the 1st cryo-pump on the Rupture Disk Section). If a single device (e.g. the cryo-panels) is split in more than one surface, the different surfaces are numbered in the last part of the surface names.

Table E.1: ^{85}Kr distribution

JNUML= 2 Kr 85 T1/2=	10.70y -	total=	8155	2.271	GBq
A Berst 1 Kryo	sum=	311	86.604	MBq	
A Berst 2 Kryo	sum=	340	94.679	MBq	
A Multi Kryo	sum=	22	6.126	MBq	
B Kryo	sum=	7482	2.084	GBq	

Table E.2: ^{89}Sr distribution

JNUML= 4 Sr 89 T1/2=	50.50d -	total=	1849	39.820	GBq
Quelle	sum=	68	1.464	GBq	
A panel stirn	sum=	80	1.723	GBq	
A panel a1	sum=	383	8.248	GBq	
A panel a2	sum=	12	258.430	MBq	
A panel i1	sum=	27	581.467	MBq	
A panel i2	sum=	28	603.003	MBq	
A panel i3	sum=	100	2.154	GBq	
A panel i4	sum=	76	1.637	GBq	
A panel i5	sum=	13	279.966	MBq	
A Schlitze	sum=	518	11.156	GBq	
B panel st+a1	sum=	285	6.138	GBq	
B panel a2	sum=	207	4.458	GBq	
B panel i1	sum=	52	1.120	GBq	

Table E.3: ^{90}Y

JNUML= 6 Y 90 T1/2=	2.67d -	total=	38	15.498	GBq
	A panel i2	sum=	8	3.263	GBq
	A Schlitze	sum=	12	4.894	GBq
	B panel st+a1	sum=	6	2.447	GBq
	B panel a2	sum=	12	4.894	GBq

Table E.4: ^{90}Sr

JNUML= 5 Sr 90 T1/2=	29.00y -	total=	191143	19.639	GBq
	Quelle	sum=	8508	874.157	MBq
	A Rohr innen 1	sum=	166	17.056	MBq
	A Rohr innen 3	sum=	58	5.959	MBq
	A panel stirn	sum=	6871	705.963	MBq
	A panel a1	sum=	32459	3.335	GBq
	A panel a2	sum=	1233	126.685	MBq
	A panel i1	sum=	5743	590.066	MBq
	A panel i2	sum=	4090	420.228	MBq
	A panel i3	sum=	15543	1.597	GBq
	A panel i4	sum=	8114	833.675	MBq
	A panel i5	sum=	2081	213.813	MBq
	A panel i6	sum=	55	5.651	MBq
	A panel i7	sum=	36	3.699	MBq
	A panel i8	sum=	41	4.213	MBq
	A Schlitze	sum=	51014	5.241	GBq
	B Rohr innen 2	sum=	8	.822	MBq
	B Rohr Mitte	sum=	14	1.438	MBq
	B panel st+a1	sum=	25762	2.647	GBq
	B panel a2	sum=	18962	1.948	GBq
	B panel i1	sum=	10268	1.055	GBq
	B panel i2	sum=	117	12.021	MBq

Table E.5: ^{91}Y distribution

JNUML= 7 Y 91 T1/2=	58.50d -	total=	3819	70.998	GBq
	Quelle	sum=	341	6.339	GBq
	A Rohr innen 1	sum=	7	130.135	MBq
	A Rohr innen 3	sum=	7	130.135	MBq
	A panel stirn	sum=	167	3.105	GBq
	A panel a1	sum=	430	7.994	GBq
	A panel a2	sum=	7	130.135	MBq
	A panel i1	sum=	81	1.506	GBq
	A panel i2	sum=	76	1.413	GBq
	A panel i3	sum=	232	4.313	GBq
	A panel i4	sum=	119	2.212	GBq
	A panel i5	sum=	20	371.815	MBq
	A Schlitze	sum=	1581	29.392	GBq
	B panel st+a1	sum=	399	7.418	GBq
	B panel a2	sum=	195	3.625	GBq
	B panel i1	sum=	157	2.919	GBq

Table E.6: ^{93}Zr distribution

JNUML= 8 Zr 93 T1/2=	1.50M -	total=	186803	.371	MBq
	Quelle	sum=	108737	.216	MBq
	A Rohr innen 1	sum=	384	.001	MBq
	A Rohr innen 2	sum=	15	.000	MBq
	A Rohr innen 3	sum=	56	.000	MBq
	A panel stirn	sum=	367	.001	MBq
	A panel a1	sum=	1707	.003	MBq
	A panel a2	sum=	28	.000	MBq
	A panel i1	sum=	313	.001	MBq
	A panel i2	sum=	222	.000	MBq
	A panel i3	sum=	911	.002	MBq
	A panel i4	sum=	383	.001	MBq
	A panel i5	sum=	121	.000	MBq
	A panel i6	sum=	8	.000	MBq
	A Schlitze	sum=	70539	.140	MBq
	B Rohr innen 2	sum=	16	.000	MBq
	B Rohr Mitte	sum=	31	.000	MBq
	B panel st+a1	sum=	1301	.003	MBq
	B panel a2	sum=	1072	.002	MBq
	B panel i1	sum=	592	.001	MBq

Table E.7: ^{95}Nb distribution

JNUML= 12 Nb 95 T1/2=	35.00d -	total=	5198	161.518	GBq
	Quelle	sum=	5121	159.125	GBq
	A Schlitze	sum=	77	2.393	GBq

Table E.8: ^{95}Zr distribution

JNUML= 9 Zr 95 T1/2=	64.00d -	total=	4501	76.486	GBq
	Quelle	sum=	4455	75.704	GBq
	A Schlitze	sum=	46	781.683	MBq

Table E.9: ^{125}Sb distribution

JNUML= 14 Sb125 T1/2=	2.70y -	total=	289	318.929	MBq
	Quelle	sum=	245	270.372	MBq
	A Rohr innen 1	sum=	8	8.828	MBq
	A Schlitze	sum=	36	39.728	MBq

Table E.10: ^{129}I distribution

JNUML= 22 I 129 T1/2=	17.00M -	total=	14332	.003	MBq
	A Schlitze	sum=	1583	.000	MBq
	A Berst 1 Kryo	sum=	557	.000	MBq
	A Berst 2 Kryo	sum=	476	.000	MBq
	A Multi Kryo	sum=	18	.000	MBq
	A Absorber	sum=	8	.000	MBq
	B Kryo	sum=	11690	.002	MBq

Table E.11: ^{135}Cs distribution

JNUML= 28 Cs135 T1/2=	3.00M -	total=	356736	.354	MBq
	A panel stirn	sum=	17967	.018	MBq
	A panel a1	sum=	88582	.088	MBq
	A panel a2	sum=	2857	.003	MBq
	A panel i1	sum=	16436	.016	MBq
	A panel i2	sum=	11688	.012	MBq
	A panel i3	sum=	40760	.040	MBq
	A panel i4	sum=	22343	.022	MBq
	A panel i5	sum=	5287	.005	MBq
	A panel i6	sum=	249	.000	MBq
	A panel i7	sum=	84	.000	MBq
	A panel i8	sum=	96	.000	MBq
	A Berst 1 Kryo	sum=	71	.000	MBq
	A Berst 2 Kryo	sum=	56	.000	MBq
	A Multi Kryo	sum=	13	.000	MBq
	B panel st+a1	sum=	70448	.070	MBq
	B panel a2	sum=	50089	.050	MBq
	B panel i1	sum=	28128	.028	MBq
	B panel i2	sum=	263	.000	MBq
	B Kryo	sum=	1319	.001	MBq

Table E.12: ^{137}Cs distribution

JNUML= 29 Cs137 T1/2=	30.00y -	total=	333786	33.152	GBq
	Quelle	sum=	15068	1.497	GBq
	A Rohr innen 1	sum=	53	5.264	MBq
	A Rohr innen 3	sum=	6	.596	MBq
	A panel stirn	sum=	12889	1.280	GBq
	A panel a1	sum=	65453	6.501	GBq
	A panel a2	sum=	2131	211.652	MBq
	A panel i1	sum=	11522	1.144	GBq
	A panel i2	sum=	7990	793.570	MBq
	A panel i3	sum=	30139	2.993	GBq
	A panel i4	sum=	16596	1.648	GBq
	A panel i5	sum=	3759	373.345	MBq
	A panel i6	sum=	150	14.898	MBq
	A panel i7	sum=	66	6.555	MBq
	A panel i8	sum=	64	6.357	MBq
	A Schlitze	sum=	58608	5.821	GBq
	B panel st+a1	sum=	50710	5.037	GBq
	B panel a2	sum=	36991	3.674	GBq
	B panel i1	sum=	21386	2.124	GBq
	B panel i2	sum=	205	20.361	MBq

Table E.13: ^{141}Ce distribution

JNUML= 32 Ce141 T1/2=	33.00d -	total=	115	3.790	GBq
	Quelle	sum=	36	1.186	GBq
	A Schlitze	sum=	79	2.604	GBq

Table E.14: ^{144}Ce distribution

JNUML= 34 Ce144 T1/2=	284.00d -	total=	63066	241.507	GBq
	Quelle	sum=	60687	232.397	GBq
	A Rohr innen 1	sum=	47	179.983	MBq
	A Schlitze	sum=	2332	8.930	GBq

Bibliography

- [1] T. Baumann, The NSCL coupled cyclotron project: Status and latest news, in: Proceedings of the 16th international conference on the application of accelerators in research and industry, Denton, Te, American Institute of Physics, Melville, New York, 2001, p. 631.
- [2] U. Georg, J. Bennett, U. Bergmann, R. Catherall, P. Drumm, V. Fedoseyev, T. Giles, O. Jonsson, A. Junghans, U. Köster, E. Kugler, J. Lettry, V. Mishin, T. Nilsson, H. Ravn, K. Schmidt, H. Simon, C. Tamburella, the ISOLDE Collaboration, Radioactive ion beams at ISOLDE/CERN, recent developments and perspectives, in: B. Rubio, M. Lozano, W. Gelletly (Eds.), Experimental Nuclear Physics in Europe, ENPE'99, Sevilla, June 1999, AIP Conf. Proc. 495, Woodbury, NY, 1999, pp. 349–352.
- [3] D. Forkel-Wirth, G. Bollen (Eds.), ISOLDE – a laboratory portrait, Vol. 129, Hyp. Int., 2000.
- [4] T. Nilsson, et al., REX-ISOLDE – post-accelerated radioactive beams at CERN-ISOLDE, in: J. Duggan, I. Morgan (Eds.), Applications of Accelerators in Research and Industry, Proc. of the Sixteenth Int. Conf., Denton, AIP Conf. Proc. 576, Woodbury, NY, 2000, pp. 265–268.
- [5] D. Lunney, private communication.
- [6] Y. T. Oganessian, et al., Phys. Rev. C 70 (2004) 064609.
- [7] A. V. Belozеров, et al., Eur. Phys. J. A 16 (2003) 447–456.
- [8] ISAC-II a project for higher energies at ISAC, Tech. rep., TRIUMF, Vancouver, BC, Canada (1999).
- [9] <http://www.ganil.fr/eurisol>.
- [10] The HIE-ISOLDE report (draft), Tech. rep., CERN AB department (2005).
- [11] B. Fogelberg, H. Mach, L. Jacobsson, The OSIRIS facility and ion source at Studsvik, in: T. von Egidy, et al. (Eds.), Int. Workshop on Research with Fission Fragments, Benediktbeuern, October 1996, World Scientific, Singapore, 1997, pp. 69–73.
- [12] L. Jacobsson, B. Fogelberg, B. Ekström, G. Rudstam, An unconventional bi-mode ion source (ANUBIS) for the OSIRIS facility, Nucl. Instr. Meth. B 26 (1987) 223–226.
- [13] S. Borg, et al., On-line separation of isotopes at a reactor in Studsvik (OSIRIS), Nucl. Instr. Meth. 91 (1971) 109–116.
- [14] U. Köster, J. Pinston (Eds.), PIAFE (Production, Ionisation et Accélération des Faisceaux Exotiques), Project Report, Institut des Sciences Nucléaires, Grenoble, 1998.
- [15] U. Köster for the PIAFE Collaboration, Status report of the PIAFE project, in: G. Fioni, H. Faust, S. Oberstedt, F. Hamsch (Eds.), Nuclear Fission and Fission-Product Spectroscopy, Second Int. Workshop, Seyssins, France, AIP Conf. Proc. 447, Woodbury, NY, 1998, pp. 119–125.

- [16] Overview of the PIAFE project, Tech. rep., ISN Grenoble (1994).
- [17] G. de France (Ed.), The scientific objectives of the SPIRAL2 project, GANIL, Caen, 2006.
- [18] A. Mosnier (Ed.), The SPIRAL2 project APD report, GANIL, Caen, 2005.
- [19] <http://www.ganil.fr/research/developments/spiral2/index.html>.
- [20] T. Faestermann et al., The Munich Accelerator for Fission Fragments - MAFF, Nucl. Phys. 746 (2004) 22c–26c.
- [21] T. von Egidy, P. Kienle, U. Köster, D. Habs, M. Groß, O. Kester, H. Maier, P. Thirolf, the MAFF Collaboration, The Munich Accelerator for Fission Fragments (MAFF) at the new reactor FRM-II, Acta Phys. Slovaca 49 (1) (1999) 107–116.
- [22] O. Kester, D. Habs, M. Groß, R. Rao, T. Sieber, H. Bongers, A. Kolbe, H. Maier, P. Thirolf, T. von Egidy, U. Köster, E. Steichele, P. Kienle, H. Körner, A. Schempp, U. Ratzinger, The Munich accelerator for fission fragments (MAFF), in: K. Shepard (Ed.), Heavy Ion Accelerator Technology, HIAT'98, Chicago, October 1998, AIP Conf. Proc. 473, Woodbury, NY, 1998, pp. 536–545.
- [23] <http://www.frm2.tu-muenchen.de>.
- [24] G. Pfennig, H. Klewe-Nebenius, W. Seelmann-Eggebert, Karlsruher nuklidkarte sixth edition, Forschungszentrum Karlsruhe (1995).
- [25] D. Habs, R. Krücken, M. Groß, W. Assmann, L. Beck, T. Faesterman, R. Großmann, S. Heinz, O. Kester, H.-J. Maier, P. Thirolf, P. Maier-Komor, F. Nebel, E. Szerypo, J. amd Zech, MAFF - Munich Accelerator for Fission Fragments, Tech. rep., FRM-II (2004).
- [26] H.-J. Maier, D. Habs, M. Groß, R. Großmann, O. Kester, F. Ospald, P. G. Thirolf, MAFF fission target development, Tech. rep., FRM-II (2001).
- [27] H. Maier, D. Habs, M. Gross, R. Grossmann, O. Kester, P. Thirolf, Target development for the Munich fission fragment accelerator MAFF, Nucl. Instr. Meth. A 480 (2002) 1–6.
- [28] M. Groß, Berechnung zur Neutronik und Aktivierung des MAFF-Targets, Tech. rep., Sektion Physik d. LMU, Garching (1999).
- [29] U. Köster, Yields and spectroscopy of radioactive isotopes at LOHENGRIN and ISOLDE, Ph.D. thesis, TU München (2000).
- [30] F. Ospald, Aufbau und Test eines Ionenquellen-Prototypen für den Münchner Spaltfragmentbeschleuniger, LMU, Diplomarbeit (2003).
- [31] P. Maier-Komor, W. Assmann, M. Groß, D. Habs, J. Szerypo, O. Kester, P. G. Thirolf, F. Nebel, E. Zech, T. Faestermann, R. Krücken, The vacuum system for the Munich Fission Fragment Accelerator, Nucl. Instr. Meth. A 561 (2006) 66–75.
- [32] P. Thirolf, private communication.
- [33] D. Habs, T. von Egidy, M. Groß, O. Kester, P. Kienle, U. Köster, J. Pinston, P. Thirolf (Eds.), MAFF, Munich Accelerator for Fission Fragments, Physics Case and Technical Description, Ludwig-Maximilians-Universität, München, 1998.
- [34] S. Heinz, J. Äystö, D. Habs, S. Hegewisch, J. Huikari, A. Nieminen, S. Rinta-Antila, M. Schumann, J. Szerypo, A radio frequency ring electrode cooler for low-energy ion beams, Nucl. Instr. Meth. A 533 (2004) 239.

- [35] A. Nieminen, et al., Beam cooler for low-energy radioactive ions, *Nucl. Instr. Meth. A* 469 (2001) 244–253.
- [36] O. Kester, D. Habs, M. Gross, H. Maier, P. Thirolf, T. Sieber, T. Faestermann, T. von Egidy, U. Köster, Rnb production with thermal neutrons, *Nucl. Phys. A* 701 (2002) 71c–77c.
- [37] O. Kester, F. Wenander, R. Becker, Charge breeding of stable and radioactive ion beams with EBIS/T devices, *J. Phys. Conf. Ser.* 2 (2004) 107–116.
- [38] O. Kester, private communication.
- [39] NuPECC, Roadmap for Construction of Nuclear Physics Research Infrastructures in Europe.
- [40] T. Aumann, Reactions with fast radioactive beams of neutron-rich nuclei, *Eur. Phys. J. A* 26 (3) (2005) 441–478.
- [41] D. Habs, K. Blaum, M. Gross, S. Heinz, O. Kester, V. S. Kolhinen, J. Neumayr, U. Schramm, T. Schaetz, J. Szerypo, P. Thirolf, Penning trap system in Munich, *Eur. Phys. J. A Direct (ENAM)* DOI:10.1140/epjad/i2005-06-197-7.
- [42] N. Warr, J. Eberth, G. Pascovici, H. G. Thomas, D. Weihaar, MINIBALL: The first gamma-ray spectrometer using segmented, encapsulated germanium detectors for studies with radioactive beams, *Eur. Phys. J. A* 20 (2004) 65–66.
- [43] J. Simpson, et al., The AGATA Spectrometer, *Acta Physica Polonica B*36 (2005) 1383.
- [44] C. Düllmann, et al., Chemical investigation of hassium (element 108), *Nature* 418 (2002) 859–862.
- [45] J. Dvorak, W. Bröchle, M. Chelnokov, R. Dressler, C. E. Düllmann, K. Eberhardt, V. Gorschkov, E. Jäger, R. Krücken, A. Kuzentsov, Y. Nagame, F. Nebel, Z. Novackova, Z. Qin, M. Schädel, B. Schausten, E. Shimpf, A. Semchenkov, P. Thörle, A. Türler, M. Wegrzecki, B. Wierczinski, A. Yakushev, A. Yeremin, Doubly Magic ^{270}Hs , *Phys. Rev. Lett.* to be accepted.
- [46] H. Wollnik, *Optics of charged particles*, Academic Press, 1987.
- [47] U. Bergmann, L. Axelsson, J. Bennett, M. Borge, R. Catherall, P. Drumm, V. Fedoseyev, C. Forssén, L. Fraile, H. Fynbo, U. Georg, T. Giles, S. Grévy, P. Hornshøj, B. Jonson, O. Jonsson, U. Köster, J. Lettry, K. Markenroth, F. Marqués, V. Mishin, I. Mukha, T. Nilsson, G. Nyman, A. Oberstedt, H. Ravn, K. Riisager, G. Schrieder, V. Sebastian, H. Simon, O. Tengblad, F. Wenander, K. W. Rolander, Light exotic isotopes: recent beam developments and physics applications at ISOLDE, *Nucl. Phys. A* 701 (2002) 363c–368c.
- [48] D. Dahl, SIMION 3D v7.0, www.simion.com.
- [49] M. Reiser, *Theory and design of charged particle beams*, John Wiley & Sons Inc., 1994.
- [50] R. Becker, W. B. Hermannsfeldt, IGUN - a program for the simulation of positive ion extraction including magnetic fields, *Rev. Sci. Instr.* 63 (4) (1992) 2756–2761.
- [51] J. Matauch, R. Herzog, New mass spectrograph, *Z. Phys.* 89 (11-12) (1934) 786–795.
- [52] P. Spolaore, J. D. Larson, C. Signorini, S. Beghini, X.-K. Zhu, H.-Z. Si, A recoil mass spectrometer for the XTU tandem at LNL, *Nucl. Instr. Meth. A* 238 (1985) 381–392.

- [53] R. G. Gordon, H. Liang, Surface reactions in the chemical vapor deposition of highly transparent and conductive fluorine-doped zinc oxide, Book of Abstracts, 216th ACS National Meeting, PHYS-201, Boston, 1998.
- [54] R. Fairman, B. Ushkov, Properties of Chalcogenide Glasses, Academic Press, 2004.
- [55] G. Class, Movak3D, www.lv-soft.de (2004).
- [56] F. Nebel, E. Zech, T. Faestermann, R. Krücken, P. Maier-Komor, W. Assmann, J. Szerypo, M. Groß, D. Habs, O. Kester, P. G. Thirolf, R. Grötzschel, Time dependent radioactivity distribution at MAFF, Nucl. Instr. Meth. A 561 (2006) 83–89.
- [57] R. A. Haefer, Cryopumping, Clarendon Press, Oxford, 1989.
- [58] J. Galy, B. Fogelberg, F. Storrer, H. Mach, Yields of products from fast neutron-induced fission of ^{233}U measured by means of an Isotope Separator On-Line (ISOL) system, Eur. Phys. J. A 8 (2000) 331–354.
- [59] G. Rudstam, et al., Yields of products from thermal neutron-induced fission of ^{235}U , Radiochim. Acta 49 (1990) 155–191.
- [60] A. Wahl, Nuclear-charge distribution and delayed-neutron yields for thermal-neutron-induced fission of ^{235}U , ^{233}U and ^{239}Pu and for spontaneous fission of ^{252}Cf , At. Data Nucl. Data Tables 39 (1988) 1–156.
- [61] R. Firestone, V. Shirley (Eds.), Table of Isotopes, 8th Edition, John Wiley & Sons, New York, 1996.
- [62] K. Siegbahn, Alpha-, Beta-, and Gamma ray spectroscopy, North Holland, 1965.
- [63] P. Marmier, Kernphysik, Verlag des Vereins der Mathematiker und Physiker an der ETH Zürich, Zürich, 1968.
- [64] H. Krieger, Grundlagen der Strahlenphysik und des Strahlenschutzes, Teubner Verlag, 2004.
- [65] U. Köster, private communication.
- [66] K. H. Lieser, Nuclear and Radiochemistry, VCH, Weinheim, New York, 1997.
- [67] P. Rödder, et al., Hochflussneutronenquelle München (FRM-II) Betriebshandbuch, FRM-II, München, 2004.
- [68] D. R. Lide (Ed.), CRC Handbook of Chemistry and Physics, 82nd Edition, CRC Press, Boca Raton, 2002.
- [69] European Commission, Directive 96/62/EC (1996).
- [70] European Commission, Directive 99/30/EC (1999).
- [71] P. Maier-Komor, SPD Katalog, Materials Research GmbH, München, 1981.
- [72] H. Stöcker, Taschenbuch der Physik, Verlag Harri Deutsch, Frankfurt a. M., 2004.
- [73] V. Avrigeanu, S. Sudár, C. M. Buczkó, A. A. Filatenkov, S. V. Chuvaev, R. Dóczy, V. Semkova, V. A. Zelentsky, Energy dependence of the isomeric cross section ratio in the $^{58}\text{Ni}(n,p)^{58}\text{Co}^{m,g}$ reactions, Phys. Rev. C 60 (1999) 017602.
- [74] J. F. Ziegler, SRIM - The stopping and range of ions in matter, www.srim.org, 2004.

-
- [75] W. Eckstein, private communication.
- [76] J. W. Klett, Process for making carbon foam, US-patent: 6033506, 1997.
- [77] S. Emmhofer, LMU, Diplomarbeit (2001).
- [78] M. Wutz, H. Adam, W. Walcher, Theorie und Praxis der Vakuumtechnik, Friedr. Vieweg und Sohn, Braunschweig/Wiesbaden, 1981.
- [79] H.-J. Bargel (Ed.), Werkstoffkunde, Springer, Berlin, 2005.
- [80] C. Kittel, Einführung in die Festkörperphysik, Oldenbourg, München, 2006.
- [81] K. N. R. Taylor, M. I. Darby, Physics of Rare Earth Solids, Chapman and Hall Ltd., London, 1972.
- [82] L. Pauling, The Nature of the Chemical Bond, Cornell Univ., Cornell, 1960.
- [83] J. Buon, Beam phase space and emittance, CERN Accelerator School - Fifth General Accelerator Physics Course I (1994) 89.
- [84] P. M. Lapostolle, IEEE Trans. Nucl. Sci. NS-18 3 (1971) 1101.
- [85] E. D. Courant, H. S. Snyder, Theory of the Alternating-Gradient Synchrotron, Annals of Physics 3, 1-48, 1958.
- [86] A. Wilfart, Untersuchungen zur Optimierung von Ionenstrahlkühlern, LMU, Diplomarbeit (2002).

Acknowledgments

I like to thank all those who helped to make this work a success and supported me over the years.

In particular I would like to thank Prof. Dr. R. Krücken for giving me the opportunity to work on this interesting topic. I am grateful for his enduring support especially during times, when the overall perspectives of the project were dire. I am also thankful for the opportunities to present my work at various conferences and his help with the publication of parts of this work in respected journals.

This work has been financed by funds of the MLL and supported by many of the staff members. As a representative for all the MLL employees I thank W. Carli, who offered practical advice and fast uncomplicated support on many occasions.

Also this work did benefit from the friendly atmosphere at E12 and the immense knowledge already available at this chair. Exemplarily I would like to mention and thank Dr. R. Gernhäuser, Dr. T. Faestermann as well as Dr. P. Maier-Komor for sharing their knowledge whenever necessary.

Most of the technical investigations in this work would not have been possible without the help of the engineers of the FRM-II, where my thanks go to P. Jüttner. I also would like to thank the mechanics of the physics department and E12, especially R. Lang and M. Klöckner for their fast and unbureaucratic assistance.

In addition, I would like to thank Dr. T. Faestermann, Dr. P. Maier-Komor and Prof. Dr. R. Krücken for reading this work in advance and their helpful suggestions how this work can be improved.

My special thanks go to the other members of the MAFF collaboration. First of all I would like to thank Dr. M. Groß and Dr. P. G. Thirolf, who put a lot of time and dedication into the project from the very beginning until today. I also would like to thank R. Stöpler, who brought structure into the project and helped to focus the efforts of the various collaborators.

Finally, I would like to thank all those, who have helped to complete this work, but have not been mentioned by name.

Thank you all.